UNIVERSIDADE TÉCNICA DE LISBOA

INSTITUTO SUPERIOR TÉCNICO

Study of Anomalous Quartic Gauge Couplings and Search for Fermiophobic Higgs at LEP2

Sofia Andringa Dias

(Mestre)

Dissertação para obtenção do grau de Doutor em Física

Orientador: Doutor Mário João Martins Pimenta
Júri:
Presidente:
Reitor da Universidade Técnica de Lisboa
Vogais:
Doutor Augusto Manuel Carvalho Albuquerque Barroso
Doutor José Mariano Rebelo Pires Gago
Doutor Jorge Manuel Rodriques Crispim Romão
Doutor Jan Timmermans
Doutor Mário João Martins Pimenta

Setembro de 2003

UNIVERSIDADE TÉCNICA DE LISBOA

INSTITUTO SUPERIOR TÉCNICO

Study of Anomalous Quartic Gauge Couplings and Search for Fermiophobic Higgs at LEP2

Sofia Andringa Dias

(Mestre)

Dissertação para obtenção do grau de Doutor em Física

Orientador: Doutor Mário João Martins Pimenta

Júri:

Presidente:

Reitor da Universidade Técnica de Lisboa

Vogais:

Doutor Augusto Manuel Carvalho Albuquerque Barroso

Doutor José Mariano Rebelo Pires Gago

Doutor Jorge Manuel Rodriques Crispim Romão

Doutor Jan Timmermans

Doutor Mário João Martins Pimenta

Setembro de 2003

Resumo

O objecto da tese é o estudo de estados finais $W^+W^-\gamma$ e $q\bar{q}\gamma\gamma(\gamma)$, utilizando os dados recolhidos por DELPHI na operação do colisionador LEP a energias de centro de massa de 180 a 210 GeV. As análises são motivadas por pesquisas de nova física, nomeadamente de acoplamentos anómalos entre quatro bosões electrofracos e de assinaturas do cenário fermiofóbico dos modelos de dois dubletos de Higgs. Em ambos os casos, as análises são também sensíveis à implementação das correcções radiativas nos cálculos dos dois processos, que são dos mais importantes na Física de LEP.

A secção eficaz medida para a produção de W^+W^- com um fotão energético, central e isolado é de:

$$\begin{aligned} &0.19 \pm 0.09 \pm 0.02 \text{ pb (a } \sqrt{s} = 189 \text{ GeV);} \\ &0.44 \pm 0.09 \pm 0.03 \text{ pb (a } \sqrt{s} = 198 \text{ GeV);} \\ &0.34 \pm 0.09 \pm 0.03 \text{ pb (a } \sqrt{s} = 206 \text{ GeV).} \end{aligned}$$

Não havendo indicação de contribuições anómalas neste processo, os valores possíveis para os acoplamentos anómalos entre quatro bosões electrofracos são restringidos aos intervalos $a/\Lambda^2 \in [-0.063, +0.032]$ GeV^{-2} para o para o vértice $W^+W^-\gamma\gamma$, e $a/\Lambda^2 \in [-0.18, +0.17]$ GeV^{-2} para o vértice $W^+W^-\gamma\gamma$, com um nível de confiança de 95%.

Também os estados finais de $q\bar{q}\gamma\gamma(\gamma)$ são bem descritos pelas previsões do Modelo Padrão, levando a que o espaço de parâmetros do modelo de Higgs Fermiofóbicos considerado seja fortemente limitado. No caso particular em que o bosão de Higgs mais leve mantém os acoplamentos aos bosões electrofracos previstos no Modelo Padrão, o valor mínimo possível para a sua massa, determinado com um nível de confiança de 95%, é de 102.2 GeV/c^2. A combinação deste resultado com outros obtidos pelas quatro experiências de LEP traduz-se num limite de 109.7 GeV/c^2, com o mesmo um nível de confiança.

Palavras Chave

LEP, DELPHI, Fotões, Correcções Radiativas, Acoplamentos de Quatro Bosões Electrofracos, Bosões de Higgs Fermiofóbicos

Abstract

The thesis presents a study of $W^+W^-\gamma$ and $q\bar{q}\gamma\gamma(\gamma)$ final states, using the data collected by DELPHI, during the LEP operation at centre-of-mass energies ranging from 180 to 210 GeV. The analysis are motivated by searches for new physics, namely for anomalous quartic gauge couplings and for signatures of the fermiophobic scenario of two Higgs doublet models. In both cases, the analyses are also sensitive to the implementation of radiative corrections in the two processes, which are among the most important ones in LEP physics.

The measured cross-section for the production of W^+W^- with a hard, central and isolated photon in the final state is:

$$0.19 \pm 0.09 \pm 0.02 \text{ pb (at } \sqrt{s} = 189 \text{ GeV);}$$
$$0.44 \pm 0.09 \pm 0.03 \text{ pb (at } \sqrt{s} = 198 \text{ GeV);}$$
$$0.34 \pm 0.09 \pm 0.03 \text{ pb (at } \sqrt{s} = 206 \text{ GeV).}$$

There is no evidence of contributions from anomalous quartic gauge couplings and the corresponding coupling parameters are constrained to be: $a/\Lambda^2 \in [-0.063, +0.032]$ GeV^{-2}, for $W^+W^-\gamma\gamma$, and $a/\Lambda^2 \in [-0.18, +0.17]$ GeV^{-2}, for $W^+W^-Z^0\gamma$, at 95% confidence level.

Also the $q\bar{q}\gamma\gamma(\gamma)$ final states are well described by the Standard Model expectations, and thus the allowed parameter space of the Fermiophobic Higgs model considered is severely constrained. In particular, if the lightest Higgs boson has SM-like couplings to the electroweak gauge bosons, its mass is limited to be above 102.2 GeV/c^2, at 95% confidence level. The combination of this result with others obtained by the four LEP collaborations leads to a limit of 109.7 GeV/c^2, with the same confidence level.

Keywords

LEP, DELPHI, Photons, Radiative Corrections, Quartic Gauge Couplings, Fermiophobic Higgs Bosons

Acknowledgments

This thesis is the product of many years working in the LIP DELPHI group, and obviously could not have been accomplished by myself alone. My supervisor, Prof. Mário Pimenta, has had a great impact on my work, by encouraging me at all times, by sharing his enthusiasm and all the time and energy. I have to thank him for all that and for giving me the opportunity to work in a fantastic group.

I would like to thank LIP for giving me the best conditions with an excellent working environment, this is of course merit of the institution itself but mainly of all the people there. It was always interesting to talk to people in the different experiments, and in particular I have learned a lot from all the people in the DELPHI group, whose experience, knowledge and kindness have helped me in many ways. For physics and for the rest, I have to thank everybody, but specially the colleagues with whom I shared the office for longer times, Patrícia and Bernardo, and, again, Mário.

Working in a collaboration like DELPHI also gave me the opportunity to discuss and learn from many other people from many different places. The times spent at CERN were exceptionally useful, and I have to thank all who worked more directly with me, in DELPHI and in the other LEP collaborations; and people who, even when doing different things, were ready to discuss my analyses and doubts. I think particularly of Daniel, but there are also others I will remember as friends.

The work in experimental physics is also more interesting when we can exchange ideas and learn from theorists. I had the chance to be helped by Prof. Augusto Barroso and Prof. Jorge Romão in many occasions; and to have long discussions with Lars Brücher, even longer ones with Rui Santos, about and around the Fermiophobic Higgs, which were highly motivating.

Of course my friends and specially my family are also important for my work, and deserve a particular kind of acknowledgment, better stated in other forms than here.

This PhD was done with financial support of the European Union (FSE/QCAIII) and of the Fundação para a Ciência e a Tecnologia.

Contents

Figure List

Table List

Chapter 1

Introduction

The Large Electron Positron (LEP) collider has had a fundamental role in the testing of the Standard Model (SM) of particle physics. It provided the highest energies in leptonic colliders up to today ($\sqrt{s} \sim 200$ GeV) and with high luminosity ($\mathcal{L} \sim 2000$ pb^{-1}); LEP's results are thus of extreme importance and will stand as the reference for the years to come. In this thesis, the data collected by the DELPHI experiment, from 1998 to the end of LEP in 2000, is used to test the SM and its extensions.

There were two main goals for LEP2, the second phase of operation of the collider. It should continue the precise measurements of LEP1, that had confirmed the SM to unprecedented precision, and make a first direct measurement of the couplings between electroweak gauge bosons, to confirm or not the non-abelian nature of the Electroweak model and the absence of new interactions in this sector. On the other hand, the energy increase allowed for the search of any new physics and, in particular, the search for the missing Higgs boson, the only particle predicted by the SM which is to today undiscovered.

All the measurements made by LEP were found to be compatible with the SM predictions, the direct measurement of the Triple Gauge boson Couplings showed an impressive agreement with the Electroweak theory predictions and, although the Higgs boson was not discovered, the LEP results put tight bounds on its allowed mass. There were some hints of a possible Higgs signal in the LEP data at the highest centre-of-mass energies, but this could not be ruled out nor confirmed due to a lack of statistically significant data, as the operations ceased shortly after.

The final states analysed in this thesis are particular phase space regions of two of the most important processes in LEP2 – $f\bar{f}$ and W^+W^- production – with photons in the final states. Within the SM, the corresponding cross-sections are low as the photons appear due to radiative corrections – these final states are very sensitive to the details of the theoretical calculations and provide important checks of the Electroweak model.

The measurement of the cross-section for $e^+e^- \rightarrow W^+W^-\gamma$, only possible at LEP2 energies, is described in detail. The same final states could arise from direct Quartic Gauge boson Couplings. In the framework of the SM, the contributions of the $W^+W^-Z^0\gamma$ and $W^+W^-\gamma\gamma$ vertices are negligible at LEP energies. However, anomalous couplings between four bosons could arise as low energy manifestations of a new interaction important at higher energy scales. The allowed range for such new couplings is determined.

$f\bar{f}\gamma\gamma$ final states could be the signal of the production of a neutral Higgs boson decaying into photons. A neutral Higgs boson does not couple to (massless) photons and in the SM the branching ratio for this decay leads to negligible rates. But if the Higgs boson has suppressed (or absent) couplings to fermions, the decay to photons can be dominant.

A possible way to extend the Standard Model's symmetry breaking mechanism is to introduce two Higgs doublets instead of one, leading to more Higgs particles and new production modes at LEP. It can happen that the lightest SM-like Higgs particle does not couple to fermions. Such a fermiophobic model is analysed in detail.

The search for Fermiophobic Higgs is a complement of a previous work [1] in which Higgs decays to photons were explored in the formalism of general anomalous couplings. In the present case, it is a full consistent model which is studied and so new relations can be introduced and tighter bounds can be obtained.

It was this search that first aroused the interest in the description of radiative corrections, which was also studied in [1]. The same idea was explored in the

$W^+W^-\gamma$ analysis, using similar methods for analysing events with jets and isolated photons.

The formalism of general anomalous couplings, in this case Quartic Gauge Couplings, is again used to give, in parallel, a more qualitative evaluation of possible disagreements of data with the SM predictions.

The first chapter of the thesis gives a summary of the continuous **Testing the Standard Model at LEP**, reviewing the Standard Model while focusing on the LEP contribution to the model testing. It describes also the theory behind each of the studied scenarios to motivate and support the analyses performed. A brief description of the **DELPHI experiment** is given after, including the LEP collider and the DELPHI detector and, mainly, the data reconstruction. It serves as an introduction to the analyses. The $\mathbf{W^+W^-}\gamma$ chapter reports the analysis of that final state, the cross-section measurement and the estimation of possible quartic gauge boson contributions. The **Fermiophobic Higgs** chapter reports the search for the lightest neutral particles predicted in a model where a Higgs boson decays preferentially to photons. To extract more information about each of the studied topics, the results are then combined with the ones from the other LEP experiments. The **LEP Combined Results** chapter is followed by the **Conclusions**.

Chapter 2

Testing the Standard Model at LEP

In this chapter the Standard Model of Particle Physics (SM) is briefly reviewed[1], with emphasis on the Electroweak part and on the LEP contribution to the model testing.

In many cases, the test of the Standard Model predictions is more precisely done by confronting the data with model extensions, in which the possible deviations are parametrized explicitly, or by analysing directly alternative models.

Together with the main points of standard LEP physics, and an introduction to the physics channels studied in the thesis, the extensions to the SM which will be explored are also described.

2.1 Standard Model

The Standard Model of Particle Physics explains the basic behavior of Nature in terms of its elementary particles and the fundamental interactions between them.

The elementary particles of matter are 12 fermions, divided in leptons and quarks of three generations, and characterized by fundamental quantized charges (in ta-

[1] Deeper reviews of the SM can be found, for example, in [2].

ble 2.1). Although only the first generation appears in everyday Nature, all the fermions can be produced and studied in the laboratory. The two last ones to be directly discovered, already during LEP's lifetime, were the top-quark [3] and the tau neutrino [4]. Even if the top-quark is too heavy to be pair produced and the neutrinos are not directly identified at LEP, its measurements had already given indirect evidence for the tau neutrino and an estimate of the top-quark mass, as will be explained in the next section.

The interactions between these particles depend on their charges and are described in mathematical terms by rotations within symmetry groups where the global charge is conserved. The generators of the groups are identified with other fundamental real particles, the gauge bosons.

	Particle	T	T_3	Y	Q	C
Leptons	ν_l	1/2	+1/2	–1	0	–
	l_L	1/2	–1/2	–1	–1	–
	l_R	0	0	–2	–1	–
Quarks	U_L	1/2	+1/2	+1/3	+2/3	R,G,B
	D_L	1/2	–1/2	+1/3	–1/3	R,G,B
	U_R	0	0	+4/3	+2/3	R,G,B
	D_R	0	0	–2/3	–1/3	R,G,B
Gauge Bosons	B^0	0	0	0	0	–
	W^+	1	+1	0	+1	–
	W^0	1	0	0	0	–
	W^-	1	–1	0	–1	–
	Gluons	0	0	0	0	(RGB)
Higgs	H	1/2	–1/2	1	0	–

Table 2.1: Elementary particles in the Standard Model: there are three generations of fermions, with the same quantum numbers but different masses, in the table the values for generic neutrino, charged lepton, up-type quark and down-type quark are shown. For each fermion there is an anti-particle with opposite charges but the same mass. L and R stands for the fermion helicity. The charges and the gauge bosons are each characteristic of one interaction: T is the weak isospin and T_3 its projection, Y is the weak hypercharge (the quantity $Q = T_3 + Y/2$, is conserved and is identified with the electrical charge) and C = Red, Green or Blue is the color charge. The real photon and Z^0 are linear combinations of B^0 and W^0.

In the case of the Standard Model, the fundamental group is obtained as a product of $SU(3) \times SU(2) \times U(1)$ and the fundamental gauge bosons are: eight gluons (mediating exchanges of the color charges of the strong interaction), the W^+, W^- and Z^0 bosons (for weak charges) and the photon (for electrical charge)[2].

Quarks have electromagnetic, weak and strong charges but the strong interaction, described by the $SU(3)$ group can be seen as an independent piece of the SM, the Quantum Cromo Dynamics theory (QCD[5]).

The case for the Electromagnetic and Weak interactions is more complex: the Electromagnetic interaction can be described within a $U_Q(1)$ symmetry group, with the photon as generator, as is done in the Quantum Electro Dynamics theory (QED [6]), but the simple description of the Weak interaction, within a $SU(2)$ group, does not describe the observed physics. In fact the charged and neutral weak currents present similarities – in strength, for example – but also fundamental differences – in particular, the charged currents only act on left-handed fermions but the neutral ones have both left and right-handed components. The neutral weak currents are similar to the electromagnetic current, but they act also on electrically neutral fermions. The observation of the differences between charged and neutral weak currents and of the similarity between the neutral weak and electromagnetic currents, lead to the development of a general Electroweak theory, by Glashow, Weinberg and Salam, the so-called Standard Model of Electroweak interactions[7].

In the Standard Model of Electroweak Interactions, the fundamental group is a $SU_L(2) \times U_Y(1)$, with two different fundamental coupling constants (g and g'), acting on weak isospin charge (T) and weak hypercharge (Y), and 3 W + 1 B vector bosons as generators. The left-handed fermions are organized in $SU(2)$ doublets and carry weak isospin while right-handed fermions are singlets[3] and insensitive to the $SU_L(2)$ symmetry. All fermions carry weak hypercharge, related to the electrical charge by $Y = 2(Q - T_3)$. Notice that, while B^0 is a singlet carrying no charges, the W-triplet, gives rise to two electrically charged and one electrically neutral particle all with weak isospin, and will thus have self-couplings (the theory

[2]Gravity is the only fundamental interaction which is not incorporated in the SM. No quantum field theory exists for gravity, but also its microscopic effects are small enough, when compared to electroweak interactions, for it not to be necessary to describe physics at the M_Z scale.

[3]Right-handed neutrinos are absent in the SM.

is non-abelian).

The physical W^+ and W^- bosons correspond to pure $SU_L(2)$ generators, while the Z^0 and the photon (γ) are linear combinations of W^0 and B^0, chosen in order to obtain the observed characteristics of the weak and electromagnetic currents. The two couplings constants must then be related and their values must be of the same order of magnitude. The feebleness of the weak interaction when compared to the electromagnetic interaction is explained not by a small coupling constant but by the masses of the corresponding gauge bosons – a larger mass implies a shorter range and a smaller effective coupling. However, a simple introduction of mass terms in the lagrangian would spoil the local symmetries and render a non-renormalizable theory: the calculation of many physical quantities would then lead to unphysical results of infinite numbers.

In the Standard Model, the gauge bosons acquire mass after the spontaneous breaking of the $SU_L(2) \times U_Y(1)$ symmetry by what is known as the Higgs mechanism [8]. A complex scalar doublet ϕ, obeying the local $SU_L(2) \times U_Y(1)$ symmetry, is introduced and it is assumed that its vacuum expectation value is not necessarily zero. The symmetry of the interaction is then kept but the vacuum of the theory is made non-symmetric by assuming a non-zero vacuum expectation value (v) with weak isospin and hypercharge.

The interactions of ϕ with the gauge bosons, will then lead to mass terms of the form g.v.WW and g'.v.BB. The photon and Z^0 can be obtained as the – zero and non-zero – mass eigenstates of the two neutral gauge bosons, giving the expected linear combinations of W^0 and B^0. The relation between the Z^0 and $W^\pm$ masses is fixed by the two couplings g and g', expressed in terms of the Weinberg angle $\tan\theta_W = g/g'$ and $M_W/M_Z = \cos\theta_W$ – a fundamental prediction that has been confirmed to a high precision.

Of the four degrees of freedom of ϕ, three are absorbed as the longitudinal components of the three gauge bosons which became massive and one will correspond to a real scalar particle, the Higgs boson – with the vacuum quantum numbers. The masses of the gauge boson will fix both their couplings to the Higgs boson and the Higgs doublet vacuum expectation value.

For simplicity, it is assumed that the same phenomena can explain the masses of the elementary fermions and again this fixes the couplings of fermions to the Higgs boson – $\phi f_L f_R$. In this case, however, there is no fundamental prediction and the terms that appear in the Lagrangian are all set arbitrarily to match the experimental data.

Apart from the fermion masses, the Electroweak theory has only four free parameters, which can be chosen to be, for example: the electromagnetic coupling $\alpha_{em} = \frac{(g.\sin\theta_W)^2}{4\pi}$, the Fermi coupling constant $G_F = \frac{\sqrt{2}.g^2}{8.M_W^2}$, the Z^0 mass (known to precisions of 2.10^{-4}, 10^{-5} and 2.10^{-5}, respectively, at LEP energies [9]) and the Higgs mass, the only parameter that can not yet be related to any direct measurement.

The fermion masses have all been measured except for the neutrino masses. In the original formulation of the SM the neutrinos are supposed to be exactly massless, as no right-handed neutrinos were observed there could not be Dirac mass terms and Majorana mass terms were not considered. However, recent results [10, 11] indicate that the neutrinos do have mass, although very small ones when compared to the other fermions.

For the QCD part of the SM, the extra parameters are the strong coupling constant α_s at a fixed energy (or, alternatively, Λ_{QCD} which determines the running of α_s, defining a separation between the color confinement and asymptotic freedom regimes), an extra parameter $\bar{\theta}$ defining the QCD vacuum which can not be fixed theoretically (but would introduce strong CP violation and is measured indirectly to be close to 0) and the four parameters which define the quark mixing CKM[12] matrix[4]. The precision to which all of those are known is lower than the one achieved on the electroweak parameters but several dedicated experiments exist, in particular to measure the CKM parameters related to the weak CP-violation in the quark sector.

With all parameters measured except for the Higgs mass, the Standard Model seems to be a consistent and complete theory, up to the Plank scale where gravity is

[4]Since the $SU(3)$ symmetry is left untouched by the Higgs mechanism, the gluons have no mass. It is possible to give also mass to the gluons by extending the Higgs sector to color particles[13], but there is no experimental evidence for gluon masses.

expected to play a role. The Standard Model is also renormalizable: the calculation of all physical amplitudes at any order in perturbation theory renders finite values. In addition, the theory should also obey unitarity bounds that limit the growth of the amplitudes with the available energy.

A clear example of the importance of the unitarity conditions is the production of two longitudinally polarized gauge bosons ($V_L V_L \rightarrow V_L V_L$ and $f_+ \bar{f}_+ \rightarrow V_L V_L$, where V=W,Z and f_+=fermion with positive helicity). $f\bar{f} \rightarrow WW$ production described only by $ff'W$ vertices is strongly dependent on the available energy and diverges as the energy increases; with the introduction of the non-abelian triple gauge boson vertices – ZWW and γWW– the dependence becomes weaker; but only the introduction of Higgs exchange makes the amplitude tend to a constant value at high energy (this still requires the Higgs mass to be below ∼1 TeV/c/^{2}). $WW \rightarrow WW$ has also a cancellation between the triple and quartic gauge couplings contributions and the Higgs exchange contribution.

Apart from indicating a preferred upper limit for the Standard Model Higgs mass, the unitarity conditions are also useful to favour or disfavour alternative models: if the Higgs sector is to be extended to more particles care must be taken so that the unitarity conditions are not spoiled by the new particles. On the other hand, in models without Higgs bosons, other interactions should appear to cancel the above divergence.

2.2 Measurements at LEP

The operation of the Large Electron Positron collider was divided in two distinct phases (LEP1 and LEP2) with different goals in terms of the Standard Model testing. LEP has had an important contribution for the study of QCD but was primarily designed to test the Electroweak sector, which will be focused here.

In a first phase (1989-1995), LEP was run at a centre-of-mass energy around the Z^0 mass. The results obtained gave a remarkable confirmation of the Standard Model, at an energy much above the characteristic scale of the Fermi theory for which the model had been developed. Many of the SM parameters, noticeably the

Z^0 mass, were measured with a high precision.

In a second phase, the centre-of-mass energy was basically doubled to extend the measurements to higher energies, and, in particular, to study the production of $W^\pm$ pairs and to search for the Higgs boson and any unexpected New Physics.

Although interferences are always present and thus the processes can not be exactly separated, we can classify LEP physics into:

- Fermion Pair Production:
  all light fermions can be produced via e^+e^- annihilation into Z^0/γ^*. This process is resonant at LEP1, due to the Z^0 pole; at LEP2 it has decreased cross-section but is still important: many of the LEP2 events are produced at an effective collision energy of $\sqrt{s'} \sim M_Z$ accompanied by photon radiation. The production of e^+e^- has an additional, dominant, contribution of a γ exchange in the t-channel.

- Gauge Boson Pair Production:

  - Photons pairs are produced via a virtual electron t-channel exchange. The cross-section is almost purely described by QED and very precisely calculated.

  - W^+W^- production is described by three electroweak diagrams. It is one of the most important processes at LEP2.

  - Z^0Z^0 production has a much lower cross-section. It is an important background for the SM Higgs search.

- "4-fermion production":
  apart from the ones that come from W^+W^- and Z^0Z^0 production, there are

  - "Virtual Photon Collisions" where the electron/positron beam interact via a double virtual photon t-channel exchange, leading to low energy $e^+e^-f\bar{f}$ events, with a very high cross-section.

  - "Single boson production" also t-channel processes where an on-shell massive boson is produced together with two fermions.

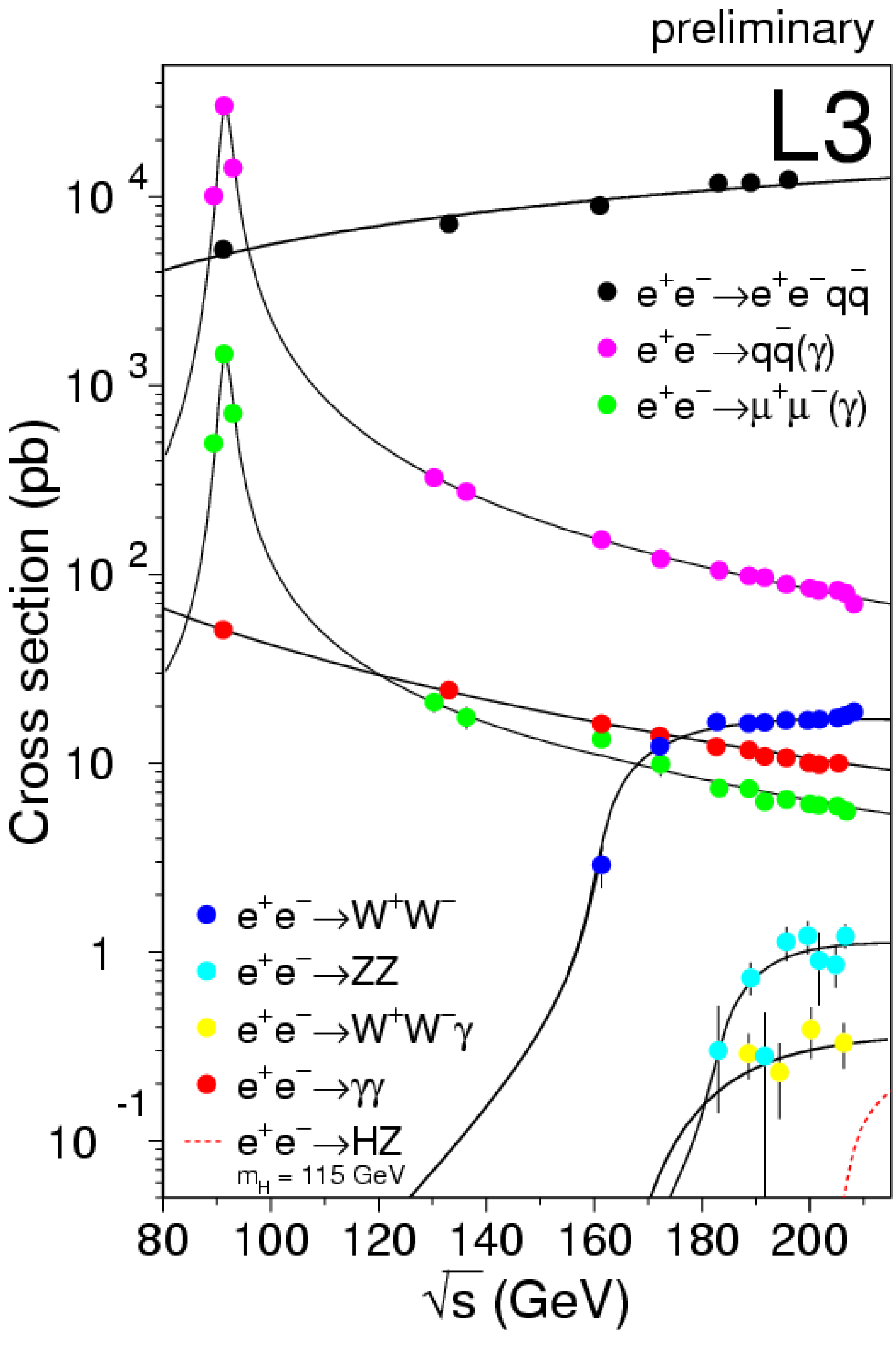

Figure 2.1: Standard model at LEP: the plot shows the cross-sections for some of the more relevant physics processes measured by L3, one of the LEP collaborations, as a function of the centre-of-mass energy. Also shown, in dashed line, the expected cross-section for production of a Higgs boson of 115 GeV/c^2[14].

Figure 2.1 shows the cross-sections for some of the most relevant physics processes at LEP, as measured by one of the collaborations, showing an impressing agreement with the Standard Model predictions, in a wide range of centre-of-mass energies and for a wide range of cross-section values. All the four LEP collaborations – ALEPH, DELPHI, L3 and OPAL – have reported a good agreement with the expectations in most of the analysed processes. The combination of the results from the four collaborations allowed for a more precise determination of the cross-section values and thus of the SM parameters.

LEP1 has fixed the Z^0 mass to be 91.1875 $\pm$0.0021 GeV/c^2 [9]. In addition, the study of the production cross-section, the Z^0 lineshape and its branching ratios gives much more information. It was shown that the decays of the Z^0 to light neutral particles was consistent with the production of three SM-like neutrinos, that the decays to quarks and leptons and the angular distributions of the final state fermions gave consistent results for $\sin\theta_W$, and fitting together all the results and the corresponding SM expectations with loop-corrections from the top-quark mass, gave a probable value of M_{top} = 171 $\pm$10 GeV/c^2 [9] (consistent with the value measured directly [3], some years later, of 174 $\pm$5 GeV/c^2).

The measurements done at LEP gave not only precise determination of the SM parameters, but also lead to the development of more precise theoretical calculations of the observables. In particular, to be compared with precise measurements, the calculated cross-sections have to take into account corrections due to higher order diagrams with loops and real emission of undetectable particles at low angles or energy.

At LEP2, the statistics are much lower and the precision achieved is naturally smaller. In addition, the corrections to the calculations, due to loops and real particle emission became even more important. The main measurements are the W mass (M_W =80.45 $\pm$0.04 GeV/c^2 [9]), width and branching ratios and, in particular, its pair production cross-section as a function of the centre-of-mass energy.

W^+W^- production is difficult to isolate as $W^\pm$ bosons have short life-times and only their decay products are detected – this implies that the final states are common to many other processes, and all the interferences must be considered.

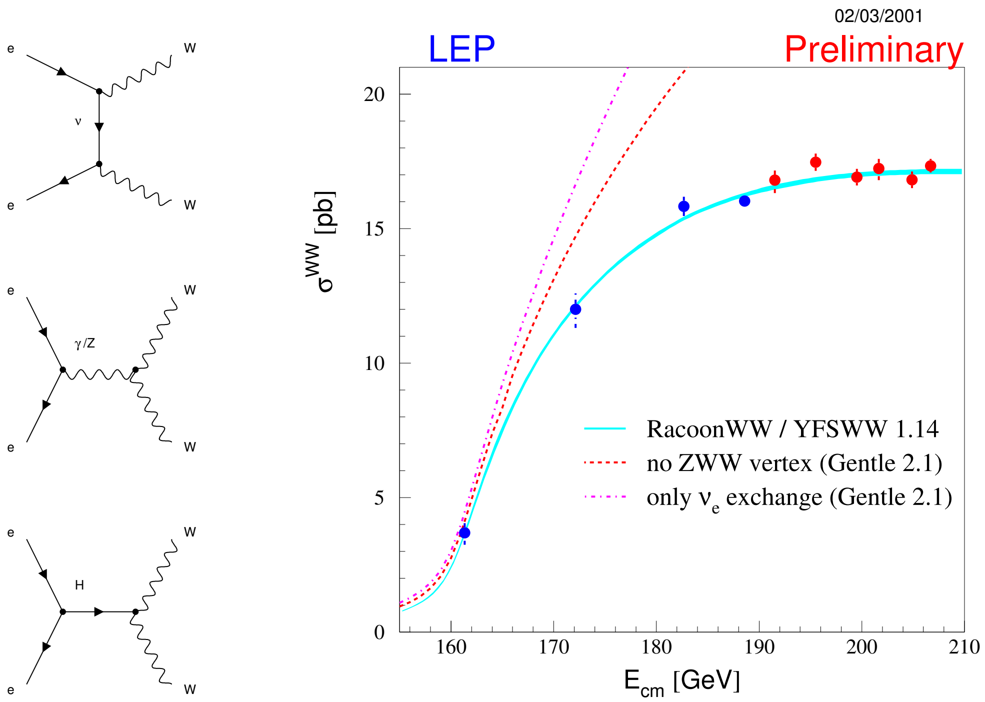

Figure 2.2: W pair production at LEP: in the left the Feynman diagrams of the CC03 processes are shown; the right plot shows the measured cross-section compared to the SM predictions, and with the calculation with the $We\nu_e$ vertex only. The Higgs diagram gives a negligible contribution at LEP energies.

The real W^+W^- production, on the other hand, is described at tree level by a small number of Feynman diagrams (see figure 2.2): an electron neutrino exchange in the t-channel, with a cross-section that diverges as the centre-of-mass energy increases; the divergence is canceled at LEP energies by the extra contribution of Z^0/γ^* exchange in the s-channel, possible only because the electroweak theory is non-abelian; at even higher energies, the W^+W^- production cross-section diverges again, and is canceled only by the exchange of a Higgs boson.

2.2.1 Radiative Cross-sections

The comparison of the LEP results with the theoretical predictions must be done in such a way that higher order corrections are correctly introduced but also the phase space region is well defined to reproduce the experimental conditions. The best way to achieve this is to simulate the processes using Monte Carlo generators for each physics channel, in which the higher order corrections are implemented – exactly or in an approximate way – according to the characteristics of the events being generated.

Special care must be given therefore to the computation of radiative corrections which can be divided into virtual or real: the virtual ones corresponding to loops or particle lines connecting two parts of a tree-level Feynman diagram; and the real ones to the production of additional particles which can be detected or not. Since the electromagnetic force is much stronger than the weak force, the major part of the electroweak corrections comes from real and virtual photon emission.

The real corrections are dominated by the emission of low energy photons close to the direction of the radiating charged particle. This corresponds to an exact infra-red divergence and to an "almost" divergence for collinear emission from low mass particles, and renders the perturbative approach insufficient to precisely account for these effects. It is also important to have a correct description of the non-divergent parts of the cross-sections, with high energy photons isolated from the initial and final state particles. A study of different ways of including these effects on MC physics generators was presented in a previous work [1].

At LEP2, the emission of high energy photons by the electron/positron beams – know as Initial State Radiation (ISR) – becomes even more important due the presence of a pole in the $e^+e^- \rightarrow Z^0 \rightarrow f\bar{f}$ cross-section. In fact, the cross-section peak for centre-of-mass energies near the Z^0 mass is so strong, that a reduction of the effective collision energy to a value near the Z^0 mass leads to an increase of the total cross-section. Around half of the LEP2 $e^+e^- \rightarrow f\bar{f}$ events are actually produced at LEP1 energies, in what is called the Radiative Return to the Z^0.

On the other hand, any charged particle can radiate photons, and those processes interfere. In $e^+e^- \rightarrow W^+W^-$, the ISR is accompanied by radiation from the $W^\pm$ (WSR) and, as the $W^\pm$ decay, also by the Final State Radiation from charged fermions (FSR). All the photon emission give infra-red divergences, while the "collinear divergence" is absent in the radiation from $W^\pm$. The interference between ISR and FSR is in general suppressed by the time separation induced by the intermediate state bosons, but ISR and WSR interfere strongly in the regions away from the beams.

The high energy and luminosities achieved at LEP allow for the production of reasonable numbers of $W^+W^-\gamma$ events and $Z^0\gamma\gamma$ events and both final states will be important for the analyses in the thesis. Although the corresponding cross-sections are small, they are very sensitive to the details of the theoretical computations, which makes their study very important for checking the implementation of radiative corrections. A complete description of the MC generator setups used will be given before the corresponding analyses of $W^+W^-\gamma$ (in chapter 4) and Fermiophobic Higgs, for which the $Z^0\gamma\gamma$ represents an indistinguishable background (in chapter 5).

2.3 Gauge Boson Couplings

The existence of electroweak boson self interaction, in Triple Gauge Couplings (TGC) and in Quartic Gauge Couplings (QGC), is a fundamental prediction of the Standard Model.

One of the most important tests of the standard Electroweak theory at LEP2, was the direct confirmation of the TGCs in W^+W^- production[5]. However, the cross-section behavior by itself is not sufficient to show that the non-abelian structure is exactly as expected, and a more detailed study must be done to confirm the exact form of the couplings.

In the Standard Model, the coupling between neutral bosons only is forbidden and the only allowed triple and quartic boson vertices require at least, two charged bosons. These vertices are described by the following Feynman rules:

TGC: $iF(g^{\alpha\beta}(k_1 - k_2)^\gamma + g^{\beta\gamma}(k_2 - k_3)^\alpha + g^{\gamma\alpha}(k_3 - k_1)^\beta),$

QGC: $iG^2(g^{\alpha\delta}g^{\beta\varepsilon} + g^{\alpha\varepsilon}g^{\beta\delta} - 2g^{\alpha\beta}g^{\varepsilon\delta}),$

where k_i are the boson momenta and the greek letters are the different polarizations

[5] A first, indirect, indication of the existence of TGCs comes from the LEP1 precision measurement. It was shown that gauge boson loops were required in the calculation of the gauge boson self-energies [15].

(α, β, γ for the particles with k_1, k_2 and k_3; δ and ε corresponding to the W bosons in the QGCs).

The values of the couplings F are fixed by the universal $SU(2) \times U(1)$ coupling (F is e in $WW\gamma$ or $g \cos\theta_W$ in WWZ) and the QGCs are suppressed by an extra factor (G^2 is e^2 in $WW\gamma\gamma$, $eg\cos\theta_W$ in $WWZ\gamma$, $g^2 \cos{\theta_W}^2$ in $WWZZ$ and $-g^2$ in $WWWW$).

For the determination of the TGCs, extensive studies of differential distributions were made in the $W^{\pm}$ pair production, in $We\nu$ production and in $\nu\bar{\nu}\gamma$ production from t-channel W-fusion. The most general parametrization of possible structures of these couplings, represented by anomalous charge-like, dipole-like and quadrupole-like couplings between the charged and neutral bosons, were used to measure the possible deviations from the SM structure. The corresponding phenomenological Lagrangian is given by:

$$-i.g_{WWV}.(g_1^V(W^+_{\mu\nu}W^{-\mu}V^{\nu} - W^+_{\mu}V_{\nu}W^{-\mu\nu}) + k_V W^+_{\mu}W^-_{\nu}V^{\mu\nu} + \lambda_V/m_W^2 W^+_{\mu\nu}W^{-\nu\rho}V^{\mu}_{\rho})$$

The final results from LEP confirm the SM coupling values, the results reported for the deviations induced by anomalous couplings are[16]:

$\Delta g_1^Z = -0.002^{+0.023}_{-0.025}$, for the change in the charge-like coupling $W^+W^-Z^0$ from the SM value $g_1^Z = 1$;

$\Delta k_\gamma = -0.057^{+0.055}_{-0.055}$, for the change in the dipole-like coupling $W^+W^-\gamma$ from the SM value $k_\gamma = 1$;

$\lambda_\gamma = -0.020^{+0.024}_{-0.024}$, for the quadrupole-like coupling, absent in the SM.

The other possible deviations allowed in the general parametrization are, after imposing electromagnetic gauge invariance and CP conservations rules, set to: $\Delta g_1^\gamma = 0$, $\Delta k_Z = \Delta g_1^Z - \Delta k_\gamma \tan^2\theta_W$ and $\lambda_Z = \lambda_\gamma$.

Neutral TGCs are absent in the SM but they were also searched for at LEP by studying Z^0Z^0 and $Z^0\gamma$ production. In this case the parametrization of all possible anomalous couplings is more complicated but all the results are compatible with the SM prediction of no neutral gauge couplings and the possible values are severely constrained[16].

With the luminosities achieved at LEP, the contribution of the QGC vertices is too small to be directly detected. The motivation to study QGCs at LEP is then, not the direct test the Standard Model through a precision measurement of a tree-level coupling, but the search for anomalous processes from non-standard physics which can be described effectively as QGCs.

2.3.1 Anomalous Quartic Gauge Couplings

There are good reasons to think that the QGCs would be drastically modified by subtle changes in the electroweak model: on the one hand, they are closely related to the symmetry breaking sector, for which the fundamental direct evidence – the Higgs boson – is still missing (the existence of the VVH (V=W,Z) couplings is necessary to avoid violation of unitarity in $VV \rightarrow VV$ scattering, which can be expressed as an effective QGC); on the other hand, because the tree-level QGC are small in the Standard Model (suppressed by an extra α factor in relation to the TGC), the existence of higher order interactions could contribute at a similar level to the coupling values and structure.

The existence of new heavy particles that couple to the electroweak gauge bosons could generate effective triple and quartic gauge boson couplings at LEP2 energies. Loops of heavy particles could introduce significant changes in the TGC and QGC structures and the exchange of these heavy particles between pairs of bosons can also be parametrized as contact interactions contributing to the QGCs. It can happen that, in some scenarios, the anomalous loop contributions to TGCs are canceled out while contact interaction contributions to the QGCs are still important.

The anomalous couplings created by new interactions with new heavy particles can be described in an effective Lagrangian, parametrized by the scale of new physics Λ (of the order of the mass of the new heavy particles) and new coupling parameters giving the strength for each possible operator. There is an infinite number of terms, in increasing powers of Λ^{-2} and of higher dimension operators. However, at present energies, a cut off keeping only the lower dimension terms proportional to Λ^{-2} can be made.

Some of the new operators generate both triple and quartic couplings. For example if there is an anomalous quadrapole moment of the $W^{\pm}$ described by λ_γ, gauge invariance implies that such an operator will induce both a $WW\gamma$ coupling with strength $e\lambda_\gamma$ and a $WW\gamma\gamma$ coupling with strength $e^2\lambda_\gamma$. In this case, the most sensitive search for its effects would be done by analysing its changes in TGCs, as the QGC sensitivity is suppressed by a factor of e.

Other operators, however, generate only QGCs and are the ones studied in what follows. In addition, the observed $U_Q(1)$ symmetry and the custodial $SU(2)$ symmetry[6] must be imposed, in order to obey some physics constraints. This amounts to separating the purely electromagnetic effects (and the vertices with photons) from the purely weak effects, while imposing charge conservation and a symmetry between the Z and W bosons, namely guarantying that $\rho = M_Z/M_W \times \cos\theta_W = 1$.

For testing alternative symmetry breaking scenarios, the vertices with maximum number of massive bosons would be the most important ones. There are at least two operators obeying the above symmetries and that give rise to $WWWW$, $WWZZ$ and $ZZZZ$ vertices (the neutral vertex, that does not exist in the Standard Model, must appear here due to the custodial symmetry imposed – the new interaction acts on the SU(2) triplet). Unfortunately these vertices can not be tested directly at LEP energies: there is not enough energy to produce three massive bosons in the final state, and the alternative process, of a double t-channel with massive bosons fusion, is suppressed to very small cross-sections by the amount of transfered energy necessary to produce the two massive gauge bosons in the final state.

For the vertices with photons, the $U_Q(1)$ symmetry requires derivatives that result in higher dimension operators: dimension 6 for one or two photons, and at least dimension 8 for more photons. Different ways of constructing the possible operators have been considered in the literature. In [18], several C and P conserving operators are shown to be $SU(2) \times U(1)$ gauge invariant. In [20], a reduced set is

[6]Custodial SU(2) symmetries were introduced in the framework of Technicolor models[17]. In order to get $\rho = M_W/M_Z \cos\theta_W = 1$ at all levels in the presence of new interactions, these are demanded to conserve some symmetry – isospin or other – under which the generators of SU(2) transform as a triplet.

considered, but extra operators which violate one of the (C,P) discrete symmetries are introduced, in a total of 5 operators to be added to the Standard Model:

[**(0)** Standard Model: $-\frac{g^2}{4}\xi_{ijk}\xi_{ilm}W^{\mu}_{(j)}W^{\nu}_{(k)}W_{(l)\mu}W_{(m)\nu}$,
written in terms of the original $SU_L(2)$ triplet;]

(1) $-\frac{\pi\alpha}{4\Lambda^2}a_c F_{\alpha\mu}F^{\alpha\nu}(\overrightarrow{W}_\nu.\overrightarrow{W}^\mu)$;

(2) $-\frac{\pi\alpha}{4\Lambda^2}a_0 F_{\alpha\beta}F^{\alpha\beta}(\overrightarrow{W}_\mu.\overrightarrow{W}^\mu)$;

(3) $-\frac{\pi\alpha}{4\Lambda^2}\tilde{a}_0 F_{\alpha\beta}\tilde{F}^{\alpha\beta}(\overrightarrow{W}_\mu.\overrightarrow{W}^\mu)$;

(4) $-\frac{\pi\alpha}{4\Lambda^2}a_n \epsilon_{ijk}W^{(i)}_{\mu\alpha}W^{(j)}_{\nu}W^{(k)\alpha}F^{\mu\nu}$;

(5) $-\frac{\pi\alpha}{4\Lambda^2}\tilde{a}_n \epsilon_{ijk}W^{(i)}_{\mu\alpha}W^{(j)}_{\nu}W^{(k)\alpha}\tilde{F}^{\mu\nu}$.

where the field strengths $F_{\mu\nu}$ and $\overrightarrow{W}_{\mu\nu}$ are defined by $F_{\mu\nu} = \partial_\mu A_\nu - \partial_\nu A_\mu$ and $\overrightarrow{W}_{\mu\nu} = \partial_\mu \overrightarrow{W}_\nu - \partial_\nu \overrightarrow{W}_\mu$, respectively, and $2\tilde{F}_{\mu\nu} = \epsilon_{\mu\nu\rho\sigma}F^{\rho\sigma}(\epsilon^{0123} = 1)$; A_μ is the photon field and $\sqrt{2}\overrightarrow{W}_\mu = \left((W^+ + W^-)_\mu\, , i(W^+ - W^-)_\mu\, , \frac{\sqrt{2}}{\cos\theta_W}Z_\mu\right)$ is the triplet of massive gauge bosons. The non-abelian part of the $W_{\mu\nu}$ field tensor is omitted as it would give rise to vertices with 5 bosons. The parameter Λ has units of energy and represents the scale at which new physics would become manifest, and a_c, a_0, $\tilde{a}_0$, a_n and $\tilde{a}_n$ are dimensionless parameters determining the separate contributions of each operator.

This is the set which will be used in this thesis as, although reduced, it is sufficient to study the possible existence of anomalous QGC in a variety of scenarios.

Operators (1) and (2) were the first to appear in the literature[18], they explicitly conserve the discrete symmetries C, P and CP. The two terms give rise to $WW\gamma\gamma$ which can come from loops, but also from the exchange of new scalar particles, $(a_0)WW \to A_0 \to \gamma\gamma$ or $(a_c)W\gamma \to A_+ \to W\gamma$. The custodial symmetry imposed implies that a coupling with same structure and similar strength must also exist in $ZZ\gamma\gamma$ vertices, even if in that case there can be no exchange of a charged particle (the SM does not obey the custodial symmetry and thus does not have the totally neutral vertex).

The other terms were introduced later in [19] and [20]. Operator (3) contributes again to the above vertices, while (4) and (5) give rise to a $WWZ\gamma$ vertex. Each of them conserves one of the C/P symmetries: (5) conserves CP but violates the separate symmetries C and P, (3) conserves only C and (4) conserves only P.

The terms with $\tilde{a}_0$ and $\tilde{a}_n$ are very similar to the ones in a_0 and a_n, in fact the helicity amplitudes differ only by factors of i. The differences would arise when using polarized beams or only at very high energies but, at least in total cross-sections, are absolutely negligible at LEP.

Since the custodial symmetry implies that the $WW\gamma\gamma$ and $ZZ\gamma\gamma$ vertices have the same structure and related strengths, the same names are used for the couplings in both cases. However, it must be considered that this requirement is only absolute when the vertices are considered to be tree-level, and does not make sense when the full higher energy model is considered. The combination of the constraints on a_c, a_0 and $\tilde{a}_0$ coming from different vertices implies further model dependency, and a combination of the coupling values should be avoided.

In this thesis, charged QGCs involving photons are searched for, using the process $e^+e^- \to Z^0/\gamma^* \to W^+W^-\gamma$. At LEP, the other processes that include charged QGCs present double t-channel exchange of bosons and are thus suppressed, the one with highest cross-section is the exchange of two Ws giving two photons and two forward neutrinos in the final state (the analyses by other LEP collaborations will be briefly reviewed before the combined LEP results are described).

2.4 Higgs Sector

Although the Higgs boson has not been observed experimentally, the only unknown left in the Standard Model is the Higgs mass (and its self-couplings which also depend on this quantity), ie, all the cross-sections for Higgs production and decay within the SM can be calculated exactly except for the corrections due to Higgs loops.

At LEP the Higgs boson would be produced in association with a Z^0 boson in what is called the Higgs-*strahlung* mechanism, $e^+e^- \to Z^0 \to Z^0H$, for a maximum mass of $M_H = \sqrt{s} - M_Z$. For higher masses, there is a small additional contribution from $e^+e^- \to H\nu_e\bar{\nu}_e$ with W^+W^- fusion in the t-channel. For the probed masses, the main Higgs decay is to $b\bar{b}$ and, at a much lower level, $\tau^+\tau^-$. The search is heavily dependent on the tagging of b-quarks and taus, and all the possible Z^0 decays are analysed. The combination of the four LEP experiments' results gives a lower limit on the Higgs mass 114.4 GeV/c^2 with a Confidence Level (CL) of 95% [21].

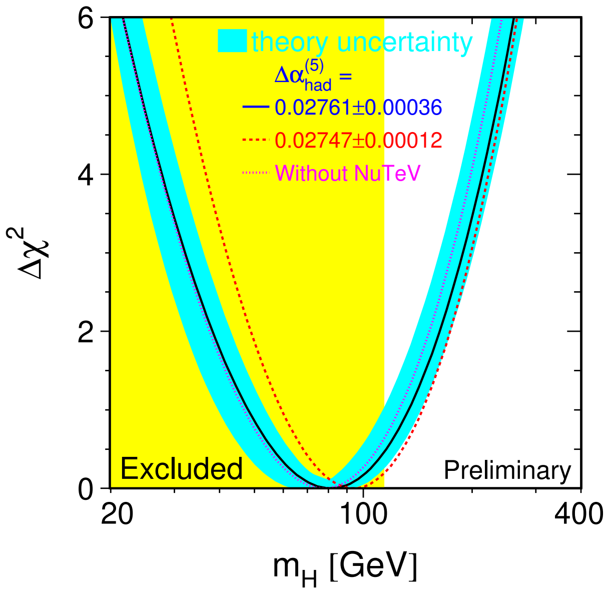

Figure 2.3: Standard Model Higgs: the plot shows the $\Delta\chi^2$ measuring the quality to a fit of all Electroweak data – dominated by the LEP measurements – as a function of the Higgs boson mass. The direct limit from Higgs searches at LEP is also shown. At 95% CL, the Higgs is constrained to be 114 GeV/c^2 $< M_H <$ 193 GeV/c^2.

On the other hand, the corrections due to Higgs loops that appear in the calculation of other quantities can be used to constrain the Higgs boson mass. The precise measurements made at LEP and other experiments depend mildly on the Higgs mass, usually logarithmically. The dependence on the Higgs mass is hard to isolate as it appears in calculations with other parameters which are not directly measured and which are always determined with experimental and theoretical uncertainties. However, a higher Higgs mass would imply a lower $W^{\pm}$ mass and a lower Z^0 width, for example – the measured M_W and Γ_Z values from LEP favour light Higgs boson of around 100 GeV/c^2. On the other hand, a higher Higgs mass would also imply a higher $\sin\theta_W$ – the measured value[7] seems to indicate a Higgs boson mass of around 1000 GeV/c^2. All the information is put together in a fit, giving a χ^2

[7] $\sin\theta_W$ is measured in neutrino-nucleon scattering [22] giving results which are 3σ away from the fitted SM parameters.

which depends on the Higgs mass, in figure 2.3.

The Standard Model Higgs mass is then constrained to be [9] 114 GeV/c^2 $< M_H <$ 193 GeV/c^2 at 95% CL, but both these numbers assume that the Higgs boson couplings to the known particles are the Standard Model ones. Many of the proposed extensions of the Standard Model change the properties of the Higgs particles, either by the effect of new interactions at higher energy scales or directly by assuming a non-minimal Higgs sector. The first hypothesis was analysed in detail in a previous work [1] and the second will be in focus in this thesis.

In fact the Higgs mechanism, as presented in the Standard Model, is the simplest way to achieve masses for all the elementary particles but there is no particular reason, apart from simplicity arguments, to assume that the same mechanism is responsible for all the masses and that there is only one Higgs boson.

The most natural extension will be to assume, in addition to the complex Higgs doublet, extra multiplets of complex scalars. However the good properties of the simple SM Higgs mechanism must be kept and some constraints should be obeyed by these extensions:

- $\rho = \mathbf{m_W^2/(m_Z^2.\cos^2\theta_w) = 1}$.

  This is imposed by construction of the electro-weak unification and the addition of extra singlets or doublets will not change it. For higher order multiplets, a fine tuning can be made such that contributions of extra multiplets cancel each other.

- **Unitarity Conditions**

  To keep the SM bounds on the amplitudes for massive gauge boson production, it must be ensured that both the gauge boson and the fermions couple to the scalar multiplets in such a way that the sum over all the neutral CP-even scalars exchange diagrams give the same result as in the SM ($g^2_{\phi VV}$ and $g_{\phi VV} g_{\phi f\bar{f}}$) and, thus, cancel the purely electroweak diagrams.

In addition, the presence of new particles can generate unwanted features to the theory that should be restricted:

- **FCNC should be absent or very small**

  Flavour Changing Neutral Currents can occur when fermions of the same type (neutrinos, charged leptons, u-type quarks or d-type quarks) have non-diagonal mass matrices. The absence of FCNC can only be guaranteed for Higgs doublets, postulating that each kind of fermion couples to only one of the doublets. In other cases, FCNC can be reduced by setting the Higgs masses high enough so that their contribution to loops is negligible.

- **CP violation should be small or absent from the Higgs sector**

  The experimental measurements constrain CP violation to be small. Unless the model is built specifically to explain the existing CP violating measurements, it must be avoided that explicit CP-violating terms are present in the Higgs potential and also guaranteed that the induced spontaneous CP violation is small.

The easiest way to keep all the characteristics of the SM without needing fine tuning is to make a theory with only doublets, starting with two doublets. It has been shown that such a general model is renormalizable [23].

2.4.1 2 Higgs Doublets Models

The existence of two complex scalar doublets would enlarge the SM particle spectra. The two doublets correspond to 8 degrees of freedom, three of which will be absorbed by the massive gauge bosons (Z^0 and $W^{\pm}$), while other 5 will give rise to physical Higgs bosons. The real components, corresponding to the vacuum expectation values, give rise to two neutral scalar particles (h^0, H^0), and the imaginary components give the goldstone boson associated to the Z^0 (as in the SM) plus a CP-odd neutral scalar (A^0), the other components of the two doublets give rise to the goldstone bosons associated to $W^{\pm}$ (as in the SM) and two charged scalars ($H^{\pm}$).

The new potential describing the two complex scalar doublets used to break the $SU_L(2) \times U_Y(1)$ symmetry can be written in a general form as:

$$\mathbf{V = A_i x_i + 1/2. B_{ij} x_i x_j}, \qquad \mathbf{B_{ij} = B_{ji}} \qquad \mathbf{i, j = 1, 2, 3, 4}$$

in which x_i represent the several invariants that can be constructed,
$x_1 = \phi_1^+\phi_1$, $x_2 = \phi_2^+\phi_2$, $x_3 = \mathcal{R}(\phi_1^+\phi_2)$ and $x_4 = \mathcal{I}(\phi_1^+\phi_2)$.

The requirement that the potential does not violate CP, explicitly or spontaneously, can be guaranteed in two different ways (hereafter labeled as Potential A and Potential B) which will reduce the number of variables in the potential to 7 independent ones[24] (to be added to the two vacuum expectation values):

$V = -\mu_1^2 x_1 - \mu_2^2 x_2 - \mu_{12}^2 x_3 + \lambda_1 {x_1}^2 + \lambda_2 {x_2}^2 + \lambda_3({x_3}^2) + \lambda_4({x_4}^2) + \lambda_5(x_1 x_2)$ with

- **A)** $\mu_{12} = 0$, by making the potential invariant under a $\phi_1 \to \phi_1$ and $\phi_2 \to -\phi_2$ symmetry
- **B)** $\lambda_3 = \lambda_4$, by making the potential invariant under the global U(1) symmetry (which is only softly broken by the μ_{12} term): $\phi_1 \to \phi_1$ and $\phi_2 \to e^{i\theta}\phi_2$

Two of the 9 free parameters are fixed by the choice of the minima for the potential but seven free parameters are still to be determined by experiment. The sum of the squares of the vacuum expectation values is already determined by the Z and W masses, while the other parameters – usually expressed as the Higgs masses (M_{h^0},M_{H^0},M_{A^0} and $M_{H^\pm}$), the ratio of the two vacuum expectation values ($\beta = \arctan(v_2/v_1)$) and the mixing angle of the two neutral CP-even scalars (α) – will have to be determined only when the Higgs bosons are discovered. The Feynman rules are expressed as functions of these physical parameters (the angle $\delta = \alpha - \beta$ will be used).

couplings between Higgs bosons

The triple scalar vertices are proportional to g/M_W and the quartic scalar vertices are proportional to $(g/M_W)^2$. The specific constant of each vertex is determined by the Higgs potential and depends on the Higgs masses, as well as on the angles α and β.

As stated above, there are two alternative potentials, applying different constraints to the free parameters. These slight differences lead to two very distinct "models" in what concerns the relations between model parameters and the couplings between the Higgs bosons.

couplings between Higgs bosons and gauge bosons

The Feynman rules for the couplings of the 2HDM Higgs bosons to the gauge bosons can be understood with the help of some simple considerations, based on the extrapolation of the SM and symmetry rules:

- The allowed couplings between the two gauge bosons and the Higgs boson that give the particle masses are similar to the SM ones. Only the neutral scalars couple to the massive gauge bosons:
  - $h^0Z^0Z^0$, $H^0Z^0Z^0$, $h^0W^+W^-$ and $H^0W^+W^-$,
    Defining $v = \sqrt{2}M_W/g$ (and $v_1 = v.\cos\beta$,$v_2 = v.\sin\beta$) and using the rotation matrix (α) to get the mass eigenstates from the $SU(2)_L$ doublets, leads to:
    $g^2.W^\mu W_\mu(\cos\beta\phi_1 + \sin\beta\phi_2)=$
    $=hW^\mu W_\mu gM_W(\cos\beta\sin\alpha - \sin\beta\cos\alpha)$ $+HW^\mu W_\mu gM_W(\cos\beta\cos\alpha + \sin\beta\sin\alpha)$,
    so $g_{H^0VV} = g_{\phi_{SM}VV}\cos(\beta-\alpha) = g_{\phi_{SM}VV}\cos\delta$
    and $g_{h^0VV} = g_{\phi_{SM}VV}\sin(\beta-\alpha) = -g_{\phi_{SM}VV}\sin\delta$

    The SM couplings are suppressed by $\sin\delta$ for h^0, or by $\cos\delta$ for H^0. This guarantees that $\rho = 1$ and the unitarity condition for boson-boson scattering ($g^2_{H^0VV} + g^2_{h^0VV} = g^2_{\phi_{SM}VV}$)
  - The CP-odd boson, A^0, can not couple to pairs of gauge bosons as that would violate CP-conservation. Couplings of charged scalars with W and Z/γ are also forbidden (the coupling with a photon would violate electromagnetic current conservation).

- The couplings between one gauge boson and two Higgs bosons are forbidden for equal particles due to Bose symmetry. The only allowed couplings are:
  - $h^0A^0Z^0$ and $H^0A^0Z^0$, with different CP states,
    To "guess" the coupling values, the unitarity conditions can be used. Knowing that the vertices with two scalars and one vector depend on the vector polarization and on the energy difference between the two scalars and imposing the unitarity conditions:
    $\sigma(A^0Z^0 \to W^+W^-) \to cte$ and $\sigma(A^0Z^0 \to A^0A^0) \to cte$
    implies that
    $g_{AZh}g_{WWh} + g_{AZH}g_{WWH} = 0$ and $g^2_{AZh} + g^2_{AZH} = cte$
    ie, $g_{WW\phi_{SM}}(-g_{AZh}\sin\delta + g_{AZH}\cos\delta) = 0$
    $\Rightarrow g_{AZH} = g_{AZh}\tan\delta \Rightarrow g^2_{AZH}(\tan^2\delta + 1) = cte$
    and, finally: $g_{AZH} = C\cos\delta$ and $g_{AZh} = C\sin\delta$.

    in complete agreement with what is obtained directly from the Lagrangian expansion.

- $W^+_\mu H^- h^0$, $W^+_\mu H^- H^0$ and $W^+_\mu H^- A^0$, (and charge conjugates)

  The symmetry with the above case applies to define the vertices $H^+W^-h^0$ and $H^+W^-H^0$, while $H^+W^-A^0$ does not depend on δ.
- and $H^+H^-Z^0$ and $H^+H^-\gamma$, with couplings defined by the charge only;

- The couplings with two gauge bosons and two Higgs include:
  - $VVHH$ with $V = W^\pm, Z^0$ and $H = h^0, H^0, A^0$ all with the same couplings, equal to the SM ones, for all neutral Higgs particles;
  - $H^+H^-W^+W^-$, $H^+H^-Z^0Z^0$, $H^+H^-Z^0\gamma$, $H^+H^-\gamma\gamma$;
  - H^+W^- with any choice of a neutral Higgs boson and a Z^0 or γ.

couplings between Higgs bosons and fermions

To ensure the absence of FCNC in 2HDM, it is necessary that only one of the doublets couples to each kind of fermion. The coupling of each CP-even neutral scalar is then defined by $-\sin\alpha$ or $\cos\alpha$ according to its first or second doublet component, normalized by a $\cos\beta$ or $\sin\beta$ giving the vacuum expectation values of the corresponding doublet [25].

	u-type	d-type	lepton
I	$\frac{\cos\alpha}{\sin\beta}$	$\frac{\cos\alpha}{\sin\beta}$	$\frac{\cos\alpha}{\sin\beta}$
I'	$\frac{\cos\alpha}{\sin\beta}$	$\frac{\cos\alpha}{\sin\beta}$	$\frac{-\sin\alpha}{\cos\beta}$
II	$\frac{\cos\alpha}{\sin\beta}$	$\frac{-\sin\alpha}{\cos\beta}$	$\frac{-\sin\alpha}{\cos\beta}$
II'	$\frac{\cos\alpha}{\sin\beta}$	$\frac{-\sin\alpha}{\cos\beta}$	$\frac{\cos\alpha}{\sin\beta}$

Table 2.2: Coupling of the lightest CP-even Higgs boson to fermions, for different choices of the doublet which couples to each fermion type. If neutrinos were required to have mass, the number of possible combinations would be doubled.

Table 2.2 shows the possible combinations of couplings for the lightest scalar Higgs boson (h^0), when the doublet ϕ_2 (with the highest vacuum expectation value) is assumed to couple to u-type quarks. For the heavier scalar Higgs boson (H^0) the corresponding couplings will be affected by an interchange of $\cos\alpha \leftrightarrow -\sin\alpha$, and so summing over both scalars always keeps the unitarity condition satisfied. The $A^0 f\bar{f}$ couplings are similar to the $h^0 f\bar{f}$ ones but with α replaced by β.

2.4.2 Fermiophobic Higgs Model

With six unknown parameters and two potentials, a wide range of phenomenology is available. To choose interesting working points, some restrictions can be applied based on experimental data, ensuring still that the phenomenology is different from the SM one and can be tested with the available data.

In the general 2HDM, the limits when β is 0 or $\pi/2$, tend to reproduce the SM (ie, only one doublet with vacuum expectation value different from 0); but also if α is 0 or $\pi/2$, the two CP-even neutral scalars do not mix and the SM phenomenology is partially recovered (with the additional 4 particles): in that case the 2 CP-even neutral scalars are needed to give mass for the gauge bosons, but only one of them gives the mass to each fermion type. For a type I model, the phenomenology of the SM would be more closely reproduced by h^0 if $\alpha = 0$ or by H^0 if $\alpha = \pi/2$.

The scenario investigated in this thesis will be the fermiophobic Higgs model [26]. Setting $\alpha = \pi/2$, within a model type-I, makes the observable phenomenology far from the SM one by reducing the couplings of the lightest neutral CP-scalar Higgs to the massive gauge bosons and by decoupling it from the fermion sector. In this case, the heavier scalar H^0 has SM like couplings to the fermions (enhanced by $1/\sin\beta$) and to gauge bosons (suppressed by $\cos\beta$), while the couplings of A^0 depend always only on β.

Although the extreme points of β (0 or $\pi/2$) are not interesting as a definite parameter point (there would be no need for one of the doublets) they represent interesting limits to explore non-standard phenomenology. If $\beta = \pi/2$, h^0 would be also bosophobic, and could only couple at tree-level to other scalars; while, if $\beta = 0$, h^0 would have SM couplings to the gauge bosons but not to the fermions. Table 2.3 shows the Higgs couplings as a function of β ($\delta = \pi/2 - \beta$) in the fermiophobic model and for both potentials A and B.

There are still some general analysis that can constrain this model. General 2HDM analysis constrain $M_{H^\pm}$ to be close or above $M_{W^\pm}$ [27] (the production of the charged Higgs bosons are determined by their electrical and weak charges, only their decays vary from model to model). On the other hand, extrapolations of the SM Higgs searches constrain the mass of neutral Higgs bosons, together with the

HZ production cross-section (expressed as a factor to the SM cross-section) and the decay Branching Ratio (BR) of Higgs to $b\bar{b}$, as seen in figure 2.4.

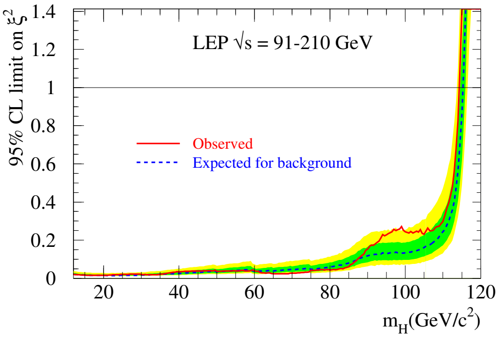

Figure 2.4: Limits from SM Higgs search expressed as limits on the product of the scale factor to $\sigma(HZ)_{SM}$ and $BR(H \to b\bar{b})$ ($\xi^2 = \sin^2\delta.BR^2$ for h^0 and $\cos^2\delta.BR^2$ for H^0), as a function of the neutral Higgs boson mass.

In the fermiophobic model, only H^0 couples at tree-level to $b\bar{b}$, but at 1-loop level the decay $h^0 \to b\bar{b}$ can exist. In fact, although all other decays to $f\bar{f}$ can be neglected, the decay to $b\bar{b}$ can be important for light Higgs bosons.

In what follows it will be assumed that both the H^0 and $H^{\pm}$ are heavy and the phenomenology of h^0 and A^0 will be explored.

The main production modes for neutral Higgs bosons at LEP are: $e^+e^- \to Z^0 \to h^0Z^0$ and $e^+e^- \to Z^0 \to h^0A^0$ and since their cross-sections are proportional to $\sin\delta$ or $\cos\delta$, one of them will be seen, whatever the value of β, so long as the masses are within the LEP reach: $M_{h^0} + 91.2 \leq \sqrt{s}$ and $M_{h^0} + M_{A^0} \leq \sqrt{s}$.

The properties of the two potentials might indicate that these particles are light, particularly for small δ [28]:

- in Potential A, $m_{h^0} = \sqrt{2\lambda_1}v\cos\beta$;
- in Potential B, $m_{h^0} = \sqrt{m^2_{A^0} - 2(\lambda_3 + \lambda_5 - 2\lambda_1)v^2\cos^2\beta}$;

They ensure that, for $\delta = 0$, either h^0 becomes massless (A) or h^0 and A^0 become degenerate (B). Unfortunately, a small δ implies that hZ production is suppressed and hA enhanced and then an indication of the A^0 mass is needed.

Table 2.3 shows that, although the production vertices are the same in both potentials A and B, the decays of h^0 differ whenever M_{A^0} is different from 0. For A^0,

vertex	Pot.	coupling	comments
$h^0 f\bar{f}$	[A=B]	0	**fermiophobic**
$h^0 H^0 H^0$	[A]	0	$\Rightarrow$ no-mixing
	[B]	$-ig/(4M_W) \times M_{A^0}^2 \cos\beta$	[only with A^0]
$h^0 h^0 h^0$	[A]	$ig/(2M_W \cos\beta).3M_{h^0}^2$	self-coupling
	[B]	$ig/(2M_W \cos\beta).(3M_{h^0}^2 + 3M_{A^0}^2 \sin^2\beta)$	
$h^0 XX$	[A]	$ig/(2M_W \cos\beta).(M_{h^0}^2 + \Delta\cos^2\beta)$	depend on M_{h^0},M_X,β [and M_{A^0}]
	[B]	$ig/(2M_W \cos\beta).(M_{h^0}^2 + \Delta\cos^2\beta \mp M_{A^0}^2)$	
$X = A^0, H^\pm$		with $\Delta = 2M_X^2 - M_{h^0}^2$	
$h^0 W^+ W^-$	[A=B]	$igM_W g_{\mu\nu} \cos\beta$	depend only
$h^0 Z^0 Z^0$	[A=B]	$igM_W g_{\mu\nu} / \cos\theta_W \cos\beta$	on β
$h^0 W^+ H^-$	[A=B]	$ig/2.(p_{h^0} - p_{H^-})_\mu \sin\beta$	depend only
$h^0 Z^0 A^0$	[A=B]	$g/(2\cos\theta_W).(p_{h^0} - p_{A^0})_\mu \sin\beta$	on β
$H^0 f\bar{f}$	[A=B]	$-ig/(2M_W \sin\beta) m_f$	with: M_{H^0}, $\sin\beta \leftrightarrow \cos\beta$, charged conj.
$H^0 XY$		as h^0 for (X, Y=any bosons)	
$A^0 f\bar{f}$	[A=B]	$-g\cot\beta/(2M_W) m_f$	
$A^0 W^+ H^-$	[A=B]	$-g/2.(p_{A^0} - p_{H^-})_\mu$	(fixed)
$H^+ \nu_i \bar{l}_i$	[A=B]	$-ig\cot\beta/(2\sqrt{2}M_W)(1+\gamma_5)m_f$	
$H^+ \bar{u}_i d_j$	[A=B]	$ig\cot\beta/(2\sqrt{2}M_W)[(1-\gamma_5)m_{u_i} - (1+\gamma_5)m_{d_j}]V_{ij}$	CKM matrix
$H^+ H^- \gamma$	[A=B]	$ie(p_{H^+} - p_{H^-})_\mu$	charge only
$H^+ H^- Z^0$	[A=B]	$ie(-\cot 2\theta_W)(p_{H^+} - p_{H^-})_\mu$	(fixed)

Table 2.3: Higgs boson couplings in fermiophobic model

on the other hand, the decays are fixed by δ and do not depend on the potential. The decays of h^0 and A^0 in typical situations, are represented in figures 2.5 and 2.6 (from [28]).

h^0 could have tree-level decays to Z^0Z^0, W^+W^-, A^0A^0, H^+H^-, A^0Z^0 or H^+W^-. For the ranges of masses considered, only A^0A^0 may be kinematically allowed (and in that case will have a $BR \sim 1$) but, on the other hand, decays through virtual pairs (and 4 fermions in the final state) are also possible – being that the decays through gauge bosons are favoured since their widths are larger. Such decays compete with the 1-loop-level decays, to $b\bar{b}$, $\gamma\gamma$ and $Z^0\gamma$, which can be dominant for light h^0.

The dominant diagram for $b\bar{b}$ has a loop of H^+H^-t, which is favoured in relation to other fermion pairs (the coupling Hbt is proportional to the top mass) but, on the other hand, makes the partial decay width very dependent on the Higgs masses that govern the $H^+H^-h^0$ vertex (and M_{A^0}, in potential B). The decay to b-quarks decreases fast with $M_{h^0} - 2M_b$, and at its peak has an extra factor of $\tan^2\delta$ when compared to the corresponding diagram (with $H^+H^-H^+$) giving two photons[8]. The decays $h^0 \to f\bar{f}$ are then negligible in all parameter space, except for the region $M_{h^0} \sim 10$ GeV/c^2 and $\sin(\delta) > .75$ which is excluded by the results in figure 2.4.

The decay to two photons is then the dominant one in a large region of parameters, while in the SM the BR is $\leq 10^{-3}$. The dominant decay modes for $M_{h^0} < M_Z$ are then $h^0 \to A^0A^0$ (tree level) if $M_{h^0} > 2M_{A^0}$ and $h^0 \to \gamma\gamma$ (one loop) otherwise. The decays of h^0 to other boson pairs can be important when $M_{h^0} > M_Z$: namely the one loop decay $h^0 \to Z^0\gamma$ can have a BR as large as 20% for very small δ values, while the decay to WW^* is important for large δ values.

Figure 2.5 shows the branching ratios of h^0 for a $\sin^2\delta = 0.1$ both for potential A and B. In potential A, the BRs to photons are constant for higher $\sin^2\delta$ and increase for lower values, as the decays to heavy gauge bosons are suppressed. In the case of potential B, the $h^0H^+H^-$ coupling has an additional dependence on M_{A^0} which leads to cancellations of the $h^0 \to \gamma\gamma$ decay for specific combinations

[8]Even if $\sin\delta = 1$, $|h^0W^+W^-|/|h^0H^+H^-|=(M_W/M_H)^2$ in Potential A, and $h^0H^+H^-$ is even larger in Potential B.

of M_{A^0}, $M_{H^\pm}$ and $\sin^2\delta$. For higher values of $M_{H^\pm}$ and $\sin^2\delta$, however, there are regions free of such cancellations for the A^0 masses accessible at LEP.

The tree level decay modes of the A^0 boson are: $A^0 \to f\overline{f}$, $A^0 \to Z^0h^0$, and $A^0 \to W^\pm H^\pm$ (when kinematically allowed). The main decay of A^0 is into a fermion-antifermion pair, namely a $b\overline{b}$ pair if $M_{A^0} > 10$ GeV/c^2. However, above the Z^0h^0 threshold, the decay $A^0 \to Z^0h^0$ dominates for all $\sin\delta < .95$. Below this threshold, the three level decays are proportional to $\tan\delta$ and the total width dominated by this parameter: for very low δ ($\sin\delta < 10^{-3}$) the A^0 can leave the detector before decaying. These small values of δ correspond to a band of $M_{A^0} \sim M_{h^0}$, in Potential B; but, in the case of Potential A, small values of δ can result in totally invisible final states as $e^+e^- \to Z^0 \to h^0A^0 \to 3A^0$.

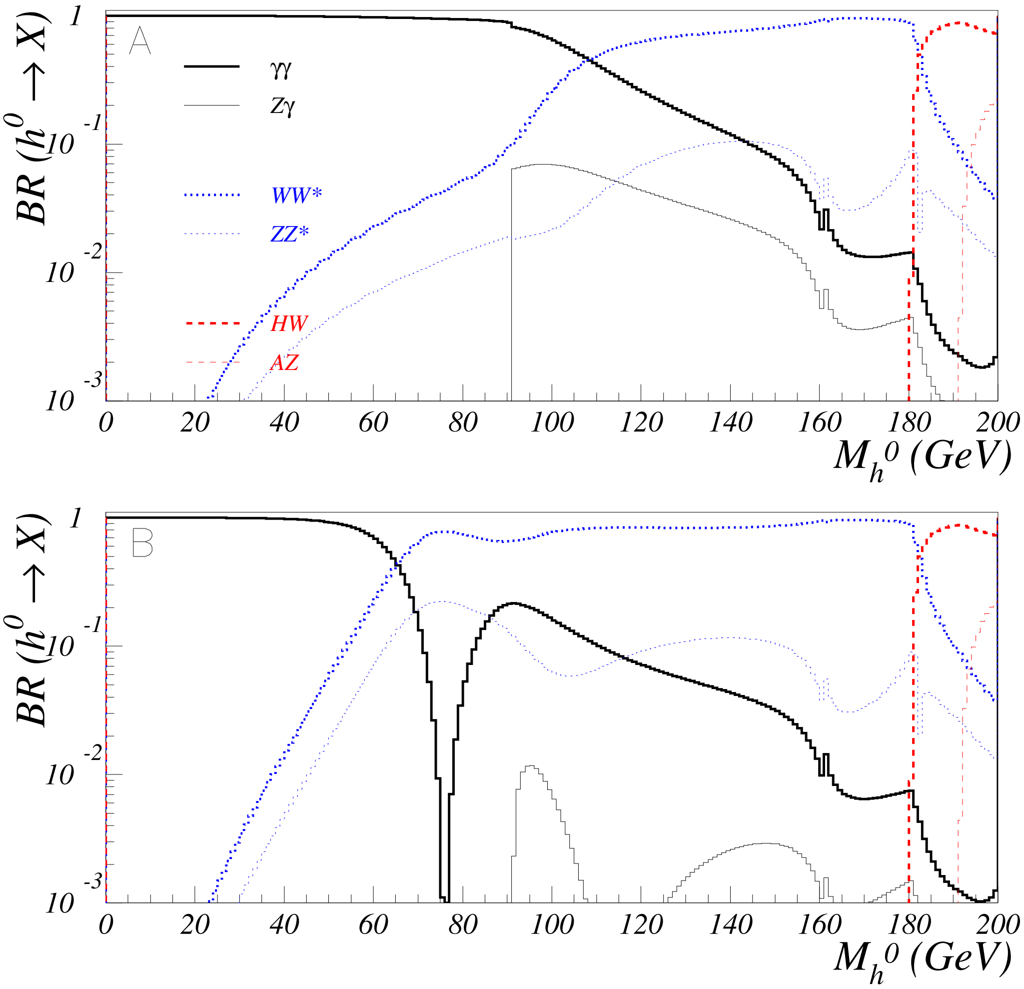

Figure 2.5: h^0 branching ratios in Potential A (top) and B (bottom) as a function of the mass. The other parameters are fixed in both cases to be $M_{A^0} = M_{H^\pm} = 100$ GeV/c^2, $M_{H^0} = 1$ TeV/c^2 and $\sin^2\delta = 0.01$.

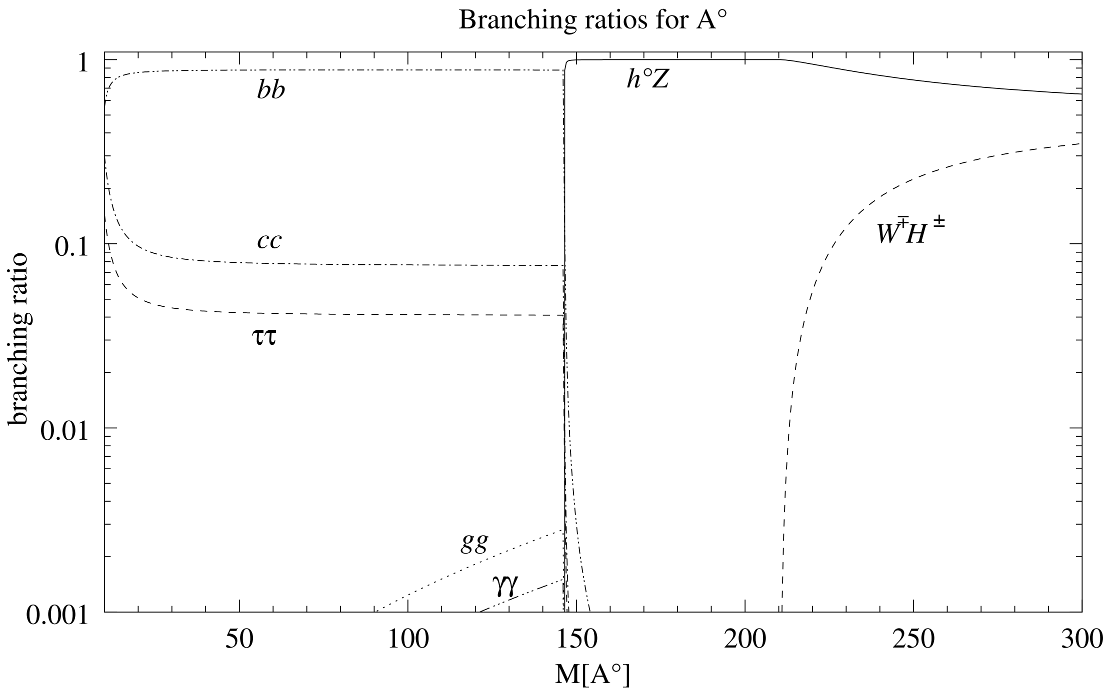

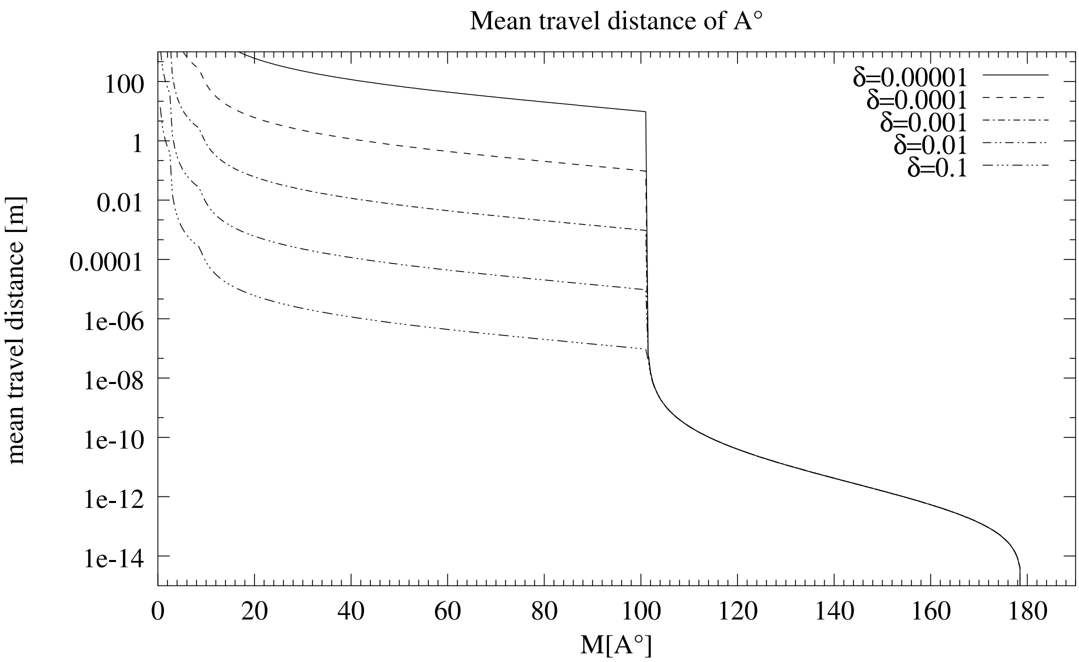

Figure 2.6: A^0 decays are equal in potential A and B. The top plot shows the branching ratios for $\delta = 0.1$, $M_{H^\pm} = 130$ GeV/c^2, $M_{H^0} = 300$ GeV/c^2 and $M_{h^0} = 55$ GeV/c^2. The lower plots shows the mean travel distance (for $\sqrt{s} = 189$ GeV) for several δ values and $M_{h^0} = 10$ GeV/c^2.

Chapter 3

DELPHI Experiment

This chapter describes the experimental setup for physics analysis in DELPHI, including the processes of acceleration in LEP, detection in DELPHI and the data reconstruction.

The general analysis principles are introduced and, in particular, the reconstruction and identification of isolated photons in hadronic events is explained.

3.1 LEP accelerator chain

The production of electron and positron beams with energies ranging between 45 GeV (at LEP1) and 104 GeV (at LEP2) required a chain of five accelerators. The electrons were produced by the "electron gun" and shot on to a tungsten target to produce the positrons. After that, both beams followed the same chain: passing first two linear accelerators, working at 200 MeV and 600 MeV, an accumulator at this energy, and from there being injected in the CERN Proton Synchrotron (PS) operating at 3.5 GeV and the Super PS operating at 20 GeV. From the SPS the beams would be injected in LEP. Both the PS and the SPS were originally built for proton beams, and their use for LEP was done in such a way that it did not affect their original purpose. The filling of LEP was done in 4 cycles during the dead time between two consecutive proton cycles and, as an effect of this, the beams entered LEP in what is called the four bunch mode, each bunch with around 10^{11}

particles.

The LEP tunnel is an approximate circumference of 27 km, composed of 8 straight sections and 8 arcs, at a depth of $\sim$100 m. The acceleration at LEP was done in the straight sections, by RadioFrequency (RF) cavities, while the arcs were equipped with magnets for bending and focusing the beams. The four LEP detectors (ALEPH, DELPHI, L3 and OPAL) were located at the centre of straight sections.

One of the problems of circular colliders is the loss of energy due to synchrotron radiation. At LEP, in each turn, a 100 GeV beam would loose 3 GeV (the energy lost scales with E^4) but that energy was replaced by the RF system continuously. The fact that the detectors were placed in straight sections reduced the effect of the synchrotron radiation at detection time.

Near each of the LEP detectors both beams had to be made to approach each other in order to produce the collision but also each of the beams had to be focused again into even smaller dimensions, so that high luminosities could be achieved. A set of superconducting quadrupoles with very strong field gradients focused the transverse beam dimensions to about 10 μm and 250 μm in the vertical and horizontal planes, respectively.

The two parameters that characterize the accelerator and the physics produced by it are the energy and luminosity. Both were determined separately by LEP – based on its own measurements of the beams – and by the four experiments – already with the data analysis, as will be explained after. The energy of the beams was measured with different techniques [29], relying on their polarization (at LEP1 energies) or on the effect of dipole fields acting on them. By accurately measuring the magnetic field and the bending created by it, it was possible to know the beam energy to about 5 MeV. The luminosity, ie the rate and dimensions at which collisions may occur, is determined by the number of bunches, number of particles per bunch, bunch sizes and revolution frequency, the typical values for LEP were $10^{32}/(s.cm^2)$.

During the active life of LEP, both the energy and luminosity were continuously increased. At LEP1, the accelerator was run at around 90 GeV, the peak of cross-section for electron-positron annihilation, and the luminosity accumulated in the 7 years of operation was of 221 pb^{-1}, corresponding to more than 10 million events. When the LEP2 phase started, with progressively higher energies, the total cross-section decreased and the luminosities achieved per year became crucial. The luminosity was enhanced progressively by a better tunning of the beams – the spread in x and y were reduced to 70% and 25% of the LEP1 values and the intensity of the beams was increased in 30% – when, in 1999, LEP overcame its construction limit of 200 GeV, the luminosity per year had increased by a factor of 10. In 2000, the last year of operation, a new running scheme was introduced: the beams were used to get high luminosities at a first energy, but as their intensity diminished and further acceleration became possible, the same beams were used to get to higher energies – fully using the RF cavities capabilities.

Even if the luminosities achieved at LEP2 were impressive, in each year LEP was run for some days at the Z pole, in order to provide large number of events, at a well studied energy, for detector calibration.

3.2 DELPHI detector

DELPHI stands for DEtector with Lepton, Photon and Hadron Identification. The detector was composed of several sub-detectors, installed as a cylindrical box covering a section of the LEP tube (as shown in figure 3.1), the two end-caps of the cylinder could be opened to allow the access to the sub-detectors. A detailed description of DELPHI and its performance can be found in [30, 31] and here it will be only briefly reviewed, from the point of view of the event reconstruction and with special emphasis in particle identification.

The sub-detectors are organized in layers in the barrel part of DELPHI and complemented by similar devices in the forward part (that is in the end-caps). Full coverage of the solid angle around the collision point is intended and the coverage of DELPHI extends down to less than 3° of polar angle from the beam pipe axis[1].

[1]The DELPHI coordinate system is defined from the interaction point, with the z-axis along the direction of the electron beam, the x-axis pointing towards the center of LEP and the y-axis upwards; the polar angle θ is defined with respect to z and the azimuthal angle ϕ with respect to x; $r = \sqrt{x^2 + y^2}$.

From the central interaction point, the particles crossed, in sequence, tracking devices (which signal the passage of all charged particles) and Čerenkov detectors (which measure their velocity); electromagnetic calorimeters (which measure the energy of mainly electrons and photons) and hadronic calorimeters (which measure the energy of charged and neutral hadrons), and muon chambers. The tracking devices allow for the reconstruction of the trajectories of charged particles, and were surrounded by a magnetic field of 1.2 T which curved the trajectories according to the momentum of each particle so that it could be measured. In addition, other detectors gave information about the passage of particles and, in particular, time information useful for the full event reconstruction and to trigger the data acquisition systems.

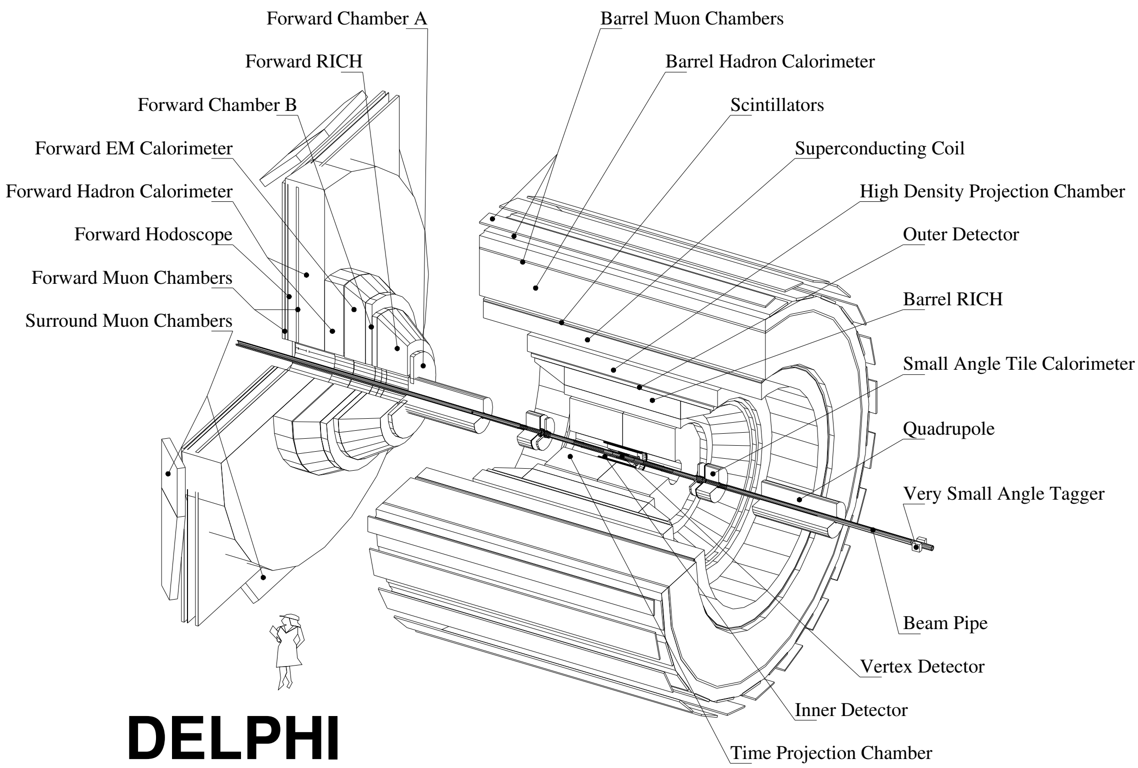

Figure 3.1: DELPHI detector

The particle type, momentum and energy can be inferred for most of the particles which crossed the detector:

- muons are the only charged particles that get to the muon chambers (the other particles will leave their energy in the calorimeters),
- electrons are charged particles which leave their energy in electromagnetic calorimeters,
- charged hadrons leave their energy in the hadronic calorimeters, their momentum is measured in the tracking and their velocity in the RICH – so the different types can be separated by mass,
- neutral hadrons are depositions in the hadronic calorimeter not initiated by a charged track,
- photons are energy deposition in electromagnetic calorimeters with no associated charged track;
- neutrinos are accounted for in the missing energy and momentum which can be calculated due to the detector's hermeticity,
- taus and other particles which decay promptly must be reconstructed from the corresponding final state particles.

This is, of course, a schematic idea. In fact the detection is not that straight forward and the measurement of energy and momentum can be subjected to large errors, in some cases leading also to mis-identification of the particle types. For a true event reconstruction, the sub-detectors properties and their interplay must be explored and their limitations must be well understood.

The main characteristics of the DELPHI tracking devices and calorimeters are summarized in tables 3.1 and 3.2, respectively. In addition, other sub-detectors exist which are particularly important for fast signaling and time measurement.

All the four LEP detectors had similar structure but each of them had features which made it different and more suitable for specific physics channels. For DELPHI, the main vocation was the careful identification of all particles and it was the only one to have Ring Image Čerenkov (RICH) detectors, both in the barrel and the forward regions. The RICH's detection principle is based on the Čerenkov radiation, produced by charged particles traveling at a speed higher than that of

Barrel	R (cm)	θ coverage	hit resolution (μm)	N_{hits}
VD	6.3, 9.0, 10.9	$> 25°$	8(rϕ); 10(z)	6(3D)
ID	12 to 23	$> 15°$	50(rϕ); 1.5 mrad(ϕ)	24($r\phi$)
TPC	40 to 110	$> 20°$	250(rϕ); 880(rz)	16(3D)
OD	197 to 206	$> 42°$	110(rϕ); 3.5 cm(z)	3(3D)+2($r\phi$)
Forward	$\|z\|$ (cm)			
VFT	—	10° to 25°	100	4
FCA	∼160	11° to 32°	290(xy)	6
			8.5(θ); 24(ϕ) mrad	
FCB	∼275	11° to 36°	150(xy)	12
			3.5(θ); $4/\sin\theta(\phi)$ mrad	

Table 3.1: DELPHI tracking detectors: their contribution to the track reconstruction in what respects spatial resolution and number of points is given, together with their angular coverage and location. DELPHI is symmetric in z; the complementary values θ and $180° - \theta$ are always assumed.

Barrel	R (cm)	θ coverage	Depth	$\sigma(E)$/E (E in GeV)	Space r.
HPC	208 to 260	$> 43°$	$18X_0/\sin\theta$	$0.043 \oplus 0.62/\sqrt{E}$	1.0 mrad (θ)
					1.7 mrad (ϕ)
HCAL	320 to 479	$> 43°$	$6\lambda/\sin\theta$	$0.21 \oplus 1.12/\sqrt{E}$	2.96°(θ)
					3.75°(ϕ)
Forward	$\|z\|$ (cm)				
FEMC	284 to 340	8° to 35°	$20X_0$	$0.052\oplus 0.27/\sqrt{E}$	0.5 cm
				$\oplus$ 0.11/E	
STIC	220 to 260	3° to 11°	$27X_0$	$0.015 \oplus 0.135/\sqrt{E}$	0.25 to
					1.20 mm
HCAL		11° to 48°	6λ	$0.21 \oplus 1.12/\sqrt{E}$	2.62°(ϕ)

Table 3.2: DELPHI calorimeters: their contribution to the reconstruction, in terms of energy and spatial resolution, is given together with their polar angle coverage, location and dimension in terms of radiation or interaction lengths (X_0 and λ). The STIC covers angles down to 1.7° but the acceptance below 3° is not considered in the analysis.

light in the same medium. The Čerenkov photons are emitted at a fixed angle which is a function of the velocity of the charged particle. The DELPHI RICH was composed of two different radiator materials in order to be sensitive to different ranges of momentum. In some momentum ranges, the RICH information on velocities was complemented by TPC measurements.

The Time Projection Chamber (TPC) was the main tracking device in DELPHI, giving the most precise 3D position information for the reconstruction of charged tracks and an indirect measurement of the charged particle velocity. The detection principles of the TPC were based on the ionization of a gas by the passage of charged particles. It was divided in 12 chambers, each equipped with cathode pad rows, which measured the $r\phi$ positions at which the electrons were created, and sensitive wires, which counted the total number of electrons produced, giving a measure of the energy loss (proportional to the velocity). The electrons, subjected to a constant electrical field, were drifted in the z direction, towards one end of the chamber. The time mediating between the electrons production and their collection would be related to the z coordinate of the original charged particle track. Each track left up to 16 points in the TPC, with resolutions of 250 μm in $r\phi$ and 900 μm in z.

Another important tracker was the Vertex Detector (VD), a silicon strip detector with three concentric layers, located near the beam pipe. The overlap of the sectors in each layer allowed for the reconstruction of a maximum of 6 points per track with very good $r\phi$ resolution while the z position was measured just in the first and third layers, with a slightly worse resolution. Since it was located near the beam pipe, it gave a very precise extrapolation of the charged tracks to the collision point, useful for the separation of tracks coming from the primary and secondary vertices. This information is fundamental for particle identification: the two most clear examples which will be used in the analyses are the tagging of secondary vertices from B-meson decay and the separation of electron tracks from photons converting after the VD. The vertex detector was extended for LEP2 [32], and now covers polar angles above 11 degrees. For low polar angles, however, the conversion of photons and the effect of multiple scattering in the beam-pipe material limit the above identification capabilities. The VD information will be used only above 25°.

The other two trackers in the barrel were the Inner Detector (ID) and Outer Detector (OD) whose names are related to their positions relatively to the TPC and the RICH. Both of them had fast signaling devices which was important for the triggering of events during data taking. In the forward regions of the detector the tracking was completed by the Forward Chambers A and B.

Surrounding the tracking devices, in which the charged particles interact with very few material without loosing much of their energy, there was a layer of very dense material – the calorimetric detectors – in which both charged and neutral particles may leave all their energy. The principle of a calorimeter is to force the initial particle to have multiple interactions thus loosing its energy which must then be collected to reconstruct the total particle energy. In addition, since they are the only devices sensitive to neutral particles, the reconstruction of particle directions is also an important feature.

In an electromagnetic calorimeter, the photons convert into electron/positron pairs and the electrons radiate photons; the multiplication of these processes originates a cascade which spreads until the final particles are left with very low energy. Heavier particles, however, do not radiate that much and will pass the electromagnetic calorimeters leaving only a small part of their energy. They then reach the much larger hadronic calorimeters where the energy is deposited by strong interaction with the detector's nuclea.

The cascades evolve longitudinally to the initial particle direction – to a dimension that is characteristic of each calorimeter material, and is measured in radiation lengths for electromagnetic calorimeters or interaction lengths for hadronic calorimeters (X_0 and λ, respectively, both defined as the distance after which the initial energy is reduced by a factor e) – but also transversely. The calorimeters must be large enough to contain all the energy of the initial particle (at LEP energies that corresponds to around 20 radiation lengths for the electrons and photons and 5 interaction lengths for the hadrons) and the energy collection must be segmented in such a way that energy depositions originating from two different particles can be distinguished and that the analysis of the cascade shape allows for the reconstruction of the initial particle direction.

Neutral and charged particles give rise to the same kind of cascades but it must be taken into account that the charged ones, in particular electrons, lost additional energy in the tracking and namely while crossing the RICH. For charged particles, the energy information from the calorimeters can be complemented with the momentum and velocity measurements discussed above, while for neutral particles the measurements of the calorimeters are the only information available. For photons, the reconstruction is complicated by the fact that there can be conversions before reaching the calorimeters.

There were three electromagnetic calorimeters in DELPHI: the High Density Projection Chamber (HPC) in the barrel, the Forward ElectroMagnetic Calorimeter (FEMC) and the Small angle TIle Calorimeter (STIC) in the very forward region, to detect particles emitted at low angles. They were different in their composition and detection principles but also in their modular segmentation – the choice of the module shape and positions is important both for the position and energy resolutions. The HPC was composed of lead layers, acting as converting material, embedded in a gas where the energy was deposited; FEMC was a homogeneous lead-glass calorimeter; while STIC was a lead-scintillator sampling calorimeter.

In the HPC, the modular division was done in ϕ and θ which implied that some of the cascades would be spread between adjacent modules, and some energy lost in between them. Cascades corresponding to particles passing in these regions would not be fully contained in the calorimeter, particles emitted at $90°$ from the beam direction, would pass in between two modules and could be completely lost.

In the FEMC the several modules were truncated pyramids placed in such a way that they were approximately projective to the interaction point – the cascades could, in principle, be fully collected in a single module, improving the energy resolution. They were only slightly tilted, so that no particle could escape in between two modules.

The STIC was composed of just one cylinder in each side of DELPHI, near the beam-pipe, and was thus totally hermetic. The scintillator planes were divided in ϕ and θ with the readout done in an absolutely projective way, leading to a better energy resolution.

Given their different locations in DELPHI, the distribution of matter before the three calorimeters was also very different. Before reaching the HPC, photons crossed around 0.8 $X_0/\sin\theta$ and thus half of them converted: 7% of these would be detected as e^+e^- pairs in the TPC, but most conversions occurred in the exterior TPC wall or in the RICH and were thus undetected. This degrades the energy resolution, because of the extra energy loss suffered by the electron pairs, and also the position resolution, as the electron and positron keep only approximately the original photon direction. For the FEMC, photon conversion represents a more serious problem as the total material corresponded there to around $2X_0$ and was located far from the detector, implying that electron and positron would be separated in space. Before the STIC, there were no detectors but conversions could still occur in the beam-pipe and on support structures located at low polar angles.

The energy resolutions reported in table 3.2 (from the studies in [33]) take all these effect into account. Notice that the STIC and the FEMC together cover all the forward part of DELPHI but in between the FEMC and the HPC there was a large region without electromagnetic calorimetry, used to pass the readout cables of the inner detectors to the exterior of DELPHI. To ensure the total hermeticity above 3°, a set of scintillators was installed to detect the passage of particles in this region, the scintillators were covered with lead so that photons would convert and be also detected. Although left without an energy measurement in these regions, the scintillators allow for the distinction between missing energy from lost photons or from weakly interacting neutral particles like neutrinos. The same approach was used to recover the small insensitive regions in the HPC module divisions.

3.3 Data Samples

Data Taking and Trigger

In DELPHI, the data taking operations were performed by three different systems: the Data Acquisition System (DAS), the Slow Control system (SC) and the Quality Checking system (QC). The DAS, responsible for the event readout, also controlled the conditions of data taking, including the trigger modes and LEP status; the SC took care of the detector status at each moment, both for the individual subdetectors and for the connections between them, the QC performed a first check of the data to reveal problems undetected by the other systems.

Every 22 μs, the beams crossed at the centre of the detector. Most of the beam crossings would not result in real collisions but would produce signals due to the interaction of the beam with the surrounding rarefied air. A criterious selection was then necessary to reduce the information flow on the data acquisition system and, afterwords, the amount of information kept and processed. In DELPHI this was assured by a four stage triggering system.

The first level trigger was applied as a hardware OR of the fast sub-detectors with a very high rate of around 500 Hz in the readout level, while in the second level not only the other sub-detectors were used but an AND was required in some cases, reducing the rate to 1%. These trigger levels were activated by the BCO (Beam Cross Over) signal produced by LEP, providing responses within 3 μs or 39 μs.

The event rate was further reduced in the next two levels which required already some software processing and event reconstruction methods, as they looked for consistency on the sub-detectors response. The third level was applied before the final data storage, while the fourth level, T4, was in fact a software filter applied only on fully stored data at the analysis processing level. The final rates were reduced to half by the third level trigger, while the fourth level kept around 40% of those events, excluding from the analysis empty (or very low energy) events, beam-gas interaction events and cosmic ray events.

Luminosity and Energy measurements

The luminosity is measured independently by DELPHI by counting the number of observed Bhabha scattering events at low angle [34]. The Bhabha scattering process was chosen due to its high cross-section, calculated theoretically with a high precision, and its clear experimental signature. The luminosity is given by $N_{meas}^{Bhabha}/(\sigma_{theory}^{Bhabha}.\varepsilon)$. These events were triggered separately, as a coincidence between almost collinear energy depositions in the forward and backward sides of STIC with a very high efficiency (ε). The precision of the luminosity measurement at LEP2 is of 1%.

The beam energy was obtained by the LEP direct measurement with a precision of 10^{-4}. To confirm this precision, DELPHI studied $\mu^+\mu^-\gamma$ and $q\bar{q}\gamma$ events from radiative returns to the Z^0, looking for systematic deviation of the reconstructed M_Z, which would indicate a shift in the beam energy. The analysis of muon final states is based only on angular distributions, leading to small systematic errors, while the $q\bar{q}$ analysis has a much smaller statistical error. The results were found to be compatible with the direct LEP energy measurement, but the experimental precision achieved is still much lower than the LEP one [35].

Used Data

The data samples used in this thesis were collected during the LEP2 phase, in the years of 1997 to 2000, and correspond to centre-of-mass energies of the order of 200 GeV and integrated luminosities around 650 pb^{-1}.

year	energy (GeV)	luminosity (pb^{-1})	σ_{qq} (pb)	σ_{WW} (pb)
1997	182.6	50	108.78	17.54
1998	188.6	150	100.05	18.74
1999	191.6	25	96.06	19.16
	195.5	75	91.31	19.57
	199.5	80	86.73	19.85
	201.6	40	84.56	19.97
2000	204.2	30	82.43	20.00
	205.2	50	81.18	20.10
	206.5	75	79.78	20.14
	208.0	7	78.26	20.18
(no S6)	206.3	60	79.78	20.14

Table 3.3: DELPHI data: the centre-of-mass energy and corresponding integrated luminosity, delivered to the DELPHI experiment from 1997 to 2000 are shown. For reference, the cross-sections of two of the most relevant processes at LEP2 is also shown.

While in 1997 and 1998 runs were set for constant centre-of-mass energies, in 1999, the LEP accelerator was run in four different modes aiming at achieving higher energies without decreasing the luminosity and the nominal construction limit of LEP (which was set at 200 GeV) was overcome. In 2000, this purpose was taken to its last consequences and a new scheme of running was introduced: instead of running at a previously set centre-of-mass energy, the acceleration was done in finner steps, which allowed to get high luminosity at relatively high energies and increase the energy as the intensity of the beam decreased. A significant part of the collected data was taken at energies which were considered beyond the reach of the accelerator.

Also in 2000, the DELPHI detector suffered from a problem which affected one sector of its main tracking device, the TPC, which corresponds to 1/12 of the total coverage of this detector, the data collected after this point corresponds to almost 10% of the full luminosity used in this thesis, and it was analysed separately.

The exact luminosities used in each analysis depend on specific detector quality requirements, table 3.3 shows indicative values of integrated luminosities for the different centre-of-mass energy bins used in the analysis. For reference, the cross-section of two of the LEP physics processes most relevant for the analyses, are also shown.

3.4 Simulation

The detector response to the predicted final states must be known to high accuracy to allow the comparison of the data with the expectations from the Standard Model or other new processes. Monte Carlo (MC) physics generators are used to describe each process and the corresponding final state particles, which then undergo a careful simulation of their interactions with the material in DELPHI, their energy depositions in the detectors and cascade reactions. The outcome of all these processes are recorded in a structure that reproduces the sub-detectors electronic signals that are used for real data.

The detailed simulation of each sub-detector is described in [36]. Each year, the real detector conditions changed and the data bases were updated with the slight changes in relative position of the sub-detectors and their calibration.

Generators

The theoretical expectation for the most important Standard Model processes were generated at each centre-of-mass energy, and with the corresponding DELPHI status, to be compared with the real data. The following MC physics generators were used:

- Fermion Pair Production:
  KK2f [37] for $q\bar{q}$, $\mu^+\mu^-$ and $\tau^+\tau^-$, KoralZ [38] for $\nu\bar{\nu}$, BHWIDE [39] for e^+e^-

at high polar angle and BHLUMI [40] for e^+e^- at low polar angle;

- Gauge Boson Pair Production:
  [41] for photon pairs and WPHACT[42] for W^+W^- and Z^0Z^0 production;

- "4 fermion production":
  Pythia[43] and [44] for "virtual photon collisions" and WPHACT for "single boson production", including parts of the phase space in which the two processes overlap.

For all cases in which there are quarks in the final state, the fragmentation and hadronization was performed by Pythia. In many cases these bulk generators were interfaced with other codes to perform radiative corrections, this will be explained when relevant.

The generators used for the signal processes studied in this thesis will be described in the corresponding chapters.

3.5 Event Reconstruction

The real and simulated event reconstruction in DELPHI is done in a general code, DELANA[45]. It starts with the analysis of the information from each sub-detector, which is then combined, first for the several calorimeters and then into a search for individual charged tracks.

In the barrel region, the TPC track-elements are extrapolated to the inside and outside of DELPHI to find compatible elements in ID and OD; in the TPC divisions (or in the TPC dead sector in the last period of 2000) the ID and OD are used together to make a first guess of the track direction. In the forward region it is the FCB which defines the first search hypothesis (together with the constraint that the track comes from near the interaction point).

The several possible tracks compatible with the initial main track-elements are then fitted together with track-elements from the other tracking sub-detectors and from the barrel and forward RICH. The ambiguities are solved at this level by cross-checking the compatibilities between the outer detectors. Only then are the tracks extrapolated all the way in to the VD and out to the muon chambers. The tracks are refitted with these additional constraints, and then associated to energy depositions in the calorimeters. For very low energy tracks, which are bended inside the magnetic field and do not reach the TPC, ID track-elements can be connected directly to the VD, but this leads to much less trustful tracks.

After all tracks have been found, the global reconstruction is checked for superpositions and ambiguities and the final set of charged and neutral particles is identified. The particular case of photons, of central interest in this thesis, is explained in detail in sub-section 3.6.

The final momentum resolutions achieved depend on the composition of track-elements and is, in average, lower in the forward region. For a 45 GeV muon, it is of around $\sigma(1/p) = 3\times10^{-3}(GeV/c)^{-1}$ in the forward and 4 to 5 times better in the barrel region. The energy resolution depends only on the calorimeters but needs to be corrected in cases in which there is leakage to outside calorimeter boundaries or into another detector.

The directions of these particles are then used to reconstruct the vertices of the primary interaction but also secondary vertices from long lived particle decay. The outcome allows for a preliminary classification of the event and identification of particles as muons[46], electrons and photons[47] and charged and neutral hadrons (π,K,Λ,etc)[31].

The individual physics analysis are done only after the creation of this common basic elements and follows several steps: first a general selection is applied which avoids badly reconstructed or very low energy particles. Then, isolated energy depositions or charged tracks are searched for and reconstructed as photon or lepton candidates. In high multiplicity events – the ones in which we are interested in this thesis – the remaining particles are probably hadrons coming from the fragmentation of initial quarks (or hard gluons) and they are clustered into jets which try to reproduce these particles. In addition, when looking for a precise final state, kinematic fitting may be useful to get better energy and momentum resolutions.

General Selection

To avoid signals which correspond to electrical noise in the detector, to beam-gas interactions or to cosmic rays crossing the detector during beam crossing, some basic cuts can be applied: charged tracks are only considered if their momentum is greater than 0.1 GeV/c and their impact parameters are below 4 cm, in the transverse plane and 4 cm $/\sin\theta$, in the beam direction; neutral depositions (unassociated with charged tracks) are only considered if their energy is above 0.3 GeV. In addition, energy depositions below 3° are discarded from the events, to avoid contamination from off-momentum beam electrons which are deflected and reach the lower edge of the STIC.

In the global event, requirements on the minimum numbers of charged tracks with some characteristics may be imposed to further reject these unwanted signals. In general, when looking for hadronic events, the number of charged tracks is required to be above 5 and from those there should be at least 3 with TPC information. Finally, a reasonable fraction of the total momentum (at least 10%) should be carried by long length tracks – to avoid events dominated by ID/VD only tracks which are subjected to large momentum errors as their curvature is hard to measure.

For most analysis it is also necessary to reject the "virtual photon collision" events which are produced with a high cross-section and hard to describe by simulation. In most of this events, the final electron and positron will follow approximately the beam direction – being lost in the beam-pipe, or at most detected in STIC. These events are rejected by setting minimum values (usually around 20% of the centre-of-mass energy) on the total transverse energy/momentum or on the total energy/momentum detected above 20°.

Isolated Particles

The concept of "isolated particles" is obviously not exact. All the particles when interacting with the detector produce different signals which are not always put together by the general algorithms, while some particles which we want to identify as belonging to a same group – an initial quark, for example – can be distant in space from the group bulk.

Although a preliminary identification of the final particles is already performed, the final analysis aims at reconstructing the particles which directly describe the primary interaction: leptons, quarks; hard photons and gluons; and eventually neutrinos and massive gauge bosons – and not the details of hadron decay, for example.

In case only a particular kind of event is to be selected, for example $q\bar{q}l\nu$ events, the lepton can be found by looking for the particle which has a higher transverse momentum in relation to the particles closer to it in space and then be selected or not according to a minimum value for this variable – this is the approach followed to search for the leptons in the $W^+W^-\gamma$ analysis.

However, if the aim is to reconstruct and classify unambiguously any kind of event, a more careful treatment is needed and it is possible in any case to reclassify the event *a posteriori*, reassigning the isolated particle to a jet. This method, adapted from [48], is followed for photon selection in $W^+W^-\gamma$ and, for lepton and photon selection, in the analysis of fermiophobic higgses.

Isolated particles are defined by constructing double cones centered around the axis of the neutral cluster or charged particle track, and requiring the energy density in the outer cone to be low, in order to ensure isolation. The energy of the isolated particle is then re-evaluated as the sum of the energies or charged particle track momenta inside the inner cone, and also its direction is recalculated (the isolation conditions are re-checked after the association). For well identified photons, electrons and muons, no extra association needs to be done and the isolation requirements can be weakened, but the cone method is still used. In general, the search for photons is done after the search for leptons so that they can start by being associated to the particles which originated them.

The specific case of isolated photons in hadronic events will be discussed in the next section.

Hadronic Jets

The particles which are not identified as isolated are forced into jets. Many different algorithms can be used to define the jets, they are, in general, iterative methods and in each iteration the particles which are closer to each other are grouped together. The main point is the definition of how to measure this "distance": it can be an absolute distance in space, or can be weighted by the particle momentum, or a combination of the two. The method used in this thesis is the DURHAM algorithm [49]. The "distance" is defined from the two particles' momentum (P_i, P_j), the angle between them (α_{ij}) and the total event energy (E_{tot}) as $y = 2.\min(P_i, P_j)^2.\cos\alpha_{ij}/E_{tot}^2$.

The iteration can be continued until a predefined y_{max} value is reached or, as is done in both analysis, a pre-determined number of jets (N_{jet}) is found. The last value of y, the y_{cut}, then gives an estimate of how N_{jet}-like the event is and becomes an important characteristic of the event.

Kinematic Fits

The directions and momentum of most particles are very well determined in DELPHI, however, some of the particles are not fully reconstructed – for example, the neutrinos are not reconstructed at all, some of the photons go through scintillator counters without any energy measurement, and the global jet 4-momenta are reconstructed with poor resolutions. Kinematic fits can be used to restore information based on some assumptions. For example, if it is assumed that no particle was lost, total energy and momentum should be conserved and the precise 4-momenta of the particles subjected to larger errors can be constrained by the 4-momenta of the other particles. Reversely, if a neutrino is expected in the final state – and is the only missing particle – the missing energy and momentum should be exactly the same and this constrains the other particles momenta.

Obviously, the measured quantities must be varied only within the experimental resolutions. On one hand the experimental resolutions (σ for each observable X) must be well described, on the other hand the result of the fit must have an associated χ^2 which states its quality according to the resolutions, $\chi^2 = \sum \frac{(X_i^{fit} - X_i^{meas})^2}{\sigma_{X_i}^2}$. The fits used in the thesis are performed according to [50].

The most precise measurements in DELPHI are those of muons – still parametrized according to the region they were detected in – and electron tracks. For photons, the angular and energy resolution depend strongly on the calorimeter they were collected in, while for photons detected in the scintillator counters a 100% error was assumed for the energy. Isolated charged leptons which can result from leptonic tau decays must be associated to neutrinos and have large errors both in the energy and direction determination. Hadronic jets are described by their global energy and direction but also by their angular spread: not only their energy but also their direction can be largely changed in the fits.

3.6 Photons in hadronic events

The reconstruction of photons in DELPHI is done is several steps, starting from the showers in the electromagnetic calorimeters. In the barrel, the procedure described in [31] is followed but, in a looser selection, showers close to the HPC divisions are accepted even if they fail the transverse shower profile criteria (and also the longitudinal one, for showers above 25 GeV). In the forward region, all STIC energy deposits with polar angle satisfying $\theta < 11°$ are taken to be photon candidates, while, for $\theta > 11°$, an algorithm is used to reduce the effects of the shower development in the detector material in front of the FEMC. Electromagnetic deposits close in space in the FEMC are clustered together and the association with reconstructed charged tracks is used for electron/photon discrimination. Care is taken to exclude those tracks which are likely to come from the development of showers outside the calorimeter. Photons with two associated tracks can be kept in a looser selection, but the tighter selection requires that no VD tracks, nor signals from different combination of other tracking detectors (depending on the shower polar angle) be associated with the electromagnetic deposit. In addition, the ratio between the electromagnetic energy and the total energy is required to be above 90% in the angular region around the cluster defined by $|\Delta\theta| < 15°$ and $|\Delta\phi| < \min(15°, 6° \cot\theta_{cluster})$, where ϕ is the azimuthal angle in the plane perpendicular to the beam direction.

As stated in the previous section, isolated photons are then selected from the above candidates by using double cones; the detailed explanation of how it is done is here followed by some checks of the methods performance.

Neutral particles above 5 GeV are considered as candidates for isolated photons, and classified as "tight" (if already tightly identified by the standard DELPHI package or detected in STIC) or "loose" (otherwise).

Tight candidates are only checked for isolation: a cone centered around the photon direction axis is defined as a function of the candidate energy. Inside this cone a maximum amount of energy is allowed to exist, following a proportionality with the sin of the opening angle (table 3.4).

For loose candidates, not only the isolation criteria are important but also some further reconstruction can be done. Two cones are constructed around the direction of the photon candidate: an inner one, of 5°, will insure that all the energy deposited by the photon is well contained, and associated to the primary object – the energy associated to charged tracks within this cone is required to be below 0.5 GeV; an outer one, of 15°, will insure the isolation of the photons, as a maximum of 1 GeV is allowed around the photon.

For both kind of photons, the hadronic energy associated to the isolated object can not exceed the 5 GeV and cannot represent more than half of the photon energy and the closest charged track with $P_{ch} > 1$GeV/c is required to be always more than 15° away from the photon.

E_γ (GeV)	α_{isol}	E_{isol} (GeV)
5	15.°	1.0
15	14.°	0.9
40	10.°	0.7
50	9.°	0.6
≥90	3.°	0.2

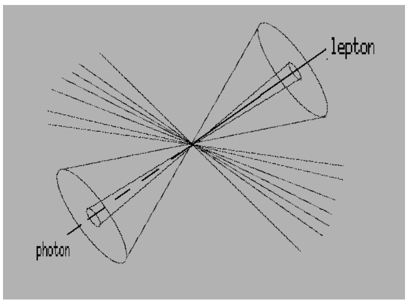

Table 3.4: Isolation conditions for photon candidates: the table shows the energy density and isolation angle cuts for tight photons, the figure shows a scheme of how the loose photons are reconstructed.

To improve the efficiency for the selection of photons radiated by final state fermions (namely leptons), one energetic particle may be allowed inside this cone. In the analysis reported in this thesis, two different criteria are used. In the $W^+W^-\gamma$ analysis, the candidates for electrons or muons from W decays will be kept out of the energy counting in the outer cone; in the other analysis this exclusion only happens for tightly identified photons – where the most energetic particle is left out of the counting – or for tightly identified leptons – which are themselves excluded from the counting.

In addition, the photon sample can be purified by requiring that the energy is not concentrated in a single HPC layer and some efficiency can be gained by recuperating energy deposits in the first layers of the hadronic calorimeter, produced by the leakage near the HPC modular divisions.

Notice that the definition of loose photons with the association of energy spread in a reasonably large cone, allows for the reconstruction of photons even in the borders of the calorimeters. These will have less well defined energies and directions but can still be used in the analyses and recuperated with kinematic fits.

The reconstruction of isolated photons was checked in a large sample of $q\bar{q}\gamma$ events, selected within the W^+W^- analysis framework, for which the photon selection was re-designed.

The selection was based on the fully-hadronic selection (in chapter 4), with the $\sqrt{s'}$ cut relaxed to 50 GeV, and excluding the W^+W^- candidate events. Figure 3.2 shows the energy and polar angle of the photon for each data set.

The peak in the energy distributions corresponds to the radiative return to the Z^0 – the ISR probability convoluted with the cross-section peak in $e^+e^- \to Z \to q\bar{q}$ cross-section. The angular distributions show the several photon detection regions in DELPHI:

- The barrel calorimeter, HPC, covers polar angles up to $|\cos\theta| < .73$ but is divided in modules.
  - The intermodular divisions are centered in ϕ=7.5° + n 15.° and are projective in relation to the center of DELPHI, meaning that the photons in this region will reach a smaller number of HPC layers, creating a drop in the the efficiency.
  - The divisions along the DELPHI axis correspond to $|\cos\theta|$=0., 0.38 and

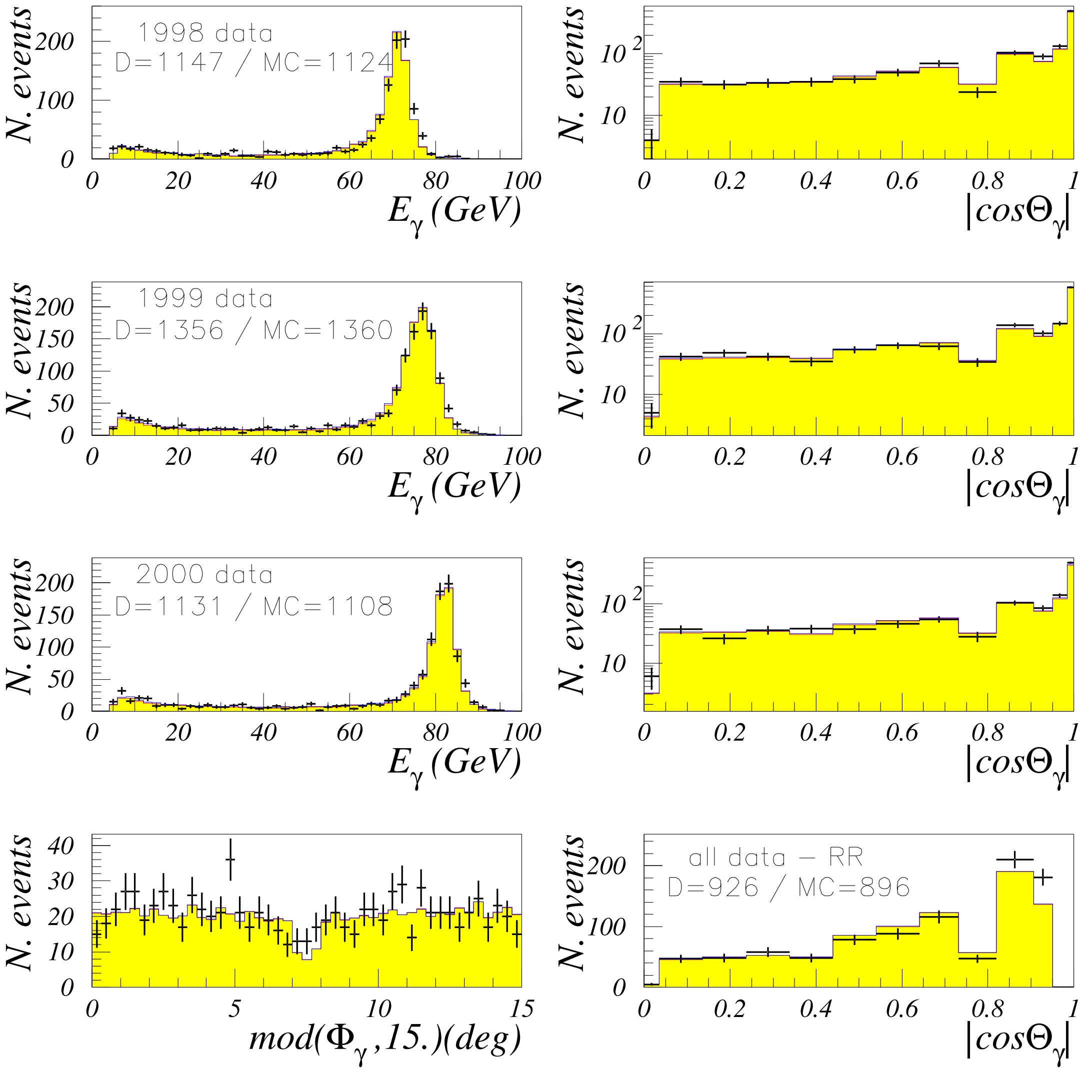

Figure 3.2: γ reconstruction for $W^+W^-\gamma$ analysis: the three upper plots show the energy (left) and polar angle (right) distributions for photons in $q\bar{q}\gamma$ events, dividing the data according to the year they were collected in. For the lower plots, only high energy and isolated photons are kept, the azimuthal angle distribution for photons in the HPC region (left) and the polar angle distribution (right) are shown.

0.62. Only the one at 90° is projective, so only there a serious drop in efficiency is seen.

- The region $0.73 < |\cos\theta| < 0.82$ is not covered by any electromagnetic calorimeter. Scintillator counters were placed in this region to identify (charged) particles going through; before the counters, photons meet a dense material where they convert into e^+e^- pairs which are then identified. There is no energy measurement. The energy of the photons is recuperated by kinematic fitting only.

- The forward calorimeter, FEMC, covers the region $0.82 < |\cos\theta| < 0.985$. In the plot, the FEMC acceptance is separated in three regions: the first one corresponds to $\theta > 25°$, to isolate the regions where the VD information is used, in contrast to the more forward part; the last one isolates the part of the distribution outside the cuts used in the W^+W^- analysis.

- The very-forward calorimeter, STIC, covers regions of $|\cos\theta| > 0.985$ all the way down to the beam-pipe $|\cos\theta| = 0.999$. It has the higher statistics from ISR, and is vetoed in the analysis.

The two bottom plots show the angular variables for photons selected as radiative return photons, excluding the above bins, and isolated in respect to the jets (in this case the events were forced to 4-jets in the framework of the $W^+W^-\gamma$ analysis).

The loose photons represent 1% (in this last selection) to 5% (in the all $q\bar{q}\gamma$ selection) of the total number of selected photons, recovering mainly low energy and less isolated photons as well as photons in the regions without calorimetry.

The study of the photon reconstruction in the framework of the fermiophobic Higgs analysis leads to the same conclusions.

Chapter 4

$\mathbf{W^+W^-}\gamma$

This chapter starts with a review of the generators more heavily used and a short presentation of the framework of the $W^+W^-\gamma$ analysis. The measurement of the cross-section and the study of anomalous couplings are then explained in more detail.

4.1 Event Generators

4.1.1 Standard $W^+W^-\gamma$ events

W^+W^- events are generated in DELPHI using the WPHACT [42] program. In addition to the W-pair production tree-level diagrams (CC03 [51], in figure 2.2), all other four fermion Feynman diagrams (with charged or neutral currents) are included, together with their interferences. The contribution of CC03 diagrams is evaluated separately and a corresponding weight assigned to each generated event, in order to give a better assessment of the W parameters to be compared to theoretical predictions.

As usual, WPHACT is interfaced with Pythia [43] which then performs the final state radiation (FSR) and the fragmentation and hadronization for final states with quarks, with PHOTOS [52] and TAUOLA [53] which perform the final state photon radiation by charged leptons and with YFSWW [54] which performs extra radiative corrections, including the initial state radiation (ISR) effects.

The experimental sensitivity achieved by the LEP combined results on $W^\pm$ pair production away from threshold showed a discrepancy of -2% on the CC03 cross-section when compared to the theoretical calculations available in the beginning of LEP2[55]. This indicated that some important radiative corrections could be missing and led to the development of more precise calculations of the four-fermion production cross-sections [56]. However, the amount of Feynman diagrams that appears when radiative corrections are introduced is too large and renders the full calculation impossible. Since the main focus is on the CC03 processes, the approach chosen was the so-called Double Pole Approximation (DPA). The matrix elements for four-fermion production are expanded around the real $W^\pm$ poles keeping as first term the CC03 diagrams with on-shell $W^\pm$ and adding correction factors for the distance to the real masses. It is then possible to calculate precisely the radiative corrections for the first terms and propagate them to the full matrix elements.

There is still a large number of diagrams to be considered: diagrams in which virtual photon lines connect initial fermion lines, final fermion lines and intermediate boson lines (non-factorizable), others in which there are virtual correction or real photon emission just in one part of the diagram (initial, final or intermediate). It is known that the contribution of non-factorizable corrections to the inclusive cross-section cancels up the *Bremsstrahlung* effects up to $\alpha\Gamma_W/M_W$ in the DPA approximation, however this is not the case for exclusive distributions [51]. Within YFSWW they are implemented according to the Khoze-Chapovsky *ansatz* [57], while the factorizable corrections are exactly computed at 1-loop level or higher. The virtual and soft factorizable corrections present infra-red divergences and large Sudakov logarithms ($\log(s/m_e)$) but they are canceled when added together. There are still divergences from the real emission of collinear photons (of the form $2\alpha/\pi log(Q/m)$) and, in the virtual corrections, the Coulomb singularity, that arises from the long range electromagnetic interaction between the two W bosons.

The corrections from real hard photon emission are, of course, more important for this thesis, where we concentrate in $W^+W^-\gamma$ final states. The radiation from the $W^\pm$ (WSR) interferes negatively with initial and final state radiation, and tends to decrease the energy lost in ISR. The additional interference between ISR and FSR is also negative but suppressed by the time separation induced by the W lifetime (expressed in a factor of $\alpha\Gamma_W/M_W$). While radiation from the initial state and from the $W^{\pm}$ is computed within the YFS exponentiation method [58] up to $O(\alpha^3)$, the final state radiation is included in the YFSWW calculations only as an overall factor and the corresponding photons are generated *a posteriori* and in a more approximate way. This must be done because there is no way to separate the photon and gluon radiation by quarks, and is justifiable as the FSR does not change much of the shape of the events (which would change their DPA weights).

The corrected CC03 cross-section is now compatible with the LEP measurements (the ratio between combined cross-section at all energies and the YFSWW prediction is 0.998 ±0.009 [55]), and the results from YFSWW calculations were compared to others (namely RacoonWW [59]) showing agreement to the level of less than 0.5%, even in differential distributions.

For events with visible photons the LEP statistics are lower, but comparisons between different calculations give an indication of the precision. Tests have been made using YFSWW and RacoonWW – using an independent Improved Born Approximation approach – in different conditions [20]. The photon distributions from the two generators agree at the 2% level when FSR is not included. The FSR contribution can be implemented in the matrix element calculation by RacoonWW (prior to the gluon radiation) and is described in YFSWW by *a posteriori* correction with PHOTOS (as in the DELPHI setup), the comparison between the two shows an agreement at the level of 5%. A systematic error of 5% will thus be assigned to the visible $W^+W^-\gamma$ cross-sections obtained with the WPHACT (YFSWW corrected) samples, to allow, in particular, for the deficient description of FSR.

4.1.2 Anomalous $W^+W^-\gamma$ events

To consider anomalous quartic gauge couplings, a dedicated generator is needed. The EEWWG [60] program was used to generate the anomalous $W^+W^-\gamma$ events. The original version of the program generates $\mu^+\nu_\mu\mu^-\bar{\nu_\mu}\gamma$ final states in which the fermions come from two on-shell W bosons and the photon is radiated either from the initial beams, from the internal W lines or from a quartic gauge coupling (QGC), as shown in figure 4.1. It includes all those diagrams and respective interference, with the contribution of anomalous quartic gauge couplings, parametrized as a function of a new energy scale, Λ, and three coupling parameters, a_c, a_0 and a_n.

For the present analysis, the two other possible couplings – $\tilde{a}_0$ and $\tilde{a}_n$ – were included, according to [20], by replacing $a_0 \to a_0 + i\tilde{a}_0$ and $a_0 \to a_n + i\tilde{a}_n$.

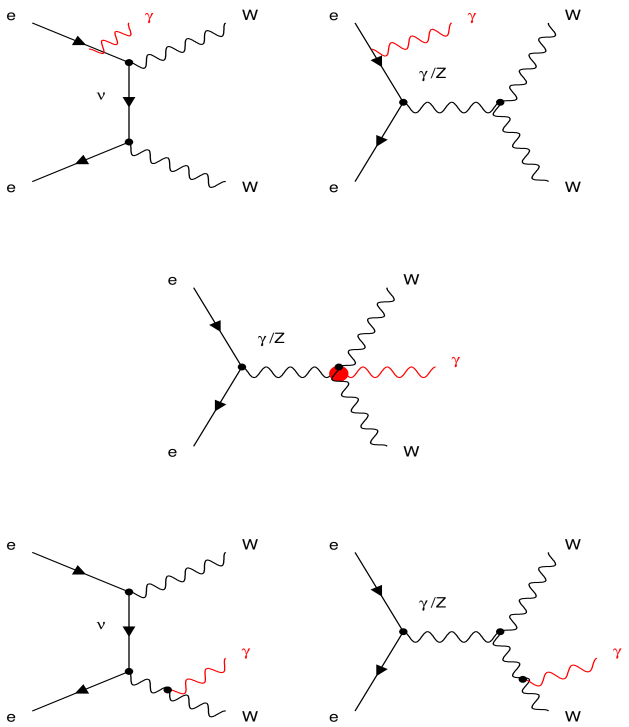

Figure 4.1: Processes in EEWWG: the top diagrams represent the ISR, the lower ones the WSR and, in between, the QGC. Extra ISR corrections are performed by interfacing Excalibur, and FSR is done by Pythia.

Several trivial changes had to be made to the program: change the final fermions to other pairs (which implies neglecting interference with additional four fermion diagrams), include photon radiation from the charged final state fermions and hadronize the final state quarks.

A more important and delicate point is the addition of QED corrections to the cross-section calculation. This is done only for the extra ISR corrections which are the most significant ones: the initial state radiation lowers the amount of energy available for real $W^{\pm}$ production and thus the total cross-section; the photons are in general collinear to the beam direction and have low energies, characteristics of *Bremsstrahlung*. The ISR corrections are implemented through a radiator function from another MC program (Excalibur [61]). This function describes the reduction in effective centre-of-mass energy and the boosts caused by the emission of collinear photons by both the electron and positron beams. The decrease in cross-section and the change in the photon distributions are shown in figure 4.2 for SM events generated at $\sqrt{s}$ =189 GeV.

This extra ISR factor is needed to get the right total cross-section and the available energy for the following W^+W^- process and corresponds to a large number of lost photons going down the beam pipe. The fact that the visible photons are generated always after this, and with decreased energies, can cause slight distortions in the spectra of the visible ISR contribution. There can be also small double counting effects in terms of total cross-sections.

Figure 4.3 shows again the photons spectra of EEWWG (now at $\sqrt{s}$ = 206.5 GeV) but compared to the WPHACT predictions with and without the inclusion of WSR (and DPA corrections). Although EEWWG dismisses the virtual corrections of the DPA calculations, it includes the ISR/WSR and interference at $O(\alpha^1)$ which is the main point for the description of $W^+W^-\gamma$. There is a good agreement with the full DPA corrected curve.

The photons emitted by the $W^{\pm}$ are in general collinear to their direction and have low energies, like in the ISR *Bremsstrahlung*, although slightly different spectra are induced by the explicit dependence of the $W^+W^-\gamma$ vertex on the photon 4-momenta. The correction to the original WPHACT calculation is negative and does not depend on the photon energy but on its polar angle: it is stronger in the regions where the ISR is suppressed and, since the WSR is comparatively small, it is then the negative ISR/WSR interference that dominates.

At this stage the Standard Model $W^+W^-\gamma$ cross-sections, obtained with the corrected EEWWG and WPHACT+DPA corrections (but no FSR) can be compared. Table 4.1 shows they are compatible within one sigma, when considering the statistical errors only. The total ISR$\oplus$WSR+FSR cross-sections, which are the measurable quantities, are also shown as well as the original, non-corrected, ISR-only

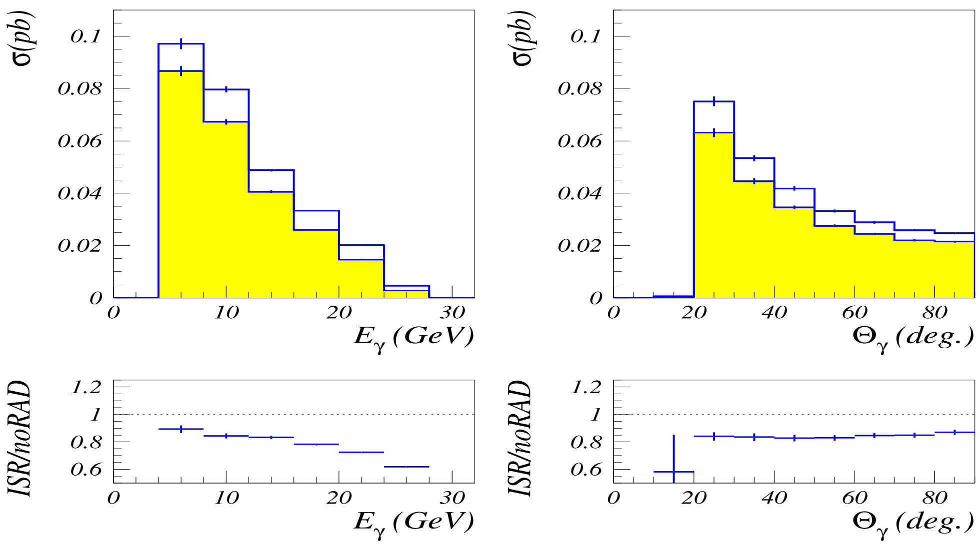

Figure 4.2: Effect of the introduction of the collinear ISR in total cross-section and in the spectra of the photon produced by EEWWG at $\sqrt{s}$ = 189 GeV. The top plots show the differential distributions for the energy and polar angle of the photon before (in white) and after the ISR correction (in grey), and the lower ones show the ratio between the ISR corrected cross-sections and the original ones.

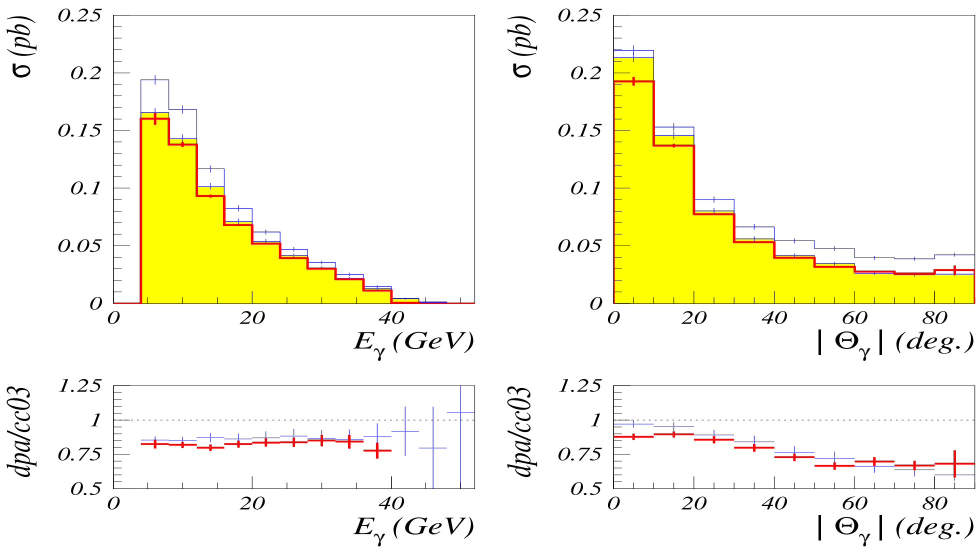

Figure 4.3: Effect of the introduction of WSR and DPA corrections in the spectra of the ISR/WSR photon produced in CC03 W^+W^- events at $\sqrt{s}$ = 206.5 GeV. The top plots show the energy and polar angle of the photon before (in white) and after the DPA correction (in grey) and the lower ones the ratio between the DPA cross-sections and the original ones. The thicker lines show the prediction of EEWWG after the ISR correction.

cross-section (without WSR, FSR or DPA corrections). The cross-sections shown correspond to acceptance cuts of the signal definition used in the analysis, ie. $E_\gamma > 5$ GeV, $|\cos\theta_\gamma|$ <0.95 and $\cos\alpha_\gamma$ <0.90 (and changes around these cuts). The table shows also the SM branching fractions for the considered W^+W^- decays, comparing them with the fraction of events in each final state for each considered cross-section, showing that the FSR contribution is larger for final states with leptons.

Although the table shows only MC statistical errors, systematic errors must also be assigned to these cross-sections. The ISR$\oplus$WSR cross-sections are assumed to have an error of 2%, but the uncertainty on the full cross-section including FSR is higher: the description of FSR within WPHACT is done by different programs with less precision and the interference is neglected. The full SM cross-section are assumed to have a systematic error of 5%.

The generated events then go through the detector simulation program and are reconstructed as the real data. However, to each EEWWG event is assigned a weight different from one that depends on the value of the anomalous parameters that are being considered: the same 50000 events are used in figure 4.4 to show how the photon spectra changes when a_0 is different from 0.

In fact, EEWWG is dedicated to the anomalous contribution and most events are generated in the phase space regions dominated by the QGC diagram. For the same sample, the statistical errors are reduced if the signal is defined by assigning to the events the weights $W(anom) = W(a_c, a_0, \tilde{a}_0, a_n, \tilde{a}_n) - W(0,0,0,0,0)$, ie. Standard Model contributions will be subtracted from the total cross-sections or distributions, as shown in figure 4.4. The SM contribution will be described with WPHACT.

This choice has a practical advantage that each generator is then used to describe the phase space region for which it was originally developed – and thus smaller samples of simulated events are needed; and also the advantage that it minimizes the negative effects of the simplified description within EEWWG. FSR effects will be partially included in the spectra obtained in the presence of anomalous couplings and the distortion caused by the introduction of the radiator function will be felt only in the interference term between ISR and QGC.

$\sqrt{s}$ (and cuts)	WPHACT Cross-Section (fb) ALL	ISR (only)	ISR$\oplus$WSR	EEWWG Cross-Section (fb)
189 GeV	340 $\pm$3	(274 $\pm$3)	226 $\pm$3	219 $\pm$2
192 GeV	365 $\pm$5	(303 $\pm$4)	250 $\pm$4	243 $\pm$4
196 GeV	385 $\pm$5	(331 $\pm$5)	270 $\pm$4	270 $\pm$5
200 GeV	394 $\pm$5	(355 $\pm$5)	279 $\pm$4	275 $\pm$1
202 GeV	400 $\pm$6	(369 $\pm$6)	285 $\pm$6	287 $\pm$4
206.5 GeV	420 $\pm$3	(398 $\pm$3)	304 $\pm$3	302 $\pm$4
and $\cos\theta < .998$		(751 $\pm$7)	647 $\pm$7	660 $\pm$6
BR_{qqqq}	39.6 $\pm$0.5	(45.0 $\pm$0.5)	45.0 $\pm$0.6	45.6%
$\mathrm{BR}_{ql\nu}$	47.1 $\pm$0.5	(44.5 $\pm$0.5)	44.3 $\pm$0.6	43.9%

Table 4.1: $W^+W^-\gamma$ cross-sections in EEWWG and WPHACT, at several centre-of-mass energies. The cross-section shown correspond to the signal definition defined below. "ALL" stands for the total (ISR$\oplus$WSR+FSR) cross-section which will be measured; "ISR$\oplus$WSR" shows the non-FSR cross-section to be compared with the one from EEWWG; "ISR (only)" is the WPHACT cross-section before corrections. The errors shown are statistical only. The BR for the fully-hadronic and semi-leptonic channel in the first columns give the fraction of events in each category, the last column shows the SM W^+W^- BRs.

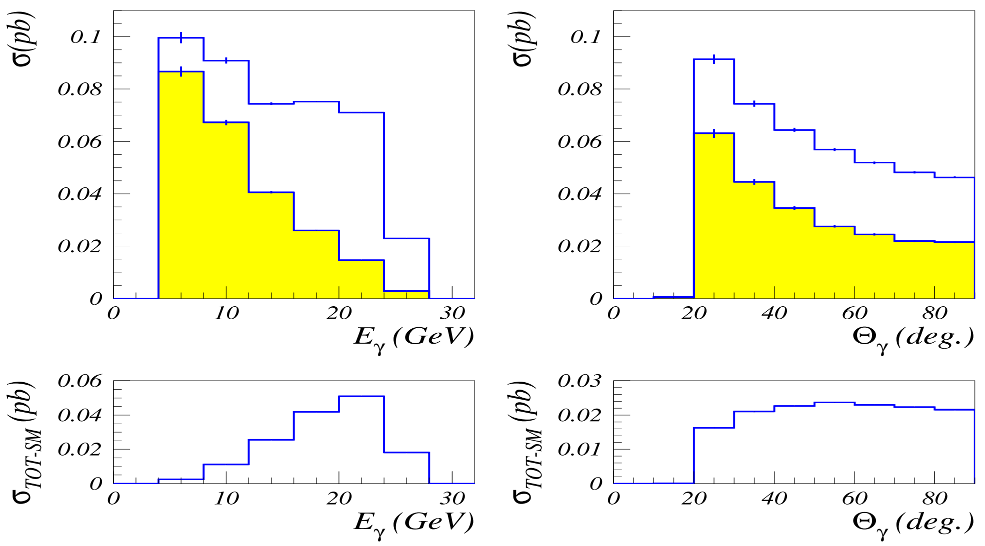

Figure 4.4: Effect of the introduction of anomalous QGC in the total cross-section and in the spectra of the photon produced by EEWWG at $\sqrt{s} = 189$ GeV. The top plots show the differential distributions for the energy and polar angle of the photon in the SM (in grey) and with $a_0/\Lambda^2 = 0.05$ GeV^{-2} (white), and the lower ones show the difference between the two, which will be used to define the "anomalous signal" in what follows.

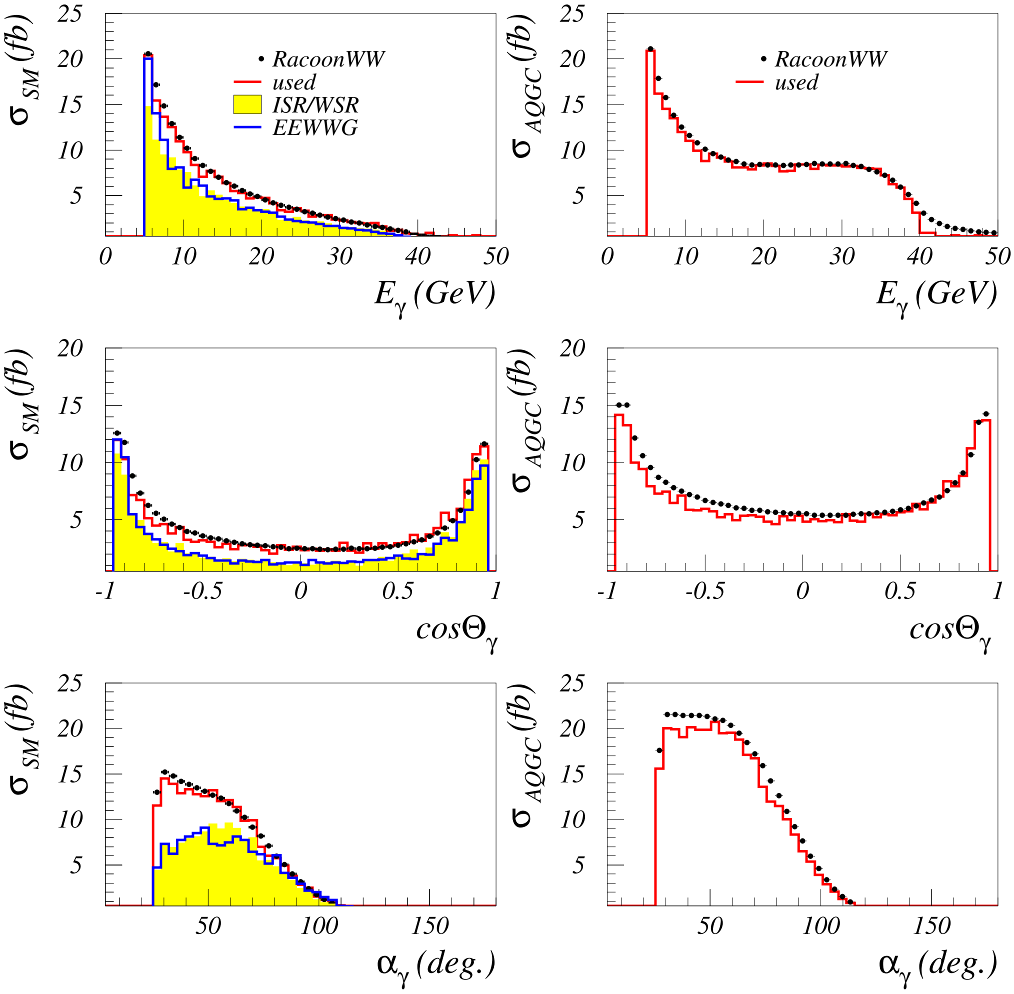

Figure 4.5: Cross-check with RacoonWW for the photon energy, cosine of polar angle and isolation angle, in the SM (left) and for $a_c/\Lambda^2 = 0.06$ GeV^{-2}. The distributions from RacoonWW (dots) are compared with the ones from WPHACT (+EEWWG) (line). Also shown is the comparison between the SM part of EEWWG and the corresponding WPHACT sample without FSR. The small discrepancies are discussed in the text.

It should also be noted that within EEWWG the two W boson are generated on-shell, that is with a fixed $M_{f\bar{f}'} = 80.4$ GeV/c^2, while in WPHACT, the full 4-fermion calculation is made, and thus $M_{f\bar{f}'}$ is distributed according to a Breit-Wigner. The cross-section is the same, but the energy available for ISR photons is different. If the calculations with anomalous couplings would include off-shell Ws, the effects could be slightly larger than the ones described here, which are thus a conservative estimate.

A cross-check of the final setup was done by comparison with RacoonWW, including anomalous QGC with the proper interference with FSR diagrams, within the Improved Born Approximation approach. Figure 4.5 shows the photon energy, polar angle and isolation angle obtained in the $q\bar{q}l\nu\gamma$ final states at $\sqrt{s} = 206$ GeV, both for the SM and in the presence of an anomalous QGC.

For the SM case, the assymmetry in the polar angle distribution can be understood as in RacoonWW only negative leptons are being generated, the small effects for low energy and low isolation angles are below 5% and can be due to the different FSR descriptions. For the anomalous QGC case, there is a slightly larger cross-section in RacoonWW, which is mainly due to the presence of an upper limit on the energy photon in EEWWG, due to the fact that the $W^\pm$ are generated on-shell. The discrepancy seen for low isolation angles, which is below 10%, is increased by this fact even if it can also reflect a small effect due to the absence of the FSR matrix element in EEWWG. The cross-sections for anomalous contributions obtained with WPHACT+EEWWG will be taken with a 5% systematic error.

4.2 The common W^+W^- analysis

Within DELPHI, most of the analysis related to $W^\pm$ bosons are done in a common baseline analysis [62], in which the events are processed, reconstructed and ultimately classified as fully-hadronic W^+W^- ($q\bar{q}q\bar{q}$) candidates, semi-leptonic W^+W^- ($q\bar{q}l\nu$) candidates or fully-leptonic W^+W^- ($l\nu l\nu$) candidates.

After a general pre-selection and reconstruction, different selections are done separately for each kind of events, relying on different discrimination techniques. Only semi-leptonic and fully-hadronic W^+W^- events will be considered in the $W^+W^-\gamma$ analysis, the specific selections are explained in more detail in the following subsections.

The reconstruction and identification of W^+W^- events starts with the construction of global event variables and the search for isolated particles. The events are then forced into each of the allowed configurations: 4 jets if they are compatible with fully-hadronic W^+W^- events (ie. $N_{part} > 10$ and the effective collision energy, left after ISR, $\sqrt{s'} > 100$), 2 jets and one charged lepton if they are compatible with semi-leptonic W^+W^- events (ie. $N_{part} > 5$, $E_{ch} > 0.1\sqrt{s}$, $E_{em} < .9\sqrt{s}$) or just two charged leptons and missing energy if they are compatible with fully-leptonic W^+W^- events (ie, $N_{part} \in [2,7]$, $E_T > .05\sqrt{s}$). All the interesting events fit in at least one of the categories and are kept at this level. In what follows, only fully-hadronic and semi-leptonic events will be considered, which corresponds to 89.5% of the possible W^+W^- decays.

The identification of isolated photons was explained in section 3.6. The identification of the leptons coming from the W decays is based on the standard DELPHI packages for electrons [47] and muons [46], and the leptons with higher transverse momentum with relation to the other charge particles in the event are selected. For taus, a search for the most isolated single track or low multiplicity jet is done.

The jet clustering is performed with the Durham algorithm and forcing all particles in the event to the required number of jets; only the identified isolated photons are left always as separate objects. For the events compatible with fully-hadronic W^+W^-, the leptons are included in the 4-jets clustering; for events compatible with the semi-leptonic hypothesis, the jet algorithm is repeated for each of the possible lepton types (electron, muon or tau), forcing to 2 jets all particles but the lepton candidate of that type which has the highest transverse isolation with respect to other charged particles.

After all the objects are defined, the event is fitted in several different ways: imposing only energy-momentum conservation, imposing energy-momentum conservation and two equal masses or, finally, imposing energy-momentum conservation and the W mass in each of the two systems. For the 4-jet configurations, all different jet combinations are taken into account in the fits which impose mass constraints. All the photons in the events are left as not belonging to any of the mass systems, so in fact treated as ISR photons reducing the energy available for the W^+W^- system.

The fit is important as we are dealing with events in which there are neutrinos (several in the case of $qq\tau\nu$ or one in $qql\nu$) or many jets. A first guess for the neutrino 4-momentum is given by the missing energy but it will be completely overruled by the other objects in the fit. The jets are measured also with large errors (due to problems in the reconstruction of the several low energy particles that constitute them, in the association of charged and neutral energies and in the jet reconstruction algorithms used) and in the fit not only their energies will be changed but also their directions will be corrected within the uncertainty dominated by the jet broadenings. The taus have also large errors because they are low multiplicity jets which also contain neutrinos. The identified electrons, muons and photons have much smaller errors when compared to the other objects and will strongly constrain the fitted quantities.

Treating FSR photons as ISR can introduce a bias in the fitted masses and this is not the ideal situation; however, since both mass systems have a neutrino or jets, if masses are imposed in the fit most systems will be able to readjust to it (even if leading to higher χ^2). Figure 4.6 shows the change induced by FSR in the invariant mass of the two fermions coming from the same W, obtained at generator level for the $W^+W^-\gamma$ signal events. It shows that, since the largest fraction of events comes from ISR, the loss of efficiency which can arise from this incorrect treatment is small.

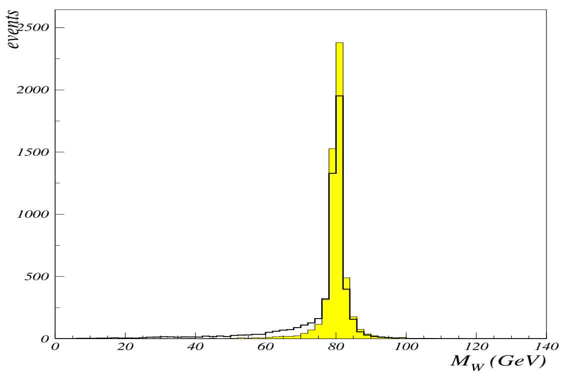

Figure 4.6: W mass before (shaded) and after (dark line) FSR at generator level for $W^+W^-\gamma$ events generated at 189 GeV.

4.2.1 Semi-leptonic W^+W^-

The selection of semi-leptonic W^+W^- events is based on an Iterative Discriminant Analysis (IDA) [63]. The events are selected in different categories, according to the leptonic decay of the W in muon, electron or tau. First a selection of muons is performed, then a selection of electrons and only then the tau selection. Only the events which were not selected before are considered, which assures the exclusivity of the samples.

The training of the IDA is done over signal samples of $e^+e^- \to W^+W^- \to qql\nu$ for each lepton type, and $e^+e^- \to Z^0/\gamma \to qq$ and $e^+e^- \to Z^0Z^0 \to qqll$ background samples.

A basic pre-selection is done requiring that the jets have a minimum of 3 particles (of each at least one charged particle), the total transverse energy is above 45 GeV (40 GeV, in the case of taus), the missing energy above 10 GeV (and below 80 GeV, in the case of taus), the total visible energy in the event is between $0.40\sqrt{s}$ and $1.10\sqrt{s}$ (or between $0.35\sqrt{s}$ and $1.00\sqrt{s}$, in the case of taus). Events which failed the kinematic fit imposing two equal masses are rejected.

The discriminant analysis is then based on a set of 9 to 11 variables, which distinguish between WW-like events and background. These are: the total multiplicity of the event, the visible energy, the ratio $\sqrt{s'}/\sqrt{s}$, the missing momentum and its polar angle, the lepton isolation angle and the fitted W mass, the lepton energy (for electrons and muons) or charged multiplicity (for taus), the transverse energy (for electrons) or the angle between the lepton and the missing energy direction (for muons and taus) and, in the case of taus, also the tau jet spread and the acoplanarity of the event.

The discriminant analysis works in several steps which deal with each kind of background, the discriminant power of each variable at each step changing due to the different background compositions. The non-CC03 events ($We\nu$, for example) are considered as background for the W^+W^- selection.

4.2.2 Fully-hadronic W^+W^-

For the selection of fully-hadronic events a Neural Network (NN) is used [64]. The NN is trained with samples of $e^+e^- \rightarrow W^+W^- \rightarrow qqqq$ signal events and $e^+e^- \rightarrow Z^0/\gamma \rightarrow qq$ events at several centre-of-mass energies, to improve separation between 4 and 2 fermion processes.

A pre-selection is done requiring that the visible energy is above 40% of the centre-of-mass energy, the charged energy above 10% , the transverse energy above 20%, and $\sqrt{s'}$ above 65%. The transition from 4 to 3 jets is required to have $ycut >$ 0.0015, with at least one jet with energy above 1 GeV and more than two particles. Events which failed the fit imposing energy-momentum conservation are rejected. In the $W^+W^-\gamma$ analysis, to ensure the exclusivity of the samples, only events which were not selected in the (more efficient but more restrictive) semi-leptonic mode are accepted.

The Neural Network will use again the above variables together with the minimum angle between jets, the difference between the maximum and minimum jet energies, the minimum multiplicity, the χ^2 of the best fit imposing W mass and event shape variables. The event shape variables are quantities based on the 4-momentum vector of the N particles in the event, and were designed specifically for the identification of two-jet events. They are defined as [65]:

- Sphericity: 3/2 of the two lower eigenvalues of the tensor $S^{\alpha\beta} = \frac{\sum_i p_i^\alpha p_i^\beta}{\sum_i |p_i|^2}$ (=0 for two-jet events, =1 for isotropic events)
- Thrust: $T = \frac{\sum_i |n_i.p_i|}{\sum_i |p_i|}$ where the thrust axis, n is the vector which maximizes the value of T (=1 for 2-jet events, =1/2 for isotropic events)
- Fox-Wolfram moments: $H_l = \sum \frac{|p_i||p_j|}{E_{vis}^2}.P_l(\cos\theta_{ij})$, in which θ_{ij} is the angle between two particles, P_l are the Legendre Polynomials and E_{vis}^2 is the visible energy of the event. In this case, H3 and H4 (Hl are normalized quantities H_l/H_0, as H_0 is 1 when masses are neglected) are used.
- Jet broadenings: $B_j = \frac{\sum_i P_i \sin\theta_{P_i Th}}{2\sum_i |P_i|}$, measure the opening angle of 2-jets (1 per hemisphere) assumed in the thrust axis. The minimum value between the two hemispheres is used.

The non-CC03 contribution is now larger than for semi-leptonic events, as it includes the ZZ process, leading to the same final state but that must be identified as background.

4.3 Standard $W^+W^-\gamma$ final states

To look for small effects of anomalous Quartic Gauge Couplings in $W^+W^-\gamma$ events, it must first be checked that the events coming from the standard processes are correctly described. First checking qualitatively the description of W-pair production with photons and then measuring a well defined cross-section within a well defined phase-space region where the SM cross-section is well known and the sensitivity to anomalous effects is maximized.

The cross-section to be measured is defined as the one for W-pair production (requiring the CC03 components of the 4-fermion processes) with a hard, central and isolated photon within the following phase space region:

- the photon energy is above 5 GeV,
- the photon isolation in relation to the beams direction has $|\cos\theta| < 0.95$,
- the photon isolation in relation to the charged fermions has $\cos\alpha < 0.90$.

At least one photon per event must obey these conditions and no cuts are applied on extra photons. The photons coming from the decay of hadrons are considered as background, but their contribution is minimized by the energy and isolation cuts. While the cut on the photon energy is mainly due to experimental requirements, the stronger cuts on polar and isolation angles are designed to suppress regions almost entirely dominated by the standard production modes of ISR and FSR and to select a region for which all processes contribute and anomalous effects are enhanced.

The analysis will be made in three different selection levels:

- **(0)** corresponding to the standard W^+W^- selection, to check if the common selection is suitable also for $W^+W^-\gamma$ analysis;
- **(1)** with some extra cuts on the W^+W^- characteristics, and requiring an identified photon, to check the description of radiation;
- **(2)** applying also the cuts on the photon polar and isolation angle, according to the signal definition.

The data samples selected in the W^+W^- common framework [66] include around 2000 fully-hadronic and 1400 semi-leptonic events, per year, with expected efficiencies and purities of the order of 80% to 90%. At level 0, the $W^+W^-\gamma$ signal-like events correspond to around 2% of the selected W^+W^- events. The analysis is separated in four channels: $q\bar{q}\mu\nu$, $q\bar{q}e\nu$, $q\bar{q}\tau\nu$ (semi-leptonic) and $q\bar{q}q\bar{q}$ (fully-hadronic) made exclusive by construction (requiring that an event can only be selected in one channel if it was not in the previous ones). The fully-leptonic channel is not analysed.

The purity for $W^+W^-\gamma$ events is necessarily lower than the one for W^+W^- selection, as in other LEP2 physics processes, namely the large 2 fermion (in particular $q\bar{q}(\gamma)$) background, the phase space available for initial state radiation is much higher, and increased by the radiative returns to the Z^0 pole. This explains why some extra cuts were added for the $W^+W^-\gamma$ analysis, at level 1. The maximum energy of the photon was required to be below $\frac{s-(2M_W)^2}{2\sqrt{s}}$ - 5 GeV, to select events above the W^+W^- threshold, and then extra cuts were applied differently for each channel.

In the semi-leptonic sample, the fit imposing equal $q\bar{q}$ and $l\nu$ masses was required to converge with a χ^2 below 10, which helps to guarantee the existence of a neutrino with reconstructed 4-momentum. In the case of the tau channel, there can be more than one neutrino but then also the errors on the charged lepton 4-momentum are increased in the fit. The lepton and the fitted neutrino were also required to be isolated in relation to the jets by 10° and 5°, respectively.

In the fully-hadronic selection, the χ^2 of the fit imposing energy-momentum conservation was required to be below 10 and then the output from the neural-network was used: only events with a NN-output value greater than 0.70 were kept. This corresponds to a purity above the 70% for W^+W^-, but a purity of around 50% for $W^+W^-\gamma$.

The cut on the χ^2 is a rather loose selection in all the final states and aims only at rejecting very rare background events which are not properly treated in the IDA and NN. It was checked that it does not have a strong impact in the final results. Also the isolation cuts affect only a small number of the previously selected events; these are variables with delicate description in the simulation and care was taken in checking that the cuts had the same effect in data and expectations. The cut on the NN-output was also checked to be in a region where data and expectations are in good agreement and is set in the clearer separation between signal and background.

4.3.1 Standard Signal Studies

Before proceeding into the analysis, it is interesting to study one signal sample in detail to understand the differences in the reconstruction of several W^+W^- decay modes and of the photons with different origins, namely from ISR/WSR or FSR.

Table 4.2 shows how a $W^+W^-\gamma$ signal, generated at a centre-of-mass energy of 206.5 GeV and including all W^+W^- decay channels, is reconstructed. In particular the cross-section is divided in ISR-like (including ISR and WSR) photons and FSR-like photons, for which the selection is less suitable. It shows, in addition, the distribution according to both Ws decay modes and according to the four selection channels considered. The numbers at level 0 and level 2 are presented (level 1 is irrelevant for the signal behavior). The signal is selected within WPHACT by applying the CC03 weights (the contribution from other diagrams is considered background).

The discriminant analysis and neural network were trained separately for different centre-of-mass energies and, since the W^+W^- cross-section goes up with energy while the main backgrounds' cross-sections go down, to achieve similar purities the selection efficiencies must be different. The numbers shown in this section are thus to be taken as indicative only, but reflect general trends.

decay mode	reconstruction as $qqqq(\gamma)$	$qqe\nu(\gamma)$	$qq\mu\nu(\gamma)$	$qq\tau\nu(\gamma)$	lost	TOTAL
$qqqq\gamma$	118+X+23	-	-	2+X+0	19+ X+ 6	139+ X+30
	56+X+10	-	-	2+X+0	81+ X+20	
$qqe\nu\gamma$	0+0+ 0	36+6+3	0+ 0+0	4+ 4+1	5+ 6+ 2	45+16+ 5
	-	18+4+1	-	3+ 2+0	25+ 9+ 4	
$qq\mu\nu\gamma$	0+0+ 0	0+0+0	38+ 9+4	2+ 3+0	6+ 5+ 2	45+17+ 5
	-	0+0+0	22+ 6+2	1+ 2+0	23+ 9+ 4	
$qq\tau\nu\gamma$	1+0+ 0	1+0+0	1+ 0+0	25+ 7+2	16+ 7+ 3	45+15+ 5
	-	1+0+0	1+ 0+0	15+ 5+1	29+ 9+ 4	
$l\nu l\nu\gamma$	-	-	-	-	30+23+X	30+23+X
$l\nu l\nu\gamma$	-	-	-	-	30+23+X	
TOTAL	119+0+23	37+6+3	39+10+4	33+14+3	77+41+11	304+70+45
(γ sel)	56+0+10	18+4+1	22+ 6+2	20+ 9+2	188+51+31	

Table 4.2: 206 GeV signal distribution according to generated and reconstructed channels. The first line for each generated channel corresponds to the W^+W^- selection only (level 0), and the second one to the γ selection (at level 2) within that sample. The three terms in each column refer to ISR+FSR$_l$+FSR$_q$ photons. The cross-sections (σ) are given in fb, and have associated statistical errors lower than $0.2\sqrt{\sigma}$.

Around 13% of the signal comes from $l\nu l\nu\gamma$ final states, which are not analysed, resulting in a maximum possible efficiency of 87% for the selection of the total $W^+W^-\gamma$ signal. The signal is mostly composed by ISR/WSR but the FSR component is non-negligible: it is smaller for fully-hadronic ($\sum Q^2 = 10/9$) events and higher for fully-leptonic ($\sum Q^2 = 2$) events. On the other hand, the table is non-diagonal: the fully-leptonic mode is not analysed and completely absent of the selection, the fully-hadronic mode is almost independent from the semi-leptonic selection but the $q\bar{q}\tau\nu\gamma$ selection is important to recover efficiency, mainly from the other semi-leptonic modes.

Looking only at the level 0 selection, the efficiencies for the selection of each decay mode in $W^+W^-\gamma$ and W^+W^- can be compared:

	$qqqq$	$qqe\nu$	$qq\mu\nu$	$qq\tau\nu$	ALL
W^+W^-[66]	86% + 0%	70% + 7%	85% + 3%	59% + 7%	70%
$W^+W^-\gamma$	83% + 2%	59% +15%	74% + 7%	53% + 7%	68%
W^+W^-+ISR	85% + 2%	78% +11%	83% + 4%	56% + 8%	75%
W^+W^-+FSR$_l$	——	36% +27%	54% +18%	47% + 4%	42%
W^+W^-+FSR$_q$	77% + 1%	51% +12%	66% + 4%	40% + 6%	75%

The efficiencies, defined as the percentage of the events generated in each decay mode which are reconstructed in any analysis channel (in the table the efficiency in the corresponding analysis channel are shown separately, to be summed to the crossed-efficiencies), are almost the same for events with no photons or ISR/WSR events, but decreased by as much as 15%-20% for FSR events in semi-leptonic decay modes. This effect can be due to the use of kinematic fits imposing mass constraints, where the photons are left out of the W system. In the case of the FSR events, the crossed efficiency gained by using all channels is even more important than for ISR/WSR: there is, in particular, a recuperation of efficiency in the tau channel.

The second line of table 4.2 for each decay mode shows the selected cross-section after the imposition of cuts on the photon (level 2). The final efficiencies for selecting each W^+W^- decay mode vary between 34% (for $qq\tau\nu\gamma$) and 47% (for $qq\mu\nu\gamma$).

The photon selection efficiency, within each reconstruction channel, is similar in all semi-leptonic channels, but lower in the fully-hadronic channel. In the signal events, $\cos\alpha_{q\gamma} < .90$, but (due to the large spread of the jets) the photon can have hadrons around and not be reconstructed as isolated. In addition, because not always the jet direction reconstructs exactly the original quark direction, the corresponding (level 2) cut, $\cos\alpha_{jet\gamma} < .90$, also excludes signal events. The efficiencies with which the photon is selected in each of the analysis channels are less dependent on the ISR/FSR nature, since the very low polar angles, characteristic of ISR, and the low isolation angles, characteristic of FSR, are already outside the signal definition:

	reconstruction channel				
	$qqqq\gamma$	$qqe\nu\gamma$	$qq\mu\nu\gamma$	$qq\tau\nu\gamma$	ALL
γ	50%	58%	57%	61%	52%
ISR	47%	49%	57%	61%	51%
FSR$_l$	-	65%	63%	68%	65%
FSR$_q$	41%	41%	44%	52%	42%

Finally, the contribution of each channel to the full $W^+W^-\gamma$ analysis is:

	reconstruction channel				
	$qqqq\gamma$	$qqe\nu\gamma$	$qq\mu\nu\gamma$	$qq\tau\nu\gamma$	ALL
$W^+W^-\gamma$ εff.	15.7%	5.7%	7.1%	7.2%	36%
ISR εff.	18.5%	5.9%	7.3%	6.4%	38%
FSR$_l$ εff.	-	5.8%	8.5%	13.1%	27%
FSR$_q$ εff.	21.2%	2.4%	3.6%	3.6%	31%

Although the efficiency for the generated $qq\tau\nu\gamma$ mode is the smallest one, the $qq\tau\nu\gamma$ analysis allows for the recuperation of an important part of the total cross-section due to mis-identification of events from other modes.

The global $W^+W^-\gamma$ efficiency is thus of 36%, being 38% if only ISR/WSR events are considered as signal and 29% if only FSR is considered.

Due to an error in the generator implementation, FSR from taus is absent is some of the used samples, but correct in two samples at 189 GeV and 206.5 GeV. This not only lowers the total cross-section but also changes the efficiencies slightly. After the comparison of this two extreme energy points, the effect is found to be relatively constant and is corrected for in the analysis[1]: 20 fb are added to the total cross-section used in efficiency calculations, 4.5 fb to the selected FSR contribution in the tau channel and also 4 fb to the background at first selection level in that channel.

In order to take into account this error and other possible effects of deficient modeling of the relative importance of the ISR/WSR and of the FSR contribution (which imply also different relative importances of each analysis channel), a systematic uncertainty of 5% will be assumed for each final efficiency. This uncertainty accommodates changes from the full generated signal to a 100% ISR/WSR signal or to a signal with a FSR contribution of 50%.

The global efficiency at 206 GeV is then of 36% ±2%. If the fully-hadronic and semi-leptonic analysis would be taken independently, the efficiencies would be of 39% ±2% and 42% ±2%, respectively.

[1]In the following the plots are done using the available samples but the numbers in tables are corrected.

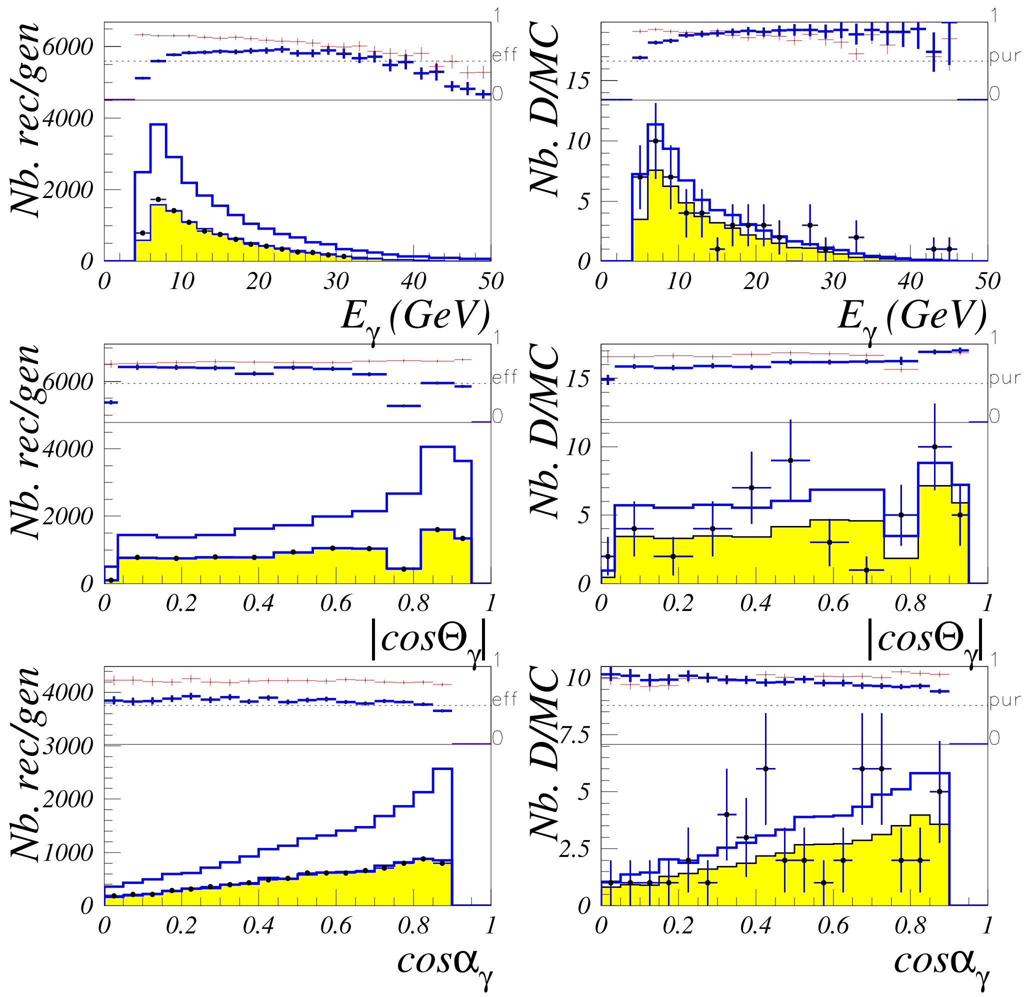

Figure 4.7: Photon distributions in semi-leptonic W^+W^- events: energy, polar angle and isolation angle for all data. The left-hand plots show the generator level distributions for all generated signal events (in white) and the selected ones (in grey) together with the reconstructed quantities for the selected events (in dots); and the W^+W^- (thin line) and γ (tick line) selection efficiencies in the top plots; the right-hand plots show the selected data and MC events in the semi-leptonic channels, the signal events are shown in grey, and the W^+W^- and γ purities in the top plots. Events with isolation angles above 90° are not display, these are 4 events in data, with 3.3±0.1 expected from simulation.

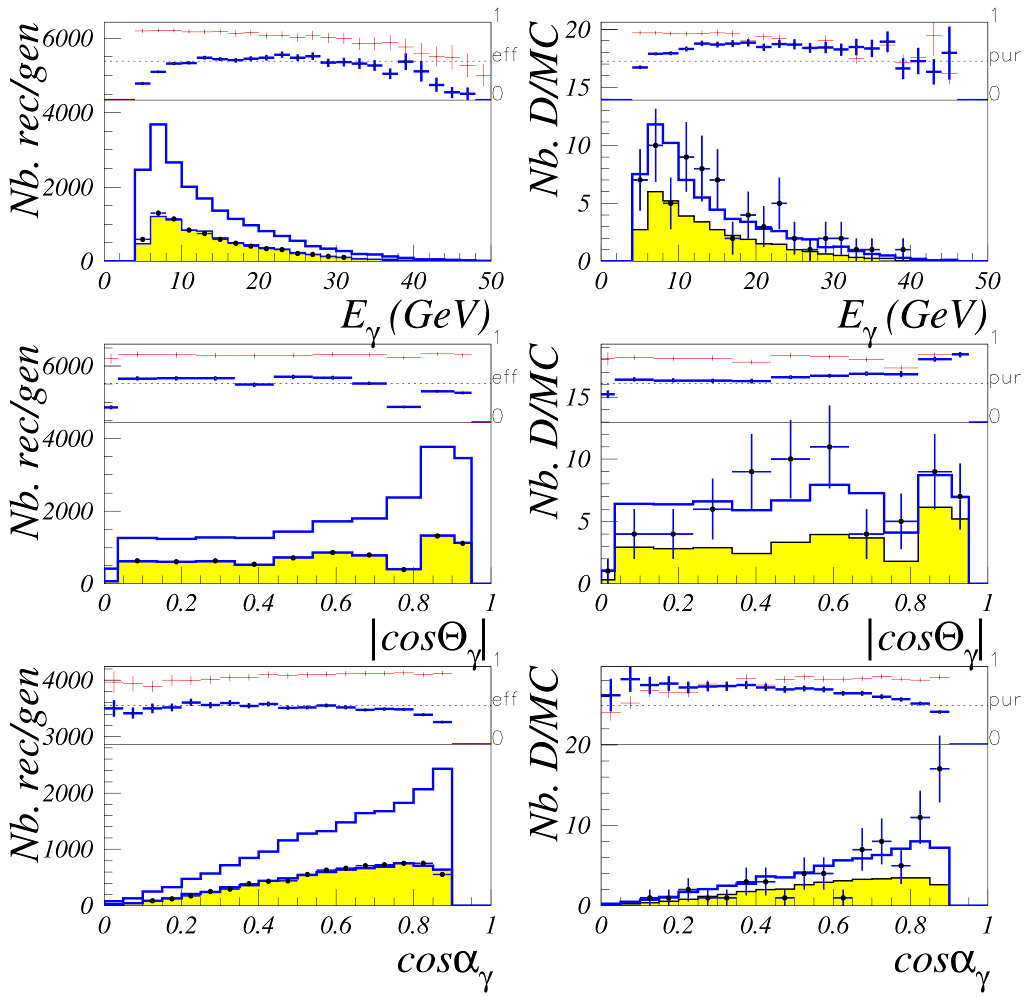

Figure 4.8: Photon distributions in fully-hadronic W^+W^- events: energy, polar angle and isolation angle for all data. The left-hand plots show the generator level distributions for all generated signal events (in white) and the selected ones (in grey) together with the reconstructed quantities for selected events (in dots); and the W^+W^- (thin line) and γ (tick line) selection efficiencies in the top plots; the right-hand plots show the selected data and MC events in the fully-hadronic channel, the signal events are shown in grey, and the W^+W^- and γ purities in the top plots.

4.3.2 Data Analysis

The $W^+W^-\gamma$ cross-section at centre-of-mass energies between 189 GeV and 209 GeV was measured with the data collected in the LEP runs of 1998 to 2000.

The full simulation of the 4-fermion SM processes (generated with WPHACT) and hadronic 2-fermion processes (generated with KK2f) was done for the different centre-of-mass energies samples within each year of data tacking (and separately for the part of the data collected after the problem on the TPC), but the presentation of the Data/MC agreement is best done putting together all data or separating it per year, at the average centre-of-mass energy, since the analyses deal with low numbers of events.

The selection of W^+W^- is roughly independent of the photon characteristics and compatible with the global W^+W^- efficiency (as seen above) and purities [66]; both the efficiency and purity are, however, somewhat lower for high energy and well isolated photons.

The selection of γ, on the contrary, is more difficult for low energy and less isolated photons – decreasing both efficiency and purity. It depends also on the polar angle of the photon: the efficiency is lower for the forward region and very much decreased in the regions without calorimetric information.

Figures 4.7 and 4.8 show these behaviors together with the distributions for the generated signal events (total and selected) and the selected data and reconstructed background and signal simulation events. In average for all signals, and considering the analysis of the two separate channels, the efficiencies and purities of the selections are:

	W^+W^-		γ		$W^+W^-\gamma$	
	Eff.	Pur	Eff.	Pur	Eff.	Pur
semi-leptonic	80%	86%	55%	78%	44%	67%
fully-hadronic	86%	82%	44%	63%	38%	52%

Table 4.3 shows the number of events selected in each channel, separated in three average centre-of-mass energies (according to the year the data was collected in). The observed number of events is compared to the total number expected from simulation, showing a global good agreement. The number of events from $W^+W^-\gamma$

Channel		Data	MC_{tot}	4-fermion	$W^+W^-\gamma$	Eff.	Pur.
1998: $\sqrt{s}$ =189 GeV, $\mathcal{L}$=154 pb^{-1}							
$q\bar{q}e\nu\gamma$	(1)	6	8.3±0.2	8.0±0.2	3.0±0.1	5.6%	36%
$q\bar{q}e\nu\gamma$		4	4.0±0.2	3.8±0.1	2.9±0.1	5.5%	72%
$q\bar{q}\mu\nu\gamma$	(1)	9	10.2±0.2	10.1±0.2	3.5±0.1	6.8%	35%
$q\bar{q}\mu\nu\gamma$		5	4.6±0.2	4.6±0.1	3.5±0.1	6.6%	76%
$q\bar{q}\tau\nu\gamma$	(1)	9	12.4±0.3	10.0±0.2	3.7±0.1	7.0%	30%
$q\bar{q}\tau\nu\gamma$		1	6.4±0.3	4.9±0.2	3.6±0.1	6.8%	56%
$q\bar{q}q\bar{q}\gamma$	(1)	25	31.3±0.6	25.3±0.4	7.9±0.2	15.0%	25%
$q\bar{q}q\bar{q}\gamma$		11	15.8±0.4	12.6±0.2	7.6±0.2	14.5%	48%
1999: $\sqrt{s}$ =198 GeV, $\mathcal{L}$=221 ($q\bar{q}l\nu$) and 227 ($q\bar{q}q\bar{q}$) pb^{-1}							
$q\bar{q}e\nu\gamma$	(1)	11	14.5±0.3	13.6±0.2	4.8±0.1	5.7%	33%
$q\bar{q}e\nu\gamma$		5	6.7±0.2	6.2±0.2	4.7±0.1	5.6%	71%
$q\bar{q}\mu\nu\gamma$	(1)	15	16.1±0.3	16.0±0.3	6.2±0.2	7.3%	38%
$q\bar{q}\mu\nu\gamma$		9	7.5±0.2	7.5±0.2	6.0±0.2	7.1%	80%
$q\bar{q}\tau\nu\gamma$	(1)	25	22.6±0.3	18.6±0.3	6.5±0.2	7.7%	29%
$q\bar{q}\tau\nu\gamma$		11	10.9±0.2	8.6±0.2	6.3±0.2	7.5%	58%
$q\bar{q}q\bar{q}\gamma$	(1)	56	52.6±0.6	44.6±0.5	13.8±0.3	15.8%	26%
$q\bar{q}q\bar{q}\gamma$		30	25.2±0.4	21.1±0.3	13.4±0.3	15.3%	53%
2000: $\sqrt{s}$=206 GeV, $\mathcal{L}$=199 ($q\bar{q}l\nu$) and 219 ($q\bar{q}q\bar{q}$) pb^{-1}							
$q\bar{q}e\nu\gamma$	(1)	14	14.9±0.3	14.0±0.3	4.8±0.2	5.8%	32%
$q\bar{q}e\nu\gamma$		6	6.4±0.2	6.0±0.2	4.7±0.2	5.6%	73%
$q\bar{q}\mu\nu\gamma$	(1)	14	16.9±0.3	16.8±0.3	6.1±0.2	7.3%	36%
$q\bar{q}\mu\nu\gamma$		6	7.2±0.2	7.2±0.2	5.9±0.2	7.0%	81%
$q\bar{q}\tau\nu\gamma$	(1)	12	22.1±0.4	18.4±0.3	6.2±0.2	7.4%	28%
$q\bar{q}\tau\nu\gamma$		5	10.4±0.3	8.3±0.2	6.0±0.2	7.1%	57%
$q\bar{q}q\bar{q}\gamma$	(1)	59	58.0±0.7	49.3±0.5	14.9±0.3	16.2%	26%
$q\bar{q}q\bar{q}\gamma$		29	27.1±0.5	22.7±0.3	14.4±0.3	15.6%	53%

Table 4.3: Number of selected events per channel for each year of data taking, compared to the total expected number of SM events and, within those, the total 4-fermion and $W^+W^-\gamma$ signal events (the efficiency and purity for the signal are shown in the last columns). The first line for each channel (1) shows the events selected as $W^+W^-\gamma$ (level 1), and the second shows the events selected within the signal phase space cuts (level 2).

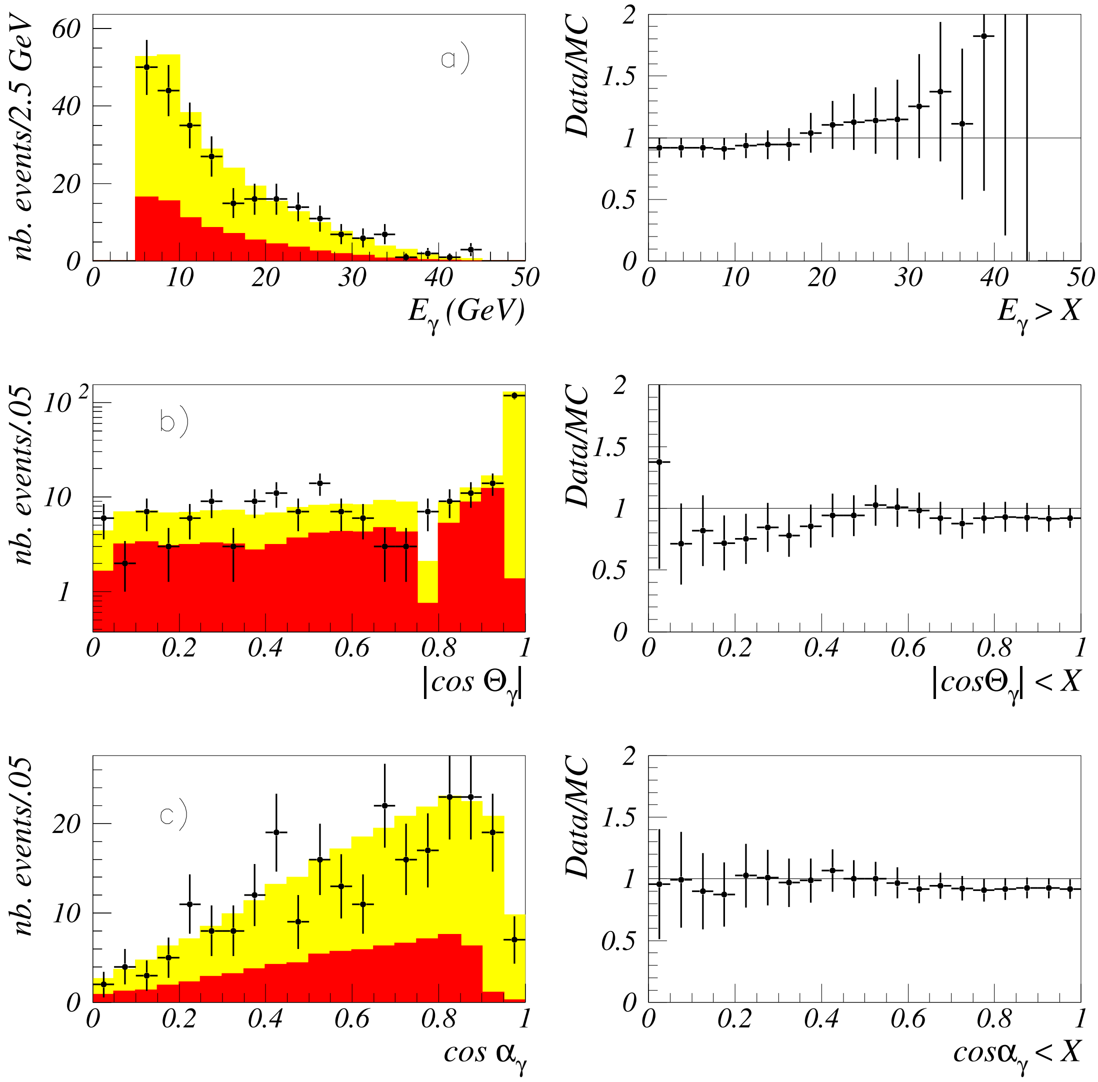

Figure 4.9: Photonic distributions for $W^+W^-\gamma$ events: distributions for the (a) energy, (b) polar angle and (c) isolation angle of the photons, in all data samples and all channels, before the imposition of the signal definition cuts - level 1. In the left plots, the data (dots) are compared to the total SM prediction (light histogram) and the SM $W^+W^-\gamma$ signal is shown in the dark histogram. The right plots show the evolution of the data/MC agreement when cutting away the higher density part of each distribution.

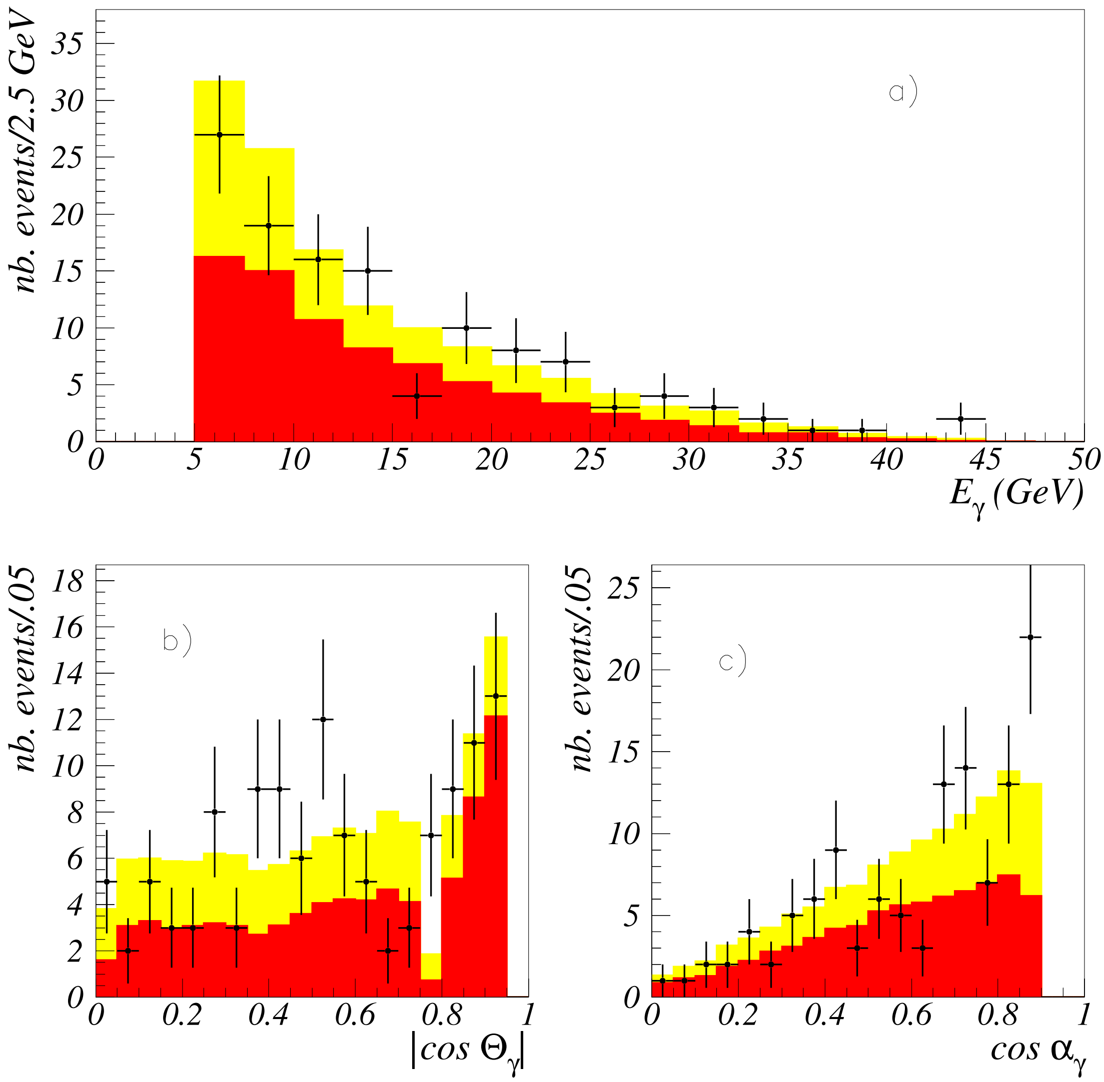

Figure 4.10: Photonic distributions for $W^+W^-\gamma$ signal-like events: distributions for the (a) energy, (b) polar angle and (c) isolation angle of the photons in all data samples and all channels, after the signal definition cuts - level 2. The data (dots) are compared to the total SM prediction (light histogram). The SM $W^+W^-\gamma$ signal is shown in the dark histogram.

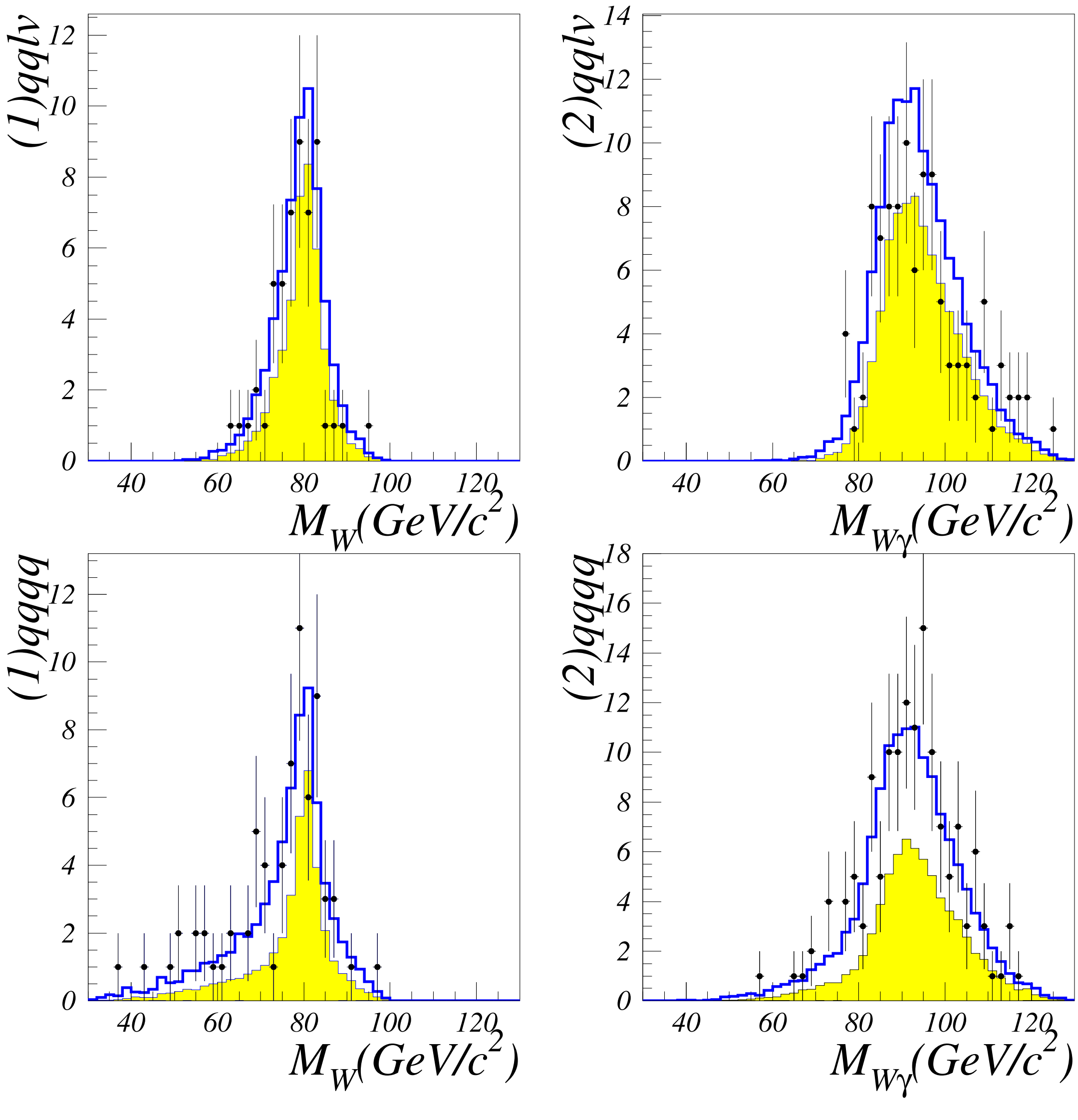

Figure 4.11: Invariant mass distributions in $W^+W^-\gamma$ events, the $W^\pm$ mass (left) – obtained in a fit requiring energy and momentum conservation and two equal masses and – and the two $W^\pm\gamma$ masses (right), after the same fit. The top plots correspond to semi-leptonic events and the lower ones to the fully-hadronic events. The data (dots) are compared to the expected SM distributions; the signal is represented by the grey histogram.

signal and other 4-fermion events is also shown, together with the efficiencies and purities. The first line for each channel in the table shows a broad selection of $W^+W^-\gamma$ events, before the signal definition cuts (level 1), the comparison between data and SM expectations at this level is also shown in figure 4.9 for the photonic variables. The cumulative plots show that there is a small deficit of events (but an excess for high energy photons) and that the angular distributions, which are typical of ISR and FSR, are reasonably described – which guarantees that there is no big distortion of the relative importances of the two processes. The general good agreement shows that the typical events with ISR and FSR (forward or non-isolated) photons are well described by the simulation.

The second line of table 4.3, for each channel, corresponds to the imposition of the signal definition angular cuts (level 2) – and to the numbers used in the subsequent analyses. The photonic distributions after these cuts are shown in figure 4.10, the reconstructed $W^\pm$ masses and $W^\pm\gamma$ invariant masses are shown in figure 4.11. The $W^\pm\gamma$ invariant mass is expected to peak at ~80 GeV/c^2 for FSR photons, but could present other peaks if there was a resonance $W^* \to W\gamma$. Due to lack of statistics it is difficult to take conclusions based on the figure, but no large effects are seen and the distribution is explainable just by the available phase space for $W^+W^-\gamma$.

4.3.3 Cross-section measurement

The cross-section for $W^\pm$-pair production with a hard, central and isolated photon in the final state is obtained, with each channel and centre-of-mass energy, using the above numbers as

$$\sigma = \frac{Data - (MC_{tot} - W^+W^-\gamma)}{\mathcal{L}.\varepsilon}$$

where $Data$ is the number of observed events, MC_{tot} the total number expected from simulation and $W^+W^-\gamma$ the expected number of signal events; $\mathcal{L}$ is the luminosity and ε is the efficiency, from simulation. The results obtained with each individual channel are presented in table 4.4.

The statistical error is given by $\Delta\sigma = \pm\frac{\sqrt{Data}}{\mathcal{L}\varepsilon}$ and the systematic error includes several sources (whose individual contributions will be added in quadrature):

- Finite MC statistics:
  $\pm\frac{\sqrt{\delta MC_{tot}^2+\delta W^+W^-\gamma^2}}{\mathcal{L}\varepsilon} \oplus \frac{\delta\varepsilon}{\varepsilon}\sigma.$
  This error was checked to include, by large, the possible systematic errors in the 4-fermion background descriptions, including radiative correction errors.

- Data/MC comparison:
  detailed studies in other analysis have given bounds for the errors – from possible differences between data and MC – on the W^+W^- and γ selection efficiencies, separately. For the $W^+W^-\gamma$ analysis the statistics are too low and it is difficult to choose parallel channels in which to investigate the differences between the MC descriptions and the data behavior. The numbers from [66] and [33] are adopted as independent and slightly increased values are used, 1.5% and 3%, respectively.
  These errors propagate to an error proportional to the measured cross-section, as does the error propagated from the luminosity determination (of 1% [34]). The three contributions added together quadratically reflect on a 3.5% error.

- Signal modeling:
  the systematic uncertainty from WPHACT modeling of the $W^+W^-\gamma$ signal region is reflected on the expected signal cross-section error of 5% but does not affect the background so strongly, and so does not influence the measurement. However, the effect of the signal modeling on the cross-section determination is reflected in a possible change of efficiency mainly due to different photon spectra. In particular, a possible incorrect balance between ISR-like and FSR-like photons or the presence of new contributions to the spectra, should be accounted for.

  For the study of anomalous contributions, the EEWWG generator was used and anomalous QGCs were varied within a wide range of values, resulting on a maximum of 5% difference in the fully-hadronic selection. The study of the ISR/FSR balance, above, gave compatible numbers for the overall analysis. A conservative error of 5% can thus be taken in a general $W^+W^-\gamma$ cross-section measurement.

- Modeling of $q\bar{q}$ background:
this is the major background, namely in the fully-hadronic and the tau channel. The total hadronic cross-section measurements in DELPHI agree with the Standard Model prediction[67]. However, since the modeling of three and four jets and a photon is not studied in detail, a conservative systematic error will allow for variations in the $q\bar{q}$ background up to 20%: $\pm\frac{\delta q\bar{q}}{\mathcal{L}\varepsilon}$.

$\sqrt{s}$ (GeV)	channel	σ (fb)	(stat)	(syst)
188.6	$q\bar{q}e\nu$	344	±237	±32
197.7	$q\bar{q}e\nu$	247	±182	±27
206.0	$q\bar{q}e\nu$	383	±218	±34
188.6	$q\bar{q}\mu\nu$	381	±219	±31
197.7	$q\bar{q}\mu\nu$	479	±192	±35
206.0	$q\bar{q}\mu\nu$	333	±175	±28
188.6	$q\bar{q}\tau\nu$	-176	±96	±42
197.7	$q\bar{q}\tau\nu$	393	±201	±41
206.0	$q\bar{q}\tau\nu$	38	±157	±39
188.6	$q\bar{q}q\bar{q}$	127	±148	±35
197.7	$q\bar{q}q\bar{q}$	523	±158	±42
206.0	$q\bar{q}q\bar{q}$	477	±158	±42

Table 4.4: $W^+W^-\gamma$ cross-sections for the three samples with each channel. The obtained cross-sections are given with the statistical uncertainty and systematic uncertainty from MC statistics, efficiency determination and $q\bar{q}$ background modeling.

In order to be sensitive to systematic effects affecting each channel, the cross-section is computed using each channel separately, but putting together all the data. The results are shown in table 4.5. The average centre-of-mass energy is 198.1 GeV but, since the differences are large and the cross-section is not linear in $\sqrt{s}$, the combined cross-section does not necessarily correspond to the cross-section computed at this energy. To provide a comparison, the calculation is repeated replacing the number of data by the number of expected SM events.

The uncertainties are still dominated by the statistical errors. Even if only those are considered, the tau channel is the only one which is more than 2σ distant from the expectations – which reflects in the $q\bar{q}l\nu$ cross-section. As can be seen in table 4.4, at 189 GeV the tau channel gives a negative cross-section, and at 206 GeV the cross-section is also low; at 198 GeV, however, it is above the expectation, and so there is no clear indication of a systematic problem.

The breakdown of the systematic error in its several components shows that the overall measurement is affected mostly by the $q\bar{q}$ modeling and by the signal modeling (affecting the overall efficiency). For the fully-hadronic and the $qq\tau\nu$ channels, the $q\bar{q}$ background is large and fully dominates the systematic error. In the other two semi-leptonic channels, the signal modeling is the largest contribution to the uncertainty, but its order of magnitude is comparable to the other error sources.

channel	$\sigma(W^+W^-\gamma)$(fb)	(stat)	(syst)	partial error stat	$\varepsilon + \mathcal{L}$	$W^+W^-\gamma$	$q\bar{q}$
$q\bar{q}e\nu$	320	$\pm$121	$\pm$24	13 $\oplus$	11 $\oplus$	16 $\oplus$	7
$q\bar{q}\mu\nu$	402	$\pm$112	$\pm$27	11 $\oplus$	14 $\oplus$	20 $\oplus$	1
$q\bar{q}\tau\nu$	126	$\pm$100	$\pm$33	13 $\oplus$	4 $\oplus$	6 $\oplus$	29
$q\bar{q}q\bar{q}$	408	$\pm$92	$\pm$37	9 $\oplus$	14 $\oplus$	20 $\oplus$	26
$q\bar{q}l\nu$	278	$\pm$64	$\pm$22	7 $\oplus$	10 $\oplus$	14 $\oplus$	13
all	336	$\pm$54	$\pm$28	6 $\oplus$	12 $\oplus$	17 $\oplus$	19

Table 4.5: Combined $W^+W^-\gamma$ cross-sections obtained putting together all energies for each channel. The average energy is of 198.1 GeV, with a corresponding expected result of 386 $\pm$6 (stat) $\pm$28 (syst) $\pm$19 (theor) fb. The systematic errors are broken down into four components: MC statistics, data/MC comparisons, signal modeling and $q\bar{q}$ modeling.

$\sqrt{s}$ (GeV)	σ_{SM} (fb)		σ (fb)	$\pm$(stat)	$\pm$(syst)
188.6	340	$\pm$12	151	$\pm$89	$\pm$24
191.6	361	$\pm$18	470	$\pm$287	$\pm$37
195.5	380	$\pm$15	296	$\pm$143	$\pm$28
199.5	390	$\pm$15	341	$\pm$144	$\pm$32
201.6	397	$\pm$26	898	$\pm$278	$\pm$64
205.9	420	$\pm$12	351	$\pm$106	$\pm$31
(TPC)	426	$\pm$17	349	$\pm$188	$\pm$35

Table 4.6: Combined $W^+W^-\gamma$ cross-sections per energy, obtained putting together all channels for each of the separate data sets used in the analysis. The line labeled (TPC) corresponds to the data with problems in the TPC with $\sqrt{s} = 206.1$ GeV. σ_{SM} is obtained by replacing the number of data by the expected number of SM events, the error shown is from MC statistics only.

The different channels can be combined within each energy bin by simply adding the data and the expectations. Since all the selections are exclusive, the statistical and systematic errors are then calculated over the total sample.

The results obtained for each data set are shown in table 4.6, together with the results obtained by replacing the data numbers by the expected MC (with the corresponding statistical error). These expected numbers provide a cross-check of the cross-section calculation, if they are compared with the ones in table 4.1 (obtained at generator level).

However, the simple addition of the data and expectations at each energy does not take into account the different statistical significance of each analysis channel. A more significant analysis can be performed with a likelihood fit in which the channels are treated independently.

For the likelihood fit, the systematic error is divided into the part which propagates as a relative error on the cross-section and the error that affects the expected background in each channel. The fit is performed twice, including or not the systematic errors: the central value of the cross-section is obtained from the fit with systematic errors and the difference between the two 1σ errors is isolated as a contribution to be added to the propagated systematic error.

$\sqrt{s}$	calculation			likelihood		
(GeV)	σ (fb)	$\pm$(stat)	$\pm$(syst)	σ (fb)	$\pm$(stat)	$\pm$(syst)
188.6	151	$\pm$89	$\pm$24	188	$\pm$86	$\pm$18
197.7	444	$\pm$94	$\pm$34	438	$\pm$93	$\pm$31
206.0	350	$\pm$92	$\pm$31	344	$\pm$90	$\pm$26
194.5	339	$\pm$129	$\pm$28	317	$\pm$128	$\pm$26
200.2	527	$\pm$133	$\pm$40	532	$\pm$132	$\pm$38

Table 4.7: $W^+W^-\gamma$ cross-section results for the three year data-sets and two energy bins for the 1999 data. The results obtained with the likelihood fit to the independent channels are compared to the ones obtained by the simple addition of the several channels.

The results obtained with this method for each channel separately were cross-checked with the ones from table 4.4, showing that both the cross-section and the statistical error agree within 1 fb, while the systematic errors agree up to 5 fb. The comparison of the results obtained with the two methods for the central values of centre-of-mass energy is shown in table 4.7.

The final results for the three central values of centre-of-mass energy are:

- $\sigma_{W^+W^-\gamma}(189\text{GeV}) = 0.19 \pm 0.09 \pm 0.02$ pb (SM: 0.340 ±0.003 ±0.017 pb),
- $\sigma_{W^+W^-\gamma}(198\text{GeV}) = 0.44 \pm 0.09 \pm 0.03$ pb (SM: 0.385 ±0.005 ±0.019 pb),
- $\sigma_{W^+W^-\gamma}(206\text{GeV}) = 0.34 \pm 0.09 \pm 0.03$ pb (SM: 0.421 ±0.003 ±0.021 pb),

where the SM values are obtained at generator level (table 4.1). The first error on the expectation comes from MC statistics, the second is the 5% systematic error from calculation comparison.

4.3.4 Other signal definitions

Other signal definitions may be interesting to explore. Namely, the cross-section obtained when considering only ISR and WSR can be useful to be compared directly to new models affecting only the $W^+W^-\gamma$ production vertices – in such a way that the theoretical calculations can be made just up to the W^+W^- production and not for the full 4-fermion final state – and have more precise description within our generator setup, thus reducing the associated theoretical error in the expected cross-section. The error on FSR description will, in turn, affect the background expectation.

In the present situation of rather limited statistics, a significant reduction of the errors on the measured cross-section can not be expected, and thus no specific analysis was developed. Letting the analysis unchanged, the expected selected signal and respective efficiency and purities for the new signals change to the numbers in table 4.8. In the same table, the results obtained when adding a cut requiring that the $W^\pm$ boson were produced on-shell ($|M_{ff'} - M_W| < 2.\Gamma_W$)[2] are also shown.

The fact that the selection efficiencies are similar for on-shell and off-shell $W^\pm$ shows that the overall selection does not depend strongly on the reconstructed W

[2]The values used are: M_W=80.4 GeV/c^2 and Γ_W=2.15 GeV/c^2.

masses, and justifies *a posteriori* the use of kinematic fits imposing equal masses (in the semi-leptonic selection) or the W mass (fully-hadronic selection).

	no FSR			on-shell			no FSR and on-shell		
Channel	$W^+W^-\gamma$	ε	P.	$W^+W^-\gamma$	ε	P.	$W^+W^-\gamma$	ε	P.
1998: $\sqrt{s}$ =189 GeV, $\mathcal{L}$=154 pb^{-1}									
$q\bar{q}e\nu\gamma$	2.1 ±0.1	6.1	54	2.3 ±0.1	5.7	59	1.8 ±0.1	6.5	44
$q\bar{q}\mu\nu\gamma$	2.4 ±0.1	7.0	53	2.7 ±0.1	6.7	59	1.9 ±0.1	7.0	41
$q\bar{q}\tau\nu\gamma$	2.0 ±0.1	5.8	32	2.8 ±0.1	6.9	44	1.6 ±0.1	5.9	25
$q\bar{q}q\bar{q}\gamma$	6.2 ±0.2	17.7	41	6.0 ±0.2	14.8	38	4.9 ±0.2	18.0	31
1999: $\sqrt{s}$ =198 GeV, $\mathcal{L}$=221,227 pb^{-1}									
$q\bar{q}e\nu\gamma$	3.6 ±0.1	5.9	53	3.8 ±0.1	5.8	56	2.8 ±0.1	6.1	42
$q\bar{q}\mu\nu\gamma$	4.6 ±0.2	7.6	61	4.6 ±0.1	7.1	61	3.6 ±0.1	7.7	47
$q\bar{q}\tau\nu\gamma$	3.9 ±0.2	6.4	36	4.7 ±0.1	7.3	44	2.9 ±0.1	6.3	27
$q\bar{q}q\bar{q}\gamma$	11.4 ±0.3	18.3	45	10.5 ±0.2	15.6	42	8.9 ±0.2	18.7	35
2000: $\sqrt{s}$=206 GeV, $\mathcal{L}$=199,219 pb^{-1}									
$q\bar{q}e\nu\gamma$	3.7 ±0.1	6.1	58	3.6 ±0.1	5.7	55	2.8 ±0.1	6.1	44
$q\bar{q}\mu\nu\gamma$	4.4 ±0.1	7.2	61	4.5 ±0.1	7.1	62	3.4 ±0.1	7.3	47
$q\bar{q}\tau\nu\gamma$	3.9 ±0.1	6.4	38	4.4 ±0.1	7.0	42	2.9 ±0.1	6.3	28
$q\bar{q}q\bar{q}\gamma$	12.2 ±0.3	18.1	45	11.1 ±0.2	16.1	41	9.5 ±0.2	18.7	35

Table 4.8: Different signal definitions, "no FSR" means only events with ISR and WSR photons are considered signal, "on-shell" means only events with the Ws generated within $|M_{ff'} - M_W| < 2\Gamma_W$ (before FSR) are considered signal. For each case, each data set and channel, the number of selected signal events (in the final selection level) is shown together with the efficiency and purity of the selection (in percentage).

In what concerns the exclusion of FSR from the signal definition, a larger effect is seen on the selection efficiency of $q\bar{q}q\bar{q}\gamma$, which reflects primarily the fact that this channel has reduced importance when FSR is included ($\sum Q^2$ is 1.1 for fully-hadronic, and 1.6 for semi-leptonic events) and then the overall drop in efficiency for selecting FSR events. This reduction happens also in the semi-leptonic channels but the effect is masked by a higher contribution of these decay modes to the total cross-section when FSR is included.

The imposition of the kinematic fit has a larger effect on FSR events than on off-shell $W^\pm$ events. First, because energetic FSR photons distort the Breit-Wigner shape of the $W^\pm$ mass spectra, and then, because when they are treated as ISR in the fit, an extra “wrong” condition is being imposed: that the energy available for the W^+W^- system is reduced according to the energy of the photons.

$\sqrt{s}$ (GeV)	σ_{SM} (fb)	$\sigma_{W^+W^-\gamma}$(fb)	stat	syst	σ_{SM} (fb)	$\sigma_{W^+W^-\gamma}$(fb)	stat	syst
	all $W^+W^-\gamma$				and no FSR			
188.6	340 $\pm(3\oplus17)$	188	±86	±18	226 $\pm(3\oplus5)$	99	±79	±18
197.7	385 $\pm(5\oplus19)$	438	±93	±31	274 $\pm(3\oplus6)$	328	±86	±20
206.0	421 $\pm(3\oplus21)$	344	±91	±26	307 $\pm(3\oplus6)$	249	±85	±17
194.5	375 $\pm(5\oplus19)$	317	±128	±26	264 $\pm(5\oplus5)$	230	±118	±19
200.2	392 $\pm(5\oplus20)$	532	±132	±38	281 $\pm(5\oplus6)$	406	±122	±26
	$W^+W^-\gamma$ with on-shell Ws				and no FSR			
188.6	263 $\pm(3\oplus13)$	116	±84	±15	176 $\pm(2\oplus4)$	53	±78	±13
197.7	295 $\pm(4\oplus15)$	347	±92	±24	211 $\pm(4\oplus4)$	263	±85	±18
206.0	317 $\pm(3\oplus16)$	244	±89	±23	233 $\pm(2\oplus5)$	179	±83	±18
194.5	289 $\pm(4\oplus14)$	234	±127	±22	203 $\pm(4\oplus4)$	173	±116	±17
200.2	300 $\pm(5\oplus15)$	436	±130	±32	217 $\pm(4\oplus4)$	339	±120	±22

Table 4.9: $W^+W^-\gamma$ cross-section for different signals. ”all” stands for the definition used previously, ”no FSR” means only events with ISR and WSR photons are considered as signal, ”on-shell” means only events with the Ws generated within $|M_{ff'} - M_W| < 2\Gamma_W$ (before FSR) are considered as signal. The SM values are obtained at generator level and the associated errors are the statistical and theoretical errors, respectively.

The cross-sections for each case are shown in table 4.9 for five centre-of-mass energies (the numbers for 194.5 and 200.2 GeV are combined into a single number at 197.7 GeV, and can only be used instead of that one). Since no dedicated analysis was developed for each of these different signal definitions measurements, they are all strongly correlated: no extra information is derived in this table.

4.4 Anomalous $W^+W^-\gamma$ final states

The anomalous contributions, from the introduction of a_c/Λ^2, a_0/Λ^2, $\tilde{a}_0/\Lambda^2$, a_n/Λ^2 and $\tilde{a}_n/\Lambda^2$, were obtained by varying the weights in three samples of $W^+W^-\gamma$, generated using EEWWG at the average centre-of-mass energies of each year data-sets – 189, 198 and 206 GeV – and fully simulated. The SM spectra from these samples ($a_c = a_0 = \tilde{a}_0 = a_n = \tilde{a}_n = 0$) were checked to be compatible with the ones from WPHACT (excluding FSR events).

Figure 4.12 shows the measured $W^+W^-\gamma$ cross-sections as a function of the centre-of-mass energy, compared with the SM curve, obtained with WPHACT, and with the cross-sections obtained in the presence of anomalous parameters. The change in cross-section is quadratic in a/Λ^2 and for small values of a/Λ^2 it can be the interference term (between the QGC diagram and the ISR/WSR processes) that dominates; when the interference is destructive the cross-section can be reduced.

The relative importance of the interference and pure QGC terms depends on the anomalous coupling considered even if affecting the same effective vertex: while for a_c/Λ^2 this interference is strong, for a_0/Λ^2 it is almost negligible and it is further suppressed for the CP-violating $\tilde{a}_0/\Lambda^2$. The a_n/Λ^2 and $\tilde{a}_n/\Lambda^2$ terms, affecting the $W^+W^-Z^0\gamma$ vertex, have a smaller effect on the total cross-section if the same range is considered.

The effect of the anomalous parameters is stronger for higher centre-of-mass energies, where there is more phase space available for the photon. In the QGC vertices the energy tends to be more evenly distributed between the Ws and the γ than in the cases where the γ is radiated by *Bremsstrahlung*. This can be seen more clearly in figure 4.13, where the photon energy spectra in each of the three data samples is compared with the SM prediction and the predictions in the presence of the same anomalous couplings as in figure 4.12.

The effect of the anomalous couplings in other distributions is less striking. Figure 4.14 shows the highest centre-of-mass energy data, compared with the expectations with or without anomalous QGCs, for the photon polar angle and the minimum angle between the photon and the reconstructed Ws. The cuts used in the analysis

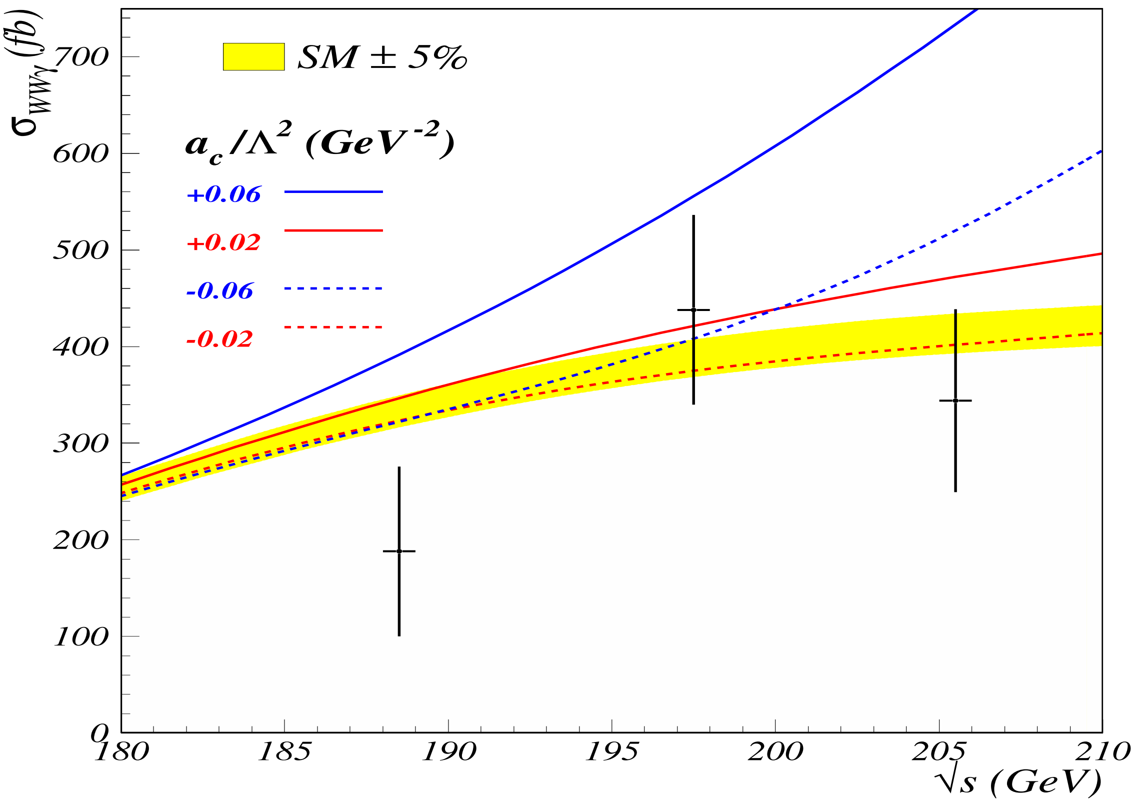

Figure 4.12: $W^+W^-\gamma$ cross-section as a function of the centre-of-mass energy. The measured cross-sections (dots) are compared to the SM prediction from WPHACT. The cross-sections obtained with EEWWG for indicative values of the anomalous parameter a_c/Λ^2 (in GeV^{-2}) are also shown.

select already the regions where the effect of ISR and FSR are reduced, and the sensitivity to the anomalous couplings is then almost constant for the considered range of these variables. In the same figure, typical distributions of W^+W^- events are also shown for semi-leptonic and fully-hadronic events: respectively, the distribution of the polar angle of the lepton weighted by its charge – which is flat for s-channel W^+W^- production (and QGC diagrams) and peaks at -1 for t-channel production – and the NN output variable for the selection of fully-hadronic W^+W^- – showing that the NN does not have a strong bias towards SM-like W^+W^- distributions and is able to selected anomalous $W^+W^-\gamma$ contributions as well.

The possible values of the anomalous couplings can be derived from the cross-

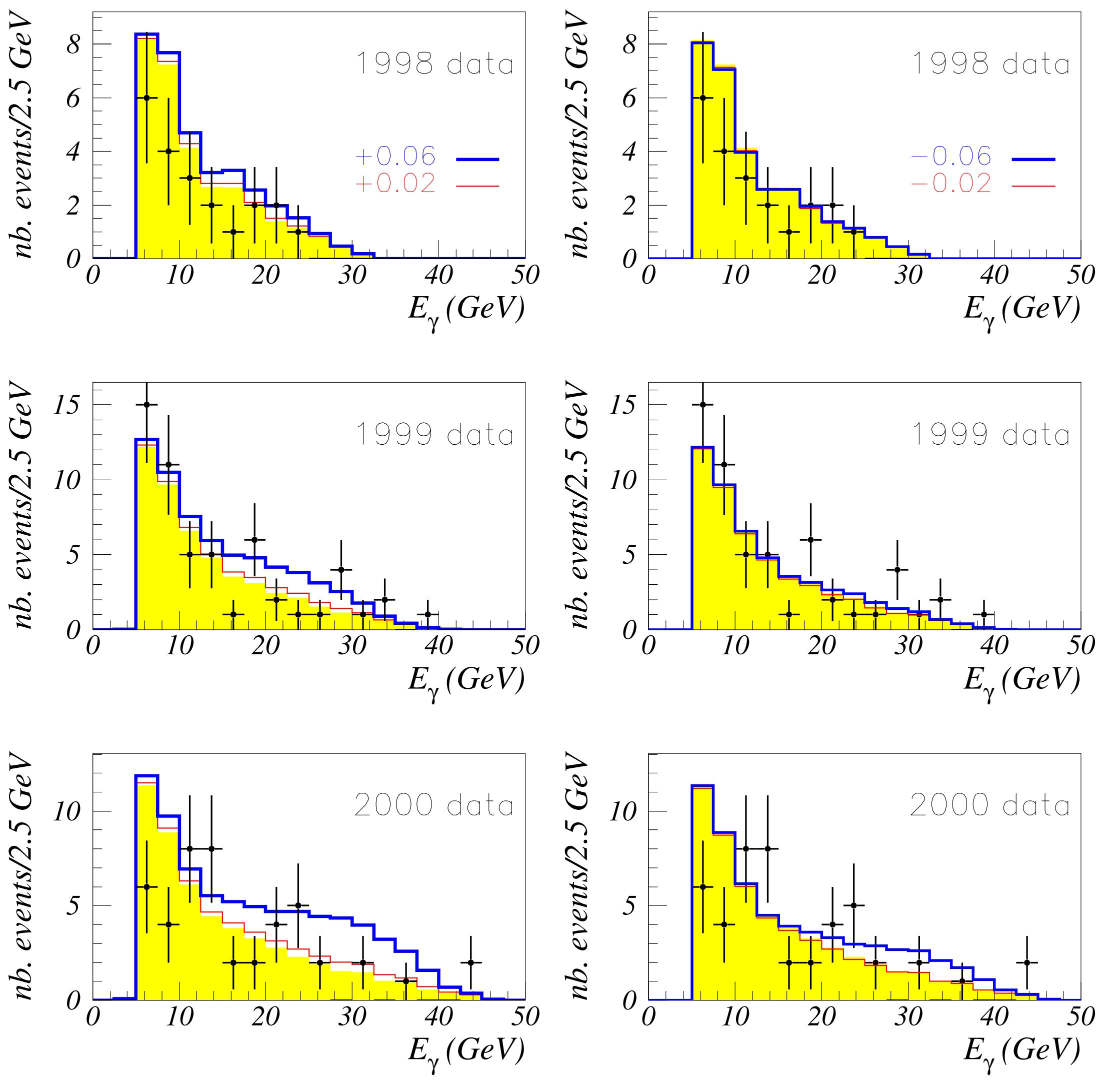

Figure 4.13: Effect of anomalous couplings in the photon energy spectra in each data sample: (top) data with $\sqrt{s}$ =189 GeV, (middle) data with $\sqrt{s}$ =198 GeV and (bottom) data with $\sqrt{s}$ =206 GeV. The data (dots) are compared to the total SM predictions (dark histogram). The expected result with anomalous QGCs are also shown for positive (left) and negative (right) values of a_c/Λ^2 (in GeV^{-2}).

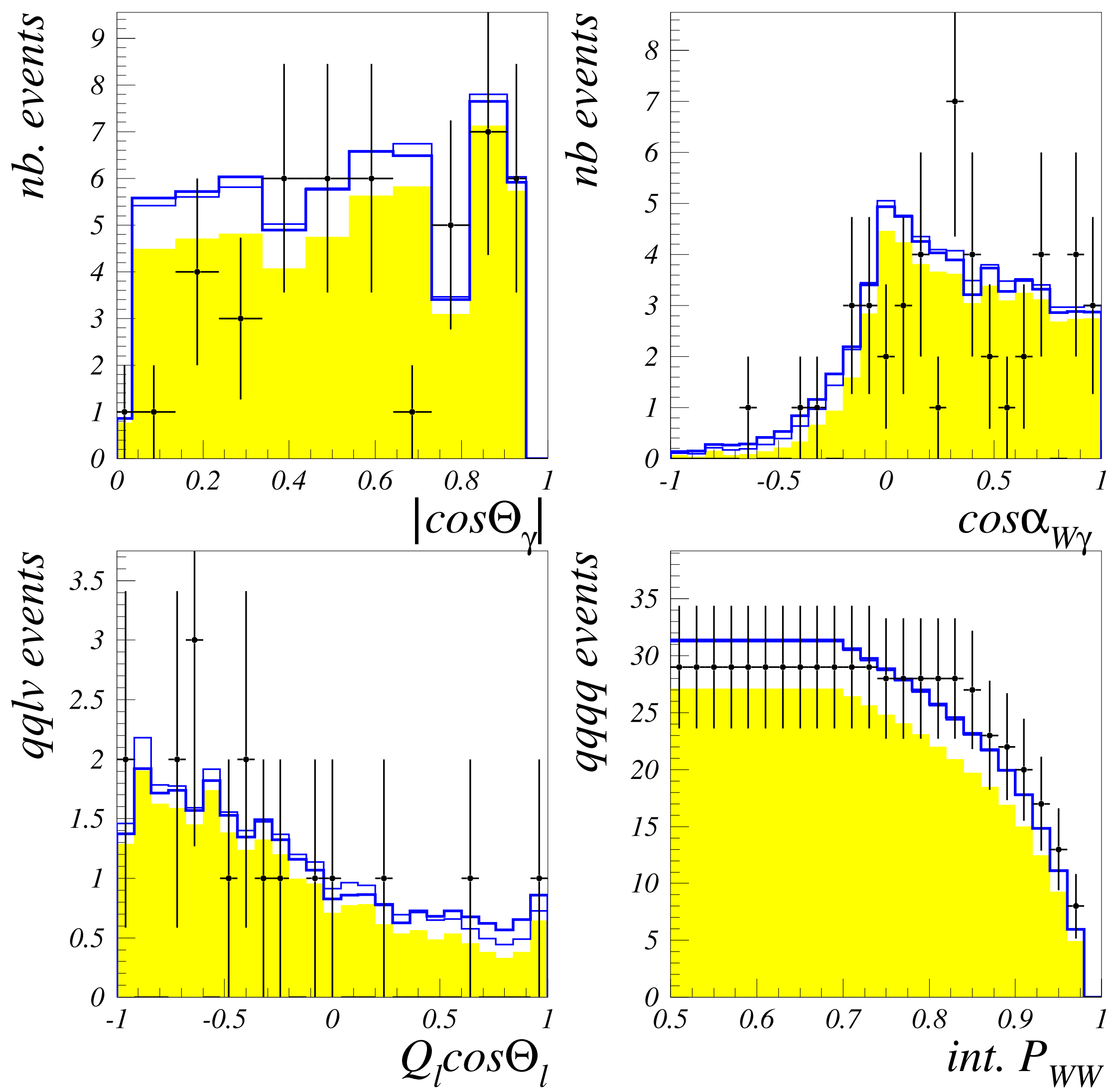

Figure 4.14: Effect of anomalous couplings in other variables: the polar angle of the photon and minimum angle between the photon and the reconstructed $W^\pm$ (for all the events selected in the 2000 data sample) and polar angle of the lepton (multiplied by the lepton charge) or the neural network W^+W^- probability, for semi-leptonic and fully-hadronic events, respectively. The 2000 data (dots) are compared with the corresponding SM predictions (dark histogram). The expected results with anomalous QGC $a_c/\Lambda^2 = -0.060$ GeV^{-2} ($a_c/\Lambda^2 = +0.030$ GeV^{-2}), are shown as the white histograms with strong (light) line.

sections measured in the analysed data. For this, a likelihood fit to the four analysis channels and three energy points will be performed as a function of each of the anomalous parameters (fixing the others at 0, their SM value). The variation from statistical fluctuations in each of the 12 samples is then taken into account. Systematic uncertainties on the SM prediction can also be included, and are considered to be uncorrelated between channels and energies. They are assumed to be of 10% in the electron and muon channels and 15% in the tau and fully-hadronic channels, which are obtained, following the studies for the total cross-section analysis, by majoring $0.035 + 0.05\ 4f/MC_{tot} + 0.20\ (1-4f)/MC_{tot}$. The systematic uncertainties were found to have a negligible impact in the fits.

In addition, differential information can also be used in the fits, namely that from the photon energy distributions, which are useful in separating the anomalous contributions from the SM. The result obtained for the a_c/Λ^2 parameter, with or without differential information, is shown in figure 4.15. The expected results (here calculated without systematic errors) show that there is a clear improvement of the parameter determination when the energy spectra information is added. It is curious to note that the difference between the observed and the expected results is also diminished by the extra information: although there is a global deficit of events – which would allow for a larger anomalous contribution – the data agreement with the SM expectation is better in the most sensitive regions of the photon spectra.

The limit is dominated by the highest energy sample. The observed upper and lower 95% limits on a_c/Λ^2 both correspond to the addition of 8 extra events in the year 2000 sample even if for the positive value of a_c/Λ^2 there would be around 8 events in the other samples, while for the negative value only around 3 events would be added.

The relative importance of each sample can be evaluated by analysing the separate likelihood curves. In figure 4.16, the likelihoods are shown as a function of a_n/Λ^2, with the corresponding lower and upper 95% CL limits reported in table 4.10. It is clear that although the limits are dominated by the higher energy data, they are sensitive to the lower energy and that the fully-hadronic and semi-leptonic samples have similar contributions to the result. Only the very low energy data is unnecessary for the limit extraction, but can still influence the parameter estimation.

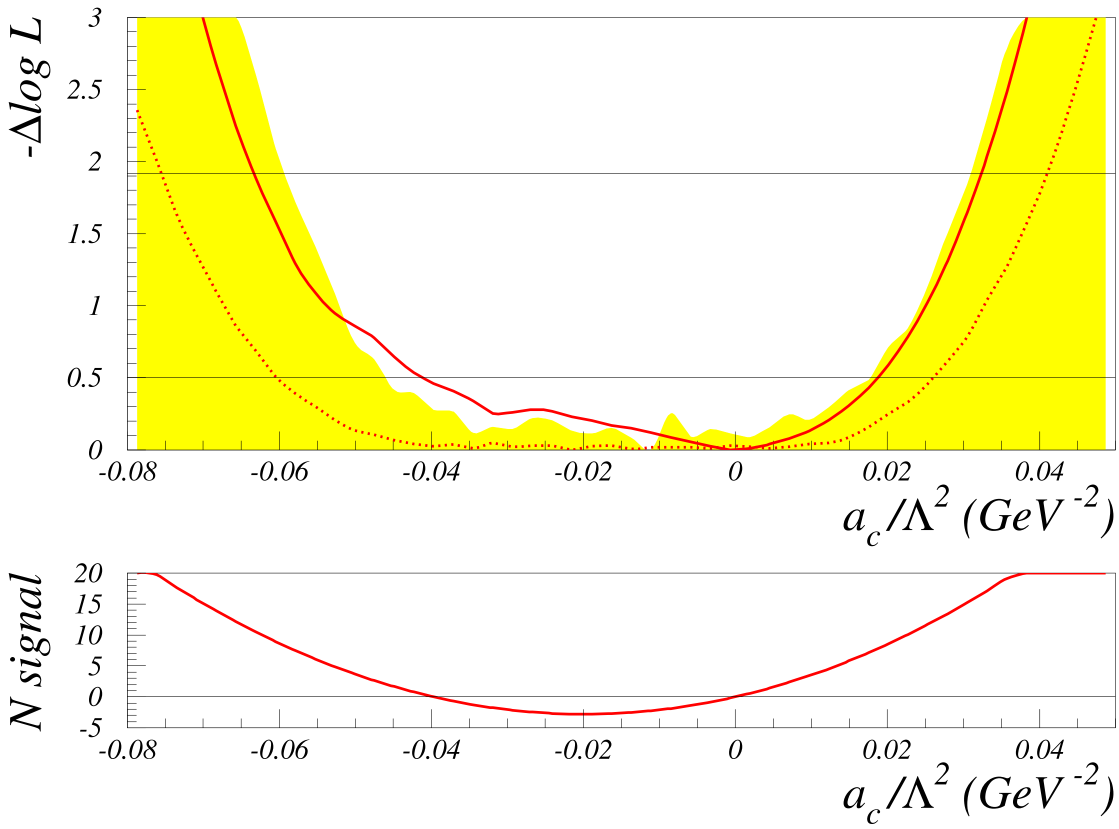

	68 % CL limits				
with number of events only	-0.047	(-0.060)	to	0.017	(0.026)
with photon energy spectra	-0.041	(-0.046)	to	0.019	(0.018)
	95 % CL limits				
with number of events only	-0.071	(-0.076)	to	0.035	(0.041)
with photon energy spectra	-0.063	(-0.059)	to	0.032	(0.031)

Figure 4.15: Determination of a_c/Λ^2: the top plot shows the expected (grey region) and observed (strong curve) $-\Delta log\mathcal{L}$ as a function of the anomalous parameter, the dotted line shows the expected curve if only the number of events would be used. The 68% CL limits are given by the crossing of the 0.5 horizontal line and the 95% CL limits by the 1.92 line. The lower plot shows the corresponding expected number of visible signal events, which can be negative when the interference with the SM dominates.

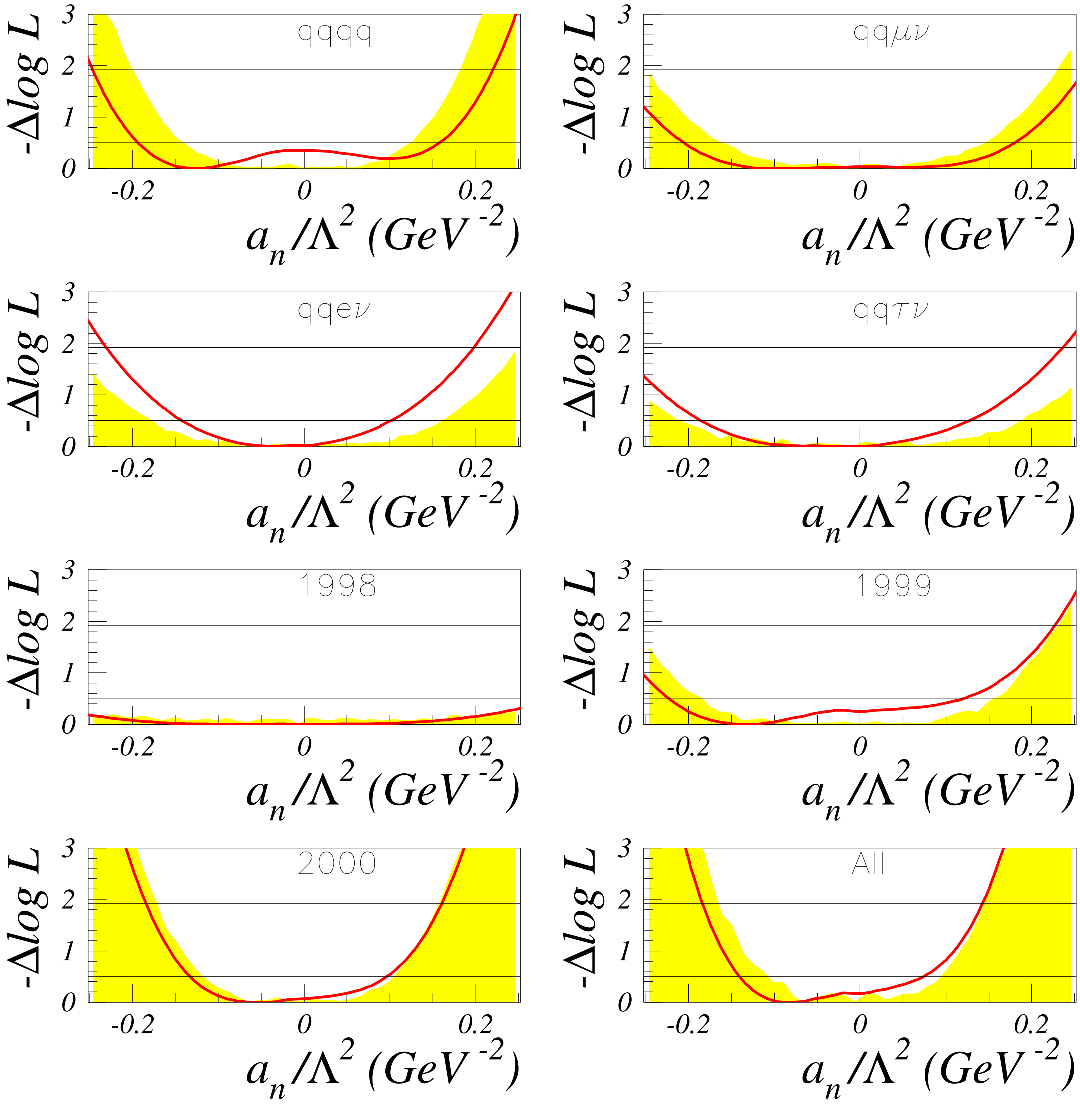

Figure 4.16: Determination of a_n/Λ^2: the top four plots shows the $-\Delta log\mathcal{L}$ for each channel, putting together all data, the lower plots show the $-\Delta log\mathcal{L}$ for each of the three separate centre-of-mass energies, considering all channels together, and finally, the total $-\Delta log\mathcal{L}$. In all cases, the grey region corresponds to the mean expected result, and the dark curve is the observed result.

$qq\mu\nu$	-0.28	(-0.25)	to	+0.26	(+0.23)
$qqe\nu$	-0.23	(-0.27)	to	+0.20	(+0.25)
$qq\tau\nu$	-0.28	($<$)	to	+0.24	($>$)
all $qql\nu$	-0.19	(-0.20)	to	+0.15	(+0.18)
$qqqq$	-0.25	(-0.20)	to	+0.22	(+0.18)
189 GeV data	outside range				
198 GeV data	-0.29	(-0.27)	to	+0.23	(+0.23)
206 GeV data	-0.18	(-0.17)	to	+0.16	(+0.16)
ALL DATA	-0.18	(-0.17)	to	+0.14	(+0.15)

Table 4.10: Anomalous parameter determination per channel and data set: the 95% CL limits on a_n/Λ^2 (in GeV^{-2}) are shown for the separate channels (all data sets considered) and for separate data sets (all channels considered). The expected results are shown in parentheses. The likelihoods were calculated in the range [-0.30,+0.30] GeV^{-2}.

lower limits			upper limits	
95% CL	68% CL	central value	68% CL	95% CL
-0.063	-0.040	$a_c/\Lambda^2 =$ -0.000 GeV^{-2}	+0.019	+0.032
-0.020	-0.014	$a_0/\Lambda^2 =$ -0.004 GeV^{-2}	+0.014	+0.020
-0.020	-0.015	$\tilde{a}_0/\Lambda^2 =$ -0.007 GeV^{-2}	+0.012	+0.020
-0.18	-0.14	$a_n/\Lambda^2 =$ -0.09 GeV^{-2}	+0.07	+0.14
-0.16	-0.10	$\tilde{a}_n/\Lambda^2 =$ +0.05 GeV^{-2}	+0.12	+0.17

Table 4.11: Results on the five anomalous QGC parameters, a_c/Λ^2,a_0/Λ^2, $\tilde{a}_0/\Lambda^2$, a_n/Λ^2 and $\tilde{a}_n/\Lambda^2$. The best fit values are shown together with the 68% CL and the 95% CL limits (including statistical and systematic errors). All results on each coupling are obtained with the other anomalous parameters fixed at 0.

The final results for each anomalous QGC parameter when fixing the others at their SM values are reported in table 4.11. The data is compatible with the absence of anomalous quartic gauge couplings within 1σ.

More general results can be obtained as the result of a five parameter fit[3]: the best fit values of the parameters are compatible with the ones in table 4.11. It is, however, more instructive to study the behavior of the likelihood curve, better done in two-dimensions, as shown in figure 4.17. The limits obtained in 1 parameter fits

[3]This is still not totally generic, anomalous couplings affecting the Triple Gauge Couplings are still assumed to be absent.

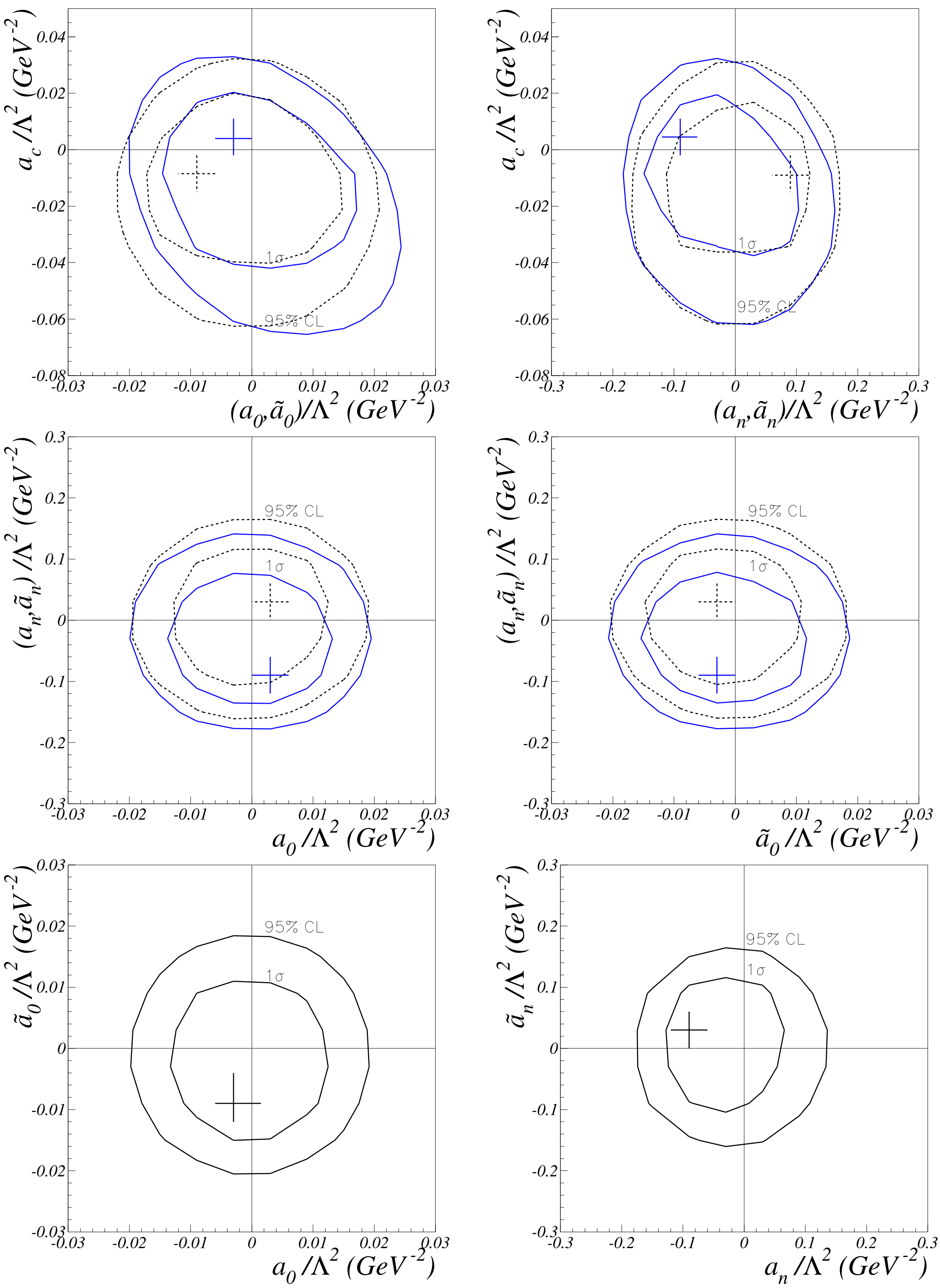

Figure 4.17: 2 parameter fits of a_c/Λ^2, a_0/Λ^2, $\tilde{a}_0/\Lambda^2$, a_n/Λ^2 and $\tilde{a}_n/\Lambda^2$: for each pair of anomalous coupling parameters, the best fit values are represented by a cross (within the determination error), and the 68% CL and 95% CL contours are represented by the closed lines. When two parameters are shown in the same axis, the solid line corresponds to a_X and the dashed line to $\tilde{a}_X$.

can in general be kept, even if several parameters are allowed to vary. The exception is that the existence of an anomalous QGC of the type $-\frac{\pi\alpha A_c}{4\Lambda^2}.F_{\alpha\mu}F^{\alpha\nu}(W_\nu.W^\mu)$ with negative A_c (within those limits), brings the total cross-section down, and thus the limits on the other parameters are weakened.

In this more general case, the 95% CL intervals become:

$$\begin{array}{rcl}
\text{-0.065 GeV}^{-2} < & a_c/\Lambda^2 & < +0.033\ \text{GeV}^{-2} \\
\text{-0.020 GeV}^{-2} < & a_0/\Lambda^2 & < +0.025\ \text{GeV}^{-2} \\
\text{-0.022 GeV}^{-2} < & \tilde{a}_0/\Lambda^2 & < +0.020\ \text{GeV}^{-2} \\
\text{-0.180 GeV}^{-2} < & a_n/\Lambda^2 & < +0.160\ \text{GeV}^{-2} \\
\text{-0.170 GeV}^{-2} < & \tilde{a}_n/\Lambda^2 & < +0.170\ \text{GeV}^{-2}
\end{array}$$

The parameters are, in general, uncorrelated. The most sizable correlation is felt between a_c/Λ^2 and a_0/Λ^2 both affecting the $W^+W^-\gamma\gamma$ vertex in a CP conserving way; the correlation of these parameters with the parity violating operator in $\tilde{a}_0/\Lambda^2$ is reduced. The correlation between a_c/Λ^2 and a_n/Λ^2 (and $\tilde{a}_n/\Lambda^2$) is smaller and is felt mostly for positive a_c/Λ^2. It is also interesting to note that although for small coupling values the effects of a_X and $\tilde{a}_X$ are different, the differences are negligible for larger values, when their effect is felt at the level of total cross-sections.

Chapter 5

Fermiophobic Higgs

The search for neutral Higgs bosons predicted in the 2HDM fermiophobic model relies on both h^0Z^0 and h^0A^0 production modes. The main decays of the h^0 are to photons, while for Z^0 and A^0 there are several decays to consider. In this chapter the final states with only jets and photons will be analysed (those are also the most important ones in terms of decay BR), but other results will be reviewed.

For these analyses, it is important to have a good description of the radiation background processes, and so the generators used are discussed in the first section. The common procedures to all the analyses are then presented, before proceeding to the analysis of h^0Z^0 and h^0A^0 production.

In the end of the chapter, all the results are put together to extract the maximum possible information on the 2HDM fermiophobic model.

5.1 Event Generators

The 2-fermion production is one of the dominant processes at LEP. The theoretical calculations have been extensively studied and experimental measurements have confirmed the predictions to a great accuracy. At LEP2 the sensitivity to the details of the radiative corrections increases and their accurate description becomes a source of concern.

This question has been addressed in a previous work [1], where the importance of the Monte Carlo and semi-analytical descriptions of real and virtual photon emission was explained and different techniques of calculation were reviewed. These can be more theoretically based or rely on more pragmatic approaches, but the fact is that, since the photon emission corresponds to higher order effects in perturbation theory, the full process can never be implemented directly.

An example of a pragmatic approach is the one implemented in Pythia [43]: a general purpose generator widely used in particle physics and, in particular, in DELPHI. Since many different physics processes can be generated in Pythia, also the radiative corrections are treated in a general way. In fact, QED corrections are included via a parton shower mechanism, developed first for the description of QCD radiation.

The event generation starts with the definition of a “hard” process – calculated at a previously chosen effective centre-of-mass energy – and the radiative corrections and photons are then added to the final state (FSR) and to the initial state (ISR) until reaching either a lower energy cut-off or the initial centre-of-mass energy to be described. The probability of each photon 4-momenta is calculated according to the Lipatov evolution equations (known as Altarelli-Parisi functions in the QCD framework), and there is no *a priori* limit to the number of photons which can be radiated.

Although the Lipatov equations have a simple form, many parameters have to be set for this mechanisms to fully describe the higher order physics processes. It is particularly sensitive to the energy scale of the calculation, to the effective electromagnetic coupling constant, to the thresholds chosen, etc. It is thus possible to tune the predictions with new experimental input. After the studies in [1] and [68], the DELPHI Pythia version was made to more closely reproduce the results from the more dedicated programs available at the time.

The advantage of using Pythia for the generation of physics events is that it has the most complete description of the QCD corrections, with the same kind of parton shower mechanism, and all the hadronic part of the process has been tuned to reproduce LEP1 data [69]. Although it is not the best generator to study the QED effects, the QED implementation is still useful when the details are of minor importance. For example, it is used to describe new physics signals, including the effects of ISR on the effective centre-of-mass spectra and the addition of an arbitrary number of photons. It will be used to generate the fermiophobic Higgs signal samples, in the following.

To describe the background to the fermiophobic Higgs search, however, Pythia is not detailed enough. In fact, the irreducible background is composed of $f\bar{f}$ events with two hard photons from ISR (and FSR), and thus the detailed description of the hard photon radiation is crucial, while the soft photon radiation is also important in the estimation of the total and differential cross-sections.

KK2f [37] appears as the most detailed generator of QED corrections to $f\bar{f}$ production at LEP, following the steps of KoralZ[38] – considered in [1] and [68]. It includes virtual and real soft radiation via YFS [58] functions and describes the hard emission through a careful re-summation of the terms in the perturbative expansion. In addition, it also includes higher order matrix elements – up to $\mathcal{O}(\alpha^3)$ – which are used after the final number of hard photons is chosen. This choice is done in such a way that the hard and soft spectra are separated according to a pre-set cut-off value, but the total calculation is independent of that value and explicitly non-divergent.

The most important development of KK2f in relation to KoralZ is the extension of the YFS method to a Coherent Exclusive Exponentiation: that is the soft emission corrections are now done at the level of the matrix element, and thus the ISR and FSR parts can be propagated together before integration over the photon phase space, including the interference by construction and taking into account the spin densities. In terms of total cross-section, KK2f reaches a precision of less than 0.2% [37].

For the $e^+e^- \to q\bar{q}$ process, however, there is an additional problem in the description of FSR. As noted before, the radiation of gluons from the final state quarks competes with the photon radiation, and neglecting that effect leads to an overestimation of the photon FSR. So, once again, it can be preferable to use the parton shower description, in which the two FSR processes are balanced by construction instead of a more precise description of photon FSR which will distort the spectra of both FSR photons and gluons, and thus the structure of the hadronic event. The description of the photon FSR itself is of minor importance in hadronic events, as most photons will be included in the hadronic jets. It is the effect on the total and differential cross-sections that is important, and to which also the ISR/FSR interference may contribute. It is thus important to study the relative importance of both effects: photon ISR/FSR interference and photon/gluon FSR competition.

In DELPHI, KK2f is also used for $\mu^+\mu^-$ production. In that case, there are no QCD corrections and so the capabilities of the KK2f calculation can be fully exploited: in particular, the ISR/FSR interference can be included. For $\nu\bar{\nu}$ and $\tau^+\tau^-$ production the generator chosen is KoralZ: in the case of $\nu\bar{\nu}$ there is no FSR, so the description is simplified, for $\tau^+\tau^-$ an extra complication occurs and the interface with a dedicated tau decay generator [53] is necessary. Bhabha events are generated with BHWIDE[39]: this is the most complex calculation, with a variety of Feynman diagrams to be considered, and specific computation difficulties due to the t-channel contribution which leads to quasi-divergences, to be overcome in the calculation. All these generators are done by the same authors and share the same kind of approaches for the QED corrections and that allows for dedicated studies which ensure that none of the points neglected would cause a big distortion in the generated samples.

Zfitter [70], an analytical program, can not be used to generate events but is also useful to control the numerical calculations of differential cross-sections. Table 5.1 shows the cross-section for $e^+e^- \rightarrow q\bar{q}$ obtained with Zfitter, KK2f and Pythia, for different regions of M_{had} – the mass after all photon radiation.

		Zfitter	KK2f all	KK2f no int.	KK2f + Pythia	Pythia
low M	$0.1 < X < 0.4$	2.95	2.91	2.89	2.65	2.55
Z^0 peak	$0.4 < X < 0.6$	68.20	68.36	68.32	68.38	67.82
valley	$0.6 < X < 0.8$	3.41	3.48	3.65	3.39	3.32
no Radiative	$0.8 < X < 1.0$	22.81	22.74	22.68	22.92	23.18

Table 5.1: Differential cross-section for $e^+e^- \rightarrow q\bar{q}(\gamma)$ (in pb) at $\sqrt{s} = 189$ GeV, obtained with Zfitter, Pythia and 3 different implementations of KK2f: with ISR$\oplus$FSR, ISR and FSR but no interference or with FSR done by Pythia – the chosen configuration. $X = M_{had}/\sqrt{s}$.

The three entries for KK2f highlight the relative importance of the photon FSR description and related questions. They correspond to the full KK2f calculation – including FSR and interference, but no interplay with the QCD FSR; the KK2f calculation without interference – which can be used to measure the impact of the interferences; and the KK2f calculation as will be used in the analysis, that is with no interference and FSR described by Pythia. The QCD corrections are in all the other cases, included as an analytic factor only, while gluon radiation can be generated after all the electroweak part of the event is produced.

The differences between the several calculation are small, of less than 1% in total cross-sections. However it is still noticeable that KK2f agrees better with the Zfitter reference than Pythia: it has a more precise description of electroweak effects, as expected. The effect of the interference alone seems to be negligible and it is then preferable to use the FSR from Pythia where the interplay with gluon radiation is incorporated.

Although it is difficult to prove that the differences between the two KK2f calculations (with no interference and with FSR from KK2f or Pythia) come from gluon radiation, the effects observed in table 5.1 are consistent with what would be expected in that case. The radiation of hard gluons reduces the amount of energy available for FSR photons, which would contribute less to the M_{had} spectra. In fact, when the gluon radiation is included with Pythia, there are more events in the two regions which correspond to soft radiation only and to radiative returns caused by ISR alone.

Another effect, observed for muons, is a change in angular distributions: for which the interference gives a higher forward-backward assymmetry. This can be seen mostly in the very forward regions and for events with soft radiation only. Due to the smaller quark charges, the effect is weaker in quark final states, and is even compensated when u-type and d-type quarks are present. However, in analysis with b-quarks only, for example, care should be taken for the use of jet angular variables.

Although the interplay between the photon and gluon FSR is important for the global event structure, most characteristics are determined by the ISR. In $e^+e^- \to q\bar{q}$ this is even increased by the dominant presence of radiative returns to the Z^0, and the main points to be described are the number of hard photons, the energy balance between them, and their relative directions.

The differences in between generators are thus very effectively observed when analysing the $e^+e^- \rightarrow h^0Z^0 \rightarrow \gamma\gamma q\bar{q}$ process, and can be seen in the analysis described in the next sections (conf. table 5.2). In fact, the cross-section for events with two photons is compatible for KK2f and Pythia until cuts are made on their angular distributions, but the selection of photons at high polar angles leads to a clear discrepancy between the two predictions. In Pythia, the photons are in general more forward and – at the end of the selection of $Z^0+2\gamma$ when the photons are hard, central and isolated – differences of 30% to 50% can be observed in relation to both the KK2f prediction and the DELPHI data. In fact, the analysis shows that the data is sensitive to the details of the implementation of QED radiative corrections and is clearly more closely described by the most precise theoretical approach in KK2f.

5.2 The Common Fermiophobic Analysis

The search for the fermiophobic Higgs is based on a common framework which allows for the study of $q\bar{q}\gamma\gamma$, $l^+l^-\gamma\gamma$ and $\nu\bar{\nu}\gamma\gamma$ final states from h^0Z^0 decays, for example. In fact, the same strategy is used for the fermiophobic Higgs and also for a variety of other searches for new physics done by the DELPHI-Lisboa group.

In this framework, three analysis lines are considered, the events being classified as "photonic", "leptonic" or "hadronic". The basic selection of good tracks and neutral depositions is common, and in all cases there should be at least one charged particle or one electromagnetic cluster with an energy greater than 5 GeV in the polar angle region above 20°, to guarantee an interesting event. The visible energy in the same polar angle region has to be above $0.1\sqrt{s}$, for the three selections.

The selection of photonic events is described in detail in [33]. It is not completely exclusive in relation to the leptonic one. In fact, the same selection can be used to select (leptonic) Bhabha events without taking into account the measured tracks, which is useful for trigger efficiency studies for the photonic analysis. The classification strategy used for photonic events is, however, necessarily different as, when no good tracks are required, there is a higher contamination from cosmic-ray events or electronic noise, for example, which lead to fake photon signals. On the other hand, the reconstruction of isolated photons can be relaxed since there are less particles in the events, with most signals coming from photons or from spurious activity in the detector.

For the leptonic and hadronic events, the main selection criteria are identical. The two categories are made exclusive by separating the events according to the number of good tracks: if there are up to five tracks the events is classified as leptonic, above five it is classified as hadronic. In addition, the visible energy cut is tightened to $0.2\sqrt{s}$, in both cases.

Figure 5.1 shows the behavior of the main variables of the hadronic selection. The cut on the number of tracks selects more than 99% of the $q\bar{q}$ events – only those with a very small effective centre-of-mass energy and thus particular hadronization mechanisms are excluded; on the other hand, it selects less that 1% of the Bhabha events and only around 5% of the $\tau^+\tau^-$ events.

The cut on the visible energy, on the other hand, excludes more than 10% of the total $q\bar{q}$. These are events in which there is radiation of a hard ISR photon in the beam direction and so all the hadronic part is also forward and below the 20° region. They correspond to processes already studied at lower energy colliders and so less interesting for new physics searches. On the other hand, the cut is necessary to avoid the "virtual $\gamma\gamma$ collision" events whose MC description presents serious problems – only part of the total spectra is represented in the figure.

The only other important process contributing to the hadronic selection is the production of 4-fermion events, namely from W^+W^-, which can be identified in the figures in the high multiplicity region (fully-hadronic part) and in between the two effective collision energy peaks (semi-leptonic part).

The treatment of the final state particles is only slightly different in the leptonic and hadronic topologies. Isolated leptons (electrons, muons, or just isolated tracks) and isolated photons are first identified and only after, in the jet clustering, do the differences arise.

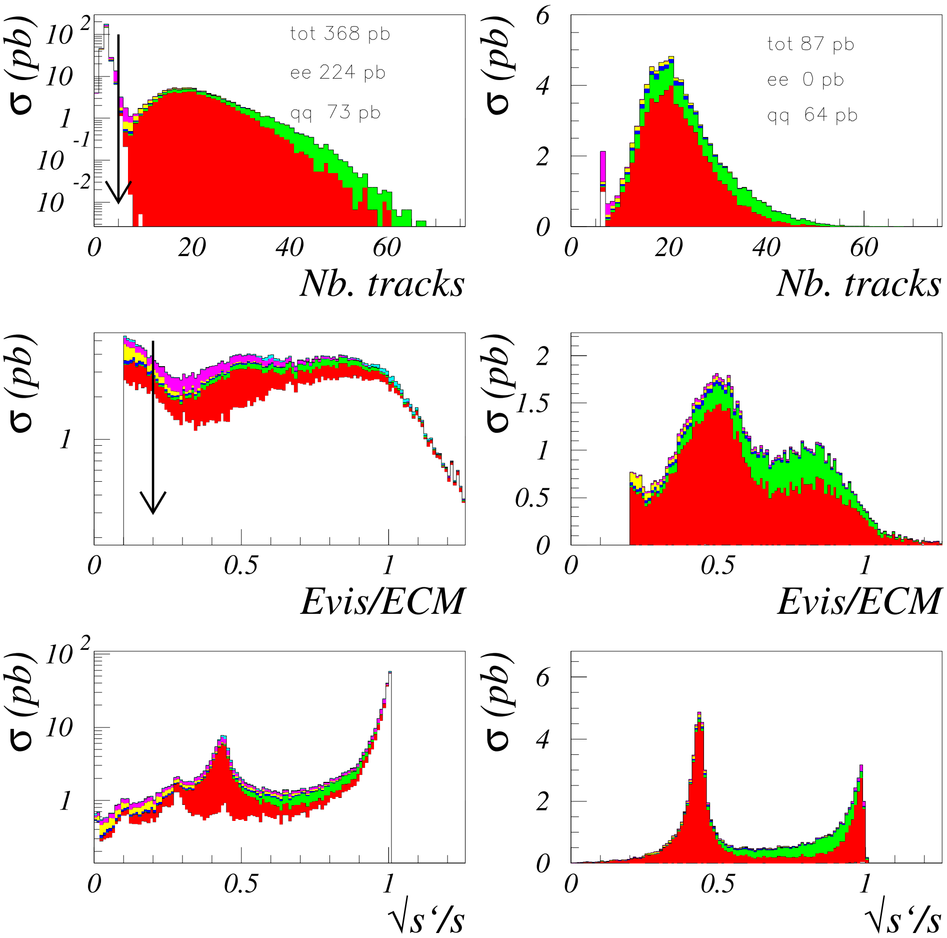

Figure 5.1: Hadronic selection: the number of good tracks per event (top), fraction of visible energy above 20° (middle) and fraction of effective centre-of-mass energy – $\sqrt{s'/s}$ (bottom) are shown for the main physics processes at LEP, at the common analysis level (left) and after the hadronic selection (right). The two cuts of the hadronic selection are indicated by the arrows. Several processes are included, in particular the Bhabha contribution is shown as the white histogram, the $q\bar{q}$ as the darker one, and 4-fermion charged current processes (namely W^+W^-) as the grey histogram.

In the leptonic topologies, jets are constructed to allow for the recuperation of energy around the lepton: all particles except for the isolated photons are forced to belong to the jet of one of the isolated leptons. In the hadronic topologies, jets are done excluding also the isolated leptons. The number of jets in each events can be left free to vary according to some separation cut – which can be viewed as an event shape variable – or forced according to a specified channel being studied, which is more useful for most analysis. Only the number of isolated leptons and photons is well determined and characterizes the event.

The analysis described in the next sections for final states with photons were pre-selected with the above and correspond to data taken in the LEP runs of the years 1997 to 2000. The data taken after the loss of one TPC sector was found to be selected with compatible efficiencies.

5.3 Search for h^0Z^0 Production

The search for h^0Z^0 production consists of three different analysis, according to the Z^0 decay to $q\bar{q}$, l^+l^- or $\nu\bar{\nu}$. They were done using the same framework and common analysis techniques but by different people.

The work described in this thesis deals only with the hadronic topologies. The next section will focus on the search for $q\bar{q}\gamma\gamma$ final states and the main points of the other two analysis will only be briefly reviewed after, they are described in [71].

The results from the three analysis are then put together to give the final results on h^0Z^0 production with a slight improvement in relation to the ones that could be obtained by the hadronic channel alone.

5.3.1 $\mathbf{q\bar{q}}\gamma\gamma$ analysis

The main channel of h^0Z^0 is characterized by a final state with two quarks from the Z^0 decay and two photons from the h^0 decay. The events were thus forced to two jets and two isolated photons were searched for.

To increase the efficiency, isolated tracks without hits in the muon chambers or in the VD were recovered as converted photon candidates. They were rechecked for their calorimetric characteristics and all the standard photon selection was applied. This was found to increase the final selection efficiency in around 2% while the addition of extra non-$q\bar{q}$ events is very small. Two photons, at most one converted, were required in the preselected sample.

The effect of forcing the events to two jets even in the case where there are three clear jets – from hard gluon radiation – was studied and proved to be a good approximation. In general, the possible third jet is put together with the one from the least energetic quark. On the other hand, some particles from the jet can be identified as isolated and that is more common than having events from other, more complicated, topologies. Extra isolated particles (leptons or photons) were allowed only if their transverse energy with respect to the jets was less than 20 GeV; in that case the event structure was not modified and the full jet recovered again by kinematic fitting.

After this preselection, further requirements were done in the isolation and polar angle of the two isolated photons to reduce both FSR and ISR contributions present in all samples. Namely, the most energetic photon had to have at least 15% of the beam energy, the minimum transverse energy of the photons with respect to the jets had to be above 7.5 GeV and the minimum polar angle above 30°.

Although the photons directions and energies are measured with high accuracy with respect to those of other particles, the energy resolutions obtained with the three DELPHI electromagnetic calorimeters are still very different, as shown in figure 5.2. The resolution is crucial for the h^0 identification in the signal, being that the raw resolution on the reconstructed $\gamma\gamma$ mass is $\frac{\delta M_{\gamma\gamma}}{M_{\gamma\gamma}} \alpha \frac{1}{2}(\frac{\delta E_{\gamma 1}}{E_{\gamma 1}} + \frac{\delta E_{\gamma 2}}{E_{\gamma 2}})$. It can be significantly improved through the use of kinematic fitting.

Since the directions and energies of the jets are subjected to very large errors, the 4-momentum of the photons are the main inputs to the fit. The simple imposition of energy-momentum conservation gives a large improvement on the M_{jj} resolution but not so much on the $M_{\gamma\gamma}$. An additional constraint was imposed on the jet-jet mass, recoiling against the two photons, requiring it to be the Z^0 mass. By constraining the jet variables, this leads to a two-fold improvement on the two photon invariant mass; the corresponding resolution is also shown in figure 5.2.

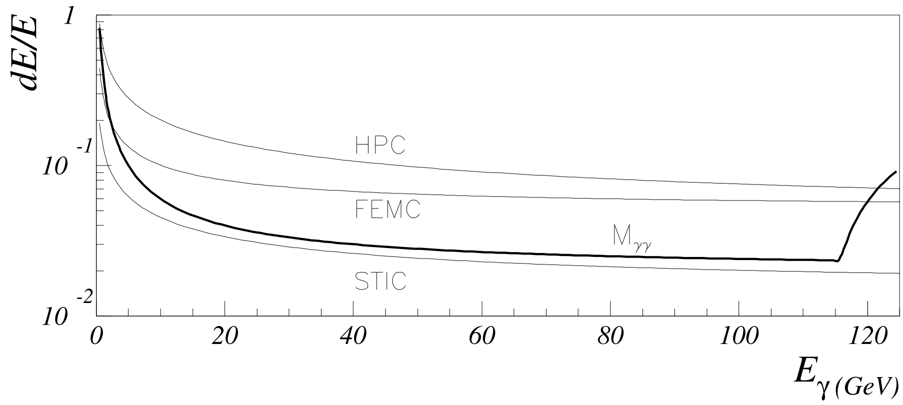

Figure 5.2: Energy and Mass resolution: the raw energy resolutions of the three electromagnetic calorimeters in DELPHI, HPC and FEMC (used in the analysis) and STIC, are compared to the resolution obtained on $M_{\gamma\gamma}$ after the kinematic fit. Above the kinematic limit for h^0Z^0 on-shell production, the fit leads to a distortion of the h^0 mass spectra, which is also represented in the corresponding curve.

The photons energies (and directions) are still the main inputs to the fit, but their precision is considerably weaker if the photons are not well contained in the calorimeters (FEMC or HPC). Events in which both photons were reconstructed near calorimeter boundaries were rejected at this stage. For the others, a partial χ^2 was constructed as:
$\frac{\chi^2_{\gamma\gamma}}{ndof} = \frac{1}{2}\sum_{i=1,2}\left(\frac{E^{fit}_{\gamma i} - E^{meas}_{\gamma i}}{\sigma . E^{meas}_{\gamma i}}\right)^2$, where σ is the relative error on the measured $E^{meas}_{\gamma i}$ from calorimeter resolution studies. For photons reconstructed in the calorimeter boundaries, this error was set to 100%.

If both photons were well contained in the calorimeters, it was required that this partial $\chi^2_{\gamma\gamma}/ndof$ was below 5; if one of the photons was not well contained, the hadronic part had a larger weight (as the photon had a 100% error) and it was the total $\chi^2_{tot}/ndof$ (defined in [50]) that was required to be below 5.

As an effect of these requirements, the non-$q\bar{q}$ background becomes almost negligible. The next step was the reduction of clear radiative return events: in most of those, the photons are forward and, usually, one of the photons carries most of the energy necessary to bring the Z boson on-shell ($E_{ret} = \frac{s-M_Z{}^2}{2\sqrt{s}}$).

Figure 5.3 shows the sum and difference of the two photon energies normalized to the radiative return energy, for data and background and for signals of different Higgs boson masses.

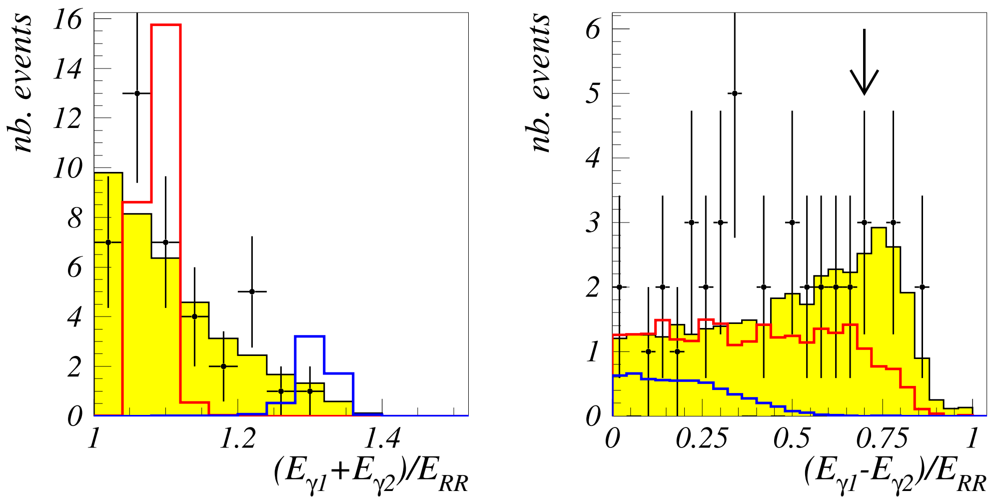

Figure 5.3: Energy of the two photons in h^0Z^0 compared to the radiative return energy, before the cut on the energy difference (indicated by the arrow). The sum (left) and difference (right) of the two photon energies divided by the radiative return energy are shown for all data (dots) and SM background (shaded area) and for two h^0Z^0 signals, with M_{h^0}=50 GeV/c^2 and M_{h^0}=100 GeV/c^2, produced with SM cross-section and a $BR(h^0 \to \gamma\gamma)$=15%.

After the kinematic fit, the sum of the two energies is constrained to be $\frac{E_{\gamma\gamma}}{E_{ret}} = 1 + \frac{M^2_{\gamma\gamma}}{s-M^2_{Z^0}}$, leading to a monochromatic signal for each M_{h^0} at each centre-of-mass energy. The energy difference, on the other hand, is constrained to be below some threshold which is lower when the mass is higher. Only events in which the energy difference between the two photons was lower than $0.70E_{ret}$ were kept, reducing the background in around 25% while keeping a high efficiency at high mass.

In the final sample, one of the photons was required to be above 42°, inside the

HPC. The efficiency for signal selection is almost unchanged, and even if the background was already severely reduced by the previous cuts, it still goes down by 5%.

Table 5.2 shows the evolution of the selection of the 2000 samples of data, SM background and signal with the analysis cuts. The contribution of the irreducible $q\bar{q}(\gamma\gamma)$ background is shown separately, and calculated for KK2f and for Pythia – in $(q\bar{q}_{old})$. The comparison of the number of events expected according to the two different generators shows that, as stated above, not only KK2f has a more accurate description of the initial state photon radiation as that leads to a better match to the DELPHI data.

selection	Data	background	$q\bar{q}$ (KK2f)	$(q\bar{q}_{old})$	eff$_{50}$	eff$_{100}$
2 photons	338	341.5 ±9.5	296.5 ±9.2	(287.9)	60%	60%
no-ISR/FSR	23	22.9 ±0.3	21.2 ±0.3	(15.9)	39%	45%
Z fit	12	12.4 ±0.2	12.3 ±0.2	(8.1)	31%	41%
$E_1 - E_2$	9	8.7 ±0.2	8.6 ±0.2	(5.8)	26%	40%
HPC	9	8.4 ±0.2	8.3 ±0.2	(5.5)	26%	40%

Table 5.2: h^0Z^0 selection in the year 2000: the evolution of the data sample with the analysis cuts is shown for the total 2000 data, compared to the total expected background (and the $q\bar{q}$ background) and the efficiencies for Higgs masses of 50 GeV/c^2 and 100 GeV/c^2. The $q\bar{q}$ expectations with Pythia $(q\bar{q}_{old})$ are shown for comparison and have similar precision.

The good agreement observed between data and the SM expectations, at all the analysis levels, indicates that no strong signal of new physics is present in this channel. In particular, there is no indication of a fermiophobic Higgs and the statistical analysis of the h^0Z^0 production will lead to limits on its possible mass. The extraction of those results is described in the next section and the inputs from the hadronic channel are discussed below. They comprise the number of observed candidate events in the last selection level for the data, SM expectations and each Higgs signal and for each of the separate data samples, and the corresponding $M_{\gamma\gamma}$ distributions.

The number of events selected per data set and the corresponding SM expectations are given in table 5.3 (together with those from the other analysis). For the signal expectations, the cross-sections and efficiencies must be known as a function of both the centre-of-mass energies and Higgs masses.

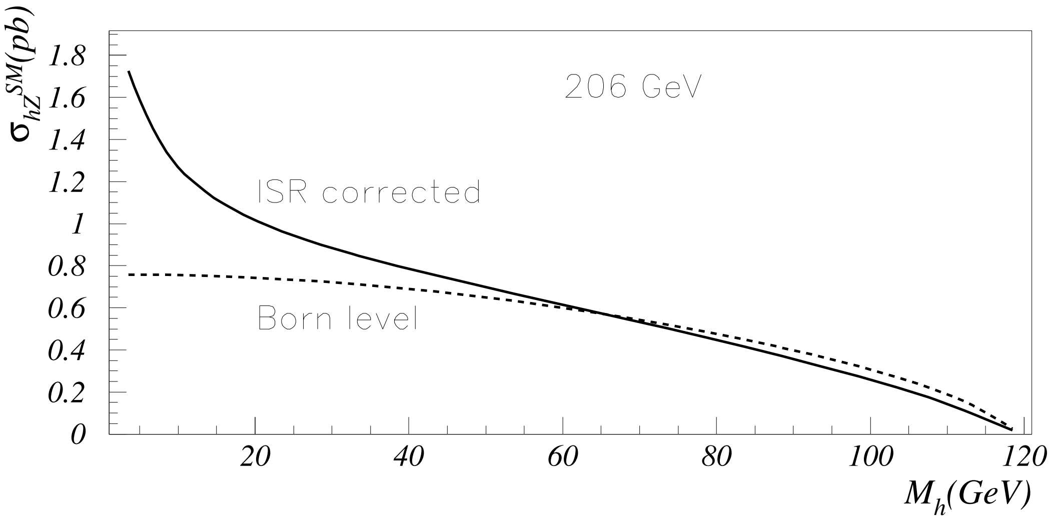

Figure 5.4: SM cross-section for h^0Z^0 production in e^+e^- collisions at $\sqrt{s}$ = 206 GeV as a function of M_{h^0}. The dashed line shows the Born level calculation, and the full line the cross-section with radiative corrections.

The cross-section for h^0Z^0 production was calculated analytically, according to ref.[72], including high order electroweak corrections – where the main changes to the total cross-section come from ISR. It is shown in figure 5.4 for a fixed $\sqrt{s}$, as a function of the Higgs boson mass. This is the cross-section for Higgs production in the SM, which is corrected by a $\sin^2\delta$ factor in 2HDM. For low Higgs masses, the h^0Z^0 production can be viewed as the radiation of a Higgs boson from a slightly off-shell Z^0 boson – the cross-section decreases with the centre-of-mass energy, in the same way as the $q\bar{q}$ cross-section at LEP2 energies. For high Higgs masses, there is a threshold at the point where the two massive bosons can not be on-shell, and the cross-section increases with the centre-of-mass energy as more phase space is available. For LEP2 energies, the separation between the high and low mass regions is at around 75 GeV/c^2.

The efficiencies for the signal selections were estimated from fully simulated samples generated with Pythia at all centre-of-mass energies and covering the available mass range. They were cross-checked with a dedicated generator HZHA[73] and found to be compatible – within the combined statistical error of 1% – for all the mass range studied. Different fragmentation/hadronization tunings were also tested and found to lead to negligible effects on the selection.

The distribution of the events as a function of the Higgs mass is a fundamental point in the limit extraction. The fitted $\gamma\gamma$ masses obtained for the final h^0Z^0 candidate events are shown in figure 5.5 together with the reconstructed jet-jet invariant masses. Since the Higgs mass is reconstructed with high resolution, the effective signal/background ratio in the statistical analysis depends only on small regions of the mass spectra, and it is thus very important to accurately reproduce the expected background and signal distributed in $M_{\gamma\gamma}$.

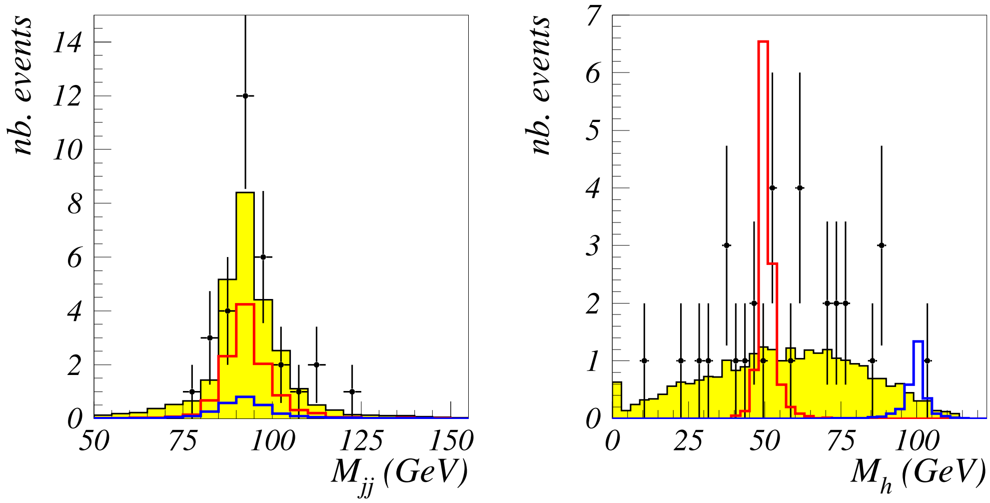

Figure 5.5: Reconstructed masses in h^0Z^0 at the final analysis level. The invariant jet-jet mass (left) before the kinematic fit and the Higgs mass (right) – obtained as the two photon invariant mass, after constraining $M_{jj} = M_{Z^0}$ – are shown for all data (dots), SM background (shaded area) and two h^0Z^0 signals, with M_{h^0}=50 GeV/c^2 and M_{h^0}=100 GeV/c^2, produced with SM cross-section and a $BR(h^0 \rightarrow \gamma\gamma)$=7.5%.

In the background, the $M_{\gamma\gamma}$ spectra is only constrained by the available phase-space: to obtain smooth distributions for all samples, the global spectrum in figure 5.5 was used, and re-weighted for each centre-of-mass energy using the information at previous selection levels, with higher event numbers. The effect of this procedure is included indirectly in the statistical error of the background – affecting mostly the smaller generated samples. The background description relied on very large samples of 4-fermion and $q\bar{q}(\gamma)$ events, while the contribution from all the other processes was expected to be of less than 1 event for all the integrated luminosity. For the main background of $q\bar{q}\gamma\gamma$, the equivalent luminosity used was around 200 times the real data's integrated luminosity, although the distribution by the various centre-of-mass energies was not uniform.

In the signal samples, and since the total Higgs boson width is negligible in comparison with the experimental mass resolution, the $M_{\gamma\gamma}$ distribution is well parametrized by a gaussian. The fit imposing the Z^0 mass implies an artificial cut on the reconstructed masses (the Z^0 should be more often produced off-shell, since its total width is larger) but this was checked to have no influence in the final results: the mass distributions at threshold are then described by a cut gaussian. These signal mass parameterizations were used to extend the signal expectations to mass points in between the fully simulated signals at all centre-of-mass energies.

5.3.2 Results on $\mathbf{h^0Z^0}$ Production

The results from the $q\bar{q}\gamma\gamma$ analysis were put together with the ones from the analysis of other Z^0 decays into fermion pairs and h^0 decays to photons [71].

A good agreement between data and SM expectations was found in all analysed channels – comprising Z^0 decays to quark pairs, neutrino pairs and charged lepton pairs – with a total of 54 events selected and 52 ± 1 expected. The final mass distributions for the neutrino and charged lepton channels are shown in figure 5.6 and the detailed numbers of selected events per channel and centre-of-mass energy are shown in table 5.3. The SM expectations in the channel with photons only are corrected for the trigger efficiencies, of the order of 97% in the barrel part of the detector; but the trigger efficiency for final states with charged particle tracks is of the order of 100% and thus the correction is negligible in comparison to the corresponding statistical errors.

$\sqrt{s}$	$\mathcal{L}$	$q\bar{q}\gamma\gamma$		$\nu\bar{\nu}\gamma\gamma$		$l^+l^-\gamma\gamma$	
(GeV)	(pb^{-1})	DATA	MC	DATA	MC	DATA	MC
183	49	4	2.64 ±0.12	2	1.59 ±0.65	–	–
189	153	8	6.85 ±0.33	5	4.82 ±0.55	1	1.70 ±0.44
192	26	0	1.17 ±0.05	1	0.93 ±0.13	0	0.27 ±0.07
196	77	4	3.24 ±0.15	2	2.29 ±0.26	2	0.62 ±0.15
200	85	4	3.15 ±0.15	2	2.31 ±0.24	0	0.60 ±0.15
202	42	3	1.66 ±0.08	1	0.99 ±0.15	0	0.25 ±0.07
205	78	3	3.13 ±0.10	2	2.46 ±0.16	0	0.61 ±0.16
206.5	55	3	2.20 ±0.10	4	1.58 ±0.53	0	0.29 ±0.07
207	84	3	3.11 ±0.14	0	2.49 ±0.16	0	0.69 ±0.17
TOT	647	32	27.15 ±0.38	19	19.46 ±1.04	3	5.03 ±0.55

Table 5.3: Selected data for $h^0 Z^0$ production and corresponding background expectations for the three topologies and all data samples considered. The errors on the background are from MC statistics.

The three analysis share some common points, namely the selection of two photons with high polar angle (and isolated) and of a recoiling system consistent with the Z^0 hypothesis; but are necessarily different in some of the cuts and on the efficiencies and mass resolutions obtained. All the analyses use kinematic fitting, imposing only energy-momentum conservation in the case of the $l^+l^-\gamma\gamma$ analysis (with four well reconstructed particles) and also the recoil mass to be the Z^0 mass in the case of $\nu\bar{\nu}\gamma\gamma$ (for which the only available information is the one from the photon pair). The mass resolution in $l^+l^-\gamma\gamma$ is still the best one: around 1% for $M_{h^0} = 100$ GeV/c^2, to be compared with 2.5% in $q\bar{q}\gamma\gamma$ and 3.5% in the $\nu\bar{\nu}\gamma\gamma$. The efficiencies, on the other hand, are lower in the $l^+l^-\gamma\gamma$ channel: around 30% for the same mass, to be compared with 40% in $q\bar{q}\gamma\gamma$ and 50% in the $\nu\bar{\nu}\gamma\gamma$.

The signals were all generated with the same program and extrapolated according to the same rules: the statistical errors on the efficiencies are all of around 1% and the systematic errors of around 3%. These systematic errors are chosen conservatively in order to incorporate all the small effects of the extrapolations explained above for the $q\bar{q}\gamma\gamma$ analysis.

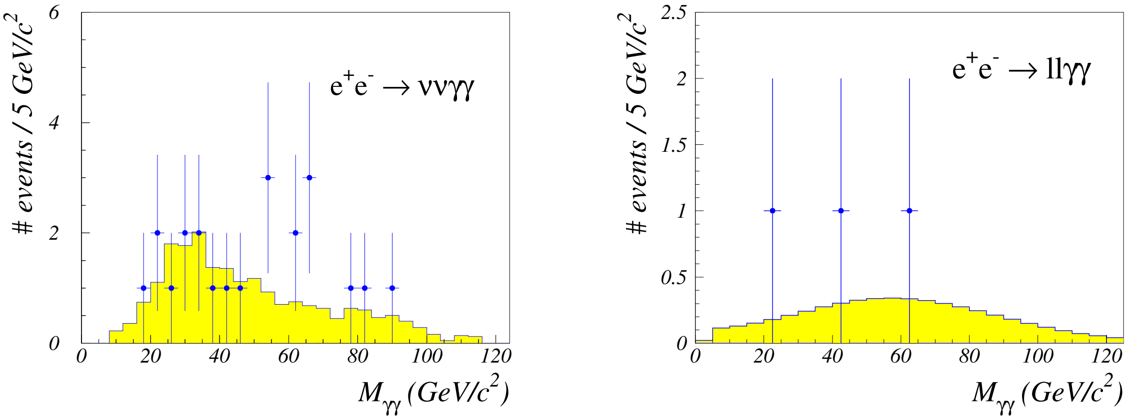

Figure 5.6: M_{h^0} distributions in $\gamma\gamma\nu\bar{\nu}$ (left) and $\gamma\gamma l^+l^-$ (right), for data (dots) and SM background (shaded area) selected at all centre-of-mass energies. In $\nu\bar{\nu}\gamma\gamma$ there are additional 3 data events (for 1.10 $\pm$0.25 expected) from data collected at $\sqrt{s}$=161 and 172 GeV.

Limits on the production cross-section of h^0Z^0 with $h^0 \to \gamma\gamma$ were obtained combining all channels, using the modified frequentist likelihood method[74]. As described in appendix A, this takes into account the measured mass spectra in each channel and data set, together with the corresponding mass probability distribution functions for the background and signal. The relative importance of each channel is fixed by the Z^0 decay branching ratios and the SM H^0Z^0 cross-section dependence on the centre-of-mass energies.

The common enhancement factor to be limited by all channels is expressed as the ratio of the h^0Z^0 production cross-section to the Standard Model (SM) one, multiplied by the branching ratio BR($h^0 \to \gamma\gamma$). Figure 5.7 shows the 95% CL upper limit on this factor as a function of the Higgs mass.

For full strength production (ie, assuming SM cross-section and BR=1) the limit obtained is equal to the expected one and set, by kinematics alone (corresponding roughly to the subtraction of the Z^0 mass from $\sim$ 206 GeV of centre-of-mass energy), at 115 GeV/c^2 at 95% CL. When only the $q\bar{q}\gamma\gamma$ final state is considered, the limit is lower, of 114 GeV/c^2. In fact, all the cross-section limit obtained with that channel alone is around 30% higher than the one obtained with all the possible decay modes; going up to 40% near the kinematic limit, probably due to the worse mass resolution, when the fit imposes a fake mass.

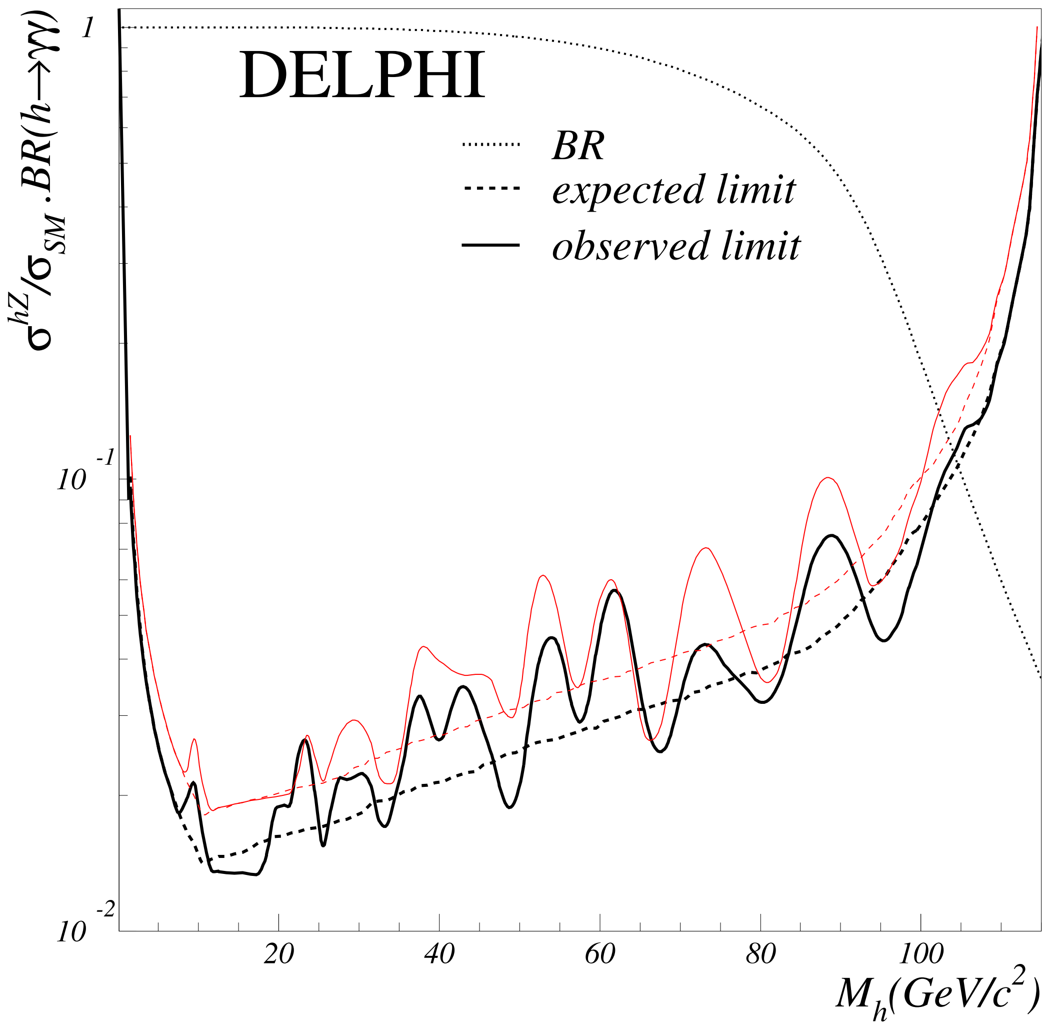

Figure 5.7: 95% CL limit on the $h^0 Z^0$ production cross-section normalized to the SM value $\times$ BR($h \rightarrow \gamma\gamma$): both the observed (full line) and the expected limits (dashed line) are shown. The thin lines correspond to the limit obtained using only the $q\bar{q}\gamma\gamma$ channel and the thick lines, using all channels. Also shown is the fermiophobic BR (dotted line), obtained by keeping the SM couplings of the Higgs to boson pairs and setting the $h^0 f\bar{f}$ couplings to 0.

In the fermiophobic 2HDM [26], the cross-section ratio is constant and equal to $\sin^2\delta$ but the BR depends also on $\sin^2\delta$ and on the other boson masses. If $\sin^2\delta = 1$ and $M_{A^0} > M_{h^0}/2$, then the BR can be obtained by using only SM couplings to bosons and forbidding couplings to fermions – the corresponding curve, obtained with [75], is also shown in 5.7. The BR increases for lower values of $\sin^2\delta$ and so this curve represents a conservative assumption.

In this scenario, a 95% CL limit on the Higgs boson mass (given by the intersection of the cross-section limit with the BR curve) is set at 104.1 GeV/c^2, while the expected limit is of 104.6 GeV/c^2. The highest mass candidate is a $q\bar{q}\gamma\gamma$ event of 103 GeV/c^2 and if only that channel is considered the observed limit is of 102.2 GeV/c^2, to be compared with an expectation of 103.4 GeV/c^2 (also shown in figure 5.7).

5.4 Search for $\mathbf{h^0A^0}$ Production

The dominant decays of the A^0 boson are to $b\bar{b}$ or to h^0Z^0. When both channels are kinematically closed, the dominant decays are to lighter fermions (c-quarks and τ-leptons) and the total A^0 width is also smaller.

In this section we consider only the final states with jets and photons, that is $h^0A^0 \to \gamma\gamma b\bar{b}$ and $h^0A^0 \to h^0h^0Z^0 \to \gamma\gamma\gamma\gamma q\bar{q}$. For the full analysis, it must be taken into account that these final states are only valid for $M_{A^0} > 10$ GeV/c^2 and that, in some special cases, the A^0 can become stable.

5.4.1 $\mathbf{b\bar{b}}\gamma\gamma$ analysis

The analysis of the $b\bar{b}\gamma\gamma$ final state is very similar to that of $h^0Z^0 \to q\bar{q}\gamma\gamma$. The two first levels of the h^0Z^0 analysis are kept but the fit imposing the Z^0 mass must be abandoned so the next selection levels are different.

A fit is performed but with less constraints. The jet-jet invariant mass is left free and an additional ISR photon is allowed in the beam-pipe direction. In fact, if $M_{h^0} + M_{A^0} < M_{Z^0}$, a significant part of the signal events may correspond to radiative returns to the Z^0 with subsequent $Z^0 \to h^0A^0$ decay. The percentage of this kind of events depends solely on the sum of the masses of the two Higgs bosons (it is around 50% for $M_{h^0}+M_{A^0} = 75$ GeV/c^2). Since M_{A^0} has to be fitted without constraints, in this case the global χ^2 must be taken into account: in addition to the previous $\chi^2/ndof$ cuts, the global $\chi^2_{tot}/ndof$ is required to be below 10 in all cases.

In the next level, it is required that $|E_{\gamma1}-E_{\gamma2}| < 0.70|E_{\gamma1}+E_{\gamma2}|$. For the radiative return background the sum is close to $E_{ret} = \frac{s-M_Z{}^2}{2\sqrt{s}}$, being lower (higher) for signals with $M_{A^0} > M_{Z^0}$ ($M_{A^0} < M_{Z^0}$). The background reduction is less powerful than the corresponding one in the h^0Z^0 analysis, but this cut is still useful.

The one but last level consists on the requirement that at least one of the photons is well contained on the HPC and, in a final level, the combined b-tagging of the event (defined in [76]) is required to be high (above -2). This b-tagging cut selects most of the Higgs signal: its efficiency depends only on the A^0 mass and is above 95% for high masses, dropping only when $M_{A^0} < 25$ GeV/c^2 (to around 50% for 10 GeV/c^2). On the other hand, the cut reduces the amount of background in more than 50%. Figure 5.8 shows the agreement of the b-tagging variable in data and SM simulation.

selection	h^0Z^0					h^0A^0			
	D	bkg	$q\bar{q}$	ε^{hZ}_{100}	ε^{hA}_{100}	D	bkg	$q\bar{q}$	ε^{hA}_{100}
no-ISR/FSR	88	72.6±0.8	67.8±0.5	45%	53%	88	72.6±0.8	67.8±0.5	53%
fit	43	38.9±0.5	38.5±0.3	41%	48%	74	64.1±0.7	61.1±0.5	49%
ΔE	33	28.2±0.5	27.8±0.2	40%	48%	61	55.7±0.7	52.7±0.4	49%
HPC	32	27.1±0.5	26.8±0.2	40%	47%	59	53.8±0.6	50.9±0.4	49%
hA / b-tag	9	12.3±0.3	12.2±0.1	8%	45%	21	22.8±0.4	21.4±0.2	46%

Table 5.4: h^0Z^0 versus h^0A^0 analysis: the comparison of data and MC selected in each analysis level for all data sets in both analysis. The efficiency for the selection of a h^0A^0 signal, with $m_{h^0} = 100$GeV/c^2 and $m_{A^0} = m_{Z^0}$ are shown for both cases and compared with the one for a h^0Z^0 signal with the same Higgs mass. The left columns in the last line show the common events in both analysis.

The comparison of the total data and background numbers selected in the h^0Z^0 and

h^0A^0 analysis – at corresponding selection levels – is shown in table 5.4 together with the selection efficiencies for h^0Z^0 and h^0A^0 signals. The mass distributions obtained for h^0 and A^0 are shown in figure 5.8, where the fitted jet-jet invariant mass for the events common with the h^0Z^0 selection is also shown.

The information for the final results, that is the numbers of events in the final selection level per data set, are detailed in table 5.6 together with the ones from the other analysed channel.

The h^0A^0 selection is less restrictive in terms of the fit, since no particular mass is imposed, but in the end a smaller number of events is achieved after the b-tagging cut. The contribution of the non-$q\bar{q}$ background also increases when no particular mass is imposed on the two jet system – it consists namely of semi-leptonic W^+W^- events, in which the electron was reconstructed as two separate neutral clusters, with invariant mass ~ 0; but is also reduced by the b-tagging and amounts to only 1.4 $\pm$0.3 events in the last selection level. In addition, the data and background are now spread over ranges of both $M_{\gamma\gamma}$ and M_{jj} and that information will be taken into account in the limit extraction.

The selection efficiencies, for the same masses, are higher for h^0A^0 production than for h^0Z^0, due to the specific differences of the two processes.

The two cross-sections are directly related to the SM cross-section for H^0Z^0 production and are complementary in the sense that h^0Z^0 is proportional to $\sin^2\delta$ and h^0A^0 to $\cos^2\delta$. However, even if $\delta = \pi/4$ and $M_{A^0} = M_{Z^0}$, there are additional differences due to the different spins of the vector boson Z^0 and the CP-odd scalar A^0, as can be seen in figure 5.9. Since the h^0A^0 production has only one allowed spin state, its cross-section is suppressed in relation to the h^0Z^0 cross-section by a factor of $\lambda/(\lambda + 12.M_Z^2/s)$ (where $\lambda = (1 - (M_1^2 + M_2^2)/s)^2 - 4.M_1^2.M_2^2/s^2$ is the kinematic factor for production of two massive particles). There is an additional suppression near threshold due to the fact that the A^0 width is smaller than the Z^0 width and so there is less off-shell production.

Also the production angles of the two bosons are different: $d\sigma/d\cos\theta$ is given by $\lambda\sin^2\theta + 8M_Z^2/s$ for h^0Z^0 and just by $\sin^2\theta$ for h^0A^0. The h^0A^0 production is more central, which explains why the selection efficiency is already higher than

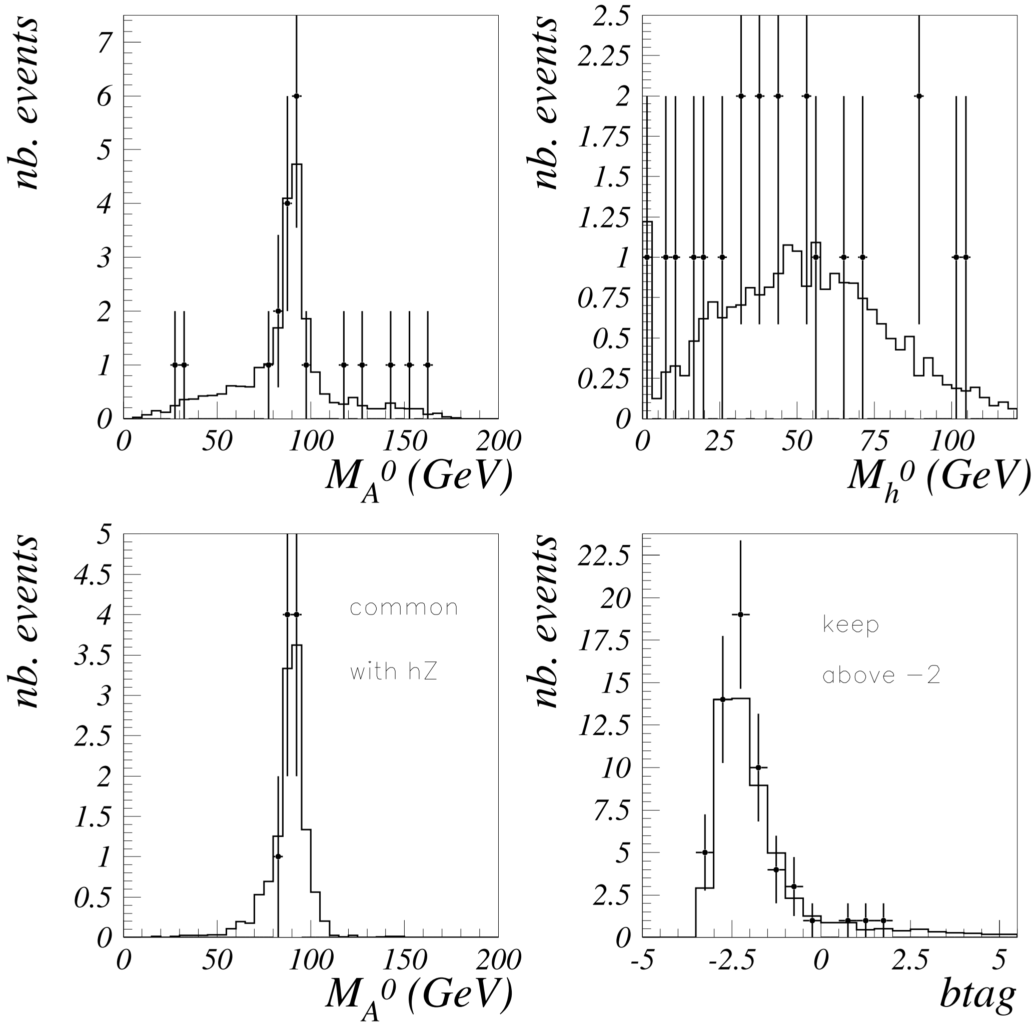

Figure 5.8: $h^0A^0 \to \gamma\gamma b\bar{b}$ analysis: the reconstructed A^0 and h^0 masses at the final analysis level are shown in the top plots for data and expected SM background in all data sets. The lower plots show the fitted jet-jet mass for events selected in both the h^0A^0 and h^0Z^0 analysis and the distribution of the b-tag variable just before the cut at -2.

the corresponding one for h^0Z^0 production at the level of anti-ISR/FSR cuts. The effect is even larger for smaller h^0 masses, due to the λ factor in the h^0Z^0 differential cross-section, and will be even more notorious on the selection efficiency since the photons keep more closely the scalar Higgs boson direction.

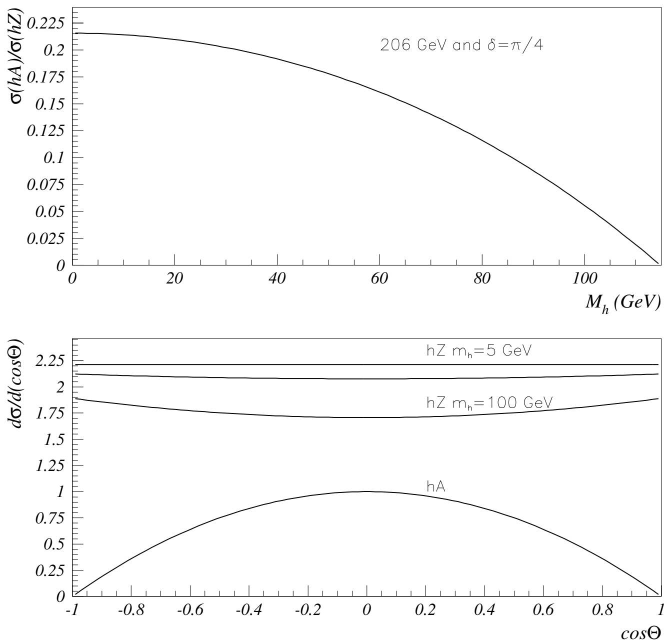

Figure 5.9: h^0Z^0 versus h^0A^0 cross-sections. The top plot shows the ratio of the two cross-sections when fixing $M_{A^0} = M_{Z^0}$ and $\sqrt{s} = 206$ GeV (the ratio is also affected by a factor of $cotg\delta$) as a function of M_{h^0}. The lower plot shows the differential cross-sections for the same conditions; the h^0A^0 differential distribution is independent of the masses, for h^0Z^0 three different M_{h^0} are shown (5, 50 and 100 GeV/c^2).

Contrary to the case of h^0Z^0, for which the efficiency depended on M_{h^0} in a polynomial way, the selection efficiency for the h^0A^0 production is not easily parametrized. The extrapolation from the study of a few fully simulated samples for different (M_{h^0}, M_{A^0}) pairs proved to be difficult and so a procedure was developed to derive the efficiencies from the four momenta of the generated particles.

Starting from the two photons and the two b-quarks at generator level, the detector effects are introduced by parameterizing the energy and angular resolution of the calorimeters and of the full tracking system. For the photons, only the electromagnetic calorimeters resolutions are used, and photons in the hermeticity counters have their energy smeared within a 100% error. For the quarks, the detector response to the full jet must be reproduced, and this is achieved by studying the jet characteristics in fully simulated samples.

By comparing the generated and fully simulated jet quantities in a set of events, they are parametrized taking into account several processes:

- 20% of the energy is lost in non detected final particles;
- the jet directions are smeared according to the initial quark directions; and with an exponential correction if they lay in the forward region;
- the energy is smeared according to the resolutions of both the electromagnetic and hadronic calorimeters;
- the momentum is smeared with a P^2 dependence and an exponential correction for forward particles;
- the total jet momentum is reconstructed from the above according to the relative importances (taken from the fully simulated samples) of momentum carried by charged (70%) and neutral (30%) particles: the first are reconstructed from the smeared momentum and the last from the energy divided in electromagnetic (60%) and hadronic (40%) energy;
- the energy is recalculated from the momentum by assuming a jet opening (mass) proportional to $P^{1/2}$.

The analysis, including the kinematic fits and cuts, are then applied on the smeared quantities. The b-tagging is applied as a final correction depending on the considered A^0 mass, again parametrized by comparing the efficiencies before and after the b-tag cut on the fully simulated samples. Figure 5.10 shows the comparison of the bosons' masses obtained with this method and the fully simulated ones, for two different samples.

The efficiencies obtained are around 40%-50% for most mass pairs but drop rapidly to about 15% for $M_{h^0} + M_{A^0} < M_{Z^0}$ or for very large $M_{h^0} + M_{A^0}$ (and namely very large M_{A^0}), as shown in figure 5.11. Also the mass resolutions are calculated as a function of both masses. The M_{h^0} resolution is around twice the one in the h^0Z^0 analysis, with a large dependence on the mass sum, but mostly on M_{h^0} (directly related to the calorimeter resolution). For M_{A^0}, on the other hand, the resolution is fairly constant and of around 4-5 GeV/c^2. These quantities were cross-checked

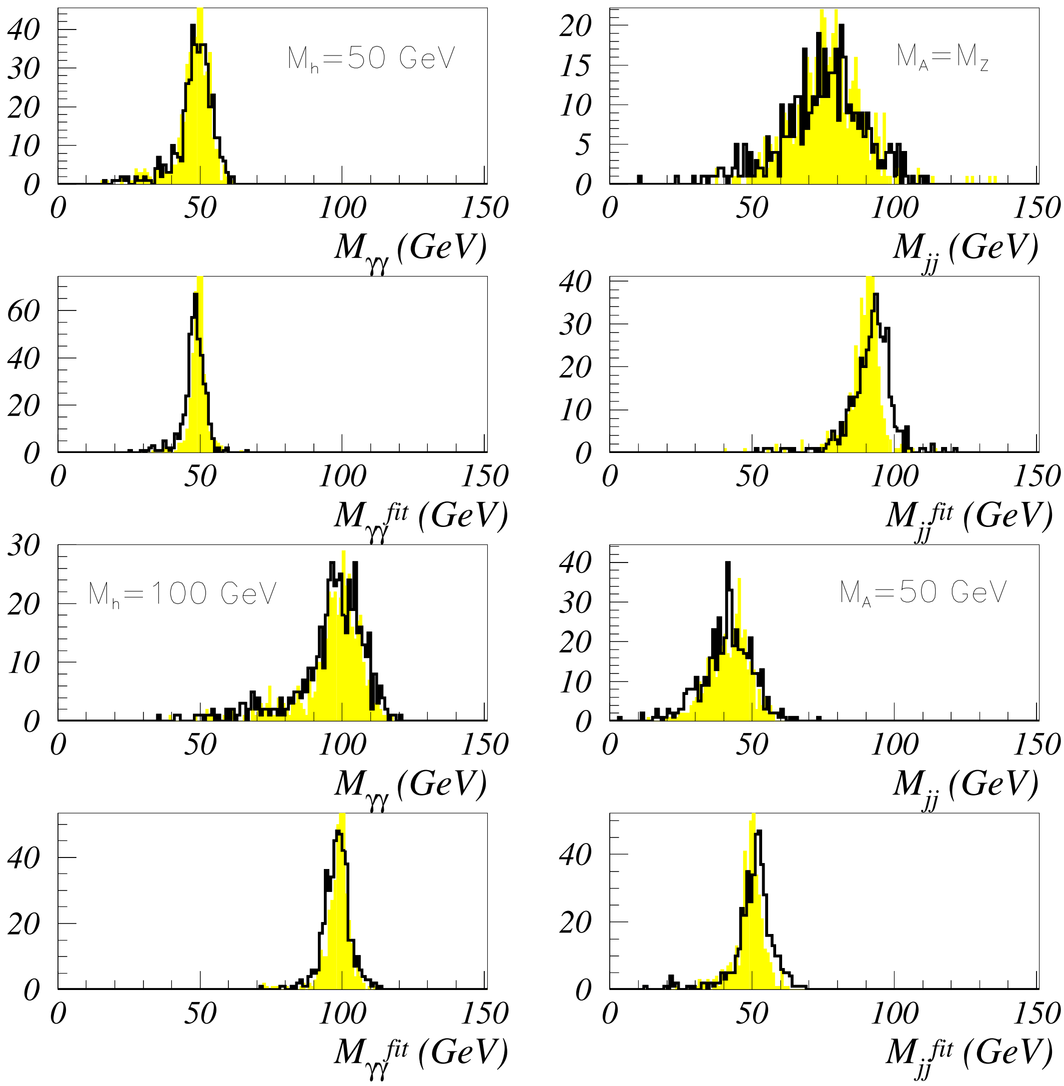

Figure 5.10: Smearing in h^0A^0: the two-photon and two-jet masses are shown before and after the kinematic fit for two different samples: with $M_{h^0} = 50$ GeV/c^2 and $M_{A^0} = 91$ GeV/c^2 (4 upper plots) and with $M_{h^0} = 100$ GeV/c^2 and $M_{A^0} = 50$ GeV/c^2 (4 lower plots). The shaded histograms show the masses reconstructed after the full simulation of the events and the tick lines show the masses, for the same events, after smearing the generator level quantities.

with fully simulated samples and found to agree within the statistical errors, in the case of the mass resolutions, and within ±5% for the efficiencies.

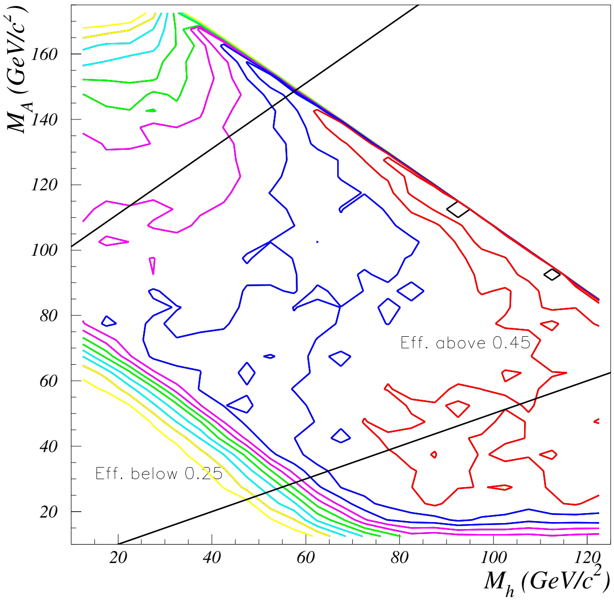

Figure 5.11: Efficiency of the $b\bar{b}\gamma\gamma$ analysis, as a function of both the h^0 and A^0 masses. The straight lines indicate the region for which this is the dominant final state to be considered – and the kinematic limit induced by the $\sqrt{s}$=207 GeV. The lighter to darker curves show the contour levels of efficiency.

5.4.2 $\mathbf{q\bar{q}\gamma\gamma(\gamma)}$ analysis

The selection of this channel is based on the same variables defined for the $q\bar{q}\gamma\gamma$ selection. Although the expected final state would have four photons, the analysis of signal samples shows that in only around 50% of the events (with a large dependence on the masses considered) are the four photons reconstructed as isolated, and so the requirement of three photons allows for a much larger efficiency.

The first level of the analysis requires the presence of at least three isolated photons, at most one converted. Of these three photons, at least two should be above 30° in polar angle and have a transverse energy in respect to any of the jets above 7.5 GeV.

No fit is performed but the jet-jet invariant mass is required to be in between 50 and 130 GeV/c^2. The difference between the energy of any of the photons and the energy carried by all the others has to be below $0.33E_{ret}$. In the last selection level, one of the photons is required to be in the HPC, and at least three photons

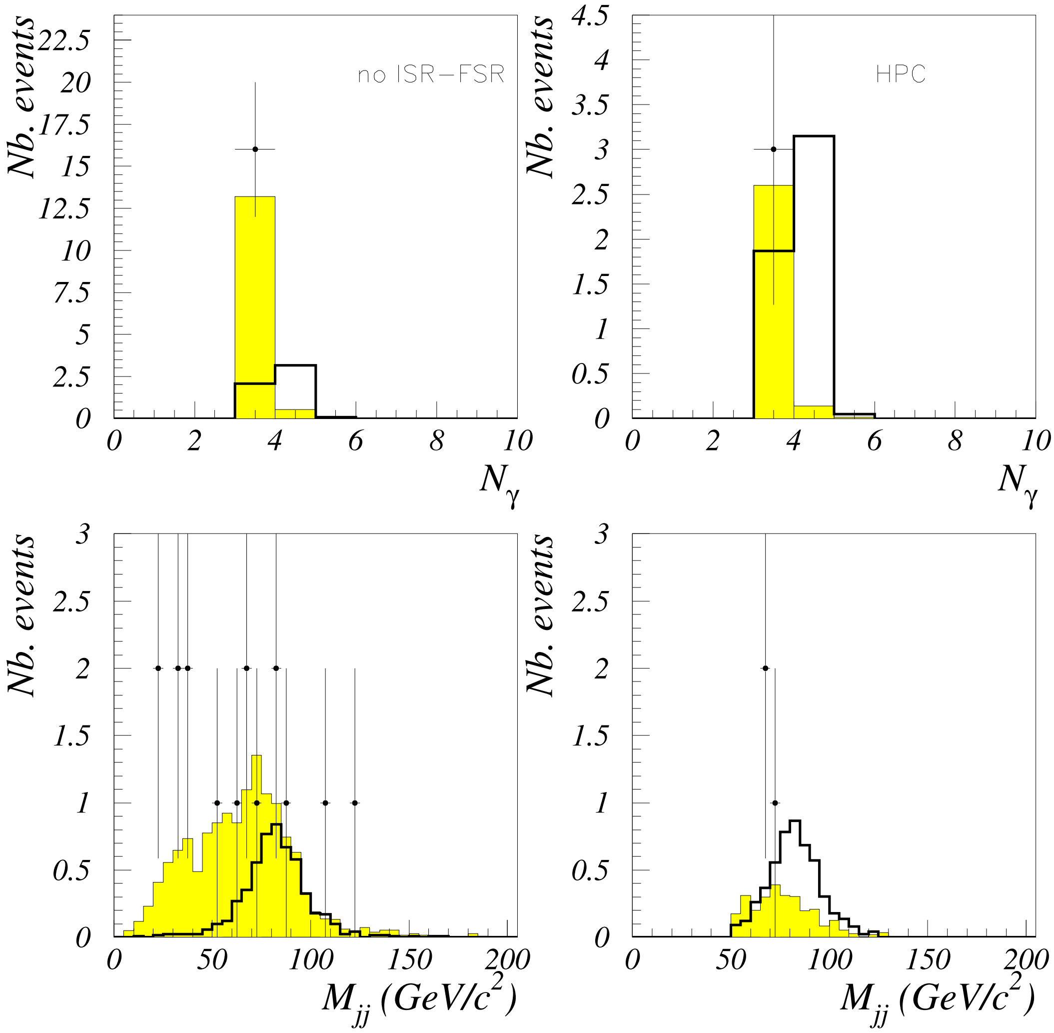

Figure 5.12: $h^0A^0 \rightarrow q\bar{q}\gamma\gamma\gamma(\gamma)$ analysis: the number of photons and the invariant jet-jet masses are shown in the first (left) and final (right) selection level for data (dots), background expectations (shaded area) and a h^0A^0 signal (strong line) with arbitrary normalization.

are required to be above 15°.

selection	D	bkg	$q\bar{q}$
no ISR-FSR	16	13.7 ±0.3	13.1 ±0.3
Z^0 mass	10	10.3 ±0.3	9.7 ±0.3
ΔE	5	5.9 ±0.2	5.4 ±0.2
HPC	3	2.7 ±0.2	2.4 ±0.1

Table 5.5: $h^0A^0 \rightarrow q\bar{q}\gamma\gamma\gamma(\gamma)$ analysis: the comparison of data and MC selected in each analysis level for all data sets is shown.

The number of events selected in all data samples, and the corresponding SM expectations are given in table 5.5. In figure 5.12 the evolution of the data set with the analysis levels is also shown for two variables: the number of photons and the invariant jet-jet mass. The detailed numbers at the final selection level, per data set, are shown in table 5.6.

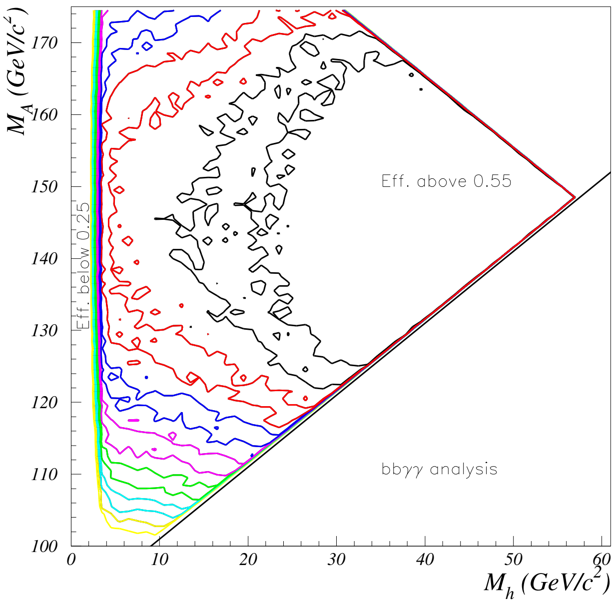

Figure 5.13: Efficiency of the $q\bar{q}\gamma\gamma\gamma(\gamma)$ analysis, as a function of both the h^0 and A^0 masses. The straight lines indicate the region for which this is the dominant final state to be considered – and the kinematic limit induced by the $\sqrt{s}$=207 GeV. The lighter to darker curves show the contour levels of efficiency.

Since only three photons are required, no mass reconstruction is attempted and, for the limit extraction, the total number of selected events is used together with efficiencies and cross-sections which depend on the chosen mass pairs. The parametrization of efficiencies is done using the smearing procedure developed for the $b\bar{b}\gamma\gamma$ channel, and cross-checked with fully simulated samples of the $q\bar{q}\gamma\gamma\gamma$

process (with different mass pairs and centre-of-mass energies) – again the efficiencies obtained are compatible with the expected ones within ±5%. The efficiencies go up to 60% for high masses, and are above 40% for most of the considered range, as shown in figure 5.13.

5.4.3 Results on h^0A^0 production

Within the framework of general 2HDM, the main decay channel of A^0 is $b\bar{b}$ for a wide range of parameters, but the decay to h^0Z^0 becomes dominant when kinematically allowed. The number of selected events in each data set and for each of the two channels is shown in table 5.6.

$\sqrt{s}$	$\mathcal{L}$	$b\bar{b}\gamma\gamma$		$q\bar{q}\gamma\gamma\gamma(\gamma)$	
(GeV)	(pb^{-1})	DATA	MC	DATA	MC
183	49	2	1.90 ±0.10	0	0.23 ±0.04
189	153	3	5.82 ±0.30	0	0.74 ±0.11
192	26	1	0.94 ±0.05	0	0.13 ±0.02
196	77	4	2.82 ±0.14	1	0.29 ±0.05
200	85	3	2.91 ±0.15	1	0.35 ±0.05
202	42	1	1.50 ±0.07	0	0.16 ±0.02
205	78	6	2.43 ±0.09	1	0.32 ±0.04
206.5	55	1	1.85 ±0.09	0	0.20 ±0.03
207	84	0	2.59 ±0.10	0	0.34 ±0.05
TOT	647	21	22.76 ±0.42	3	2.75 ±0.15

Table 5.6: Selected data for h^0A^0 production and corresponding background expectations for the two topologies and all data samples considered. The errors on the background are statistical only.

Limits were extracted with the same algorithm as for h^0Z^0. In the $b\bar{b}\gamma\gamma$ channel the reconstructed mass values for both the A^0 and h^0 were used, while for the $q\bar{q}\gamma\gamma\gamma(\gamma)$ there was no attempt to reconstruct the masses, and pure counting experiments are performed. Both channels had similar sensitivity to the signal.

To extract upper limits on $\cos^2\delta$, reference 2HDM cross-sections computed with

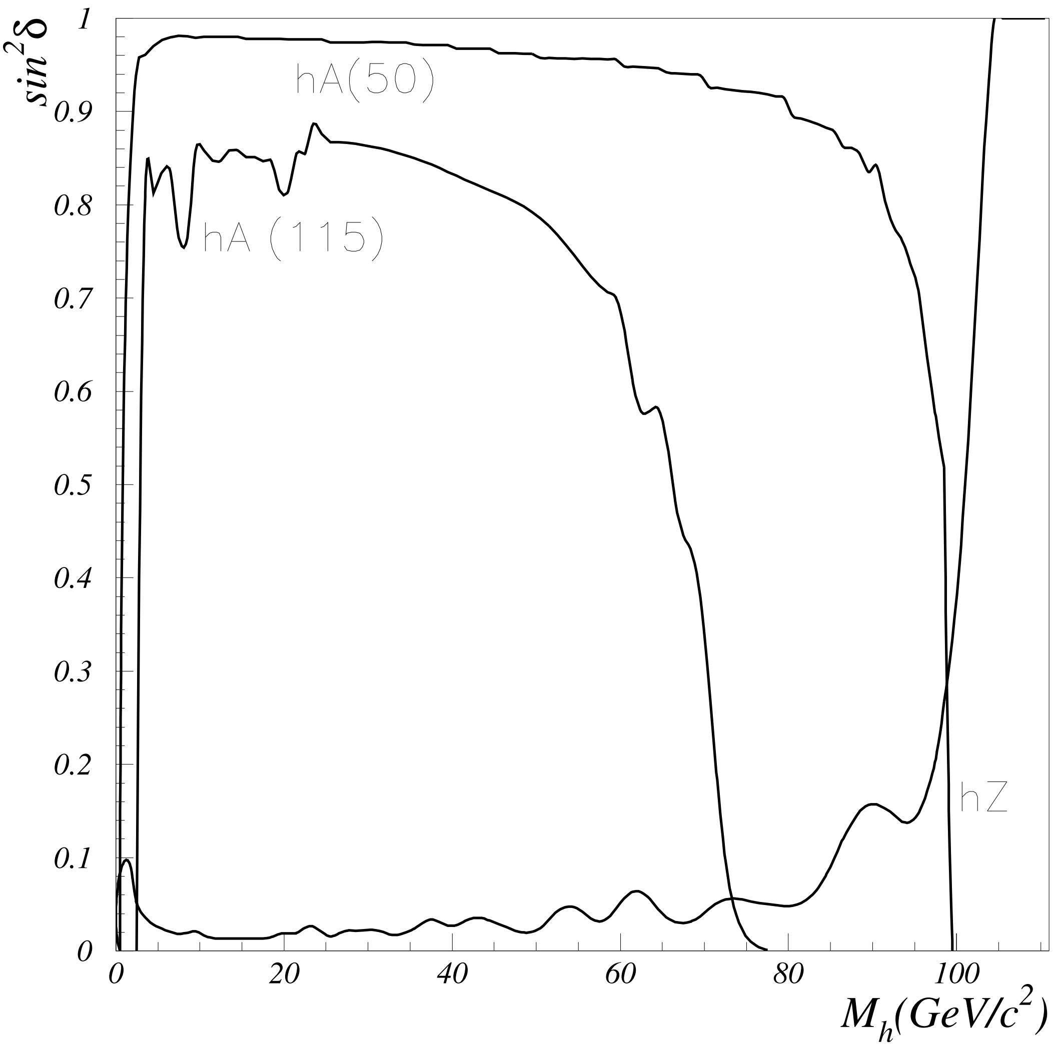

Figure 5.14: Limits in $\sin^2\delta$ from the h^0Z^0 and h^0A^0 analysis. The upper values are excluded by the h^0Z^0 analysis, the limit curve being obtained from fig.5.7 dividing the cross-section limit by the BR curve. The lower values are excluded by the h^0A^0 analysis for each specific M_{A^0}.

[73] were used. For the $h^0 \to \gamma\gamma$ decay, the BR computed with $\sin^2\delta = 1$ and shown in figure 5.7 was used, representing a conservative assumption since BR($h^0 \to \gamma\gamma$) increases for lower $\sin^2\delta$. It should be noted that for $q\bar{q}\gamma\gamma\gamma\gamma$ the BR($h^0 \to \gamma\gamma$) enters twice, but since this analysis covers only low Higgs masses, for which the BR is high ($\sim$ 1.), that does not lead to degraded limits.

Depending on the point in parameter space under consideration, the limit was derived from the dominant decay channel of the A^0 ($b\bar{b}$ or h^0Z^0) which was assumed to have 100% BR.

Figure 5.14 shows the limits from the h^0A^0 analysis, interpreted as lower limits on $\sin^2\delta$, obtained for two different M_{A^0} values as a function of M_{h^0}; together with the upper limits from the h^0Z^0 analysis. As mentioned above, these limits strongly depend on the mass hypothesis used for h^0 and A^0.

5.5 Constraints from other analysis

Although the above analysis cover most of the phase space of the 2HDM fermiophobic scenario, other constraints can be useful to cover special regions. These are briefly described before getting to the general 2HDM fermiophobic model exclusion.

5.5.1 Constraints from LEP 1

The production of Higgs bosons at LEP 1 energies would have the effect of increasing the Z^0 width. Since the Z^0 parameters are very well measured, tight bounds can be derived on the Higgs mass. However these results should be used with some care: the Higgs production would change the result for the hadronic cross-section, which plays an important role in the fitting of the electroweak parameters. In [77], a fit with more independent variables is performed, assuming that only the $e^+e^- \to Z^0 \to e^+e^-$ and $e^+e^- \to Z^0 \to \mu^+\mu^-$ have no contribution from new physics and that the new physics corrections to the other processes are not strongly flavour dependent. The limit thus obtained is almost model independent and completely independent of the efficiency with which the new modes could be selected for the $e^+e^- \to Z^0 \to$ hadrons or $e^+e^- \to Z^0 \to \tau^+\tau^-$ samples. A 95% Confidence Level (CL) upper limit of 6.3 MeV/c^2 is obtained for the change in the total Z^0 width, which yields a limit of 149.4 pb for the production cross-section of unknown particles.

This cross-section limit can be used to constrain both $h^0 Z^{0^*}$ production if $\sin^2\delta = 1$ and $h^0 A^0$ production if $\sin^2\delta = 0$. The first case corresponds to the exclusion of $M_{h^0} < 9$ GeV/c^2 at 95% CL and the second to the exclusion of a band of values corresponding approximately to $M_{h^0} + M_{A^0} < 70$ GeV/c^2 at 95% CL. The intersection of the two regions is excluded for all δ values.

On the other hand, for processes where all the decay products are invisible, the measurement of the Z^0 invisible width can be used directly, leading to tighter limits on their cross-section. LEP 1 data [9] leads to a cross-section upper limit of 67 pb at 95% CL. This limit allows the exclusion of the totally invisible final state arising from $h^0A^0 \to A^0A^0A^0$ and A^0 stable – excluding a band of values corresponding approximately to $M_{h^0} + M_{A^0} < 80$ GeV/c^2 at 95% CL.

5.5.2 Constraints from 6-jet final states

In general 2HDM, the decay $h^0 \to A^0A^0$ is the dominant one when kinematically allowed. This gives rise to final states with 6-fermions, b-jets, c-jets or τs from A^0 decays and $f\bar{f}$ from Z^0 decay.

To cover this kinematic region ($M_{h^0} > 2M_{A^0}$), the results from [78] were used. In this paper general final states, present in 2HDM and other Higgs-sector extensions, are analysed to give model independent results.

In particular, 4b-jets + Z^0 and 6b-jets final states are searched for, and interpreted as $e^+e^- \to h^0Z^0 \to A^0A^0Z^0$ and $e^+e^- \to h^0A^0 \to 3A^0$. Again, the A^0 is assumed to have a mass above 10 GeV/c^2 and decay to $b\bar{b}$.

The limits thus obtained for h^0Z^0 production – using the data with centre-of-mass energy above 183 GeV only – are slightly less tight than the ones obtained for the $h^0 \to \gamma\gamma$. Assuming full strength production ($\sin^2\delta$=1 and all BR=1), they lead to a 105 GeV/c^2 lower mass limit at 95% CL, compared to the 115 GeV/c^2 obtained for $BR(h^0 \to \gamma\gamma) = 1$, and the 105 GeV/c^2 for the Fermiophobic benchmark BR (103 GeV/c^2 if only the Z^0 decays to quarks are considered, as is the case here).

Both the search for fully-hadronic h^0Z^0 and h^0A^0 rely on the high multiplicity of the events but also on the b-tagging. The efficiencies range between 20% to 25% for h^0Z^0 and 25% and 60% for h^0A^0 with the same masses, since the final state with only b-quarks is much more easily selected.

5.5.3 Constraints from photonic final states

When δ approaches 0, the decay $A^0 \to b\bar{b}$ is suppressed and the A^0 becomes invisible for $\sin^2\delta < 10^{-6}$. For this situation, the LEP1 results on the invisible Z^0 width can be used for the low mass A^0 while for higher mass A^0 there will be final states of two acoplanar photons from h^0 decay.

An analysis of those final states was reported in [79], including only lower centre-of-mass energies (from 189 GeV to 202 GeV). That was based on a previous version of the analysis also used for $e^+e^- \to h^0Z^0 \to \gamma\gamma\nu\bar{\nu}$, with small adaptation.

However, since for $\delta \sim 0$ the h^0A^0 cross-section is maximal, this analysis covers mostly the same area as the $h^0A^0 \to b\bar{b}$ analysis does and including all data sets is not necessary.

5.6 Exclusion in the 2HDM parameter Space

All these analysis can be put together to exclude regions of the fermiophobic 2HDM parameter space.

Figure 5.14 shows how limits on $\sin^2\delta$ are derived from the h^0Z^0 and the h^0A^0 analysis. The limits obtained on the cross-sections of h^0Z^0 and h^0A^0 are divided by the $BR(h^0 \to \gamma\gamma)$ curve leading to direct upper limits on $\sin^2\delta$ and $\cos^2\delta$ (ie. lower limits on $\sin^2\delta$), respectively. For a given M_{h^0} and M_{A^0} pair, it can be that all the possible range of $\sin^2\delta$ is excluded and the mass pair is therefore completely excluded.

The BR($h^0 \to \gamma\gamma$) was calculated assuming both M_{H^0} and M_{H^+} to be large (above 500 GeV/c^2) and $\sin^2\delta = 1$. It is a conservative hypothesis in Potential A, where the BR does not depend on these masses (unless they allow for new decay channels), but is not a too general choice for potential B. In Potential B these BR is only valid for all δ if $M_{H^+} > 500$ GeV/c^2; or for $\sin^2\delta > 0.1$ (for all unexcluded M_{H^+} values).

The decay BR of A^0 must also be taken into account. The allowed decays for $M_{A^0} < 10$ GeV/c^2 were not considered, so the only analysis to be used in this region is the LEP 1 analysis. Above that mass, it is assumed that $A^0 \to b\bar{b}$ has a 100% BR (if $\sin^2\delta > 10^{-6}$) except in the region where $A^0 \to Z^0h^0$ decay is allowed and dominates for all $\sin^2\delta < 0.95$.

The obtained 95% CL exclusion on the (M_{h^0},M_{A^0}) plane is shown in figure 5.15, divided in separate regions according to the different kinematics:

I. $M_{A^0} > M_{h^0} + M_{Z^0}$

The dominant decays in this region are $h^0 \to \gamma\gamma$ and $A^0 \to h^0Z^0$ being $\gamma\gamma Z^0$ and $q\bar{q}\gamma\gamma\gamma(\gamma)$ the relevant channels. The vertex $A^0h^0Z^0$ is proportional to $\cos\delta$ and thus, the decay $A^0 \to h^0Z^0$ is dominant only for $\sin^2\delta < 0.95$. However, above this value the mass combinations are excluded by the limits on h^0Z^0 production.

II. $M_{h^0}/2 < M_{A^0} < M_{h^0} + M_{Z^0}$

Most of the parameter space region is dominated by $h^0 \to \gamma\gamma$ and $A^0 \to b\bar{b}$. However, the decay $A^0 \to b\bar{b}$ is suppressed as $\sin^2\delta$ approaches 0, and the results of the $\gamma\gamma + E_{mis}$ analysis must also be used. They cover all the exclusion region obtained from the combination of the h^0Z^0 and $b\bar{b}\gamma\gamma$ analyses for higher $\sin^2\delta$ values. The exclusion shown in figure 5.15 is thus valid for all δ.

III. $2M_b < M_{A^0} < M_{h^0}/2$

The $h^0 \to A^0A^0$ decay becomes dominant when kinematically allowed. The A^0 still decays to $b\bar{b}$ if kinematically allowed, and this gives rise to 6-fermion final states. The 6-jet analysis results for h^0Z^0 and h^0A^0 must then be combined as above.

For very low $\sin^2\delta$ there will then be a region of totally invisible final states for which the results on the invisible Z^0 width are the only available experimental information. These exclude a smaller mass region than the LEP2 6-jet analysis, and both results are represented in the figure.

The LEP1 results on the total Z^0 width are also used to cover the region where the two masses are below the reach of the present analysis.

These exclusions are valid for all the allowed parameter space in the case of Potential A, but only for M_{H^+} >500 GeV/c^2 or $\sin^2\delta > 0.1$ in the case of Potential B. For lower values of both M_{H^+} and $\sin^2\delta$, the BR($h^0 \to \gamma\gamma$) can vanish due to cancellation of the different loop contributions.

Within the two potentials considered, the exclusions given for invisible A^0 (which are more restrictive than the ones for visible final states, in region III) apply only to small mass regions because $\sin^2\delta < 10^{-6}$ implies $M_{h^0} \sim 0$ in Potential A and $M_{h^0} \sim M_{A^0}$ in Potential B. Both bands are in principle outside region III, but since the precise width of these bands is not known, the corresponding region of exclusion for invisible A^0 is also shown.

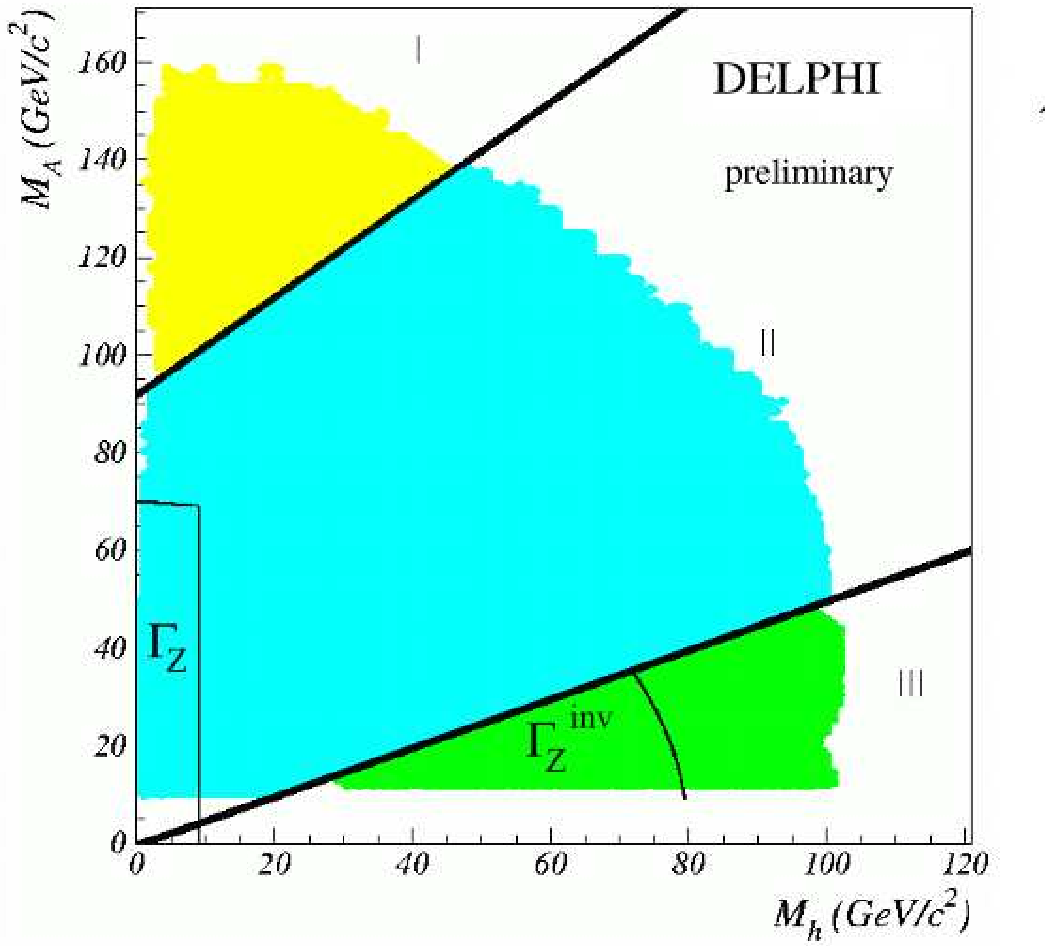

Figure 5.15: Exclusion in the (h^0,A^0) mass plane: the shaded areas correspond to mass regions excluded at 95% CL for all δ values. The plot is divided in regions according to the dominant decay modes of h^0 and A^0, as explained in the text. The curves show the exclusions from LEP 1 data, based on the total and invisible width of the Z^0.

Chapter 6

LEP Combined Results

In the two previous chapters, different kinds of results were extracted from the DELPHI data. The cross-section for $e^+e^- \to W^+W^-\gamma$ was measured, the allowed ranges for possible anomalous quartic gauge couplings were determined and new particles predicted in fermiophobic Higgs scenarios were searched for.

Other experiments have performed similar analysis and, in this chapter, those analysis will be compared with the DELPHI ones, and combined to extract more information on all the covered topics.

The comparison and combination of the results was part of the work of the LEP community. The comparison served, in many cases, to improve each of the analysis and to lead to more complete interpretations. The combination allowed for all the possible information to be extracted precisely from the data.

6.1 $\mathbf{W^+W^-\gamma}$ Cross-Section Measurement

The cross-section for the production of $W^\pm$-pairs with a hard, central and isolated photon in the final state was measured in chapter 4. The cross-section is low and so the result is limited by statistical errors, which amount to more than 20%. A combination of all the LEP data would allow for the reduction of the uncertainties to half of the original values.

The base cross-section to be measured was defined with a semi-analytical approach. The production of a $W^{\pm}$-pair was selected as the CC03 part of the 4-fermion production (that is the contribution of the Feynman diagrams with two $W^{\pm}$ lines) and the hard photon was defined as coming from a 1st order correction to those diagrams. It could be radiated by the initial state electron/positron, by the intermediate $W^{\pm}$ system or by the charged final state fermions from $W^{\pm}$ decay.

One (ISR, WSR or FSR) photon was selected within the following cuts on its energy, isolation in relation to the beams direction and to the final state charged fermions: $E_{\gamma} > 5$ GeV, $|\cos\theta_{\gamma}| < 0.95$ and $\cos\alpha_{\gamma} < 0.90$; all other photons were allowed, with no extra cuts.

The precise definition of what to measure and how to compare with the theoretical expectations is delicate, and lead to extensive debates also among the LEP collaborations and the authors of the available calculations, as will be discussed in the next sections.

6.1.1 Individual measurements

DELPHI and two other LEP collaborations have measured the $W^+W^-\gamma$ cross-sections in different phase space regions. The corresponding results are summarized in table 6.1. All the analysis are done excluding the fully-leptonic final states, and only the DELPHI one includes the $q\bar{q}\tau\nu$ channel; but all are corrected to represent the total $W^+W^-\gamma$ cross-section, irrespective of the $W^{\pm}$ decays.

All the experiments find reasonable agreement between the data and the SM expectations, within the large statistical errors obtained. The precision reached, ranging from 25 to 50%, is not sensitive to the approximations used in the calculations.

The different phase space cuts were chosen by each experiment taking into account both the performance of the data analysis and the way to compare to the SM expectations, but none is perfect.

OPAL was the first of the LEP experiments to publish results on this final state, including only 189 GeV data[82] but results at higher centre-of-mass energy are

cuts	$E_\gamma > 5$GeV $\lvert\cos\theta_\gamma\rvert < 0.95$ $\cos\alpha_\gamma < 0.90$ with all FSR no Mass cut/CC03		$E_\gamma > 5$GeV $\lvert\cos\theta_\gamma\rvert < 0.94$ $\cos\alpha_\gamma < 0.94$ no FSR no Mass cut/CC03		$E_\gamma > 10$GeV $\lvert\cos\theta_\gamma\rvert < 0.90$ $\cos\alpha_\gamma < 0.90$ with all FSR min M> 73 GeV
	DELPHI[80]		L3[81]		OPAL[82]
$\sqrt{s}$	$\sigma WW\gamma$	SM exp.	$\sigma WW\gamma$	SM exp.	$\sigma WW\gamma$
189	.19 ±.09 ±.02	.340 ±.017	.29 ±.08 ±.02	.233 ±.012	.14 ±.04 ±.01
195	.32 ±.13 ±.03	.375 ±.019	.23 ±.10 ±.02	.268 ±.013	–
200	.53 ±.13 ±.04	.392 ±.020	.39 ±.12 ±.02	.305 ±.015	–
206	.34 ±.09 ±.03	.421 ±.021	.33 ±.09 ±.02	.323 ±.016	–

Table 6.1: $W^+W^-\gamma$ cross-sections measured by different LEP experiments, for different signal definitions indicated in the first rows. The expected SM cross-section for the OPAL definition is discussed in the text.

not yet available. The measurement is compared to the expectations of several generators – 85.5 ±0.5 fb (EEWWG), 89.3 ±0.6 fb or 102.4 ±2.2 fb (from other two codes). The two first predictions do not include the non-W^+W^- final states (in EEWWG also FSR is missing), and the latest does not include WSR, and is thus an over-estimation of the cross-section.

L3 was the first to publish results at higher energy, the expected cross-section were obtained with a different version of EEWWG, and are probably over-estimated by $\sim 10\%$, as discussed in the next sub-section.

The DELPHI definition, above, was chosen taking into account the way the cross-section is calculated in the available event generators. The selection of the CC03-like diagrams became necessary because only this part of the cross-section calculation included the WSR contribution – which also exists in single $W^\pm$ final states – and the respective negative interference with ISR – which brings the cross-section down by 20%. This definition implies that the interference with the other diagrams leading to the same 4-fermion final state is neglected (included in the background estimation).

A more experimentally meaningful definition could include an invariant mass cut to select only on-shell $W^\pm$, minimizing the importance of the other contributions.

However, the definition of such a mass cut is also not trivial. The mass which enters the cross-section calculation, in the generator setup, is the invariant mass of the fermions before FSR; which is not a good observable since the FSR interferes with the other radiation processes. On the other hand, when the interference is included in the calculation, the interplay between QED/QCD radiation is lost – which represents a larger effect, only pragmatically introduced in the event generation via the parton shower mechanism. Any mass cut will thus lead to a further dependence on the event generators used.

Experimentally, the mass cut is also difficult to implement, the analysis of each W^+W^- final state used different techniques to reconstruct the $W^\pm$ masses and the corresponding resolutions also vary. The only cut which could be applied on the data would be after all the photon radiation but all photons (also the non-isolated ones), would have to be taken into account, which becomes too difficult in a hadronic environment.

The measurement of the cross-section was then done, in DELPHI, by applying only the above cuts on the photon energy and angles on the data. The same selection was then re-interpreted for different signal definitions – by changing only the efficiencies and background rates. The results obtained were summarized in table 4.9. The four cases considered are: the signal defined with the above cuts on the photon only; with also a mass cut ($|M_{ff} - M_W| < 2\Gamma_W$) applied before FSR; and, for both cases, including or not the FSR component, which is calculated and generated *a posteriori*.

6.1.2 $W^+W^-\gamma$ with no FSR

To compare with the simplest analytical calculation that can be performed to test a new model – as would be, for example, the presence of anomalous quartic gauge couplings – the CC03 component is, in general, the relevant one. In addition, it is also useful to isolate FSR. An extra cut on the mass (before FSR) can be useful to isolate the CC03 component if changes are expected also on other 4-fermion contributions.

Both DELPHI and L3 have interpreted the results in this framework, and selecting a ISR/WSR photon within the phase space cuts defined above for the DELPHI measurement. The two consistent results are shown in table 6.2, together with the value obtained by combining the two measurements, assuming fully uncorrelated errors.

	LEP	DELPHI		L3	
$\sqrt{s}$	$\sigma(WW\gamma)$	$\sigma(WW\gamma)$	SM exp.	$\sigma(WW\gamma)$	SM exp.
189 GeV	.12 ±.06	.05 ±.08 ±.01	.176 ±.004	.20 ±.09 ±.01	.190 ±.010
195 GeV	.17 ±.08	.17 ±.12 ±.02	.203 ±.004	.17 ±.10 ±.01	.219 ±.011
200 GeV	.38 ±.09	.34 ±.12 ±.02	.217 ±.004	.43 ±.13 ±.02	.242 ±.012
206 GeV	.16 ±.08	.18 ±.08 ±.02	.233 ±.005	.13 ±.08 ±.01	.256 ±.013

Table 6.2: $W^+W^-\gamma$ cross-section without FSR and with a mass cut, measured by DELPHI and L3 within the same cuts (defined in the text). The measured values are shown with separate statistical and systematic uncertainties and the expectations quoted by the experiments are shown with the corresponding theoretical uncertainty. The values obtained by combining the two measurements are also shown with only one error, combining statistical and systematic contributions.

The first thing to notice is that the two expected cross-sections for the same conditions are between 1 to 2σ away, with L3's numbers consistently around 10% higher. This discrepancy was shown to come from the different calculations. While DELPHI used WPHACT/YFSWW for the expected SM cross-sections, L3 uses EEWWG (the generator which implements the anomalous gauge couplings), with an extra correction in relation to the DELPHI version. This correction is meant to rescale the coupling constants in the $W^\pm$ production vertices from g(0) to g(M_Z^2) but seems to be unnecessary when further radiative corrections are added. The DELPHI EEWWG implementation was checked to give results compatible with the ones from WPHACT/YFSWW.

The measurements themselves are almost independent of these expectations – since they enter both in the signal and background calculations – and are, within their statistical precision, compatible between themselves. The systematic error of the L3 analysis is dominated by the modelling of photons from meson decays and amounts to 6% of the measured cross-section; in the DELPHI analysis, this effect was included separately, and inexplicitly, in the $q\bar{q}$ and signal modelling. Both the statistical and systematic uncertainties are also compatible for the two experiments.

The combined results are consistent with the expectations within 2 standard deviations, but, due to the extra cuts on the defined signal, the errors still represent more than 25% of the measured values.

6.1.3 LEP $W^+W^-\gamma$ cross-section

The LEP Working Group on 4-fermion final states decided to provide the results for the 4-fermion cross-section with a photon from ISR, WSR or FSR with the above phase-space cuts and a mass cut of $|M_{ff} - M_W| < 2\Gamma_W$, calculated after all photon radiation (to select real $W^{\pm}$ production). This definition tends to select a gauge invariant cross-section but is not well defined in any of the generators available: WPHACT/YFSWW does not implement the FSR interference with the other radiation processes, and RacconWW does it only for 1 photon and not taking into account the competition with gluon radiation present in all the analysed final states.

Studies were then performed to establish how the analysis done by each collaboration, using different signal definitions, could be extrapolated to this common framework. They are illustrated in table 6.3, for the $l\nu l\nu\gamma$ channel.

The $l\nu l\nu\gamma$ final states (which were not analysed, but for which the cross-sections were corrected by efficiency factors) represent more than 2.5% of the total $l\nu l\nu$ cross-section. This factor is larger than for other final states, since there are only two charged fermions in relation to which the photons should be isolated, and the total charge ($\sum Q^2$) in the final state is larger, leading to a higher FSR contribution.

When no cut is applied on the mass, the FSR represents almost 50% of the signal. A cut on the mass prior to FSR reduces the CC03 cross-section by a factor of ~77%, which can be calculated from the Breit Wigner expression; in addition, it selects a region where more than 98% of the 4-fermion cross-section corresponds to the CC03 component[1].

If the cut is applied on the two-fermion masses after all photon radiation, the

[1] The non-CC03 part of the cross-section can be overestimated in WPHACT/YFSWW since it does not incorporate WSR and the negative interference of ISR/WSR. On the other hand, it is not possible to isolate the CC03 component in the RacoonWW calculation.

	189 GeV	206.0 GeV	
total $l\nu l\nu$ cross-section (fb)			
ALL	2393.2 ±4.9	2616.6 ±5.9	
CC03	1719.2 ±4.1	1813.3 ±4.9	
total $l\nu l\nu\gamma$			
ALL	60.5 ±0.8	74.0 ±1.0	2.5% of σ_{tot}
CC03	47.9 ±0.7	58.8 ±0.9	80% of ALL
ISR/ALL	32.3 ±0.6	43.4 ±0.7	≥50% is ISR
ISR/CC03	24.4 ±0.5	35.1 ±0.7	up with $\sqrt{s}$
FSR/ALL	28.1 ±0.5	30.7 ±0.6	≤50% is FSR
FSR/CC03	23.5 ±0.5	23.7 ±0.6	down with $\sqrt{s}$
$l\nu l\nu\gamma$ + cut M before FSR			
ALL	37.2 ±0.6	45.1 ±0.8	selects CC03
CC03	36.9 ±0.6	44.5 ±0.8	99% of ALL
ISR/ALL	18.8 ±0.4	27.0 ±0.6	≥50% is ISR
ISR/CC03	18.8 ±0.4	26.8 ±0.6	
FSR/ALL	18.4 ±0.4	18.1 ±0.5	
FSR/CC03	18.1 ±0.4	17.7 ±0.5	
$l\nu l\nu\gamma$ + cut M after FSR			
ALL	18.8 ±0.4	26.8 ±0.6	cuts out FSR
CC03	18.5 ±0.4	26.1 ±0.6	
ISR/ALL	17.5 ±0.4	24.8 ±0.6	≥90% is ISR
ISR/CC03	17.4 ±0.4	24.6 ±0.6	
FSR/ALL	1.2 ±0.1	2.0 ±0.2	
FSR/CC03	1.1 ±0.1	1.6 ±0.1	
$l\nu l\nu\gamma$ + cut M after FSR + recombination			
ALL	19.9 ±0.4	28.3 ±0.6	recuperates
CC03	19.6 ±0.4	27.7 ±0.6	soft FSR
ISR/ALL	18.5 ±0.4	26.2 ±0.6	
ISR/CC03	18.5 ±0.4	26.0 ±0.6	
FSR/ALL	1.4 ±0.1	2.1 ±0.2	
FSR/CC03	1.2 ±0.1	1.7 ±0.1	

Table 6.3: $l\nu l\nu\gamma$ studies: the cross-sections obtained with WPHACT/YFSWW for different signal definitions are shown. The errors quoted reflect Monte Carlo statistics only, systematic errors of 5% and 2% should be assumed when including FSR or not, respectively.

relative contributions from ISR/WSR and FSR are changed dramatically. In fact, the radiation of a hard photon from the $W^{\pm}$ decay products will move the final masses out of the $W^{\pm}$ peaks, and thus the FSR contribution will be much more severely reduced. There is also a small reduction of the other contributions, tagged by ISR/WSR photons, but in which there are also final state radiation effects.

A problem connected with the check of the FSR description has been discussed for other analysis among the LEP community and the generators' authors. In many cases, it is not possible to separate the photons from the hadronic jets initiated by the quarks or the showers initiated by electrons in the electromagnetic calorimeters. Although this is reproduced by the detector simulation – and thus does not originate disagreements between data and MC expectations – it makes the study of the FSR in real data impossible for this kind of events.

A procedure was adopted for the MC generators checks: the photon 4-momenta is added to the one of the nearest charged fermion if the photon-fermion invariant mass is below 5 GeV/c^2. When this recombination is applied, however, information that could be extracted from the muon data, for example, is lost. The fact that the recombination is decided with an invariant mass threshold can also represent problems for the other final states, as it can happen that two particles distant in space are forced together so long as one of them has a low energy[2]. This recombination procedure was, nevertheless, adopted for the LEP definition of the $W^+W^-\gamma$ signal. The corresponding results are shown in the last rows of table 6.3.

Correction factors of 1.06 $\pm$0.03 can then be applied to the results with CC03 component only and no FSR (and cut on the mass before FSR) to obtain the expected numbers in the LEP common definition: for all 4-fermion cross-section with FSR (and cut on the mass after photon FSR and photon to fermion recombination). The quoted error comes from the numbers in the table, and corresponds to Monte Carlo statistics only. To be conservative, the full correction, of 6% should be considered an extra source of systematic uncertainty.

The study is done only in $l\nu l\nu\gamma$ final states to avoid problems in the definition of photon radiation from quarks. In the other final states, the FSR contribution is smaller and so the correction factor can decrease. On the other hand, the

[2] This definition is more closely reproduced by some of the jet clustering algorithms.

importance of non-CC03 contributions is within the statistical error of the study. It is expected to be also small in the other final states: while $W^+W^- \rightarrow l\nu l\nu$ interferes with both Z^0Z^0 and $We\nu$, for $qqqq$ and $qql\nu$ only one of the two processes contributes.

Clearly, the rescaling procedure is not the ideal one, as the experimental cuts should represent as closely as possible the cuts applied on the signal definition. The DELPHI results were obtained from an analysis with no mass cut, but with generator information being used to estimate the backgrounds from non-CC03 and FSR contributions. The efficiencies were checked to be reasonably independent on the mass cuts for the CC03 component but to vary strongly between the ISR/WSR and the FSR contributions. That variation, together with other variations of the photon differential distributions, was used to estimate a systematic uncertainty which should accommodate the changes in the signal definition, and lead to a greater confidence on the chosen procedure.

The combined DELPHI+L3 result can then be expressed as:

$\sigma(W^+W^-\gamma)$= .13 $\pm$.06 $\pm$.01 pb ($\sqrt{s} = 189$ GeV)
$\sigma(W^+W^-\gamma)$= .18 $\pm$.08 $\pm$.01 pb ($\sqrt{s} = 195$ GeV)
$\sigma(W^+W^-\gamma)$= .40 $\pm$.10 $\pm$.02 pb ($\sqrt{s} = 200$ GeV)
$\sigma(W^+W^-\gamma)$= .17 $\pm$.08 $\pm$.01 pb ($\sqrt{s} = 206$ GeV)

where an additional 6% uncertainty was added by the rescaling procedure.

6.2 Anomalous Quartic Gauge Couplings

Both charged and neutral quartic gauge couplings have been studied at LEP. The neutral couplings can not easily be related to the charged ones even if the custodial symmetry seems to imply that they should have the same order of magnitude. Only the results on the charged QGCS, studied in the thesis, will be reviewed here.

6.2.1 AQGC from $W^+W^-\gamma$ analysis

The analysis of $W^+W^-\gamma$ final states by DELPHI, L3 and OPAL was, in all cases, used to search for possible effects of the presence of anomalous quartic gauge couplings, $W^+W^-\gamma\gamma$ or $W^+W^-Z^0\gamma$. Both L3 and OPAL have considered only the parameters a_c/Λ^2, a_0/Λ^2 and a_n/Λ^2 (while DELPHI interpreted also the results on the related couplings $\tilde{a}_0/\Lambda^2$ and $\tilde{a}_n/\Lambda^2$) and all have used EEWWG generator to describe the anomalous expectations.

As shown in chapter 4, the estimation of the anomalous parameters is more precise if information on the photon spectra is used in addition to the measured total $W^+W^-\gamma$ cross-sections. All the analysis have used the energy spectra of the selected photon to discriminate the anomalous signal from the SM background.

The photon energy spectra and total cross-sections were obtained by each experiment using different phase space cuts and should not be combined directly, but the estimation of the anomalous parameters a/Λ^2 can be put together when expressed as $-\ln\mathcal{L}$ curves. A simple addition of the curves will give the combined $-\ln\mathcal{L}$, so long as all the systematic errors are considered uncorrelated. This is an approximation since all the experiments use the same anomalous $W^+W^-\gamma$ event generator, but is justified as all use different phase space cuts and slightly different background estimations.

In fact, even the definition of the expected photon spectra is calculated with different techniques: while in DELPHI it was chosen to add the anomalous contribution to the SM expectations from WPHACT/YFSWW, the other experiments fully rescale the SM curves to get the correct spectra in the presence of anomalous couplings, relying more heavily on the EEWWG description.

DELPHI and L3, both measure all the a/Λ^2 parameters to be compatible with their SM value, of 0, and have similar sensitivities even if they check slightly different parts of the phase space. The obtained results on each coupling, assuming all the other anomalous parameters to be absent, are shown in table 6.4.

In contrast to the DELPHI results, the errors quoted by L3 are symmetric, due to the fact that L3 results are set closer to the minimum for the expected cross-sections

AQGC (GeV^{-2})	LEP	DELPHI	L3
a_c/Λ^2	-0.006$^{+0.014}_{-0.026}$	0.000$^{+0.019}_{-0.040}$	-0.013±0.023
a_0/Λ^2	0.000±0.009	-0.004$^{+0.018}_{-0.010}$	0.000±0.010
$\tilde{a}_0/\Lambda^2$	-0.007$^{+0.019}_{-0.008}$	-0.007$^{+0.019}_{-0.008}$	-
a_n/Λ^2	0.00$^{+0.06}_{-0.09}$	-0.09$^{+0.16}_{-0.05}$	-0.002±0.076
$\tilde{a}_n/\Lambda^2$	+0.05$^{+0.07}_{-0.15}$	+0.05$^{+0.07}_{-0.15}$	-

Table 6.4: Values of the AQGCs measured by DELPHI and L3 experiments with the $W^+W^-\gamma$ process. The combined result is shown of the first column.

and with slightly higher sensitivity. A gaussian behaviour of the L3 result can then be assumed to construct a likelihood; this is added to the DELPHI likelihood to extract the combined result.

The first results of OPAL, based on the 189 GeV data alone, have lower sensitivity, and also the polar angle distribution of the photon was used in the likelihood fit to extract the anomalous parameters. In that data set, one photon is observed above 30 GeV, for a very small SM expectation of 0.03 ±0.02 events. This leads to the preference of non-SM values for the anomalous QGC parameters. OPAL does not quote 1σ errors on the anomalous parameters, but rather 95% CL limits, shown in the next sub-sections.

6.2.2 AQGC from other analysis

Anomalous contributions to the $W^+W^-\gamma\gamma$ coupling would also contribute to the W^+W^- fusion in the t-channel at LEP, leading to $\nu_e\bar{\nu}_e\gamma\gamma$ final states. That additional process was analysed by L3[81] and, preliminarily, by OPAL[83] and ALEPH[84]. It is sensitive to both a_0/Λ^2 and a_c/Λ^2 (and also $\tilde{a}_0/\Lambda^2$, which was not considered).

There are 12 "WW fusion" SM diagrams leading to the same final state, but the dominant contribution comes from double radiative returns to a Z^0 decaying into neutrino pairs. Extra anomalous contributions could also come from the neutral QGC vertex ($Z^0Z^0\gamma\gamma$, which could also give rise to $Z^0Z^0\gamma$ final states similar to those of $W^+W^-\gamma$), which are absent in the SM and are considered absent also in the charged QGC analysis.

The contribution from the anomalous $W^+W^-\gamma\gamma$ vertices leads to photons of higher energy (mainly noticeable on the least energetic photon spectra) and thus to a smaller mass recoiling against the photon-pair, which peaks at M_{Z^0} for the dominant background. The effect on the total cross-section is small, and even if the the new contribution is easily isolated from the background, the final sensitivity is smaller than the one from the $W^+W^-\gamma$ analysis.

L3 finds a good agreement with the SM, and the inclusion of the $\nu\bar{\nu}\gamma\gamma$ analysis improves the result by 20% for the a_0/Λ^2 limits and 10% for the lower limit of a_c/Λ^2. Also ALEPH finds good agreement with the SM expectations on this channel. OPAL preliminary results again lead to anomalous parameters away from their SM values, re-enforcing the conclusion from the $W^+W^-\gamma$ analysis. When taken together, the two OPAL analysis disfavour the SM by more than 2.5 standard deviations: the confidence level on the $W^+W^-\gamma\gamma$ Standard Model vertex is below 10%.

6.2.3 LEP results on AQGC

Table 6.5 compiles all the 95% CL limits available on charged QGC from the four LEP experiments.

A first comparison of the DELPHI and L3 results shows that they are compatible but that the L3 sensitivity is higher in 10% to 30%. This is true already in the $W^+W^-\gamma$ analysis and is improved by the inclusion of an extra analysis channel.

For a_n/Λ^2 ($W^+W^-Z^0\gamma$ vertex) only the $W^+W^-\gamma$ analysis contributes, and the OPAL results obtained at 189 GeV only are, of course, much less sensitive.

The preliminary results from OPAL for the other two analysed parameters are incompatible with the ones from DELPHI and L3. In fact, they exclude the SM $W^+W^-\gamma\gamma$ vertex at 95% CL, while favouring values of $a_c/\Lambda^2 \sim -0.008/+0.1$ and $|a_0/\Lambda^2| \sim 0.03$. Those results come from the combination of a low sensitivity analysis of $W^+W^-\gamma$ at 189 GeV and the analysis $\nu\nu\gamma\gamma$ at high energy.

Due to the discrepancy with the OPAL preliminary results, no attempt will be made here to combine the results from the four experiments. In the $\nu\nu\gamma\gamma$ analysis performed by the other two collaborations no large discrepancy is seen in relation to the SM expectations[3]. New results on the OPAL analysis of $W^+W^-\gamma$ at higher centre-of-mass energies are expected to appear soon.

AQGC (GeV^{-2})	DELPHI	L3	OPAL*	ALEPH*
a_c/Λ^2	[-0.063,+0.032]	[-0.048,+0.026]	[-0.15,-0.03]U U[0.05,+0.14]	[-0.080,+0.075]
a_0/Λ^2	[-0.020,+0.020]	[-0.015,+0.015]	[-0.054,-0.015]U U[0.015,+0.052]	[-0.029,+0.029]
$\tilde{a}_0/\Lambda^2$	[-0.020,+0.020]	-	-	-
a_n/Λ^2	[-0.18,+0.14]	[-0.14,+0.13]	[-0.61,+0.57]	-
$\tilde{a}_n/\Lambda^2$	[-0.16,+0.17]	-	-	-

Table 6.5: 95% CL limits on the AQGCs obtained by the LEP experiments with the $W^+W^-\gamma$ and $\nu\bar{\nu}\gamma\gamma$ processes. *The OPAL and ALEPH results on a_c/Λ^2 and a_0/Λ^2 are preliminary.

6.3 Fermiophobic Higgs Searches

Fermiophobic Higgs bosons were searched for by all the LEP experiments: all analysed the h^0Z^0 production but only DELPHI interpreted the full 2HDM scenario. Two other searches are discussed in this section. OPAL considered a more general search for two massive bosons – one decaying to two photons and the other to a fermion pair; which can be seen as a h^0A^0 signature. L3 searched for h^0Z^0 with the h^0 decaying to massive gauge bosons.

[3]DELPHI did not search specifically for AQGC in this channel, but the results in [33] do not show any large disagreement with the SM expectations.

6.3.1 $\mathbf{h^0Z^0}$

The searches for h^0Z^0 production were motivated by different theoretical models but a common – more model independent – way of expressing the results was found. The LEP benchmark for fermiophobic Higgs[85] is defined as having SM-like couplings to the gauge bosons while couplings to fermions are forbidden (and no new particles are considered). This assumption fixes not only the behaviour of the h^0Z^0 cross-section as a function of the centre-of-mass energy (it is the SM and the 2HDM behaviour), but also the $BR(h^0 \to \gamma\gamma)$ which is computed with HDECAY[75]. The result can thus be expressed as a single fermiophobic Higgs mass limit – corresponding to the point where the upper limit on the BR is lower than the expected BR.

In the framework of the 2HDM fermiophobic model, these assumptions correspond to the lightest CP-even neutral scalar (h^0) when setting $\sin^2\delta = 1$ and all other Higgs masses inaccessible, in particular $M_{A^0} > M_{h^0}/2$.

All the four experiments studied all the possible decays of the Z^0 boson. ALEPH used a global analysis insensitive to the Z^0 decay, while the three other experiments had specific analysis for $q\bar{q}$, $\nu\bar{\nu}$ and l^+l^- final states. The range of centre-of-mass energies used was however different, with two experiments (ALEPH and OPAL) including LEP1 data explicitly. ALEPH selects 23 events and OPAL 124, both using the full LEP data but different working points, DELPHI and L3 select 54 and 62 events, respectively. In total there are 263 fermiophobic Higgs candidate events, while the SM expectation is of 289.6 (1.5σ higher). DELPHI has the best data/MC agreement over all channels.

The sensitivities achieved by all the experiments are similar at high masses, but ALEPH and OPAL profit from the LEP1 data analysis for the lower mass range. The fermiophobic Higgs mass limits obtained by the individual experiments are thus compatible with eachother, all between 104 and 105 GeV/c^2 [71, 86, 87, 88].

The limits obtained by each experiment, using different statistical methods, were recalculated with the method to be used in the combination – only slightly different from the one described in the appendix A – as a cross-check of the combination program. The results obtained with different schemes were found to agree to the level of 0.5 GeV/c^2 in mass.

The combination was done using all the available information. In particular the mass spectra from all the experiments was used, together with the background expectations and signal efficiencies. The corresponding $\gamma\gamma$ invariant mass spectra above 20 GeV/c^2, is shown in figure 6.1, together with the cross-section limit obtained as a function of the mass.

The combination of all the statistics gives a much higher sensitivity: the 95% CL mass limit if BR($h^0 \to \gamma\gamma$)=1 is set at 117.2 GeV/c^2; and the limit obtained with the fermiophobic BR is 109.7 GeV/c^2 at 95% CL, with an expected limit of 109.4 GeV/c^2.

The 95% CL lower limit on the BR($h^0 \to \gamma\gamma$) – which can be also interpreted as a limit on the product of this BR with the square of the coupling constants factor in a new model (so long as the cross-sections are proportional to the SM ones) – are also shown in figure 6.1. They improve the DELPHI limits (in fig. 5.7) by a factor $\geq$2.

The only assumption in the limit extraction is a fixed (SM-like) behaviour of the cross-section with the centre-of-mass energy. The absolute value can be rescaled by the $h^0Z^0Z^0$ coupling constant, while the coupling structure, on the other hand, is fixed by the quantum numbers of the particles. The limit presented in this way can be used to constraint a large class of models in the absence of anomalous contributions from higher energy new physics (and only for CP-even scalar h^0 particles).

6.3.2 $\mathbf{h^0A^0}$

Only DELPHI analysed the 2HDM fermiophobic scenario and it is thus the only specific search for the pair production of a Higgs boson (decaying into photons) and a CP-odd boson A^0. The limits obtained are shown in figure 5.14 for two A^0 masses.

A general search for two resonances, one decaying to two photons and the other

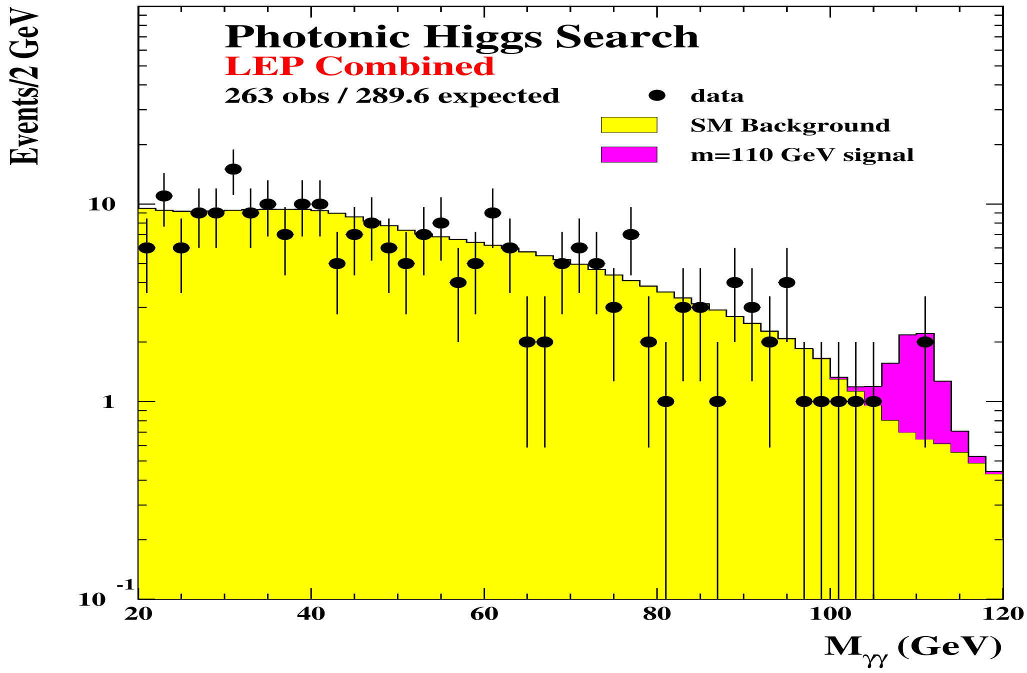

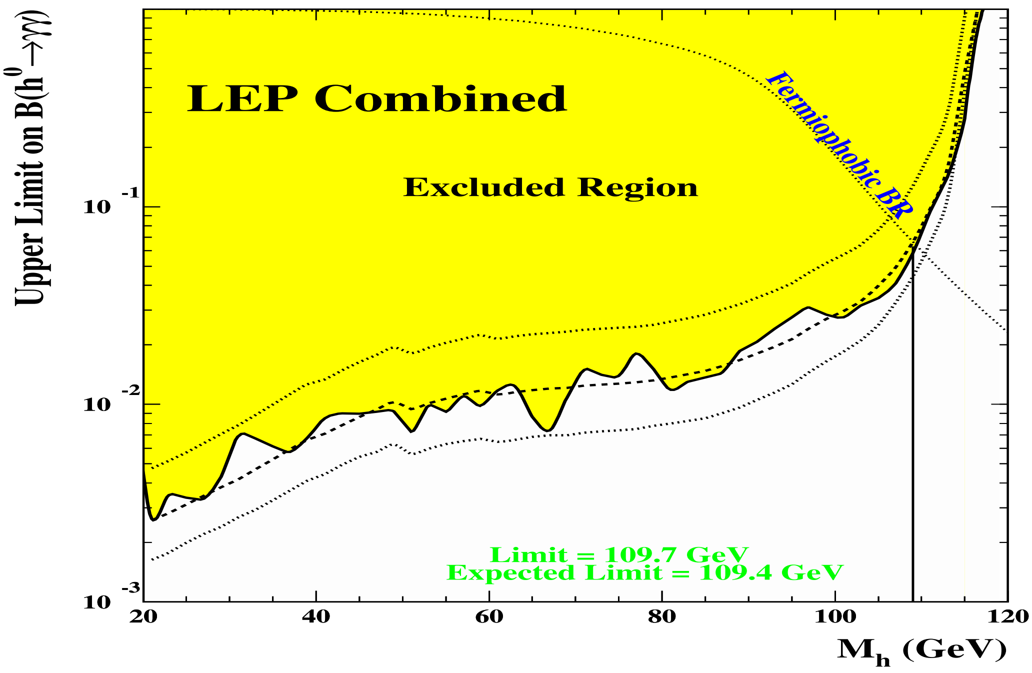

Figure 6.1: LEP results on Fermiophobic Higgs: on the top plot the reconstructed Higgs mass, for data (dots), expected background (light grey) and a Higgs boson of 110 GeV/c^2 (dark grey); on the bottom plot, the upper limit on the scale factor in relation to the SM-like cross-section times the BR($h^0 \to \gamma\gamma$) is compared with the expected limit (and $\pm 2\sigma$ bands). The fermiophobic BR in the benchmark scenario is also shown.

to fermion pairs was done by OPAL[88]. It assumes that both particles can be either scalar or vector, and the limits are given for the production cross-section multiplied by the two BR, separately for the decay to each fermion type. They range between ~ 0.055 pb and ~ 0.030 pb, for the $q\bar{q}\gamma\gamma$ final state, if $M_{A^0} \in [max(M_{Z^0} - M_{h^0}, 10), 200]$ GeV/c^2.

If those results are interpreted in terms of $h^0A^0 \to \gamma\gamma q\bar{q}$ (of which $b\bar{b}$ is a particular case), they can be compared with the DELPHI ones and give an idea of what can be gained by the design of a specific analysis. In fact, the OPAL cross-section limit when convoluted with the fermiophobic BR($h^0 \to \gamma\gamma$), and assuming a 2HDM maximum cross-section ($\cos^2\delta = 1$) allows to exclude regions of mass which form an ellipsoid ranging between M_{h^0} <100 GeV/c^2 (for $M_{A^0} \sim 0$) and M_{A^0} <140 GeV/c^2 (for $M_{h^0} \sim 0$), while the DELPHI analysis of $b\bar{b}\gamma\gamma$ (including all data, and mainly the b-tagging selection) excludes almost all mass pairs with $M_{h^0}+M_{A^0}$ <190 GeV/c^2.

On the other hand, the OPAL analysis takes the lowest efficiency in between all possible vector and scalar particle combinations, and this might be the main factor for the reduced sensitivity of such a general analysis. Similar care should thus be taken when interpreting the results from the DELPHI h^0A^0 search in non-2HDM scenarios.

6.3.3 $h^0 \to W^+W^-$

The branching ratio for $h^0 \to \gamma\gamma$ decreases with the Higgs mass, as the decay to massive gauge boson pairs becomes dominant. The mass limit established above for the benchmark fermiophobic scenario, corresponds to a BR below 10%. It may be worthwhile to look at the other possible decays, namely $h^0 \to W^+W^-$ and $h^0 \to Z^0Z^0$.

The analysis is complicated, both by the multitude of final states from the subsequent decays of the Z^0 and $W^\pm$ bosons and by the fact that, at LEP, there is not enough energy to produce three on-shell massive gauge bosons, and so the final states are characterized by 6-fermions, from which only two pairs will have defined masses (one on-shell Z^0 and one $W^\pm/Z^0$).

Even so, the analysis was done by L3 [89], and leads to 95% CL limits on the product of cross-section factors and BR which go from $\sim$ 30% for $M_{h^0} \sim 80$ GeV/c^2 to 100% for $M_{h^0} = 107$ GeV/c^2. The BR is lower than 10% in the SM (for 115 GeV/c^2 Higgs bosons, down to less than 1% for masses below 100 GeV/c^2), but above 90% for fermiophobic Higgs. In the benchmark fermiophobic scenario, this channel alone exclude masses in between $\sim$85 GeV/c^2 and $\sim$105 GeV/c^2. The exclusion for high mass is as high as the one from the photonic channel, but this means that the combination of two channels, by one experiment alone, leads to a lower limit on the fermiophobic Higgs mass of 108 GeV/c^2.

In addition, a lower mass limit of 107 GeV/c^2 is obtained at 95% CL, for a Higgs which decays only to gauge bosons ($\gamma\gamma$, W^+W^- and Z^0Z^0) – but does not have fixed BR.

6.3.4 LEP results on 2HDM Fermiophobic Higgs

The combination of the h^0Z^0 analysis from all the collaborations extends the sensitivity for each h^0 mass, and (even if only DELPHI analysed the 2HDM fermiophobic scenario) thus allows for the exclusion of lower $\sin^2\delta$ values and of higher masses.

That translates to small differences in the final exclusion plot in figure 5.15, valid for all δ values in the fermiophobic 2HDM. In the region of M_{A^0} <100 GeV/c^2, the LEP results would extend the DELPHI exclusion in M_{h^0} by 2 to 5 GeV/c^2.

The combination of the L3 results for all the fermiophobic decay channels of the h^0 shows that these results can easily be extended by a few GeV/c^2 if these decay channels are included, but this is only relevant for the high h^0 masses. In the fermiophobic-benchmark scenario the two channels could be combined; however this is not the case in the 2HDM where also $H^{\pm}$ loops contribute.

Chapter 7

Conclusions

The two main goals of LEP2 were the precise measurements of the Standard Model parameters, in particular of the couplings between electroweak bosons; and the search for new physics, in particular for the Higgs boson predicted in the SM. The work described in this thesis follows these general goals analysing in detail related physics channels.

The knowledge of the SM parameters only translates to accurate predictions if there are powerful computation techniques to implement higher order corrections to the processes calculated in perturbation theory. The analysis of final states with photons, described in the thesis, provide important checks for the description of both the radiative corrections and of some precise phase space regions which are not taken into account specifically in the calculations.

In the last years, important improvements have been made on the description of the photon radiation in $e^+e^- \to f\bar{f}$, partly motivated by the analysis of $f\bar{f}\gamma\gamma$ final states. The work on the precise description of photon radiation in $e^+e^- \to W^+W^-$ is more recent and the experimental sensitivity is still low. In this case, there is the extra complication of the emission by the intermediate charged bosons and its strong negative interference with the initial state radiation. The data is sensitive to such effects and it was checked that the available descriptions were accurate enough for the experimental precision. As for $e^+e^- \to f\bar{f}$, future improvements will be necessary when the experimental sensitivity increases in the next leptonic colliders foreseen for the future years. In particular, it could become necessary to take into account the interference with the emission from the charged final state fermion which is negligible for the present available precision.

The measurement of the cross-section for $W^{\pm}$-pair production with a hard, central and isolated photon in the final state allowed for a first quantitative check of the radiation description. It provided also an important framework to understand the importance of ISR/WSR interference (which had been neglected in previous calculations) and to discuss in detail how the implementation of the radiative corrections in complex 4-fermion final states could be done. The cross-section, measured for photons within $E_\gamma > 5$ GeV, $|\cos\theta_\gamma| < 0.95$ and with isolation in relation to the final state charged fermions of $\cos\alpha_\gamma < 0.90$, is:

$$
\begin{aligned}
&0.19 \pm 0.09 \pm 0.02 \text{ pb (at } \sqrt{s} = 189 \text{ GeV);}\\
&0.44 \pm 0.09 \pm 0.03 \text{ pb (at } \sqrt{s} = 198 \text{ GeV);}\\
&0.34 \pm 0.09 \pm 0.03 \text{ pb (at } \sqrt{s} = 206 \text{ GeV).}
\end{aligned}
$$

An extra source for photons in W^+W^- final states could be the quartic gauge boson couplings. In the Standard Model this contribution is negligible but the analysis of the $W^+W^-\gamma$ final states was also used to search for possible anomalous effects – which can be due to the existence of new interactions mediated by heavy particles, which are not directly accessible with the present colliders. Furthermore, the search for anomalous quartic gauge couplings also provides a benchmark for the detailed study of these final states, going beyond the total cross-section analysis and including the details of the photon spectra. It is again useful to quantify the agreement of the data with the available descriptions of the SM, in terms of parameters which isolate the possible anomalous effects. The results obtained are in good agreement with the SM predictions, with the anomalous parameters constrained to be:

$$
\begin{aligned}
a_c/\Lambda^2 &\in [-0.063, +0.032] \text{ GeV}^{-2},\\
a_0/\Lambda^2 &\in [-0.020, +0.020] \text{ GeV}^{-2},\\
\tilde{a}_0/\Lambda^2 &\in [-0.020, +0.020] \text{ GeV}^{-2},
\end{aligned}
$$

for the $W^+W^-\gamma\gamma$ coupling,

and:

$$a_n/\Lambda^2 \in [-0.18, +0.14] \text{ GeV}^{-2},$$
$$\tilde{a}_n/\Lambda^2 \in [-0.16, +0.17] \text{ GeV}^{-2},$$

for $W^+W^-Z^0\gamma$ couplings, at 95% Confidence Level.

Although no deviation from the SM was observed in the present analysis, the allowed parameter range is still large and, in future experiments, the search for anomalous quartic gauge couplings can well give the first indications for small changes in the electroweak model and, namely, the symmetry breaking mechanism.

The search for the particles predicted in the 2HDM fermiophobic scenario is a good example of how a multitude of different final states was explored at LEP, trying to cover all the possible symmetry breaking scenarios. The Higgs was assumed to be produced with a Z^0 boson, but also pair produced with other scalars (as the A^0 boson in 2HDM) or with a photon (which could arise in scenarios with higher order anomalous couplings between the Higgs and the gauge bosons). And, in addition to the dominant SM decays, and decays to photons and gauge bosons, also many other special cases were considered.

The combined results from a multitude of analysis done by the four LEP collaborations constrain the mass of Higgs bosons with SM-like couplings to Z^0Z^0 to be above $\sim$ 100 GeV/c^2, at 95% CL, irrespectively of their possible decays. Higgs bosons not produced with Z^0 are also excluded for most scenarios. The particular study of the 2HDM fermiophobic scenario allowed to exclude a large part of the parameter space. In particular, if the lightest CP-even scalar has SM-like couplings to the gauge bosons, its mass is limited to be above 102.2 GeV/c^2, at 95% Confidence Level, by the analysis of $q\bar{q}\gamma\gamma$ described in the thesis alone, and above 109.7 GeV/c^2 when that result is combined with other analysis from the four LEP collaborations.

On the other hand, the importance given to the search of the Standard Model Higgs at LEP2, lead to a great improvement of both the b-tagging techniques (which proved to be very important in the precision measurements of the b-quark properties) and in the reconstruction methods and statistical analysis used[1]. Although the Higgs was not found, the direct searches and the interpretation of all the available precision data constrained the Higgs mass to a small 95% CL interval of [114,193] GeV/c^2, if the Standard Model is to explain all the LEP data.

If the Higgs boson lays in this mass range, it should be easily found with the operation of the Large Hadron Collider, which replaces LEP in the CERN physics program for the near future. The search for the Higgs will again be one of the main tasks, and the decay to photons will be fundamental for some of the mass regions. Although the background processes and the analysis are completely different, the theoretical development of new models to interpret the LEP search can be important in the future interpretation if Higgs boson signals are found.

The precision measurements of the Standard Model parameters at LEP, together with the detailed study of radiative correction implementation, allow for precise predictions to be tested in the future experiments. The constraints coming from the negative results on the searches for new physics at LEP may contribute to point out directions to be followed in the continuation of those searches in the future. In the next years, the hadronic colliders can finally discover the Higgs boson as predicted by the Standard Model, or find evidence for non-standard Higgs bosons or other new particles. At the same time, also the precision tests in B-factories and ν-oscillation experiments can point out the existence of new mechanisms and of how they can be incorporated on an extended standard model. The LEP results will no doubt have to be taken into account as the model is completed, and new leptonic colliders will again be needed to continue the precision tests on a wide range of physics processes as done at LEP.

[1] The improvement in those areas had the curious effect that the search for "flavour-blind" Higgs decaying into hadronic jets, has a sensitivity almost as good as the one achieved for the SM Higgs decaying to $b\bar{b}$ ($\sim$ 113 GeV/c^2 to be compared with the 114 GeV/c^2 for the lower mass limit assuming 100% BR).

Appendix A

Statistical Methods

The cross-section measurements, anomalous parameter extraction or model testing rely on statistical methods which compare the data with different expectations. The expectations are given by a theoretical model but, in general, an analytic description is not sufficient as the detector effects must be introduced. In this appendix the statistical methods used in the analysis are described[1].

A.1 The Likelihood Function

A likelihood function that characterizes the observation in relation to an expectation can be defined as the product of Poisson distributions describing the probability of observing n_i events when μ_i are expected:

$$\mathcal{L} = \prod_i \frac{e^{-\mu_i}\mu_i^{n_i}}{n_i!},$$

where the product runs over all different countings (i), ie, different experiments, different data sets, different intervals for the value of an observable... In general, the expectation in each channel, μ_i, is given by a constant background (b) and a signal (s) which can depend on several parameters (α), ie, $\mu_i = b_i + s_i(\alpha)$.

The measurement of a cross-section or the determination of a parameter can be obtained by finding the maximum of likelihood for the ensemble of counting ex-

[1] A general review of statistical methods can be found in [90].

periments available – the corresponding $\bar{s}$ (or $\bar{\alpha}$) is the value preferred by the measurements.

Usually the maximization of the likelihood is done by minimizing

(1) $-\ln\mathcal{L} = \sum\left[(b_i + s_i(\alpha)) - n_i \ln\left(b_i + s_i(\alpha)\right) + \ln n_i!\right]$

or related functions yielding the same α dependence like

(2) $Q = \sum\left[(b_i + s_i(\alpha) - n_i) + n_i \ln\frac{n_i}{(b_i+s_i(\alpha))}\right]$.

For one channel i, the minimum is trivially found at $\bar{s}(\bar{\alpha}) = n - b$ and $Q(\bar{\alpha}) = 0$. In the combination of several channels, the absolute minimum value of Q gives an indication of the quality of the fit for $\bar{\alpha}$.

A.1.1 Statistical Error

The variation of the likelihood function with α is thus a measurement of the allowed range for the parameter.

This can be seen in simple terms for one channel. To a fixed $\bar{\alpha}$, found at the minimum of $-\ln\mathcal{L}$, corresponds the number of events $n = \sum_i n_i$. However, if the experiment is repeated many times, the number n will be distributed according to a Poisson distribution or, in the limit, a gaussian. Inversely the same is true for the signal expectation $\bar{s}(\bar{\alpha})$ measured through n.

In the case of many channels, the sum of the logarithms of M gaussian functions is distributed according to a χ^2 distribution with M degrees of freedom and $2.Q(\bar{\alpha})$ gives a χ^2 measurement of the fit quality.

If $s(\alpha)$ is a linear function, the likelihood is a gaussian estimator of the α parameter. In this way, the error on the measured $\bar{\alpha}$ is given by 1σ of the gaussian and a variation up to 1.96σ covers 95% of the probablility for α, determining the 95% Confidence Limits (CL) for its variation. This translates to

$-\ln\mathcal{L} - min = \frac{1}{2}\left(\frac{\alpha-\bar{\alpha}}{\sigma}\right)^2$ =0.5 (1σ error) or =1.92 (95% CL limit)

When α is a coupling constant which is small, and the main measurable contribution comes from the interference of the new process with background processes yielding the same final states, $s(\alpha)$ is linear. But, this is not the general case, and usually the estimation is not gaussian in α. The measurement of the 1σ errors (or 95% CL limits) as would be propagated from the number of events seen can still be done by looking at the points where $-ln\mathcal{L}(\alpha)$=0.5 (or 1.92), but these will not be related in a gaussian way.

A.1.2 Systematic Error

While the statistical errors are dealt with by assuming a gaussian behaviour on the data/signal relation, the systematic errors have to be introduced in an independent way.

Several approaches have been considered, the one followed in this thesis consists on using the expected number of events given by $b_i.x_i+s_i(\alpha)$ in the likelihood formula, and minimizing the product $-\Delta \ln \mathcal{L}.G(1, syst)$ (where $G(1, syst)$ is a gaussian of mean 1 and width given by the relative systematic error) to find the best fit of $x_i = G(1, syst)$ for each α value.

However, when different sources of systematic errors are to be introduced – errors affecting differently each background expectation, errors on the signal expectations or errors which are correlated between the several channels – this method leads to a multiple minimization which can be complicated by the appearance of several local minima. On the other hand, the uncertainties can not always be parametrized in a simple gaussian way, and this lead to the development of more general, necessarily non-analytic, methods.

A.1.3 Monte Carlo Methods

In the general case, a full integration can be used to get 95% CL limits or the errors associated to the measurement of α. Usually the integration is done numerically using Monte Carlo (MC) methods which compare the measured values of $\ln \mathcal{L}(n_i)$ with values obtained by replacing n_i by the corresponding expectation: $b_i+s_i(\alpha) \rightarrow$

n'_i. The statistical errors (although calculated from the expected number of events and not from the observed number) are then included in the choice of the n'_i values which are taken randomly according to a distribution centered in $b_i + s_i(\alpha)$.

Since the treatment of the statistical errors was transfered to the evaluation of the expectation, it becomes trivial to introduce the systematic errors as an extra variation. For gaussian systematic errors, a first random number x_i is taken according to a gaussian $G(1, syst)$ and it is then used to generate the poisson distribution with mean value $b_i.x_i + s_i(\alpha)$. Other random numbers can then be used for systematic errors affecting the signal while to obtain correlated errors a common x_i can be used. Any kind of parametrization can be used to simulate the used distributions of $n'_i = b_i + s_i(\alpha)$ and thus this treatment can also be extended to situations where the errors are not gaussian.

For the best estimate of α, when $b_i + s_i(\bar{\alpha}) = n_i$, the values obtained for $\ln \mathcal{L}(n')$ will be distributed around $\ln \mathcal{L}(n)$. When only 5% of the trials are below the value characterizing the data (for positive $s(\alpha)$) a 95% CL limit is reached – if there are both an upper and lower limit on a parameter, this will translate to a 90% CL interval. The percentage of trials rendering a likelihood lower than the one obtained for the data gives directly a confidence level in the α hypothesis being tested.

The heavy use of simulation has, however, the disadvantage that there is no expedite way of combining results. While the analytical evaluation allowed for an easy *a posteriori* combination of results just by adding the separate $-2Q$ curves, if Monte Carlo methods are used the procedure must be repeated over when a new channel is added.

A.2 Hypothesis Testing

When the question is not the measurement of a parameter but the choice between the Standard Model and an alternative model, it might be important to calculate a confidence level in the background only hypothesis (CL_b) as well as in the background+signal hypothesis (CL_{s+b}). This number will characterize the data in relation to the SM expectations although depending also on the signal being tested.

If the measured $\bar{\alpha}$ corresponds to an increase in cross-section too low to be detected, the $CL_{s+b}(\bar{\alpha})$ and $CL_b(\bar{\alpha})$ will be close; and if the question about the new model is asked differently "is there a new contribution in the data?" instead of "what is the value of a new contribution?", then the answer must be that the data is not sensitive to such a process.

A way to quantify this answer is achieved by defining $CL_s = \frac{CL_{s+b}}{CL_b}$, which corresponds to a "background subtraction" at the level of the statistical analysis[2]. The quantity defined in this way is not a proper confidence level (it can be greater than 1) but leads to more conservative statements on the model tested and on $\bar{\alpha}$. If the background correctly describes the data, then $CL_b \sim 0.5$ and the confidence level in the exclusion of a signal $(1 - CL_s)$ is reduced in relation to what would be obtained if CL_{s+b} would be used directly (from 95% to 92.5%, for example).

In extreme cases, when the data is well below the background expectation and the model being studied only predicts positive contributions to the cross-section, it might even happen that both the background only hypothesis and all the possible signals considered are both excluded at some CL... This obviously points out that either there is a problem in the background description, or another (new) process is not included in the prediction, or that the data (or used background description) just corresponds to a large fluctuation. In any case, it does not give a sensible statement on the new signal being tested. The signal can not be simply excluded under this conditions, and while CL_{s+b} is low, the CL_s value can be high as also the background hypothesis is not a good description of the data (CL_b is also low).

To test a signal discovery instead of exclusion, the adequate normalization is:
$1 - CL_b \rightarrow \frac{1-CL_b}{1-CL_{s+b}}$.

Figure A.1 shows the CL_s determination using MC integration and including the above features.

[2]This method was introduced in [74] and is known as the "Modified Frequentist Likelihood Method".

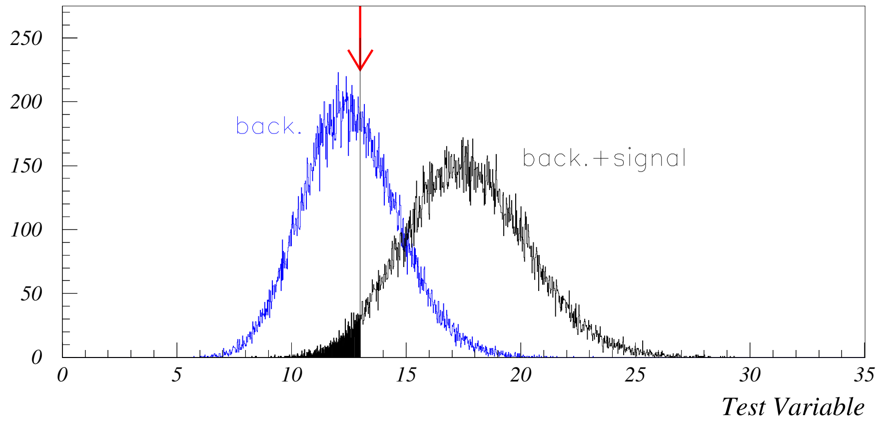

Figure A.1: MC integration of $-\Delta \log \mathcal{L}$.
The arrow denotes the value obtained for the data and the two curves the expected distributions for $n'_i \sim b_i$ and $n'_i \sim b_i + s_i$.
The mean and median of the background curve are displaced in relation to the data value, showing that there is a small excess in data in relation to the background expectation.
The widths of the two curves are given by the combination of statistical and systematic errors.
The dark region corresponds to 3.0% of the gaussian area, which implies that the hypothesis tested is excluded at 97% CL. If we are testing a lower or upper value of α this will correspond to a one-side limit of a 91% CL.
If $CL_s = \frac{CL_{s+b}}{CL_b}$ is used, the confidence level for exclusion of the signal goes down to 95% CL.

A.3 Expected Results

Indirectly, the concept of expected results is introduced by the Monte Carlo Method described above. They can be obtained by conducting large numbers of Monte Carlo (MC) experiments in which the data n_i are replaced by random integer numbers from a Poisson (+ Gaussian) with average given by the expectation[3]. The distribution of results for these MC experiments is characterized by its mean and median, the two values being different for non-gaussian distributions. The

[3] In general, to avoid large fluctuations, the expectation is calculated for the total number in one physics channel and data set and only then distributed in the several bins, according to the expected spectra.

median expected results is usually chosen as it represents more closely what would come out from a single experiment.

In all the cases used in this thesis, we are testing small deviations from the Standard Model. The relevant expected result, to be compared with the obtained result, is then the one obtained when only the background is present, $n_i = b_i$.

The comparison between the "real" and "expected" results can be useful to distinguish between the limitations of the experiments and the physical information given by the data.

A.4 Smoothing

It should be noted that the statistical methods rely heavily on the description of the signal and background processes. Since these expectations are, in general, not described in an analytic way but by finite Monte Carlo samples, some care has to be taken to ensure that the used background (and signal) density functions give a realistic description of the physics – in general continuous and smooth.

Notice that if there is a data point in a given bin with no expected background, this will be identified as a signal discovery but in most cases it is just a sign that not enough MC was produced.

For all the analysis described in this thesis, the probability density functions describing background and signal distributions are "smoothed" in such a way that there are no bins without background – they are replaced with a minimal amount given by the MC statistical error – and that sudden changes between adjacent bins (not due to physical reasons) are diminished. This is achieved by taking into account the experimental resolution on the studied variable and the statistical precision for each bin of the distribution, and allowing the contents to be changed within this limits.

References

[1] S. Andringa, “Estados Finais com Fotões em LEP2: Radiação de Travagem da QED e Decaímentos Anómalos do Bosão de Higgs”, Master Thesis (unpublished), Universidade de Lisboa, 1999.

[2] J.F. Donohue, E. Golowich and B.R. Holstein, “Dynamics of the Standard Model”, Cambridge University Press, 1992.

[3] CDF Coll., F. Abe *et al.*, “Evidence for Top Quark Production in $p\bar{p}$ Collisions at $\sqrt{s} = 1.8$ TeV”, Phys. Rev. Lett. **73** (1994) 225;
D0 Coll., S. Abachi *et al.*, “Observation of the Top Quark”, Phys. Rev. Lett. **74** (1995) 2632.

[4] DONUT Coll., K. Kodama *et al.*, “Observation of tau neutrino interactions”, Phys. Lett. **B504** (2001) 218.

[5] M. Gell-Mann, “Quarks”, Acta Phys. Austriaca **Suppl.9** (1972) 733; H. Fritzsch, M. Gell-Mann and H. Leutwyler, “Advantages of the Color Octet Gluon Picture”, Phys. Lett. **B47** (1973) 365.

[6] R. P. Feynman, “Mathematical Formulation of the Quantum Theory of Electromagnetic Interaction”, Phys. Rev.**80** (1950) 440.

[7] S.L. Glashow, “Partial Symmetries of Weak Interactions”, Nucl. Phys. **22** (1961) 579;
S. Weinberg, “A model of Leptons”, Phys. Rev. Lett. **19** (1967) 1264;
A. Salam, “Weak and Electromagnetic Interactions” in *Elementary Particle Theory*, ed. N. Svartholm (Almqvist and Wiksells, Stockholm, 1968), p.367.

[8] P. Higgs, “Broken Symmetries, Massless Particles and Gauge Fields”, Phys. Lett. **12** (1964) 132;
“Broken Symmetries and the Masses of Gauge Bosons”, Phys. Rev. Lett. **13** (1964) 508 and
“Spontaneous Symmetry Breakdown Without Massless Bosons”, Phys. Rev. **145** (1966) 1156

[9] ALEPH, DELPHI, L3 and OPAL Coll., LEP Electroweak Working Group and SLD Heavy Flavour Group, “A Combination of Preliminary Electroweak Measurements and Contraints on the Standard Model”, (unpublished), CERN-EP/2002-091, hep-ph/0212036.

[10] SuperKamiokande Coll., S. Fukuda *et al.*, “Solar 8B and hep Neutrino Measurements from 1258 Days of Super-Kamiokande Data”, Phys. Rev. Lett. **86**(2001)5651.

[11] SNO Coll., Q.R. Ahmad *et al.*, “Measurement of charged current interactions produced by ^{8}B sola neutrinos at the Sudbury Neutrino Observatory”, Phys. Rev. Lett. **87** (2001)71301
and ”Direct Evidence for Neutrino Flavor Tranformation from Neutral-Current Interactions in the Sudbury Neutrino Observatory”, Phys. Rev. Lett. **89-1**(2002)11301.

[12] L. Wolfenstein, “Parametrization of the Kobayashi-Maskawa Matrix”, Phys.Rev.Lett.**51**(1983)1945.

[13] P. Ferreira, “Can we build a sensible theory with broken charge and colour symmetries ?” (unpublished), hep-ph/0210024.

[14] This plot can be obtained from http://l3www.cern.ch/. Unfortunately, no similar plot was done by the other LEP collaborations.

[15] P. Gambino and A. Sirlin, “Evidence for bosonic electroweak corrections in the Standard Model”, Phys. Rev. **73**(1994)621.

[16] ALEPH, DELPHI, L3 and OPAL Coll. and the LEP TGC Working Group, “A Combination of Preliminary Results on Gauge Boson Couplings Measured by the LEP Experiments”, (unpublished), DELPHI 2002-094 PHYS 924.

[17] P. Sikivie, L. Susskind, M.Voloshin and V.Zakharov, “Isospin Breaking in Technicolor Models”, Nucl.Phys.**B173**(1980)189.

[18] G. Bélanger and F. Boudjema, “Probing Quartic Couplings of Weak Bosons through Three Vectors Production at a 500 GEV NLC”, Phys.Lett.**B288**(1992) 201
and “$\gamma\gamma\rightarrow$ WW and $\gamma\gamma\rightarrow$ ZZ as Tests of Novel Quartic Couplings”, Phys.Lett.**B288**(1992)210.

[19] O.J.P.Éboli, M.C. Gonzalez-Garcia and F. Novaes, “Quartic Anomalous Coulings at $e\gamma$ Colliders”, Nucl.Phys.**B411**(1994)381.

[20] A. Denner, S. Dittmaier, M. Roth and D. Wackeroth, “Probing Anomalous Quartic Gauge-boson Couplings via $e^+e^-\rightarrow$ 4 fermions + γ”, Eur.Phys.J.**C20-2**(2001)201.

[21] ALEPH, DELPHI, L3 and OPAL Collaborations and The LEP Working Group for Higgs Boson Searches, “Search for the Standard Model Higgs Boson at LEP”, Phys. Lett. **B565**(2003)61.

[22] NuTeV Coll., G.P. Zeller *et al*, ”A Precise Determination of Electroweak Parameters in Neutrino-Nucleon Scattering”, Phys.Rev.Lett. **88** (2002)91802.

[23] R. Santos, “Renormalização do Modelo Padrão com dois dubletos de Higgs: alguns exemplos e aplicações.”, PhD Thesis (unpublished), Universidade de Lisboa, 1997.

[24] J. Velhinho, R. Santos and A. Barroso, “Tree level vacuum stability in two Higgs doublet models”, Phys. Lett. **B322**(1994)213.

[25] A.G. Akeroyd, “ Non-minimal neutral Higgs bosons at LEP2”, Phys.Lett. **B377**(1996)95.

[26] A. Barroso, L. Brücher, R. Santos, “Is there a light fermiophobic Higgs?”, Phys. Rev. **D60**(1999)35005.

[27] DELPHI Coll, J. Abdallah *et al*,“Search for Charged Higgs at LEP in General 2HDM”, to be submitted to Eur. Phys. J.

[28] L. Brücher and R. Santos, “Experimental signature of a fermiophobic Higgs boson”, Eur. Phys. J. **C12** (2000) 87 .

[29] P.B. Renton, “Measurement of the Beam Energy at LEP2”, Proceedings of ICHEP’2000 (Osaka), v. 1, 687.

[30] DELPHI Coll., P. Aarnio *et al.*, “The DELPHI Detector at LEP”, Nucl. Instr. and Meth. **A303** (1991) 233.

[31] DELPHI Coll., P. Abreu *et al.*, “Performance of the DELPHI Detector”, Nucl. Instr. and Meth. **A378** (1996) 57.

[32] DELPHI Silicon Tracker group, P. Chochula *et al*, “The DELPHI Silicon Tracker at LEP-2”, Nucl. Instr. and Meth. **A412** (1998) 304.

[33] P. Gonçalves, “Test of QED and Search for New Physics in Multi-Photonic Final States at LEP2 ”, PhD thesis (unpublished), Universidade Técnica de Lisboa, 2002.

[34] B. Tomé, ”High Precision Luminosity Measurement at LEP with the DELPHI STIC Calorimeter”, PhD thesis (unpublished), Universidade de Lisboa, 1998.

[35] K. Hamilton *et al*, “Preliminary determination of E_{beam} at LEP2 using radiative 2-fermion events in DELPHI”, (unpublished) DELPHI 2002-084 CONF 618.

[36] DELPHI Coll., ”DELSIM, DELPHI event generation and detector simulation - Reference Manual”, (unpublished) DELPHI-89-67 PROG/142 (1989);
and ”DELPHI event generation and detector simulation”, (unpublished) DELPHI-89-68 PROG/143 (1989).

[37] S. Jadach and B.F.L. Ward and Z.Wąs, “The Precision Monte Carlo Event Generator KK for Two Fermion Final States in e^+e^- Collisions”, Comp. Phys. Comm. **130** (2000) 260.

[38] S. Jadach and B.F.L. Ward and Z.Wąs, “ The Monte Carlo Program KORALZ, for the Lepton or Quark Pair Production at LEP/SLC Energies: from version 4.0 to version 4.04” Comp.Phys.Comm. **124** (2000)233.

[39] S. Jadach, W. Placzek and B.F.L. Ward, “BHWIDE 1.00: O(α) YFS Exponentiated Monte Carlo for Bhabha Scattering at Wide Angles for LEP-1 / SLC and LEP-2”, Phys.Lett.**B390**(1997)298.

[40] S. Jadach, W. Placzek, E. Richter-Was and B.F.L. Ward, “Upgrade of the Monte Carlo Program BHLUMI for Bhabha Scattering at Low Angles to version 4.04”, Comp.Phys.Comm.**102**(1997)229.

[41] F.A.Berends and R.Kleiss, “Distributions for Electron-Positron Annihilation Into Two and Three Photons”, Nucl. Phys. **B186**(1981)22.

[42] E. Accomando and A. Ballestrero, “WPHACT 1.0: a Program for W W, Higgs and Four Fermion Physics at e^+e^-Colliders”, Comp.Phys.Comm.**99**(1997)270; E. Accomando, A. Ballestrero and E. Maina, “WPHACT 2.0: a fully massive Monte Carlo Generator for Four Fermion Physics at e^+e^-Colliders”, Comp. Phys. Comm. **150** (2003) 166.

[43] T. Sjöstrand *et al.*, ”High-Energy Physics Events Genaration with Pythia 6.1”, Comp. Phys. Comm.**135**(2001)238.

[44] S.Nova, A.Olchevski and T.Todorov, ”TWOGAM, a Monte Carlo event generator for two photon physics”, in “Physics at LEP2”, ed. G.Altarelli, T.Sjöstrand and F.Zwirner, CERN Report 1996-001 (1996) Vol 2,224.

[45] DELPHI Coll.,”DELANA User’s guide”, (unpublished) DELPHI-89-44 PROG/137 (1989);
M. Elsing *et al*,”Changes in the track reconstruction to recover from the TPC sector 6 failure”, (unpublished) DELPHI 2001-004 TRACK 95.

[46] L. de Boeck and G.R. Wilkinson, ”MUFLAG - A framework for muon identification”, (unpublished) DELPHI 93-14 PHYS 262.

[47] F. Cossutti, A. Tonazzo and F. Mazzucato, “REMCLU : a package for the Reconstruction of ElectroMagnetic CLUsters at LEP200 ”, (unpublished) DELPHI 2000-164 PROG 242.

[48] M.C. Espírito Santo, “ Search for Composite and Exotic Leptons with the DELPHI detector at LEP 2”, Ph.D. thesis (unpublished), Universidade de Lisboa, 1998.

[49] S. Catani et al.,"New Clustering Algorithm for Multi-Jet Cross-Sections in e^+e^- Annihilation", Phys. Lett. **B269** (1991) 432.

[50] N. Kjaer and R. Moller, "Reconstruction of invariant masses in multi-jet events", (unpublished) DELPHI 91-17 PHYS 88.

[51] W. Benakker *et al.*, "WW cross-section and distributions", in "Physics at LEP2", ed. G.Altarelli, T.Sjöstrand and F.Zwirner, CERN Report 1996-001 (1996) Vol. 1, 79.

[52] E. Barberio, B. van Eijk, Z. Wąs, "PHOTOS: A Universal Monte Carlo for QED Radiative Corrections in Decays", Comp.Phys.Comm.**66**(1991)115.

[53] S. Jadach *et al.*, "The Tau Decay Library TAUOLA: version 2.4", Comp.Phys.Comm.**76**(1993)361.

[54] S. Jadach *et al.*, "The Monte Carlo Event Generator YFSWW3 version 1.16 for W Pair Production and Decay at LEP-2 / LC Energies", Comp.Phys.Comm.**140**(2001)432.

[55] The LEP Collaborations, ALEPH, DELPHI, L3 and OPAL, and the LEP WW Working Group, "LEP W-pair, Z-pair and Single W Cross Section Results for the Summer 2001 Conferences", (unpublished) DELPHI 2001-124 PHYS 901.

[56] E. Accomando *et al.*, "Four-Fermion Production in Electron-Positron Collisions", in *Report of the WG on precision calculations for LEP2 physics* (ed. S. Jadach *et al.*), CERN 2000-009(2000);
R. Chierici and F. Cossuti, "Radiative Corrections on CC03", (unpublished) DELPHI 2000-11 PHYS 898.

[57] A.P. Chaopvsky and V.A. Khoze, "Screened Coulomb Ansatz for the nonfactorizable Radiative Corrections to off-shell WW production", Nucl.Phys.**B548**(1999)3.

[58] D.R. Yennie, S.C. Frautschi and H. Suura, "The Infrared Divergence Phenomena and Hight-Energy Processes", Annals of Physics **13**(1961)379.

[59] A. Denner *et al.*, "$O(\alpha)$ corrections to $e^+e^- \to WW \to 4$ fermions$(+\gamma)$: first numerical results from RACOONWW", Phys.Lett.**B475**(2000)127.

[60] J. Stirling and A. Werthenbach, "Anomalous Quartic Couplings in WWγ, ZZγ and Z$\gamma\gamma$ Production at Present and Future e^+e^- Colliders", Eur.Phys.J.**C14**(2000)103.

[61] F.A. Berends, R. Kleiss and R. Pittau, "Initial-state QED corrections to four-fermion production in e^+e^-collisions and LEP200 and beyond", Nucl.Phys.**B426**(1994)344.

[62] R. Chierici, C. Parkes and A. Tonazzo, "WWANA A standard package for W analysis", (unpublished) DELPHI 96-128 PROG 218.

[63] D. Jeans, "A study of $e^+e^- \rightarrow W^+W^-$ at centre-of-mass energies between 161 and 209 GeV", PhD thesis (unpublished), Oxford University, 2002.

[64] U. Müller, "Messung des hadronischen Wirkungsquerschnitts des Prozesses $e^+e^- \rightarrow W^+W^-$ mit dem DELPHI–Detektor", PhD thesis (unpublished), Bergische Universität, 2003.

[65] T. Sjöstrand, "Pythia 5.7 and Jetset 7.4", Cern-TH/7112-93, long write-up of Comp.Phys. Comm. **82** (1994) 74.

[66] DELPHI Coll., "Measurement of the W-pair Production Cross-section and W Branching Ratios in e^+e^-collisions at $\sqrt{s}$ = 161-209 GeV", to be submitted to Eur. Phys. J. C.

[67] DELPHI Coll., P. Abreu *et al*, "Measurement and Interpretation of Fermion-Pair Production at LEP Energies of 183 and 189 GeV", Phys.Lett. **B485** (2000)45.

[68] S. Andringa *et al*, "ISR in hadronic events at LEP: generators versus data" (unpublished), DELPHI 99-53 PHYS 824 PROG 237.

[69] DELPHI Coll., P. Abreu *et al*, "Tuning and test of fragmentation models based on identified particles and precision event shape data", Zeit. Phys. **C73** (1996) 11.

[70] D. Bardin *et al*, "ZFITTER v.6.21: A SemiAnalytical Program for Fermion Pair Production in e^+e^- Annihilation", Comp. Phys. Commun. **133**(2001)229.

[71] DELPHI Coll., "Search for a fermiophobic Higgs at LEP 2", in preparation.

[72] E. Gross, G. Wolf and B. Kniehl, "Production and Decay of the Standard Model Higgs boson at LEP200", Z. Phys. **C63**(1994)417 (erratum in Z. Phys. **C66**(1995)321).

[73] P. Janot "HZHA ", in "Physics at LEP2", ed. G.Altarelli, T.Sjöstrand and F.Zwirner, CERN Report 1996-001 (1996) Vol. 2, 309.

[74] A.L. Read, "Modified Frequentist Analysis of Search Results (The CLs Method)"
in "Workshop on Confidence Limits", ed. F. James, L. Lyons and Y.Perrin, CERN Report 2000-005 (2000) p.81.

[75] A. Djouadi, J. Kalinowski and M. Spira , "HDECAY: a program for Higgs boson decays in the Standard Model and its Supersymmettric extension", Comp.Phys.Comm.**108**(1998)56.

[76] DELPHI Coll., J. Abdallah *et al*, "b-tagging in DELPHI at LEP", submitted to Eur. Phys. J. C.

[77] K. Möning, "Model Independent Limit of the Z-decay-width Into Unknown Particles", CERN-OPEN-97-040 (unpublished).

[78] DELPHI Coll., J. Abdallah *et al*, "Searches for Neutral Higgs Bosons in Extended Models", to be submitted to Eur. Phys. J.

[79] DELPHI Coll., P. Abreu et al., "Search for a fermiophobic Higgs at LEP 2", Phys. Lett. **B458** (1999) 431.

[80] DELPHI Coll., J. Abdallah *et al*, " Measurement of the $e^+e^- \to W^+W^-\gamma$ Cross-section and Limits on Anomalous Quartic Gauge Couplings with DELPHI", submitted to Eur. Phys. J. C.

[81] L3 Coll., P. Achard *et al.*, "Study of the W+W- gamma Process and Limits on Anomalous Quartic Gauge Boson Couplings at LEP", Phys. Lett. **B527**(2002)29.

[82] OPAL Coll., G. Abbiendi *et al.*, " Measurement of the W+W- gamma Cross-section and First Direct Limits on Anomalous Electroweak Quartic Gauge Couplings", Phys. Lett. **B471**(1999)293.

[83] OPAL Coll., " Constraints on Anomalous Quartic Gauge Boson Couplings using Acoplanar Photon Pairs at LEP2", (upublished) OPAL Physics Note PN510(2002).

[84] ALEPH Coll., " Constraints on Anomalous Quartic Gauge Boson Coupling from Photon Pair Events from 189 to 209 GeV", (upublished) ALEPH 2001-069.

[85] LEP Higgs Working Group and ALEPH, DELPHI; L3 and OPAL Coll., "Searches for Higgs Boson Decaying into Photons: Combined Results from the LEP Experiments", (unpublished) LHWG Note 2002-02, DELPHI 2002-087 CONF 620, submitted to ICHEP'02.

[86] ALEPH Coll., A. Heister *et al.*, "Search for $\gamma\gamma$ decays of a Higgs boson in e^+e^- collisions at $\sqrt{s}$ up to 209 GeV", Phys. Lett. **B544**(2002)16.

[87] L3 Collab., P. Achard *et al.*, "Search for a Higgs Boson Decaying into Two-Photons at LEP", Phys. Lett. **B534**(2002)28.

[88] OPAL Coll., G. Abbiendi *et al.*, "Search for Associated Production of Massive States Decaying into Two Photons in e+e- Annihilation at sqrt(s)=88-209 GeV", Phys. Lett. **B544**(2002)44.

[89] L3 Collab., P. Achard *et al.*, "Search for a Higgs Boson Decaying to Weak Boson Pairs at LEP", accepted by Phys. Lett. B.

[90] L. Lyons, "Statistics for Nuclear and Particle Physicists", Cambridge University Press, 1986.